Aspects of the mechanics of metallic glasses

by

David Lee Henann

B.S., State University of New York at Binghamton (2006)
S.M., Massachusetts Institute of Technology (2008)

Submitted to the Department of Mechanical Engineering
in partial fulfillment of the requirements for the degree of

Doctor of Philosophy

at the

Massachusetts Institute of Technology

June 2011

Author .....
Department of Mechanical Engineering
May 23, 2011

Certified by .....
Lallit Anand
Rohsenow Professor of Mechanical Engineering
Thesis Supervisor

Accepted by .....
David E. Hardt
Chairman, Department Committee on Graduate Students

Aspects of the mechanics of metallic glasses

by

David Lee Henann

Submitted to the Department of Mechanical Engineering
on May 23, 2011, in partial fulfillment of the
requirements for the degree of
Doctor of Philosophy

Abstract

Metallic glasses are amorphous materials that possess unique mechanical properties, such as high tensile strengths and good fracture toughnesses. Also, since they are amorphous, metallic glasses exhibit a glass transition, and at temperatures above this glass transition, they soften dramatically and are therefore amenable to net-shape thermoplastic forming processes. This combination of superior properties and the ability to precisely form complex geometries makes metallic glasses attractive materials for structural applications. This thesis addresses several issues related to the mechanics of these materials:

- Metallic glasses are near-"ideal" isotropic materials. We have conducted numerical experiments — using molecular dynamics simulations — to develop a continuum-level isotropic elastic free energy that accounts for volumetric-deviatoric coupling effects under circumstances involving large volumetric strains.
- We have developed a large-deformation, elastic-plastic constitutive theory for metallic glasses that incorporates a cavitation mechanism to describe the onset of "brittle" failure. Using this theory, we have conducted finite element simulations of fracture initiation at notch tips in a representative metallic glass under Mode-I, plane-strain, small-scale-yielding conditions. We show that our theory predicts important experimentally-observed, fracture-related phenomena in metallic glasses.
- We have developed a large-deformation, elastic-viscoplastic constitutive theory in a temperature range, which spans the glass transition of these materials. The numerical simulation capability based on the theory is used to determine appropriate processing parameters in order to carry out a successful micron-scale hot-embossing operation for the thermoplastic forming of a Zr-based metallic glass tool for the manufacture of polymeric microfluidic devices.
- The numerical simulation capability is also used to study surface tension-driven shape-recovery of a Pt-based metallic glass and quantitatively determine the surface tension of this material above the glass transition.

Thesis Supervisor: Lallit Anand
Title: Rohsenow Professor of Mechanical Engineering

Acknowledgments

My graduate career has been completed with the support of many people. First and foremost, I would like to express my gratitude to my advisor Professor Lallit Anand for his direction, guidance, and financial support. His dedication to the field of mechanics and materials and the integrity of his research will be a standard for me throughout my career. My thesis committee, Professor David Parks, Professor Raúl Radovitzky, and Professor Christopher Schuh, have provided important input and feedback to my research. Furthermore, the support of Ray Hardin and Leslie Regan has been invaluable to my graduate experience.

The Mechanics and Materials group at MIT is an engaging and fun community. I would like to thank my friends and colleagues Shawn Chester, Vikas Srivastava, Kaspar Loeffel, Claudio Di Leo, Mary Cookson, Suvrat Lele, Nicoli Ames, Meredith Silberstein, Timothy Johnson, Allison Beese, and Matteo Salvetti. In particular, I am indebted to Shawn and Vikas for their constructive criticism and collaboration.

Finally, I thank my parents for their constant encouragement and interest in my academic pursuits, and last but not least, my fiance Stephanie for her constant support and companionship. I will be forever grateful to MIT for giving me the opportunity to meet her.

Financial support for this research was generously provided by grants from the NSF (CMS-0555614) and the Singapore-MIT Alliance (MST).

Contents

List of Figures

List of Tables

Chapter 1

Introduction

1.1 Background

Under slow-to-moderate cooling rates most metallic materials solidify in a polycrystalline form. However, under high cooling rates, certain metallic alloys solidify in a disordered form; such disordered metals are referred to as *amorphous metals* or *metallic glasses*. The first amorphous Au-Si metallic glass was developed in thin ribbon form using a very high cooling rate of $\approx 10^5 - 10^6$ K/s by Klement et al. [1], but by the late 1980s and early 1990s it was discovered that metallic glasses could be processed at relatively slow cooling rates ($1 - 100$ K/s) in *bulk* form in certain multi-component alloy systems due to the sluggish crystallization kinetics in these alloys [e.g., 2–4]. Due to the lack of long-range order, metallic glasses possess unique mechanical properties, which make them attractive materials for fabricating components for a variety of applications. For example, the commercial Zr-based alloys exhibit a reasonably high Young's modulus (≈ 90 GPa), high tensile strength (≈ 2.0 GPa), high yield strain ($\approx$2%), good fracture toughness ($\approx$ 10–50 MPa$\sqrt{\text{m}}$), and good wear resistance (e.g., [2, 3, 5]). *A particularly important characteristic of metallic glasses is their intrinsic homogeneity to the nanoscale because of the absence of grain boundaries.* This characteristic, coupled with their unique mechanical properties, makes them ideal materials for fabricating micron-scale components, or high-aspect-ratio micro-patterned surfaces, which may in turn be used, for example, as dies for the manufacture of polymeric microfluidic devices.

When a metallic glass is deformed at ambient temperatures, well below its glass transition temperature, its inelastic deformation is characterized by strain-softening, which results in the formation of intense localized shear bands. Fracture typically occurs after very small inelastic strain in tension, but substantial inelastic strain levels can be achieved under states of confined compression, such as in indentation experiments [cf., e.g., 6–9].

The micro-mechanisms of inelastic deformation in metallic glasses are not related to dislocation-based mechanisms that characterize the plastic deformation of crystalline met-

als. The plastic deformation of amorphous metallic glasses is fundamentally different from that in crystalline solids because of the lack of long-range order in the atomic structure of these materials. The underlying atomistic mechanisms of the inelastic deformation of metallic glasses have been under intense investigation for the past three decades, and are still not completely understood [cf., e.g., 6–16]. However, atomistic simulations reported in the literature [cf., e.g., 10, 13–16] show that at a micromechanical level, inelastic deformation in metallic glasses occurs by local shearing of clusters of atoms ($\approx$10 to 30 atoms), this shearing is accompanied by deformation-induced *microstructural disordering* and *inelastic dilatation* that produces *strain-softening*, which at low homologous temperatures leads to the formation of intense shear bands. The importance of *dilatancy* in the inelastic response and shear localization of soils and other granular materials, which consist of randomly packed grains, goes back to Reynolds in 1885 [17], who applied the term "dilatancy" to the property possessed by a mass of granular material to alter its volume in accordance with a change in the arrangement of its grains. While the density changes in shear bands in soils are large enough to be experimentally measureable, those in the shear bands in metallic glasses are usually quite small, $\lesssim 0.5\%$, and difficult to measure experimentally [18], and even difficult to discern in atomistic simulations [14].

When a metallic glass is deformed at an absolute temperature in the range $0.7\vartheta_g \lesssim \vartheta \lesssim \vartheta_x$, where ϑ_g and ϑ_x are the glass transition and crystallization temperatures, respectively, its inelastic response is highly rate-dependent, and it deforms approximately "homogeneously" [6]. Indeed in the supercooled liquid rage $\vartheta_g \lesssim \vartheta \lesssim \vartheta_x$ many metallic glasses are known to show superplastic behavior at sufficiently slow strain rates [19].

In recent years, an extremely promising method called thermoplastic forming has emerged [cf., e.g., 19–24]. In this process, the metallic glass is first obtained in the amorphous state by traditional die-casting. The shape in this step is not the final shape but in the form of simple plates or rods. The metallic glass plate (or rod) is then heated into the supercooled liquid region above the glass transition temperature of the material, where it may be isothermally formed to produce intricate microscale patterns and then slowly cooled. Since metallic glasses in their supercooled region are metastable, they eventually crystallize; however, the crystallization kinetics in metallic glass alloys are sluggish, and this results in a relatively large temperature-time processing window in which thermoplastic forming may be carried out without crystallization.[1] Further, since the forming is done isothermally and the subsequent cooling is rather slow, and since there is no phase change on cooling, residual stresses and part distortion can be minimized — all factors which potentially allow for a forming process which is much better controlled than die-casting. A specific thermoplastic forming process geared towards producing nano/microscale, high-aspect ratio, patterned features on surfaces is that of *micro-hot-embossing*. In this process, the metallic glass is formed in its supercooled liquid region by pressing it against a master-surface with the desired nano/microscale features (usually a patterned silicon wafer). The viability of this process has been demonstrated extensively in the literature [cf., e.g., 19–24].

[1]The temperature-time processing window for thermoplastic forming is typically much larger than that afforded by die-casting.

1.2 Contributions of thesis and related publications

This thesis address several issues related to the mechanics of metallic glasses, which are summarized below. Publications in peer-reviewed journals related to each aspect of this work are also listed.

1.2.1 A finite elasticity theory for isotropic materials

It has been shown by Anand [25, 26] that when the infinitesimal strain measure is replaced with Hencky's logarithmic finite strain measure in the classical strain-energy function of linear isotropic elasticity [27–29], the theory is in good agreement with experiments for a wide variety of materials for moderately large deformations, i.e. principal stretches ranging from approximately 0.7 to 1.3. Importantly, the shear and bulk moduli in this theory may still be determined from experimental data at infinitesimal strains. Consequently, all moderate strain non-linearities are incorporated in the logarithmic strain measure. However, when large volumetric strains, either in dilatation or compaction, are attained, this simple finite-deformation hyperelasticity model must be extended to account for such situations, and also to account for important volumetric-deviatoric coupling effects.

Since it is difficult to conduct physical experiments to determine volumetric-deviatoric coupling effects under circumstances involving large volumetric strains, we have conducted numerical experiments – using molecular dynamics simulations. Since we are concerned with a free energy function for isotropic materials, in our molecular dynamics simulations we considered an *amorphous metallic glass* as our representative isotropic material. Based on the results of these numerical experiments, we have developed a continuum-level isotropic elastic free energy that captures the observed coupling effects. The proposed free energy is simple and provides a very good description of the stress-strain results from our molecular dynamics simulations.

Further, plastic flow in metallic materials is known to be "pressure sensitive" – a sensitivity that cannot be ignored at high pressures; accordingly, we have also examined the effect of the volumetric strain on the effective shear stress required for the onset of plastic flow in the metallic glass, and correlated this dependence with the numerically-observed dependence of the elastic shear modulus on the volumetric strain.

- D. L. Henann and L. Anand. A large strain isotropic elasticity model based on molecular dynamics simulations of a metallic glass. *Journal of Elasticity*, doi:10.1007/s10659-010-9297-y.

1.2.2 Fracture of metallic glasses at notches

Experimental observations in the literature reveal some important intrinsic features of the fracture response of metallic glasses at low homologous temperatures:

1. The notch toughness, K_c, of metallic glasses decreases as the notch-root radius, ρ, decreases, with K_c decreasing linearly with ρ [30, 31].

2. Fracture in notched specimens initiates ahead of the notch root where the mean normal stress reaches a maximum value [32].

3. As the ratio μ/κ of the elastic shear modulus μ to the bulk modulus κ increases, the toughness K_c decreases, that is, the material becomes more brittle [33].

Motivated by the free energy function based on our molecular dynamics simulations from the previous section, we introduce an important modification of the finite elasticity relation in the large deformation elastic-plastic Anand-Su theory for metallic glasses [34, 35] to account for the strongly nonlinear and eventually softening, dilatational volumetric elastic response of the material. Using this theory we have conducted finite element simulations of fracture initiation at notch tips in a representative metallic glass under Mode-I, plane-strain, small-scale-yielding conditions. We show that the modified theory predicts three important experimentally-observed phenomena enumerated above.

- D. L. Henann and L. Anand. Fracture of metallic glasses at notches: Effects of notch-root radius and the ratio of the elastic shear modulus to the bulk modulus on toughness. *Acta Materialia*, 57:6057-6074, 2009.

1.2.3 Mechanics of metallic glasses in a temperature range spanning the glass transition

There is no generally accepted constitutive theory to model the large-deformation, elastic-viscoplastic response of bulk metallic glasses in the temperature range relevant to thermoplastic forming. What is needed is a unified constitutive framework that is capable of capturing the transition from a visco-elastic-plastic solid-like response below the glass transition to a Newtonian fluid-like response above the glass transition. We have developed a large-deformation, constitutive theory aimed to fill this need. The material parameters appearing in the theory have been determined to reproduce the experimentally-measured [12] stress-strain response of $Zr_{41.2}Ti_{13.8}Cu_{12.5}Ni_{10}Be_{22.5}$ (Vitreloy-1) in a strain rate range of $[10^{-5}, 10^{-1}]\,\mathrm{s}^{-1}$, and in a temperature range $[593, 683]\,\mathrm{K}$, which spans the glass transition temperature $\vartheta_g = 623\,\mathrm{K}$ of this material.

We have implemented our theory in a finite element program [36], and this numerical simulation capability is used to determine appropriate processing parameters in order to carry out a successful micron-scale hot-embossing operation. By carrying out a corresponding physical experiment, we demonstrate that micron-scale features in a Zr-based metallic glass may be accurately replicated under the processing conditions determined by use of the numerical simulation capability.

Further, we describe the thermoplastic forming of a tool made from this material, which has the (negative) microchannel pattern for a simple microfluidic device. This tool was successfully used to produce the microchannel pattern by micro-hot-embossing of the amorphous polymers poly(methyl methacrylate) ($\vartheta_g \approx 388\,\mathrm{K}$) and Zeonex-690R ($\vartheta_g \approx 409\,\mathrm{K}$)

above their glass transition temperatures. The metallic glass tool was found to be very robust, and it was used to produce hundreds of high-fidelity micron-scale embossed patterns without degradation or failure.

- D. L. Henann and L. Anand. A constitutive theory for the mechanical response of amorphous metals at high temperatures spanning the glass transition temperature: Application to microscale thermoplastic forming. *Acta Materialia*, 56:3290-3305, 2008.
- D. L. Henann, V. Srivastava, H. K. Taylor, M. R. Hale, D. E. Hardt, and L. Anand. Metallic glasses: viable tool materials for the production of surface microstructures in amorphous polymers by micro-hot-embossing. *Journal of Micromechanics and Microengineering*, 19:115030, 2009.

1.2.4 Surface tension-driven shape-recovery of metallic glasses

Recent experiments in the literature show that micro/nano-scale features imprinted in a Pt-based metallic glass, $Pt_{57.5}Ni_{5.3}Cu_{14.7}P_{22.5}$ ($\vartheta_g = 503\,K$), using thermoplastic forming at a temperature above its glass transition temperature, may be erased by subsequent annealing at a slightly higher temperature in the supercooled liquid region [37]. The mechanism of shape-recovery is believed to be surface tension-driven viscous flow of the metallic glass. We have used existing experimental data in the literature for $Pt_{57.5}Ni_{5.3}Cu_{14.7}P_{22.5}$ [38] to estimate the material parameters appearing in our constitutive equations. We have also developed a numerical scheme for calculating surface curvatures and incorporating surface tension effects in finite element simulations. By carrying out full three-dimensional finite-element simulations of the shape-recovery experiments of Kumar and Schroers [37], and using the independently-determined material parameters for the bulk glass, we estimate the surface tension of $Pt_{57.5}Ni_{5.3}Cu_{14.7}P_{22.5}$ at the temperature at which the shape-recovery experiments were conducted. Finally, with the material parameters for the underlying elastic-viscoplastic bulk response as well as a value for the surface tension of the Pt-based metallic glass fixed, we validate our simulation capability by comparing predictions from our numerical simulations of shape-recovery experiments of Berkovich nanoindents, against corresponding recent experimental results of Packard et al. [39] who reported shape-recovery data of nanoindents on the same Pt-based metallic glass.

- D. L. Henann and L. Anand. Surface tension-driven shape-recovery of micro/nanometer-scale surface features in a $Pt_{57.5}Ni_{5.3}Cu_{14.7}P_{22.5}$ metallic glass in the supercooled liquid region: A numerical modeling capability. *Journal of the Mechanics and Physics of Solids*, 58:1947-1962, 2010.

1.3 Structure of thesis

The structure of this thesis is as follows. We begin in Chapter 2 by presenting a large strain isotropic elasticity model based on molecular dynamics simulations of a metallic glass. The

Anand-Su large-deformation, elastic-viscoplastic constitutive framework for metallic glasses is presented in Chapter 3, and in Chapter 4 we describe our simulations of brittle fracture of metallic glasses at notches at temperatures below the glass transition. In Chapter 5, we specialize the theory to the high temperature range spanning the glass transition. Chapter 6 deals with the application of our theory to model microscale thermoplastic forming of metallic glasses and describes several corresponding micro-hot-embossing experiments. In Chapter 7, we simulate surface tension-driven shape-recovery of metallic glasses above the glass transition. We close in Chapter 8 with some final remarks and future research directions.

Chapter 2

A large strain isotropic elasticity model based on molecular dynamics simulations of a metallic glass

2.1 Introduction

Consider a homogeneous body B identified with the region of space it occupies in a fixed reference configuration, and denote by $\mathbf{X}$ an arbitrary material point of B.[1] A motion of B is described by a smooth one-to-one mapping $\mathbf{x} = \boldsymbol{\chi}(\mathbf{X}, t)$, with deformation gradient given by $\mathbf{F} = \nabla\boldsymbol{\chi}$, and $J = \det \mathbf{F} > 0$. The deformation gradient admits the polar decomposition $\mathbf{F} = \mathbf{VR}$, with $\mathbf{V}$ a symmetric positive definite (left) stretch tensor, and $\mathbf{R}$ a rotation tensor. The spectral representation of $\mathbf{V}$ is $\mathbf{V} = \sum_{i=1}^{3} \lambda_i \mathbf{l}_i \otimes \mathbf{l}_i$, where $(\lambda_1, \lambda_2, \lambda_3)$ and $(\mathbf{l}_1, \mathbf{l}_2, \mathbf{l}_3)$ are, respectively, the lists of principal stretches and principal directions of $\mathbf{V}$. For an *isotropic*, *hyperelastic* material, the free energy per unit reference volume may be expressed in terms of the principal stretches as

$$\psi = \bar{\psi}(\lambda_1, \lambda_2, \lambda_3), \tag{2.1}$$

[1] *Notation*: We use standard notation of modern continuum mechanics (cf., e.g., [40]). The symbols ∇ and Div denote the gradient and divergence with respect to the material point $\mathbf{X}$ in the *reference configuration*; grad and div denote these operators with respect to the point $\mathbf{x} = \boldsymbol{\chi}(\mathbf{X}, t)$ in the deformed configuration; a superposed dot denotes the material time-derivative. Throughout, we write $\mathbf{F}^{\mathrm{e}-1} = (\mathbf{F}^{\mathrm{e}})^{-1}$, $\mathbf{F}^{\mathrm{p}-\mathsf{T}} = (\mathbf{F}^{\mathrm{p}})^{-\mathsf{T}}$, etc. We write $\operatorname{sym}\mathbf{A}$, $\operatorname{skw}\mathbf{A}$, $\mathbf{A}_0$, and $\operatorname{sym}_0\mathbf{A}$ respectively, for the symmetric, skew, deviatoric, and symmetric-deviatoric parts of a tensor $\mathbf{A}$. Also, the inner product of tensors $\mathbf{A}$ and $\mathbf{B}$ is denoted by $\mathbf{A}:\mathbf{B}$, and the magnitude of $\mathbf{A}$ by $|\mathbf{A}| = \sqrt{\mathbf{A}:\mathbf{A}}$.

with $\bar{\psi}$ invariant under the permutations of the integers $(1,2,3)$. Corresponding to this free energy, the Cauchy stress $\mathbf{T}$ is given by

$$\mathbf{T} = J^{-1} \sum_{i=1}^{3} \lambda_i \frac{\partial \bar{\psi}(\lambda_1, \lambda_2, \lambda_3)}{\partial \lambda_i} \mathbf{l}_i \otimes \mathbf{l}_i, \quad \text{where} \quad J = \lambda_1 \lambda_2 \lambda_3 > 0. \tag{2.2}$$

With

$$\mathbf{E} \stackrel{\text{def}}{=} \ln \mathbf{V} = \sum_{i=1}^{3} E_i \mathbf{l}_i \otimes \mathbf{l}_i, \qquad E_i = \ln \lambda_i, \tag{2.3}$$

denoting the *logarithmic strain*, and

$$\mathbf{T}_{\mathrm{K}} \stackrel{\text{def}}{=} J\mathbf{T} \tag{2.4}$$

denoting the *Kirchhoff stress*, (2.2) may be written as

$$\mathbf{T}_{\mathrm{K}} = \sum_{i=1}^{3} \frac{\partial \hat{\psi}(E_1, E_2, E_3)}{\partial E_i} \mathbf{l}_i \otimes \mathbf{l}_i. \tag{2.5}$$

The logarithmic elastic strain $\mathbf{E}$ has the important property that

$$\operatorname{tr} \mathbf{E} = \ln J \tag{2.6}$$

represents a volumetric strain, and that the deviatoric part of $\mathbf{E}$ is given by

$$\mathbf{E}_0 = \ln(J^{-1/3}\mathbf{V}). \tag{2.7}$$

Choosing

$$I_1(\mathbf{E}) = \operatorname{tr} \mathbf{E}, \qquad I_2(\mathbf{E}) = \operatorname{tr} \mathbf{E}_0^2, \quad \text{and} \quad I_3(\mathbf{E}) = \operatorname{tr} \mathbf{E}_0^3 \tag{2.8}$$

as a list of three independent invariants of $\mathbf{E}$, we may alternatively write the stress-strain relation (2.5) as

$$\mathbf{T}_{\mathrm{K}} = \frac{\partial \tilde{\psi}(I_1(\mathbf{E}), I_2(\mathbf{E}), I_3(\mathbf{E}))}{\partial \mathbf{E}}. \tag{2.9}$$

Recall that in the classical linear theory of isotropic elasticity, with $\tilde{\mathbf{E}} = (1/2)(\nabla \mathbf{u} + (\nabla \mathbf{u})^{\mathsf{T}})$ the infinitesimal strain tensor, the free energy is taken as

$$\psi(\tilde{\mathbf{E}}) = \mu_0 |\tilde{\mathbf{E}}_0|^2 + \frac{1}{2} \kappa_0 (\operatorname{tr} \tilde{\mathbf{E}})^2, \tag{2.10}$$

where $\mu_0 > 0$ and $\kappa_0 > 0$ are the shear and bulk moduli. Motivated by the simple form of the expression for the strain energy of an infinitesimally-strained isotropic elastic body, one might ask whether an analogous expression, in which dependence upon the infinitesimal strain measure is replaced by dependence upon a *finite strain measure*, is capable of describing the behavior of a moderately-strained isotropic elastic body. A model of this type, using the

logarithmic strain measure (2.3), was introduced by Hencky [27–29] and has the form

$$\psi(\mathbf{E}) = \mu_0|\mathbf{E}_0|^2 + \frac{1}{2}\kappa_0(\mathrm{tr}\,\mathbf{E})^2, \tag{2.11}$$

where $\mu_0 > 0$ and $\kappa_0 > 0$ are the shear and bulk moduli from the classical *infinitesimal* theory. Anand [25, 26] has shown that the quadratic free energy function (2.11) and the corresponding stress relation,

$$\mathbf{T}_{\mathrm{K}} = 2\mu_0\mathbf{E}_0 + \kappa_0(\mathrm{tr}\,\mathbf{E})\mathbf{1}, \tag{2.12}$$

are in good agreement with experiments on a wide class of materials for principal stretches ranging between 0.7 and 1.3. Importantly, since the material constants μ_0 and κ_0 are the classical elastic constants, they may be determined from experimental data at infinitesimal strains. As a consequence of these results, it appears that all moderate-strain non-linearities are incorporated in the logarithmic strain measure. Indeed, for this reasonably large range of stretches, all other commonly used strain measures (including those of Green, Almansi, Swainger, Biot), when used to generalize the classical free energy for isotropic linear elasticity (using the values of μ_0 and κ_0 determined from experimental data at infinitesimal strains), give predictions (for the elastic stress response of materials) which are in poor agreement with experiments.

More recently, guided by the *universal binding energy relation* (UBER) introduced by Rose et al. [41], Gearing and Anand [42] modified the Hencky [27–29] free energy function to account for large elastic volumetric strains. Specifically, with

$$\epsilon \stackrel{\mathrm{def}}{=} \mathrm{tr}\,\mathbf{E} = \ln J \tag{2.13}$$

denoting the volumetric part of the logarithmic elastic strain, Gearing and Anand [42] proposed the following modification to (2.11):

$$\psi(\mathbf{E}) = \mu_0\,|\mathbf{E}_0|^2 + \kappa_0(\epsilon_{\mathrm{c}})^2\left[1 - \left(1 + \frac{\epsilon}{\epsilon_{\mathrm{c}}}\right)\exp\left(-\frac{\epsilon}{\epsilon_{\mathrm{c}}}\right)\right], \tag{2.14}$$

where ϵ_{c} is a critical value of the elastic volumetric strain (a material parameter), and as before, μ_0 and κ_0 are the ground-state shear and bulk moduli of infinitesimal isotropic elasticity. This three-constant free energy function was used by Gearing and Anand [42] to model the brittle cracking phenomenon observed experimentally in states of high triaxial tension in front of sharp notches in amorphous polymers.

In writing (2.14), Gearing and Anand [42] assumed that $|\mathbf{E}_0|$ does not affect the volumetric part of the free energy. Correspondingly, they also assumed that the volumetric elastic strain ϵ does not affect the deviatoric part of the free energy. As pointed out by Veprek et al. [43], this lack of interaction between the deviatoric and volumetric parts of the free energy is not well-justified, especially at large volumetric strains. To remedy this situation, they

proposed a free energy function of the form

$$\psi(\mathbf{E}) = \mu_0 \exp\left(-\frac{\epsilon}{\epsilon_c}\right) |\mathbf{E}_0|^2 + \kappa_0(\epsilon_c)^2 \left[1 - \left(1 + \frac{\epsilon}{\epsilon_c}\right) \exp\left(-\frac{\epsilon}{\epsilon_c}\right)\right]. \tag{2.15}$$

However, the coupling introduced in the first term of (2.15) by Veprek et al. [43] was based on an assumption that the classical Poisson's ratio (as defined at infinitesimal strains) remains *constant* even under large volumetric strains[2] — an assumption which is unsupported by either rigorous physical arguments or experimental observations. Indeed, estimates of the pressure sensitivity of the bulk modulus and the shear modulus from seismological studies shows that the Poisson's ratio increases with volumetric-compaction; cf., e.g., the discussion in Section 8 of Stacey and Davis [44].

Since it is difficult to conduct physical experiments to determine volumetric-deviatoric coupling effects under circumstances involving large volumetric strains, it is the purpose of this chapter

- *to conduct numerical experiments — using molecular dynamics simulations — to explore such coupling effects in the free energy, and based on the results of these numerical experiments, to propose a simple continuum-level isotropic elastic free energy that captures the observed coupling effects.*

As we are concerned here with a free energy function for *isotropic materials*, in our molecular dynamics simulations we consider an *amorphous metallic glass* as our representative isotropic material.

The plan of this chapter is as follows. In Section 2.2, we describe a simple free energy function specialized for large volumetric strains but small distortional strains. The results from our molecular dynamics simulations for various combinations of homogeneous volumetric and pure-shear deformations are described in Section 2.3. Based on the results of these numerical experiments, in Section 2.4 we construct a simple continuum-level isotropic elastic free energy that captures the volumetric-deviatoric coupling effects observed in our numerical experiments.

Plastic flow in metallic materials is known to be "pressure sensitive" — a sensitivity that cannot be ignored at high pressures; accordingly, in Section 2.5, we examine the effect of the volumetric strain on the effective shear stress required for the onset of plastic flow in the metallic glass, and correlate this dependence with the numerically-observed dependence of the elastic shear modulus on the volumetric strain.

[2]Cf., the discussion in Section 2.2 of Veprek et al. [43].

2.2 A simple free energy function that couples the deviatoric and volumetric response

As before, let $\mathbf{E}$ denote the logarithmic strain, $\epsilon = \mathrm{tr}\mathbf{E}$ the volumetric part of the strain, and $|\mathbf{E}_0|$ the magnitude of the deviatoric part of $\mathbf{E}$. For isotropic materials, the deviatoric strain $\mathbf{E}_0$ may contribute to the free energy through the second invariant $I_2 = \mathrm{tr}\mathbf{E}_0^2 = |\mathbf{E}_0|^2$ as well as the third invariant $I_3 = \mathrm{tr}\mathbf{E}_0^3$. However, *for small deviatoric strains*, we expect that the effect of I_3, which is third-order in $\mathbf{E}_0$, is significantly smaller than the effect of I_2, which is second-order in $\mathbf{E}_0$. Accordingly,

- for small values of $|\mathbf{E}_0|$, which is of primary concern in this chapter, we assume from the outset that the free energy does not depend upon the third invariant $I_3 = \mathrm{tr}\mathbf{E}_0^3$.

We provide a more detailed justification for this assumption in Appendix A.

Then, motivated by (2.15), we introduce two scalar valued functions $\mu(\epsilon)$ and $g(\epsilon)$, and consider a free energy function of the form

$$\psi(\mathbf{E}) = \mu(\epsilon)\,|\mathbf{E}_0|^2 + g(\epsilon). \tag{2.16}$$

Here $\mu(\epsilon)$ is a volumetric strain-dependent *generalized shear modulus*. We assume that

$$\mu(\epsilon) > 0 \tag{2.17}$$

for all values of ϵ considered here, and denote the ground-state value of this generalized shear modulus by

$$\mu_0 \equiv \mu(0) > 0. \tag{2.18}$$

The term $g(\epsilon)$ in (2.16) represents a purely volumetric contribution to the free energy when $\mathbf{E}_0 = \mathbf{0}$. Let

$$\bar{\sigma}(\epsilon) \stackrel{\text{def}}{=} \frac{\mathrm{d}g(\epsilon)}{\mathrm{d}\epsilon} \tag{2.19}$$

denote a mean normal stress under this circumstance, and correspondingly define a *generalized bulk modulus* by

$$\kappa(\epsilon) \stackrel{\text{def}}{=} \frac{\mathrm{d}\bar{\sigma}(\epsilon)}{\mathrm{d}\epsilon} = \frac{\mathrm{d}^2 g(\epsilon)}{\mathrm{d}\epsilon^2}. \tag{2.20}$$

We limit our discussion in this chapter to circumstances in which the generalized bulk modulus is positive-valued,

$$\kappa(\epsilon) > 0, \tag{2.21}$$

and denote the ground-state value of the generalized bulk modulus by

$$\kappa_0 \equiv \kappa(0) > 0. \tag{2.22}$$

Further, in order to ensure that the free energy at zero strain is zero-valued and that the reference configuration is stress-free, we require that

$$g(0) = 0 \qquad \text{and} \qquad \left.\frac{\mathrm{d}g(\epsilon)}{\mathrm{d}\epsilon}\right|_{\epsilon=0} = 0. \tag{2.23}$$

The Kirchhoff stress corresponding to the free energy (2.16) is then given by

$$\mathbf{T}_{\mathrm{K}} = \frac{\partial\psi(\mathbf{E})}{\partial\mathbf{E}} = 2\mu(\epsilon)\mathbf{E}_0 + \left(\bar{\sigma}(\epsilon) + \frac{\mathrm{d}\mu(\epsilon)}{\mathrm{d}\epsilon}\,|\mathbf{E}_0|^2\right)\mathbf{1}. \tag{2.24}$$

Next, let

$$\sigma \stackrel{\text{def}}{=} \frac{1}{3}\mathrm{tr}\mathbf{T}_{\mathrm{K}}, \qquad \tau \stackrel{\text{def}}{=} \frac{1}{\sqrt{2}}\,|\mathbf{T}_{\mathrm{K},0}|\,, \qquad \text{and} \qquad \gamma \stackrel{\text{def}}{=} \sqrt{2}|\mathbf{E}_0| \tag{2.25}$$

define a *mean normal stress*, an *equivalent shear stress*, and an *equivalent shear strain*, respectively. Then (2.24) gives

$$\sigma = \hat{\sigma}(\epsilon,\gamma) = \bar{\sigma}(\epsilon) + \frac{1}{2}\frac{\mathrm{d}\mu(\epsilon)}{\mathrm{d}\epsilon}\gamma^2 \qquad \text{and} \qquad \tau = \hat{\tau}(\epsilon,\gamma) = \mu(\epsilon)\gamma. \tag{2.26}$$

Thus, note that the free energy function (2.16) gives a mean normal stress that depends not only on the volumetric strain but also on the equivalent shear strain γ: the term $\bar{\sigma}(\epsilon)$ in $(2.26)_1$ represents a mean normal stress versus volumetric strain response in the absence of a shear strain, while the term $\frac{1}{2}(\mathrm{d}\mu(\epsilon)/\mathrm{d}\epsilon)\gamma^2$ represents a *shear-induced mean normal stress.* Also, the equivalent shear stress τ depends not only on the equivalent shear strain but also on the volumetric strain ϵ, with $\mu(\epsilon)$ in $(2.26)_2$ representing a volumetric strain-dependent generalized shear modulus,

In the next section, we report on our numerical experiments using molecular dynamics simulations on a metallic glass. We shall use the stress-strain results from these numerical experiments to fit specific forms for the functions $g(\epsilon)$ and $\mu(\epsilon)$.

2.3 Molecular dynamics simulations

Since we are concerned with a free energy function for isotropic materials, in our molecular dynamics simulations, we consider an amorphous metallic glass as our representative isotropic material. Also, in order to determine specific forms for the functions $\mu(\epsilon)$ and $g(\epsilon)$ in the free energy (2.16), we take a pragmatic mechanics-based approach, treating the results from molecular dynamics simulations as we would results from physical experiments, and determine $g(\epsilon)$ and $\mu(\epsilon)$ by selecting specific forms which fit our "experimental" data in the range of volumetric and shear strain levels for which we have conducted our numerical simulations.[3]

[3]For details on the theory and practice of molecular dynamics simulations, see the text by Frenkel and Smit [45].

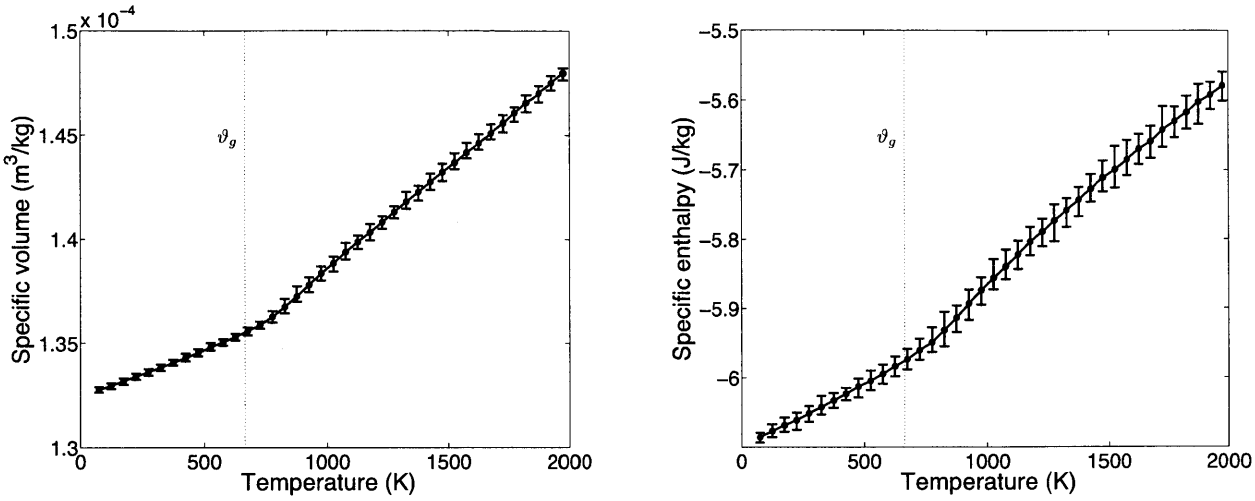

Figure 2-1: (a) Specific volume and (b) specific enthalpy versus temperature.

2.3.1 Preparation of a metallic glass specimen

Following Cao et al. [46] and Cheng et al. [47], we consider a metallic glass with a composition of $Cu_{64}Zr_{36}$ and use the embedded atom potential developed and validated (using density functional theory calculations) for this system by these authors.[4] To prepare a metallic glass specimen, we use a three-dimensional box of 10,976 atoms under periodic boundary conditions in all three dimensions. The sample was first equilibrated for 2 ns at 2000 K and zero external pressure to ensure melting and then quenched at a rate of 100 K/ns to a temperature of 50 K at zero external pressure using a Nose-Hoover thermostat and the NPT ensemble. Figures 2-1(a) and (b), respectively, show the specific volume and specific enthalpy as a function of temperature during quenching. The markers represent the average of each quantity over temperature spans of 50 K.[5] Figure 2-2 shows the radial distribution functions for Cu-Cu, Cu-Zr, and Zr-Zr pairs, confirming that the as-quenched sample is *amorphous*. From the data in Figs. 2-1(a) and (b), the glass transition temperature ϑ_g, the volumetric coefficient of thermal expansion β below ϑ_g, and the specific heat at constant pressure c_p below ϑ_g for the simulated amorphous alloy were determined to be

$$\vartheta_g = 664\,\mathrm{K}, \quad \beta = 33.6 \times 10^{-6}\,\mathrm{K}^{-1}, \quad \text{and} \quad c_p = 0.19\,\frac{\mathrm{J}}{\mathrm{kg\,K}}, \tag{2.27}$$

respectively.

[4]The embedded atom potential developed by Cao et al. [46] and Cheng et al. [47] may be found in tabular form at https://sites.google.com/a/gmu.edu/eam-potential-database/.

[5]The error bars in these figures denote the maximum and minimum values of each quantity measured over temperature spans of 50 K during the quenching simulations.

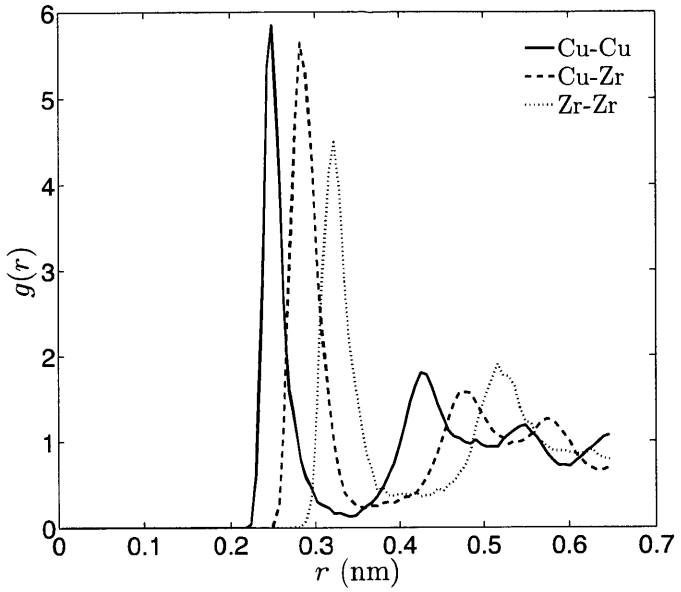

Figure 2-2: The radial distribution functions in the quenched state for Cu-Cu, Cu-Zr, and Zr-Zr pairs, confirming the amorphous structure of the as-quenched sample.

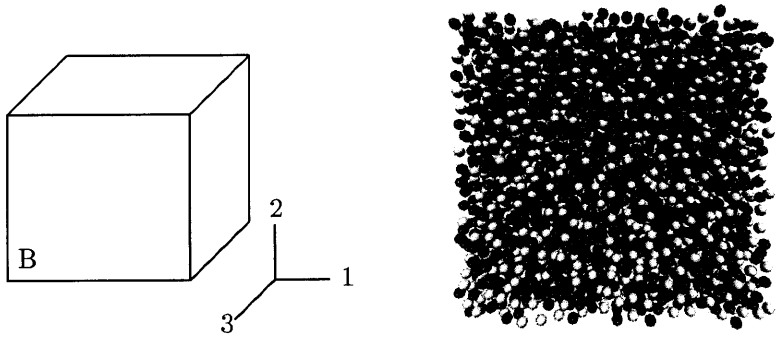

Figure 2-3: Schematic and snapshot of the undeformed configuration.

A schematic of the as-quenched configuration, which we will refer to as the reference configuration of the body B, is shown in Fig. 2-3, which also shows a snapshot of the molecular configuration of the sample; the copper atoms are copper-colored and the zirconium atoms are white. The sample after quenching has dimensions of 5.62 nm in the 1, 2, and 3-directions.

2.3.2 Numerical experiments on the metallic glass specimen

The $Cu_{64}Zr_{36}$ metallic glass sample was subjected to various combinations of volumetric and shear strain, under periodic boundary conditions and a constant temperature of 50 K, using the NVT ensemble. The various deformations considered are summarized below:

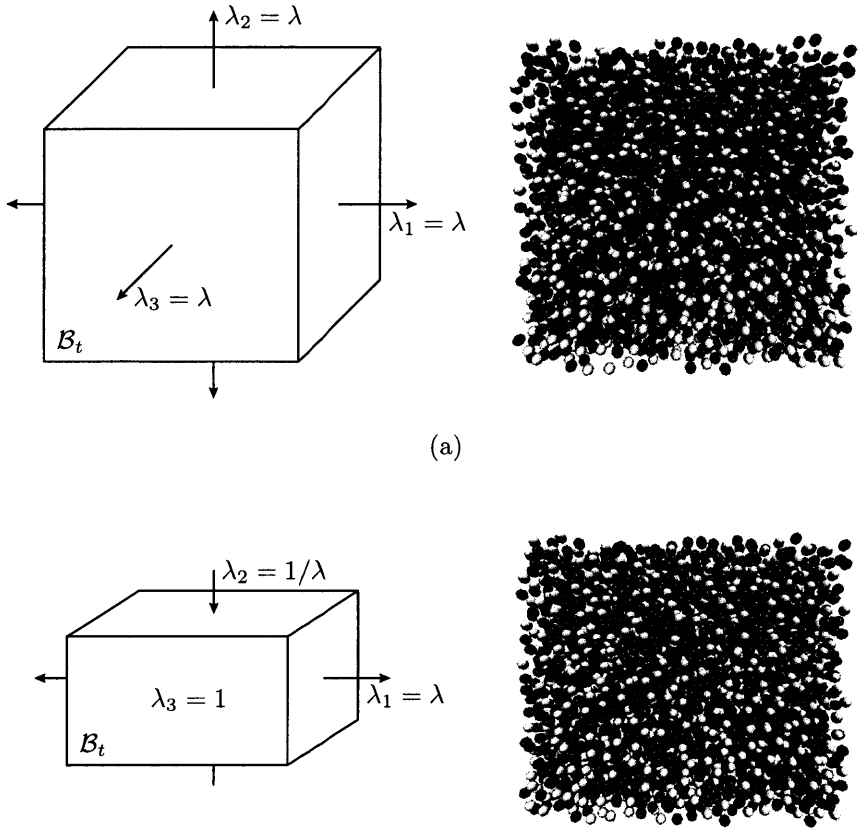

Figure 2-4: Schematic and snapshots of the (a) dilated and (b) sheared configurations.

1. **Volumetric dilatation/compaction**: The sample is subjected to purely volumetric deformation with equal principal stretches:

$$\lambda_1 = \lambda_2 = \lambda_3 = \lambda.$$

A schematic of the deformed body $\mathcal{B}_t$ for such a deformation is shown in Fig. 2-4(a);[6] this figure also shows a corresponding snapshot of the molecular configuration at a volumetric strain of $\epsilon = 0.15$.

2. **Pure shear**: The sample is subjected to volume-conserving pure shear:

$$\lambda_1 = \lambda, \qquad \lambda_2 = 1/\lambda, \qquad \text{and} \qquad \lambda_3 = 1.$$

[6]The magnitude of strain in the schematics shown in Fig. 2-4 is exaggerated for ease of visualization.

A schematic of the deformed body $\mathcal{B}_t$ for such a deformation is shown in Fig. 2-4(b); this figure also shows a corresponding snapshot of the MD configuration at a shear strain of $\gamma = 0.04$.

- *For sufficiently large shear strains, the metallic glass sample will deform plastically; however, in this numerical experiment, and in all other experiments involving shear strains that follow (except those discussed in Section 2.5), we limit the magnitude of shear strain so that the sample remains in the elastic range.*

3. **Volumetric deformation followed by pure shear**: The sample is first subjected to various levels of volumetric dilatation and compaction, and then subjected to pure shear.

4. **Pure shear followed by volumetric deformation**: The sample is first subjected to various levels of shear strain, and then subjected to volumetric dilatation and compaction.

The stress-strain results from each of these numerical experiments are discussed below.

2.3.3 Volumetric dilatation/compaction

The sample was subjected to a constant volumetric strain rate of $\dot{\epsilon} = \pm 3 \times 10^8\,\mathrm{s}^{-1}$ in dilatation/compaction. The components of the Cauchy stress may be determined from the virial stress. However, since our stress-strain relation (2.24) is given in terms of the Kirchhoff stress ($\mathbf{T}_\mathrm{K} = J\mathbf{T}$), in what follows, unless otherwise specified, *we report all stress-related quantities in terms of the Kirchhoff stress.*

Figure 2-5 shows the mean normal stress σ as a function of the volumetric strain ϵ, for ϵ in the range $[-0.30, 0.15]$. The corresponding range of mean normal stress σ is approximately $[-45, 15]$ GPa — the dependence of σ on ϵ in this large range of volumetric strains is clearly *nonlinear.*

It is important to note that at sufficiently large compressive volumetric strains the numerical metallic glass specimen exhibits *ordering*, while at sufficiently large positive volumetric strains the specimen exhibits *cavitation-induced* fracturing. Figure 2-6(a) shows the radial distribution functions for Zr-Zr pairs in the quenched state, and at a volumetric strain of $\epsilon = -0.35$, where evidence of strain-induced ordering can be observed; and Fig. 2-6(b) shows a snapshot of a slice of the molecular configuration at a volumetric strain of $\epsilon \approx 0.16$, where cavitation-related failure is evident. By examining the radial distribution functions for Cu-Cu, Cu-Zr, and Zr-Zr pairs for volumetric strains in the range $[-0.30, 0]$, we have confirmed that no strain-induced ordering occurs in our simulations; correspondingly for volumetric strains in the range $[0, 0.15]$, we do not observe any cavitation-related failure. *Thus, for ϵ in the range $[-0.30, 0.15]$ studied in this chapter, the metallic glass specimen used in our numerical experiments continues to respond as an intact, nominally-isotropic, amorphous material.*

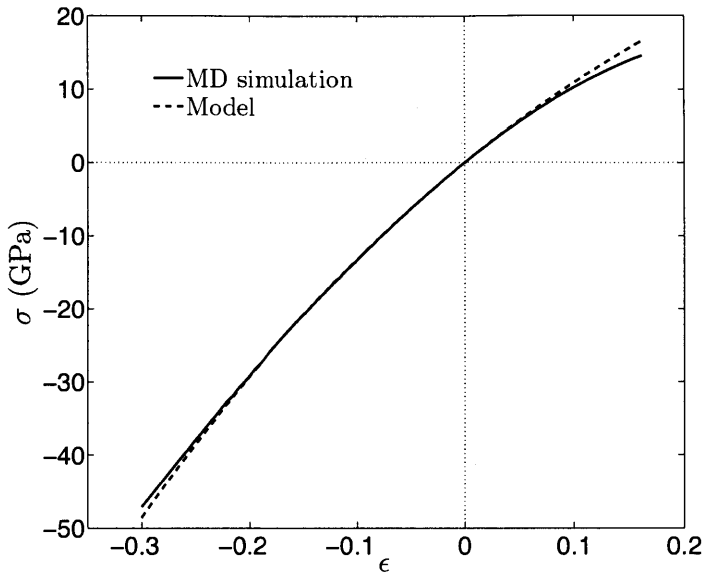

Figure 2-5: Variation of the mean stress with elastic volumetric strain. The solid line is the result of the MD simulation, and the dashed line is the result of the calibrated hyperelasticity model.

2.3.4 Pure shear

The sample was subjected to volume-conserving pure shear at a shear strain rate of $\dot{\gamma} = 1 \times 10^8\,\mathrm{s}^{-1}$ to a final shear strain of $\gamma = 0.04$.[7] The resulting shear stress τ versus shear strain γ is plotted in Fig. 2-7(a). The dependence of τ on γ in this range of shear strains is essentially linear.

Interestingly, the plot in Fig. 2-7(b) shows that *a small but non-negligible non-zero mean normal stress develops during pure shear.* More on this later.

2.3.5 Volumetric deformation followed by pure shear

The sample was first subjected to volumetric strains ranging from $\epsilon = -0.15$ to $\epsilon = 0.15$, and subsequently subjected to reversed volume-conserving pure shear to a final shear strain of $\gamma = 0.02$. For clarity, in Fig. 2-8(a) we only show the shear stress τ versus shear strain γ for volumetric strains of $\epsilon = -0.09, 0, 0.09$.

Figure 2-8(b) shows the shear modulus μ as a function of the volumetric strain ϵ, and from this figure it is evident that *the shear modulus decreases with volumetric dilatation and increases with volumetric compaction.*

[7]The strain was reversed to verify that no appreciable permanent deformation had occurred at this level of shear strain.

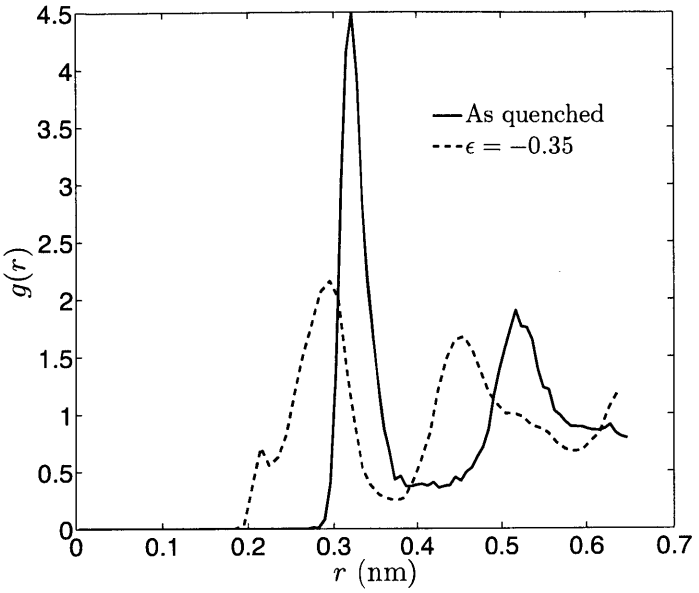

(a)

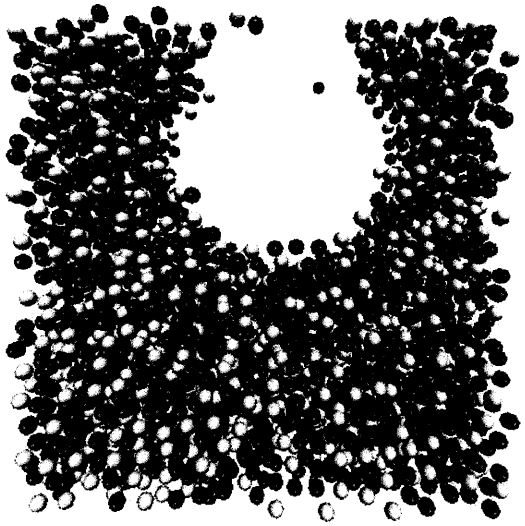

(b)

Figure 2-6: (a) The radial distribution functions for Zr-Zr pairs in the quenched state and at a volumetric strain of $\epsilon = -0.35$, showing evidence of strain-induced ordering at high compressive volumetric strains. (b) A snapshot of a slice of the molecular specimen at a volumetric strain of $\epsilon \approx 0.16$, demonstrating cavitation-related failure.

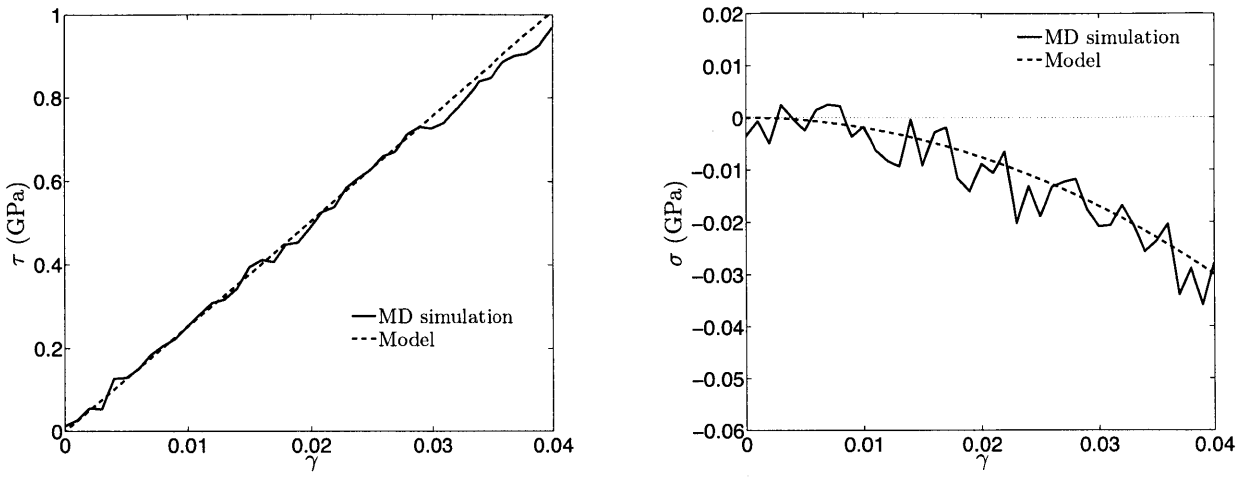

(a) (b)

Figure 2-7: Variation of (a) the shear stress and (b) the mean stress with elastic shear strain. The solid lines are the result of the MD simulations, and the dashed lines are the result of the calibrated hyperelasticity model.

2.3.6 Pure shear followed by volumetric deformation

The sample was first subjected to pure shear to strains of $\gamma = 0.02, 0.04$, then subjected to volumetric strains ranging from $\epsilon = -0.15$ to $\epsilon = 0.15$. The mean normal stress σ is plotted against the volumetric strain ϵ in Fig. 2-9(a) for the different values of prior shear strain. From this figure it is clear that *a prior shear strain, in the limited range of accessible elastic shear strains, has a negligible effect on the subsequent volumetric stress-strain response.*

Figure 2-9(c) shows the variation of the shear stress τ as a function of the volumetric strain ϵ for the two different levels of prior shear strains, $\gamma = 0.02, 0.04$. This figure clearly shows that *the shear stress generated by a prior shear strain is significantly affected by a subsequent volumetric deformation.*

2.4 Specialization of the functions $g(\epsilon)$ and $\mu(\epsilon)$

In this section, we use the stress-strain results from our molecular dynamics simulations to select and calibrate specialized forms for the functions $g(\epsilon)$ and $\mu(\epsilon)$. We emphasize from the outset that our focus is on motivating proper functional forms rather than the specific values of the parameters appearing in the specialized functions. The actual values of the material parameters will of course be valid only for this *numerical* $Cu_{64}Zr_{36}$ metallic glass, and are controlled by its underlying interatomic potential.

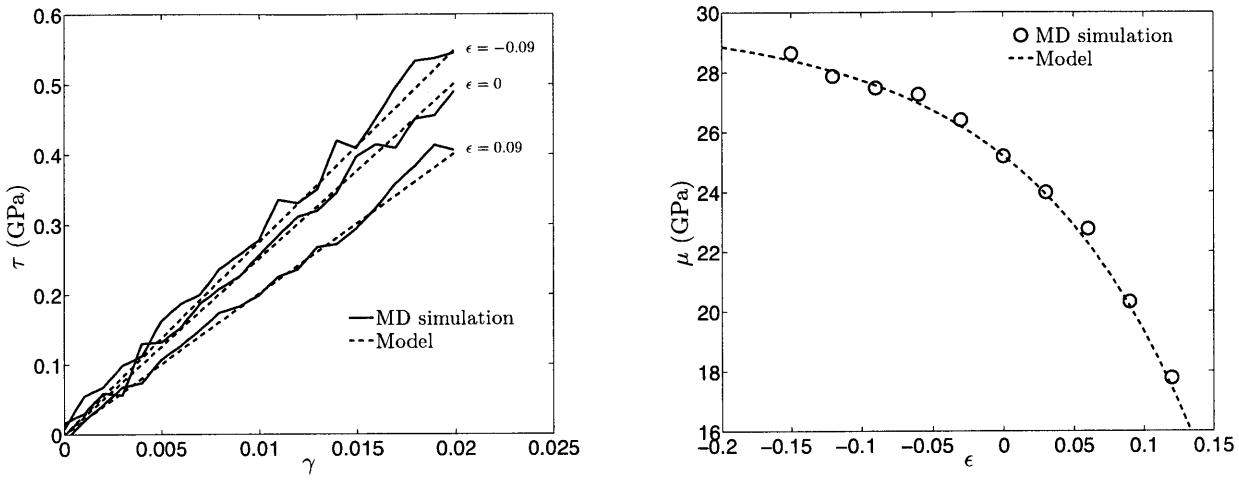

(a) (b)

Figure 2-8: (a) Variation of the shear stress with shear strain at several levels of volumetric strain and (b) variation of the shear modulus with volumetric strain. The solid lines and markers are the result of the MD simulations, and the dashed lines are the result of the calibrated hyperelasticity model.

2.4.1 Determination of the function $g(\epsilon)$

Recall from (2.19) and (2.20) that the mean normal stress in the absence of a shear strain and the generalized bulk modulus are defined in terms the function $g(\epsilon)$ by

$$\bar{\sigma}(\epsilon) \stackrel{\text{def}}{=} \frac{\mathrm{d}g(\epsilon)}{\mathrm{d}\epsilon} \qquad \text{and} \qquad \kappa(\epsilon) \stackrel{\text{def}}{=} \frac{\mathrm{d}^2 g(\epsilon)}{\mathrm{d}\epsilon^2}. \tag{2.28}$$

Following Gearing and Anand [42], we adopt[8]

$$g(\epsilon) = \kappa_0(\epsilon_c)^2 \left[1 - \left(1 + \frac{\epsilon}{\epsilon_c}\right) \exp\left(-\frac{\epsilon}{\epsilon_c}\right)\right], \tag{2.29}$$

where κ_0 is the ground-state bulk modulus, and $\epsilon_c > 0$ is another material constant representing a critical value of the elastic volumetric strain associated with *cavitation* in volumetric dilatation. Applying the relations (2.28) gives

$$\begin{aligned} \bar{\sigma}(\epsilon) &= \left[\kappa_0 \exp\left(-\frac{\epsilon}{\epsilon_c}\right)\right] \epsilon, \\ \kappa(\epsilon) &= \kappa_0 \left(1 - \frac{\epsilon}{\epsilon_c}\right) \exp\left(-\frac{\epsilon}{\epsilon_c}\right). \end{aligned} \tag{2.30}$$

[8]This form is motivated by the *universal binding energy relation* (UBER) for a one-dimensional interatomic potential introduced by Rose et al. [41].

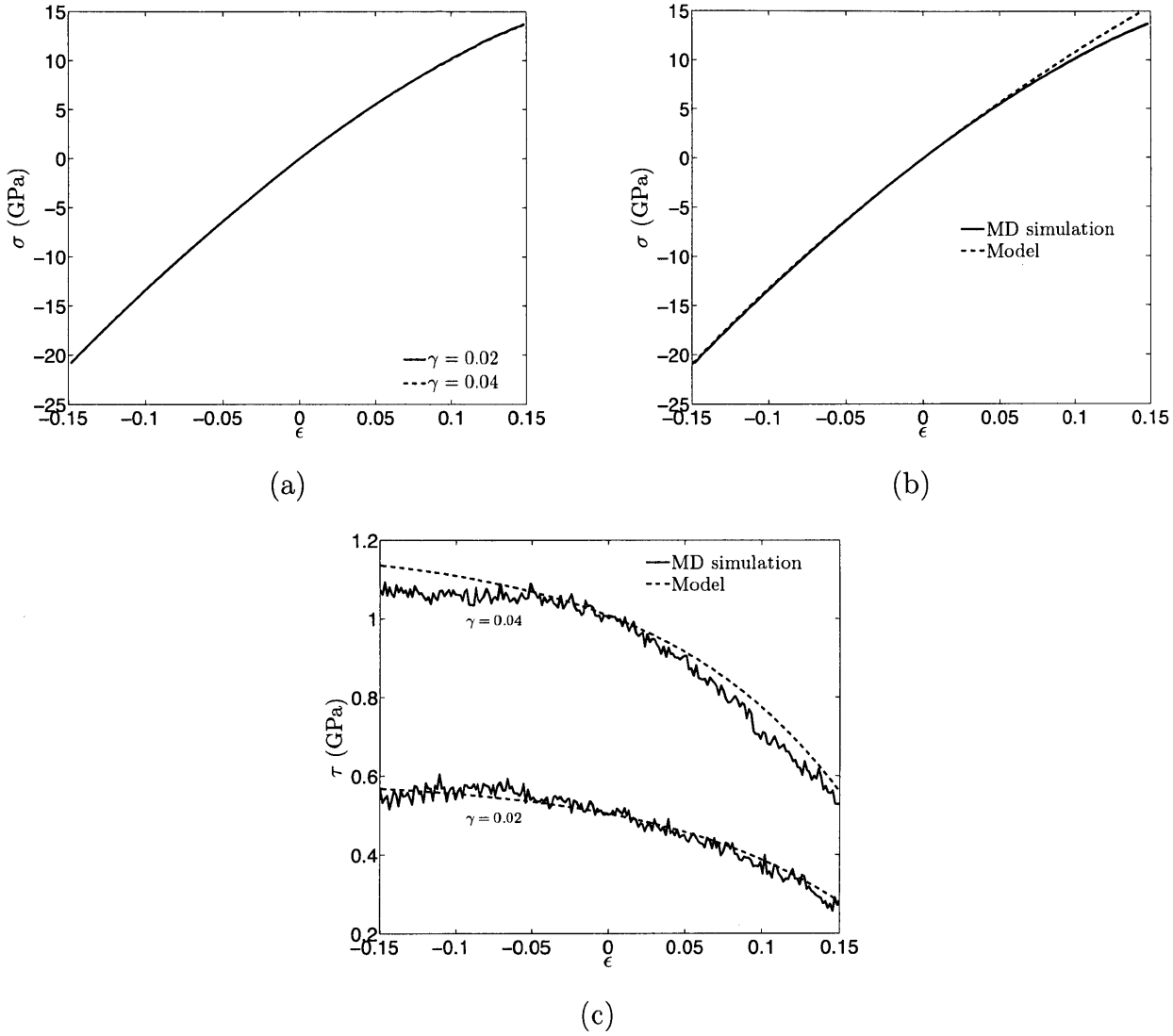

Figure 2-9: (a,b) Variation of the mean stress with volumetric strain at two levels of fixed shear strain. (a) shows only the result from the MD simulations, and (b) compares the calibrated hyperelasticity model with the results of the MD simulations for both levels of fixed shear strain. (c) Variation of the shear stress with volumetric strain at two levels of fixed shear strain. In (b) and (c), the solid lines are the result of the MD simulations, and the dashed lines are the result of the calibrated hyperelasticity model.

Fitting the function $(2.30)_1$ to the results of our molecular dynamics simulations shown in Fig. 2-5(a), gives

$$\kappa_0 = 120.0\,\text{GPa} \quad \text{and} \quad \epsilon_c = 1.0. \tag{2.31}$$

The quality of the fit for the mean normal stress versus volumetric strain response using these material parameters is shown in Fig. 2-5.

Remark: Since the generalized bulk modulus $\kappa(\epsilon)$ in $(2.30)_2$ reaches zero at ϵ_c and becomes negative for $\epsilon > \epsilon_c$, an instability will occur at $\epsilon = \epsilon_c$. Softening hyperelasticity models of this type have been used to model cavitation failure in a variety of materials (cf., e.g., [42]). However, we do not focus on cavitation phenomena or the prediction of cavitation here (cf., Fig. 2-6(b)), because it is our belief that cavitation is initiated at heterogeneities in the microstructure, which are not explicitly included in our molecular dynamics simulations.

2.4.2 Determination of the function $\mu(\epsilon)$

We determine the form of the generalized shear modulus function $\mu(\epsilon)$ by fitting the simulation results of volumetric deformation followed by pure shear, cf. Fig. 2-8(b). To this end, we choose a fitting function of the form

$$\mu(\epsilon) = \mu_r - (\mu_r - \mu_0) \exp\left(\frac{\epsilon}{\epsilon_r}\right), \tag{2.32}$$

where μ_0 is the ground state shear modulus at $\epsilon = 0$, μ_r is the value of the generalized shear modulus that is asymptotically approached as $\epsilon \to -\infty$, and ϵ_r is a reference value of the volumetric strain. Fitting the function (2.32) to the data of Fig. 2-8(b) we obtain

$$\mu_0 = 25.2\,\text{GPa}, \quad \mu_r = 29.7\,\text{GPa} \quad \text{and} \quad \epsilon_r = 0.12. \tag{2.33}$$

The quality of the fit for the shear stress versus shear strain response, and the generalized shear modulus versus volumetric strain using these material parameters, is shown in Figs. 2-8(a) and 2-8(b), respectively.

Remark: The material parameter μ_0 represents the ground-state shear modulus. We do not attribute any fundamental physical significance to the two additional material parameters (μ_r, ϵ_r); they are phenomenological constants that fit our numerically-generated data over the range of volumetric strains ϵ studied here. In particular, note that ϵ_r appearing in the expression (2.32) for the generalized shear modulus is not related to ϵ_c appearing in the expression $(2.30)_2$ for the generalized bulk modulus.

2.4.3 Partial validation of the coupled free energy function

Next we perform a partial validation of the coupled free energy function (2.16) with $g(\epsilon)$ and $\mu(\epsilon)$ given in (2.29) and (2.32). To do this we revisit the results from our numerical simulations for pure shear, and pure shear followed by volumetric deformation.

First, we note that in the case of pure shear at $\epsilon = 0$, (2.26) and (2.32) predict the following shear-induced mean stress

$$\sigma = \frac{1}{2}\left.\frac{\mathrm{d}\mu(\epsilon)}{\mathrm{d}\epsilon}\right|_{\epsilon=0}\gamma^2 = -\frac{1}{2}\frac{(\mu_\mathrm{r}-\mu_0)}{\epsilon_\mathrm{r}}\gamma^2. \tag{2.34}$$

Using the parameter list (2.33), the predicted shear-induced mean normal stress is compared to the result from the molecular dynamics simulation in Fig. 2-7(b), and the comparison is quite good. Thus,

- *the shear-induced mean stress predicted by the molecular dynamics simulations, which at first blush seems unphysical, is a direct outcome of the volumetric strain-dependent shear modulus function* $\mu(\epsilon)$.

Next, we compare the prediction of our hyperelasticity model with the molecular dynamics results for the case of pure shear followed by volumetric deformation. Using (2.26) in conjunction with $(2.30)_1$ and (2.32), our model predicts

$$\begin{aligned}\sigma = \hat{\sigma}(\epsilon,\gamma) &= \left[\kappa_0 \exp\left(-\frac{\epsilon}{\epsilon_\mathrm{c}}\right)\right]\epsilon - \frac{1}{2}\frac{(\mu_\mathrm{r}-\mu_0)}{\epsilon_\mathrm{r}}\exp\left(\frac{\epsilon}{\epsilon_\mathrm{r}}\right)\gamma^2,\\ \tau = \hat{\tau}(\epsilon,\gamma) &= \left[\mu_\mathrm{r} - (\mu_\mathrm{r}-\mu_0)\exp\left(\frac{\epsilon}{\epsilon_\mathrm{r}}\right)\right]\gamma,\end{aligned} \tag{2.35}$$

for the mean normal stress and the equivalent shear stress, respectively. The predictions from these equations, using the parameter lists (2.31) and (2.33), are compared to the molecular dynamics simulation results in Fig. 2-9. Figure 2-9(b) shows that the predicted mean stress versus volumetric strain response matches that which is observed in the molecular dynamics simulations. Note that since the final term in $(2.35)_1$ is second order in the shear strain γ, it has an indiscernible effect on the mean normal stress versus volumetric strain response for the range of shear strains considered here. In contrast, for fixed γ, the variation of the shear modulus with volumetric strain has a marked effect on the variation of the shear stress with the volumetric strain. Figure 2-9(c) shows that the predictions from $(2.35)_2$ reasonably match the results from the molecular dynamics simulation.

2.5 Pressure-dependence of the plastic flow strength

In the literature on plastic flow of metals under extreme conditions of pressure and strain rate (cf., e.g., Remington et al. [48] for a recent review), the plastic flow strength in shear (under isothermal conditions), S, is often taken to be given by

$$S = f(\bar{\gamma}^\mathrm{p}, \dot{\bar{\gamma}}^\mathrm{p})\,\frac{\mu(P)}{\mu_0}, \tag{2.36}$$

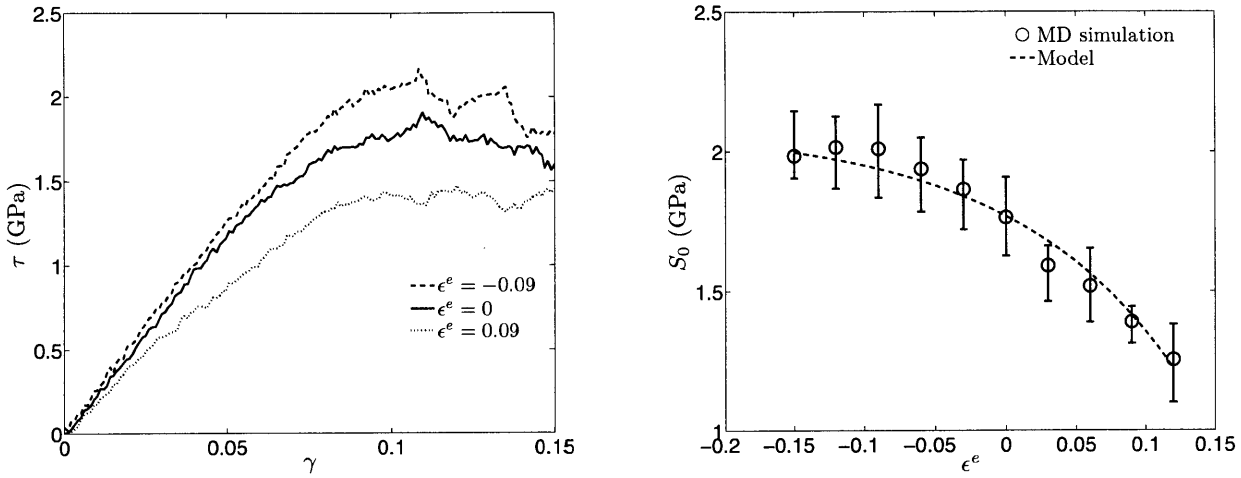

Figure 2-10: (a) Variation of the shear stress with shear strain at several levels of volumetric strain, and (b) the variation of the flow stress with volumetric strain.

where $f(\bar{\gamma}^{\mathrm{p}}, \dot{\bar{\gamma}}^{\mathrm{p}})$ is a function of the equivalent plastic shear strain $\bar{\gamma}^{\mathrm{p}}$ and the equivalent plastic shear strain rate $\dot{\bar{\gamma}}^{\mathrm{p}}$, and the flow strength S is presumed to scale with the ratio $\mu(P)/\mu_0$, where $\mu(P)$ is the pressure-dependent elastic shear modulus and μ_0 is the value of the elastic shear modulus at zero pressure. Instead of taking the shear modulus μ to be a function of the pressure P, *for our purposes* it is more useful to take μ to be a function of the elastic volumetric strain

$$\epsilon^{\mathrm{e}} \stackrel{\mathrm{def}}{=} \mathrm{tr}\,\mathbf{E}^{\mathrm{e}},$$

with $\mathbf{E}^{\mathrm{e}}$ the logarithmic elastic strain in a theory for elastic-plastic deformation of metals,[9] and alternatively write (2.36) as

$$S = f(\gamma^{\mathrm{p}}, \dot{\gamma}^{\mathrm{p}})\,\frac{\mu(\epsilon^{\mathrm{e}})}{\mu_0}. \tag{2.37}$$

In this section, we explore the correlation between the volumetric strain-dependence of the shear modulus from Section 2.4.2 and that of the plastic flow strength (2.37).

In order to determine the plastic flow strength at different levels of elastic volumetric strain, we carried out molecular dynamics simulations in which the sample is first subjected to a prescribed volumetric strain, and then subjected to increasing pure shear strain until plastic deformation ensues. Figure 2-10(a) shows the shear stress versus shear strain response up to a shear strain of $\gamma = 0.15$ at three different elastic volumetric pre-strains, $\epsilon^{\mathrm{e}} = -0.09, 0, 0.09$.

[9]Here we have in mind an isotropic theory of elastic-plastic solids based on the multiplicative decomposition of the deformation gradient $\mathbf{F} = \mathbf{F}^{\mathrm{e}}\mathbf{F}^{\mathrm{p}}$, in which $\mathbf{F}^{\mathrm{e}}$ and $\mathbf{F}^{\mathrm{p}}$ are elastic and plastic distortions, respectively, and where $\mathbf{E}^{\mathrm{e}} = \ln \mathbf{V}^{\mathrm{e}}$, with $\mathbf{V}^{\mathrm{e}}$ the left elastic stretch tensor in the polar decompostion $\mathbf{F}^{\mathrm{e}} = \mathbf{V}^{\mathrm{e}}\mathbf{R}^{\mathrm{e}}$.

In all three cases, a nominally linear elastic response is observed up to a shear strain of $\gamma \approx 0.06 - 0.08$, at which point inelastic deformation sets in. The stress-strain results from the molecular dynamics simulations are quite noisy, and the level of the shear stress in the inelastic region shows significant fluctuations; accordingly, we average the stress over the range of shear strains $\gamma \in [0.08, 0.12]$ and take this average as the value of plastic flow strength at $\bar{\gamma}^{\mathrm{p}} \approx 0$ and a high molecular dynamics strain rate of $\dot{\bar{\gamma}}^{\mathrm{p}} = 1 \times 10^8\,\mathrm{s}^{-1}$, denoting it by S_0. Such averaged plastic flow strength values S_0 are plotted as a function of the prior volumetric elastic strain ϵ^{e} in Fig. 2-10(b).[10] Using (2.37) and (2.32), the elastic volumetric strain dependence of S_0 is predicted to be

$$S_0 = f_0 \left[\frac{\mu_{\mathrm{r}}}{\mu_0} - \left(\frac{\mu_{\mathrm{r}}}{\mu_0} - 1 \right) \exp\left(\frac{\epsilon^{\mathrm{e}}}{\epsilon_{\mathrm{r}}} \right) \right]. \tag{2.38}$$

The prediction of the variation of S_0 with ϵ^{e}, using the parameter list (2.33), is also plotted in Fig. 2-10(b). The agreement from the model (2.38) with the results of the numerical simulations is quite good. This good agreement strongly indicates that one contribution to the "pressure-dependence" of plastic flow in metallic glasses is directly related to the "elastic volumetric strain-dependence" of the shear modulus of the material. Our numerical simulation results also support the scaling relation (2.36) (or equivalently (2.37)) for the "pressure-sensitivity" of plastic flow used in the metal physics community.

2.6 Concluding remarks

The Hencky [27–29]-Anand [25, 26] free energy and stress-strain relation for moderately large elastic strains are given by

$$\begin{aligned} \psi(\mathbf{E}) &= \mu_0 |\mathbf{E}_0|^2 + \frac{1}{2}\kappa_0 (\mathrm{tr}\mathbf{E})^2, \\ \mathbf{T}_{\mathrm{K}} &= 2\mu_0 \mathbf{E}_0 + \kappa_0 (\mathrm{tr}\mathbf{E})\mathbf{1}, \end{aligned} \tag{2.39}$$

with $\mu_0 > 0$ and $\kappa_0 > 0$ the classical shear and bulk moduli from the infinitesimal theory of elasticity. Based on molecular dynamics simulations of a metallic glass, we have attempted to extend the range of applicability of the Hencky-Anand theory to situations involving large volumetric strains, and have proposed the following free energy function

$$\begin{aligned} &\psi(\mathbf{E}) = \mu(\mathrm{tr}\mathbf{E})\,|\mathbf{E}_0|^2 + g(\mathrm{tr}\mathbf{E}), \qquad \text{with} \\ &\mu(\mathrm{tr}\mathbf{E}) = \mu_{\mathrm{r}} - (\mu_{\mathrm{r}} - \mu_0) \exp\left(\frac{\mathrm{tr}\mathbf{E}}{\epsilon_{\mathrm{r}}} \right), \qquad \text{and} \\ &g(\mathrm{tr}\mathbf{E}) = \kappa_0 (\epsilon_{\mathrm{c}})^2 \left[1 - \left(1 + \frac{\mathrm{tr}\mathbf{E}}{\epsilon_{\mathrm{c}}} \right) \exp\left(-\frac{\mathrm{tr}\mathbf{E}}{\epsilon_{\mathrm{c}}} \right) \right]. \end{aligned} \tag{2.40}$$

[10] The error bars in this figure denote the maximum and minimum values of shear stress encountered in defining the onset of plastic flow in our numerical simulations.

The Kirchhoff stress corresponding to the free energy (2.40) is given by

$$\begin{aligned}\mathbf{T}_{\mathrm{K}} =& 2\left[\mu_{\mathrm{r}} - (\mu_{\mathrm{r}} - \mu_0)\exp\left(\frac{\mathrm{tr}\,\mathbf{E}}{\epsilon_{\mathrm{r}}}\right)\right]\mathbf{E}_0 \\ &+ \left\{\left[\kappa_0 \exp\left(-\frac{\mathrm{tr}\,\mathbf{E}}{\epsilon_{\mathrm{c}}}\right)\right]\mathrm{tr}\,\mathbf{E} - \left[\frac{(\mu_{\mathrm{r}} - \mu_0)}{\epsilon_{\mathrm{r}}}\exp\left(\frac{\mathrm{tr}\,\mathbf{E}}{\epsilon_{\mathrm{r}}}\right)\right]|\mathbf{E}_0|^2\right\}\mathbf{1}.\end{aligned} \tag{2.41}$$

The new free energy and corresponding stress-strain relation have five material constants — the two classical positive-valued shear and bulk moduli μ_0 and κ_0 of the infinitesimal theory of elasticity, and three additional positive-valued material constants $(\mu_{\mathrm{r}}, \epsilon_{\mathrm{r}}, \epsilon_{\mathrm{c}})$, which are used to characterize the nonlinear response at large values of $\mathrm{tr}\,\mathbf{E}$. In the large volumetric strain range $-0.30 \leq \mathrm{tr}\,\mathbf{E} \leq 0.15$ but small shear strain range $\sqrt{2}|\mathbf{E}_0| \lessapprox 0.05$ numerically explored in this paper, this simple five-constant model provides a very good description of the stress-strain results from our molecular dynamics simulations.

As reviewed by Veprek et al. [43], recently-developed coating materials possess ultra-high hardness in the range of 40–100 GPa. The mechanical properties of these thin coating materials are primarily assessed by means of load-versus-depth sensing indentation techniques. During indentation tests on hard materials, a very high pressure builds up in the sample under the indenter, and this causes the elastic moduli and plastic flow strength to increase substantially. It is of central importance to account for such nonlinear behavior when simulating indentation experiments, or using experimental data from indentation experiments to infer hardness and other mechanical properties of ultra-hard materials. Our new free energy function (2.40) and the attendant stress-strain relation (2.41) should be useful in analyzing the results of load-depth indentation experiments on ultra-hard materials.

In the absence of deviatoric strains, our theory produces a pressure-volume equation-of-state (EOS) which extends a relation based on the logarithmic strain measure proposed by Poirier and Tarantola [49]. As reviewed by Stacey and Davis [44], the Poirier-Tarantola EOS is of substantial utility in describing the pressure-volume relationship in the *lower mantle* of the earth and is much better than the widely-used Birch [50] EOS. In addition to extending the range of applicability of the Poirier-Tarantola EOS to larger compressive volumetric strains, our more general theory explicitly accounts for the volumetric strain dependence of the generalized shear modulus $\mu(\mathrm{tr}\,\mathbf{E})$ — a coupling-effect which is of substantial importance in the geophysics literature on the high-pressure response of geological materials (cf., e.g., Stacey and Davis [44]).

Chapter 3

The Anand-Su large-deformation, elastic-viscoplastic constitutive theory for metallic glasses

3.1 Introduction

In this chapter, we aim to describe both the elastic and inelastic behavior of metallic glasses. An important consequence of the micro-mechanisms of inelastic deformation in metallic glasses is that at the macroscopic level, experimentally-determined yield criteria for inelastic deformation are found not to obey the classical pressure-insensitive forms [9, 51–53] but show a significant pressure sensitivity of plastic flow, which may be approximated by the Coulomb [54]-Mohr [55] yield criterion [9, 53].

The Coulomb-Mohr yield condition is widely used in soil mechanics to determine the stress required for flow of a granular material; however, the *flow rule*, that is, the equation which governs the flow behavior for this class of materials, is generally not agreed upon. An attractive *two-dimensional* (plane-strain) *rate-independent* flow rule for Coulomb-Mohr materials is the "double-shearing" flow rule [56–60]. Anand and Gu [61] have generalized this model to three-dimensions, including the effects of elastic deformation and the typical pressure-sensitive and dilatant, hardening/softening response observed in granular materials, and more recently, Anand and Su [34, 35] have further generalized the rate-independent elastic-plastic constitutive model of Anand and Gu [61] to formulate a *thermodynamically-consistent*, finite-deformation macroscopic theory for the *rate-dependent* elastic-viscoplastic deformation of pressure-sensitive, and plastically-dilatant materials. It is the purpose of this chapter to review the reasonable-general theoretical framework of Anand and Su, which will be further specialized in subsequent chapters.

3.2 Constitutive theory

The isothermal constitutive theory of Anand and Su [34, 35] for metallic glasses relates the following basic fields: $\mathbf{x} = \boldsymbol{\chi}(\mathbf{X}, t)$, motion; $\mathbf{F} = \nabla\boldsymbol{\chi}$, $J = \det\mathbf{F} > 0$, deformation gradient; $\mathbf{F} = \mathbf{F}^{\mathrm{e}}\mathbf{F}^{\mathrm{p}}$, elastic-plastic decomposition of $\mathbf{F}$; $\mathbf{F}^{\mathrm{p}}$, $J^{\mathrm{p}} = \det\mathbf{F}^{\mathrm{p}} > 0$, inelastic distortion; $\mathbf{F}^{\mathrm{e}}$, $J^{\mathrm{e}} = \det\mathbf{F}^{\mathrm{e}} > 0$, elastic distortion; $\mathbf{F}^{\mathrm{e}} = \mathbf{R}^{\mathrm{e}}\mathbf{U}^{\mathrm{e}}$, polar decomposition of $\mathbf{F}^{\mathrm{e}}$; $\mathbf{U}^{\mathrm{e}} = \sum_{\alpha=1}^{3} \lambda_\alpha^{\mathrm{e}} \mathbf{r}_\alpha^{\mathrm{e}} \otimes \mathbf{r}_\alpha^{\mathrm{e}}$, spectral decomposition of $\mathbf{U}^{\mathrm{e}}$; $\mathbf{E}^{\mathrm{e}} = \sum_{\alpha=1}^{3} (\ln \lambda_\alpha^{\mathrm{e}}) \mathbf{r}_\alpha^{\mathrm{e}} \otimes \mathbf{r}_\alpha^{\mathrm{e}}$, logarithmic elastic strain; $\mathbf{T}$, $\mathbf{T} = \mathbf{T}^{\mathsf{T}}$, Cauchy stress; $\mathbf{T}^{\mathrm{e}} = J^{\mathrm{e}}\mathbf{R}^{\mathrm{e}\mathsf{T}}\mathbf{T}\mathbf{R}^{\mathrm{e}}$, stress conjugate to the logarithmic elastic strain, $\mathbf{E}^{\mathrm{e}}$; $\vartheta > 0$, absolute temperature; ψ, free energy density per unit volume of intermediate (or structural) space. In addition, the theory employs two scalar internal variables: (i) a stress-dimensioned parameter S which represents the isotropic resistance to plastic flow in shear, and (ii) a positive-valued, dimensionless "order-parameter" φ to represent *deformation-induced disordering* of the amorphous material.[1] The set of constitutive equations used in this thesis are summarized below.

3.2.1 Elasticity relations: free energy, equation for the stress

Anand and Su [34, 35] used a simple generalization of the classical strain energy function and the equation for stress of isotropic linear elasticity, wherein they used the logarithmic measure of finite strain instead of the classical infinitesimal strain:

$$\left.\begin{aligned} \psi(\mathbf{E}^{\mathrm{e}}) &= \mu|\mathbf{E}_0^{\mathrm{e}}|^2 + \tfrac{1}{2}\kappa(\mathrm{tr}\,\mathbf{E}^{\mathrm{e}})^2, \\ \mathbf{T}^{\mathrm{e}} &= \frac{\partial\psi(\mathbf{E}^{\mathrm{e}})}{\partial\mathbf{E}^{\mathrm{e}}} = 2\mu\mathbf{E}_0^{\mathrm{e}} + \kappa\,(\mathrm{tr}\,\mathbf{E}^{\mathrm{e}})\mathbf{1}, \end{aligned}\right\} \tag{3.1}$$

where $\mu(\vartheta) > 0$ and $\kappa(\vartheta) > 0$ denote the temperature-dependent, ground-state elastic shear and bulk moduli of the infinitesimal theory.[2] These constitutive equations for the free energy and stress have been previously shown by Anand [25, 26] to be useful for modeling the response of nonlinear elastic materials for *moderately large elastic strains.*

For later use we note that the symmetric stress tensor $\mathbf{T}^{\mathrm{e}}$ has the spectral representation

$$\mathbf{T}^{\mathrm{e}} = \sum_{i=1}^{3} \sigma_i\, \hat{\mathbf{e}}_i \otimes \hat{\mathbf{e}}_i, \qquad \sigma_1 \geq \sigma_2 \geq \sigma_3, \tag{3.2}$$

where $\{\sigma_i | i = 1, 2, 3\}$ are the principal values, and $\{\hat{\mathbf{e}}_i | i = 1, 2, 3\}$ the corresponding orthonormal principal directions. We assume that the principal stresses $\{\sigma_i | i = 1, 2, 3\}$ are strictly ordered such that

$$\sigma_1 \geq \sigma_2 \geq \sigma_3. \tag{3.3}$$

[1] Deformation-induced disordering is often associated with the change in "free-volume" — a terminology first introduced in the literature by Cohen and Grest [62] for simple amorphous metals.

[2] Henceforth, we do not use the subscript 0 when discussing ground-state moduli.

3.2.2 Plasticity relations: flow rule, evolution equations for internal variables

The micro-mechanisms of inelastic deformation in metallic glasses are not related to dislocation-based mechanisms that characterize the plastic deformation of crystalline metals. The plastic deformation of amorphous metallic glasses is fundamentally different from that in crystalline solids because of the lack of long-range order in the atomic structure of these materials. Atomistic simulations reported in the literature [cf., e.g., 10, 13–16] show that at a micromechanical level, inelastic deformation in metallic glasses occurs by local shearing of clusters of atoms (≈10 to 30 atoms), this shearing is accompanied by deformation-induced *microstructural disordering* and *inelastic dilatation* that produces *strain-softening*, which at low homologous temperatures leads to the formation of intense shear bands. See Appendix B for examples of shear bands observed in two-dimensional molecular dynamics simulations.

It is of note that deformation-induced microstructural disordering in a metallic glass also occurs in the high temperature range. A macroscopic manifestation of the structural disordering in this temperature range is that in strain-controlled isothermal compression or tension experiments at constant strain rate, the microstructural disordering leads to strain-softening. However, because of the high strain rate sensitivity of the material at elevated temperatures, it does not exhibit macroscopic localized shear bands and the deformation appears as *nominally homogeneous*. Experimental examples of such macroscopic response may be found in de Hey et al. [63] for the amorphous metal $Pd_{40}Ni_{40}P_{20}$ and in Lu et al. [12] for the commercial Zr-based alloy Vitreloy-1.

In the Anand-Su theory plastic flow is presumed to occur by shearing accompanied by dilatation relative to some "slip systems," and accordingly the evolution equation for $\mathbf{F}^{\mathrm{p}}$ is taken as

$$\dot{\mathbf{F}}^{\mathrm{p}} = \mathbf{L}^{\mathrm{p}}\mathbf{F}^{\mathrm{p}}, \qquad \mathbf{F}^{\mathrm{p}}(\mathbf{X}, 0) = \mathbf{1}, \tag{3.4}$$

with

$$\mathbf{L}^{\mathrm{p}} = \sum_{\alpha} \nu^{(\alpha)}\, \mathbf{s}^{(\alpha)} \otimes \mathbf{m}^{(\alpha)} + \delta^{(\alpha)}\, \mathbf{m}^{(\alpha)} \otimes \mathbf{m}^{(\alpha)}, \qquad \text{and} \qquad \delta^{(\alpha)} = \beta \nu^{(\alpha)}. \tag{3.5}$$

Each slip system is specified by a slip direction $\mathbf{s}^{(\alpha)}$ and a slip plane normal $\mathbf{m}^{(\alpha)}$, with $(\mathbf{s}^{(\alpha)}, \mathbf{m}^{(\alpha)})$ orthonormal, and $\nu^{(\alpha)} \geq 0$ the shearing rate. The dilatation rate associated with shearing on each slip system is $\delta^{(\alpha)} = \beta \nu^{(\alpha)}$, with β a *shear-induced plastic dilatancy function.*

It is important to note that the slip systems, considered above and to be defined below, *are not the classical slip systems of crystal plasticity*, but are constructs of a mathematical model for isotropic amorphous materials. They are related to the principal directions of the stress $\mathbf{T}^{\mathrm{e}}$, and they change **both spatially and temporally** as the principal directions of stress change in a non-homogeneously deforming material.

To make clear the Anand-Su model for plastic flow by atomic-scale shear transformations on microscopic "slip systems," consider the schematic diagram in Fig. 3-1. Let $\mathbf{x}_1$ and $\mathbf{x}_2$ be the current positions of two material points in the deformed body $\mathcal{B}_t$, and let $\{\hat{\mathbf{e}}_1, \hat{\mathbf{e}}_2, \hat{\mathbf{e}}_3\}$ denote the principal directions of the stress $\mathbf{T}^{\mathrm{e}}$ at each of these points. In a non-homogeneously

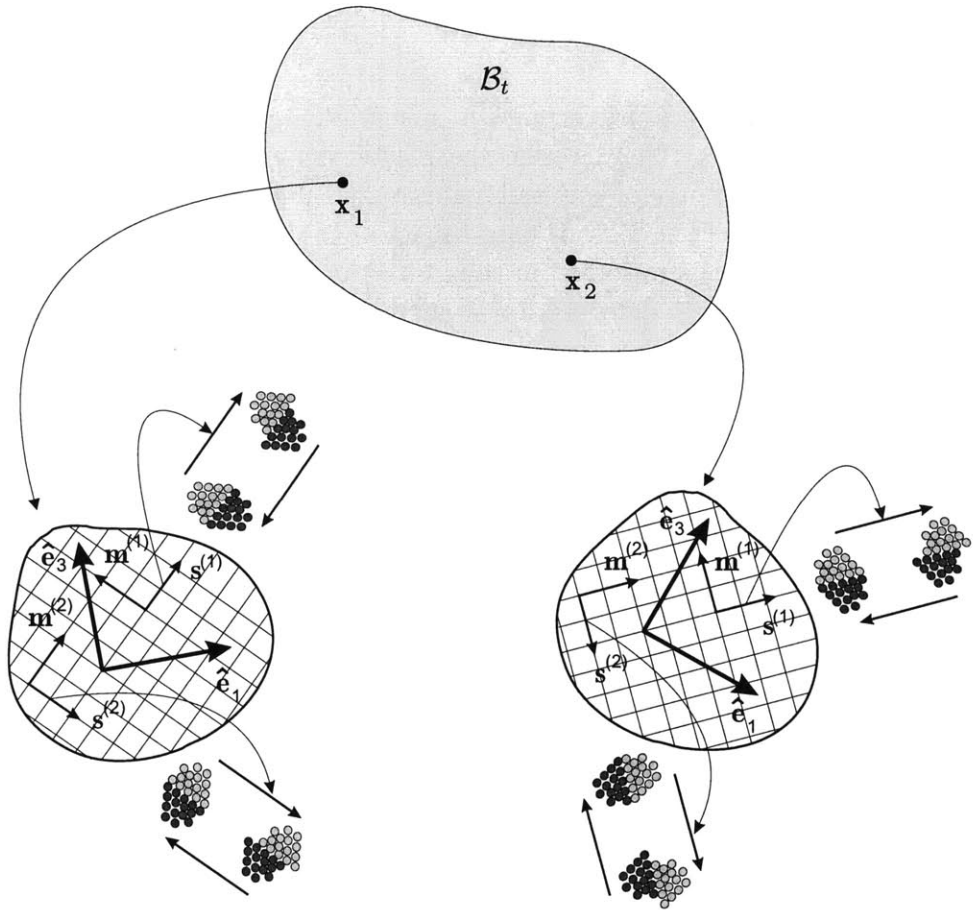

Figure 3-1: Schematic of plastic flow by atomic-scale shear transformations on microscopic "slip systems" $(\mathbf{s}^{(1)}, \mathbf{m}^{(1)})$ and $(\mathbf{s}^{(2)}, \mathbf{m}^{(2)})$ in the Anand-Su model for metallic glass plasticity.

deforming body these principal directions of the stress will in general be different for the material points at $\mathbf{x}_1$ and $\mathbf{x}_2$. In the theory there are three pairs of slip systems associated with the principal directions of $\mathbf{T}^{\mathrm{e}}$. The first pair of slip systems lie in the $(\hat{\mathbf{e}}_1, \hat{\mathbf{e}}_3)$-plane defined by the maximum and minimum principal stress directions, and are defined by

$$\left.\begin{aligned} \mathbf{s}^{(1)} &= \cos\xi\hat{\mathbf{e}}_1 + \sin\xi\hat{\mathbf{e}}_3, \quad \mathbf{m}^{(1)} = \sin\xi\hat{\mathbf{e}}_1 - \cos\xi\hat{\mathbf{e}}_3, \\ \mathbf{s}^{(2)} &= \cos\xi\hat{\mathbf{e}}_1 - \sin\xi\hat{\mathbf{e}}_3, \quad \mathbf{m}^{(2)} = \sin\xi\hat{\mathbf{e}}_1 + \cos\xi\hat{\mathbf{e}}_3, \end{aligned}\right\} \tag{3.6}$$

with

$$\xi \stackrel{\text{def}}{=} \frac{\pi}{4} + \frac{\theta_{\text{fric}}}{2}, \tag{3.7}$$

where

$$\theta_{\text{fric}} \stackrel{\text{def}}{=} \arctan\mu_{\text{fric}} \tag{3.8}$$

is an *angle of internal friction*, and $\mu_{\text{fric}} \geq 0$ an *internal friction coefficient.* These *mathematically imagined* "slip-systems" $(\mathbf{s}^{(1)}, \mathbf{m}^{(1)})$ and $(\mathbf{s}^{(2)}, \mathbf{m}^{(2)})$ are depicted as hatched lines in Fig. 3-1 for the two material points under consideration. The orientations of the slip systems at these two points is different because the local stress state at these two points will in general be different. What is important is that these slip systems are related to the directions of *local maximum shear stress* (modulo small differences when the angle of internal friction θ_{fric} is non-zero). When plastic deformation at an atomic level occurs by *local shear transformations* of clusters of atoms, it is biased by the local shear stresses and occurs in the "slip directions" as depicted schematically in Fig. 3-1. This shearing is accompanied by deformation-induced *microstructural disordering* and *inelastic dilatation.* At the macroscopic level, the collective action of numerous such shear transformations is represented by local *averaged* plastic shearing rates $\nu^{(1)}$ and $\nu^{(2)}$, and resulting the plastic velocity gradient $\mathbf{L}^{\text{P}}$ is described by (3.5).

In an entirely analogous manner there is a pair of slip systems $(\mathbf{s}^{(3)}, \mathbf{m}^{(3)})$ and $(\mathbf{s}^{(4)}, \mathbf{m}^{(4)})$ associated with the $(\hat{\mathbf{e}}_1, \hat{\mathbf{e}}_2)$-plane, and another pair $(\mathbf{s}^{(5)}, \mathbf{m}^{(5)})$ and $(\mathbf{s}^{(6)}, \mathbf{m}^{(6)})$ associated with the $(\hat{\mathbf{e}}_2, \hat{\mathbf{e}}_3)$-plane, and these are given by

$$\left.\begin{aligned}
\mathbf{s}^{(3)} &= \cos\xi\hat{\mathbf{e}}_1 + \sin\xi\hat{\mathbf{e}}_2, \quad & \mathbf{m}^{(3)} &= \sin\xi\hat{\mathbf{e}}_1 - \cos\xi\hat{\mathbf{e}}_2,\\
\mathbf{s}^{(4)} &= \cos\xi\hat{\mathbf{e}}_1 - \sin\xi\hat{\mathbf{e}}_2, \quad & \mathbf{m}^{(4)} &= \sin\xi\hat{\mathbf{e}}_1 + \cos\xi\hat{\mathbf{e}}_2,\\
\mathbf{s}^{(5)} &= \cos\xi\hat{\mathbf{e}}_2 + \sin\xi\hat{\mathbf{e}}_3, \quad & \mathbf{m}^{(5)} &= \sin\xi\hat{\mathbf{e}}_2 - \cos\xi\hat{\mathbf{e}}_3,\\
\mathbf{s}^{(6)} &= \cos\xi\hat{\mathbf{e}}_2 - \sin\xi\hat{\mathbf{e}}_3, \quad & \mathbf{m}^{(6)} &= \sin\xi\hat{\mathbf{e}}_2 + \cos\xi\hat{\mathbf{e}}_3.
\end{aligned}\right\} \tag{3.9}$$

The corresponding plastic shearing rates are denoted by $\nu^{(3)}$ through $\nu^{(6)}$.

With the resolved shear and compressive normal traction on each slip system defined by

$$\tau^{(\alpha)} \stackrel{\text{def}}{=} \mathbf{s}^{(\alpha)} \cdot \mathbf{T}^{\text{e}}\mathbf{m}^{(\alpha)}, \qquad \sigma^{(\alpha)} \stackrel{\text{def}}{=} -\mathbf{m}^{(\alpha)} \cdot \mathbf{T}^{\text{e}}\mathbf{m}^{(\alpha)}, \tag{3.10}$$

the corresponding shearing rate is given by a flow function

$$\nu^{(\alpha)} = \hat{\nu}^{(\alpha)}(\tau^{(\alpha)}, \sigma^{(\alpha)}, \vartheta, S, \varphi) \geq 0, \tag{3.11}$$

where φ is a positive-valued, dimensionless "order-parameter" introduced to represent the deformation-induced microstructural disordering of a metallic glass, and S is a stress-dimensioned internal variable which represents an isotropic resistance to plastic flow, assumed for an isotropic material to be the same for all slip systems.

It is convenient to write Λ for the list of variables

$$\Lambda = (\mathbf{T}^{\text{e}}, \vartheta, S, \varphi).$$

Using this notation, we assume that the dilatancy parameter β depends on Λ,

$$\beta = \hat{\beta}(\Lambda). \tag{3.12}$$

The dissipation inequality in the theory is

$$\mathbf{T}^{\mathrm{e}}:\mathbf{L}^{\mathrm{p}} > 0 \quad \text{for} \quad \mathbf{L}^{\mathrm{p}} \neq \mathbf{0}. \tag{3.13}$$

With $\mathbf{L}^{\mathrm{p}}$ given by (3.5), (3.6), and (3.9), the dissipation inequality requires that

$$\mathbf{T}^{\mathrm{e}}:\mathbf{L}^{\mathrm{p}} = \sum_{\alpha=1}^{6} \left[\tau^{(\alpha)} - \beta\,\sigma^{(\alpha)}\right] \nu^{(\alpha)} > 0 \tag{3.14}$$

whenever plastic flow occurs. We assume that the material is *strongly dissipative* in the sense that

$$\left[\tau^{(\alpha)} - \beta\,\sigma^{(\alpha)}\right] \nu^{(\alpha)} > 0 \qquad \text{for each } \alpha\,. \tag{3.15}$$

Thus, whenever $\nu^{(\alpha)} > 0$, we must have

$$\left[\tau^{(\alpha)} - \beta\,\sigma^{(\alpha)}\right] > 0, \tag{3.16}$$

which is a thermodynamic restriction that the dilatancy function $\beta = \hat{\beta}(\Lambda)$ must satisfy.

Recall that the internal variables of the theory are the isotropic resistance S and the order-parameter φ. In the Anand-Su theory the change in φ is taken to be due to the (small) shear-induced plastic volume change,

$$\varphi \stackrel{\text{def}}{=} \varphi_0 + \ln J^{\mathrm{p}}, \tag{3.17}$$

with φ_0 a constant, so that the change in φ from its initial value φ_0 is due to the plastic volumetric strain ($\ln J^{\mathrm{p}}$). Then, the standard kinematical relation $\dot{J}^{\mathrm{p}} = J^{\mathrm{p}}\mathrm{tr}\mathbf{L}^{\mathrm{p}}$ gives $\dot{\varphi} = \mathrm{tr}\mathbf{L}^{\mathrm{p}}$, and hence, using (3.5), we obtain the following evolution equation for φ,

$$\dot{\varphi} = \beta\nu^{\mathrm{p}} \qquad \text{with initial value} \qquad \varphi(\mathbf{X},0) = \varphi_0, \tag{3.18}$$

where β is the shear-induced plastic dilatancy function and

$$\nu^{\mathrm{p}} \stackrel{\text{def}}{=} \sum_{\alpha=1}^{6} \nu^{(\alpha)} \tag{3.19}$$

is the sum of the shearing rates on all the slip systems.

Finally, the evolution of the resistance S is *coupled* with the evolution of φ. We take the evolution of S to be governed by

$$\dot{S} = h(\vartheta, S, \varphi, \nu^{\mathrm{p}}) \qquad \text{with initial value} \qquad S(\mathbf{X},0) = S_0. \tag{3.20}$$

3.3 Concluding remarks

The constitutive framework reviewed in this chapter was specialized to model the mechanical behavior of metallic glasses at temperatures below the glass transition [34, 35]. Using the specialized theory, Anand and Su [34, 35] performed finite element simulations of plane-strain tension and compression, strip bending, and plane-strain indentation. Indeed, their simulated shear band patterns using the specialized constitutive theory are quite similar to those observed experimentally, as well as to those observed in the molecular dynamics simulations of Appendix B.

Chapter 4

Fracture of metallic glasses at notches: effects of notch-root radius and the ratio of the elastic shear modulus to the bulk modulus on toughness

4.1 Introduction

Monolithic metallic glasses exhibit exceptionally high yield strengths, but essentially zero ductility in simple tension. However, these materials do exhibit relatively high fracture toughness, but there is considerable variability in the toughness values reported in the literature. For example, the reported fracture toughness of the commercial bulk metallic glass Vitreloy-1 ($Zr_{41.25}Ti_{13.75}Cu_{12.5}Ni_{10}Be_{22.5}$) in Mode-I, varies from 16 to 55 MPa$\sqrt{\text{m}}$ [e.g. 30, 64, 65]. The significant scatter in the fracture toughness data for BMGs has been attributed to variations in the processing conditions such as (a) the cooling rate during casting of these alloys; (b) residual stresses; (c) composition fluctuations; and (d) the sharpness of the crack/notch tip [e.g. 2, 3, 66]. Even though the reported values of fracture toughness of these materials show substantial variability, experimental observations in the literature reveal some important *intrinsic* features of the fracture response of metallic glasses, which we summarize below.

Flores and Dauskardt [32] conducted tensile tests on notched bars of the metallic glass Vitreloy-1 with various notch-tip radii. The notched bars in their experiments, Fig. 4-1(a), were of 10 mm diameter in the gauge section and had a constant notch depth of 2.50 mm, while the notch-tip radius ρ varied between 0.25 and 2.50 mm. Figure 4-1(b)(i) from their work shows a typical failure surface. They found that the fracture surfaces were reasonably flat in the central region, but there was a "shear-lip" near the edges of the notch roots. From their fractographic investigations they concluded *that failure initiated at some point in the*

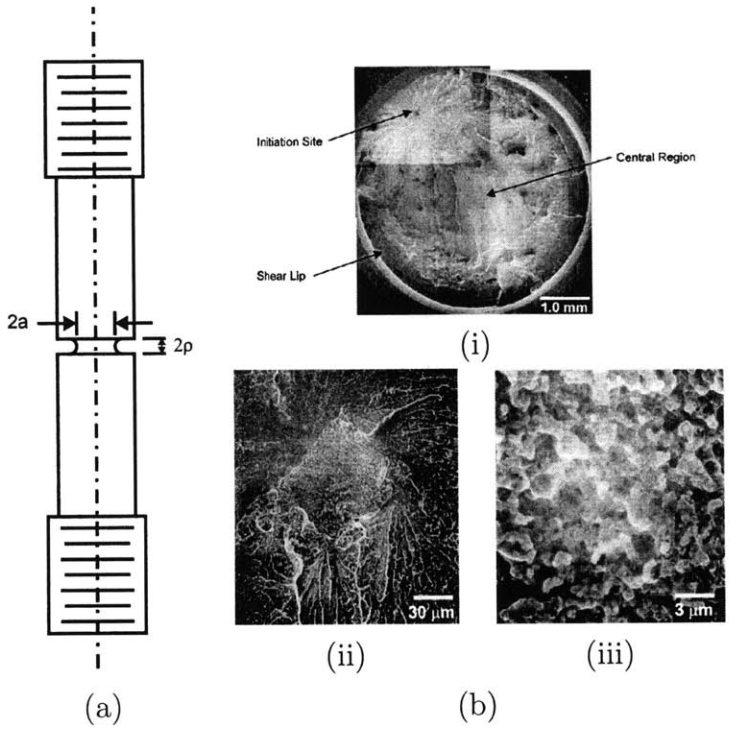

Figure 4-1: (a) Notched tensile specimen. (b) Micrographs of the failure surface of 1.25 mm notch-root radius bar. The failure initiation site is clearly visible in the upper left corner of *ahead of the notch root* (i), and is shown at higher magnification in (ii) and (iii). Note the equiaxed voids in (iii). From Flores and Dauskardt [32].

interior of the notched region of the bar, rather than at the notch tip. The initiation site in one of their specimens is shown at higher magnification in Figs. 4-1(b)(ii) and (iii); note the appearance of reasonably equiaxed voids at the initiation site. They observed that the crack front propagated radially from the crack-initiation site on a plane perpendicular to the tensile axis, followed by the formation of slanted shear lips. Flores and Dauskardt [32] conclude that failure initiation is *associated with the attainment of a critical tensile mean stress at some point in the interior of the notched region of the bar, rather than at the notch tip.* These authors write, "The fact that failure did not initiate at the notch root, where the mean stress is maximum, is a result of the stochastic nature of failure initiation. The probability of failure initiation at a small inhomogeneity increases as the volume of material sampled increases." However, they base their assertion that the mean stress is a maximum at the notch root on a purely *elastic analysis.* As we shall see shortly in our elastic-plastic calculations, the plasticity at the notch tip causes the location of the maximum mean normal stress to shift ahead of the tip of the plastic zone at the notch root, consistent with the location of their observed failure initiation site.

Lowhaphandu and Lewandowski [30] measured the toughness of a $Zr_{62.58}Ti_{10.1}Cu_{14.2}Ni_{9.65}Be_{3.47}$ (a composition slightly different from that of Vitreloy-1) bulk metallic glass on single-

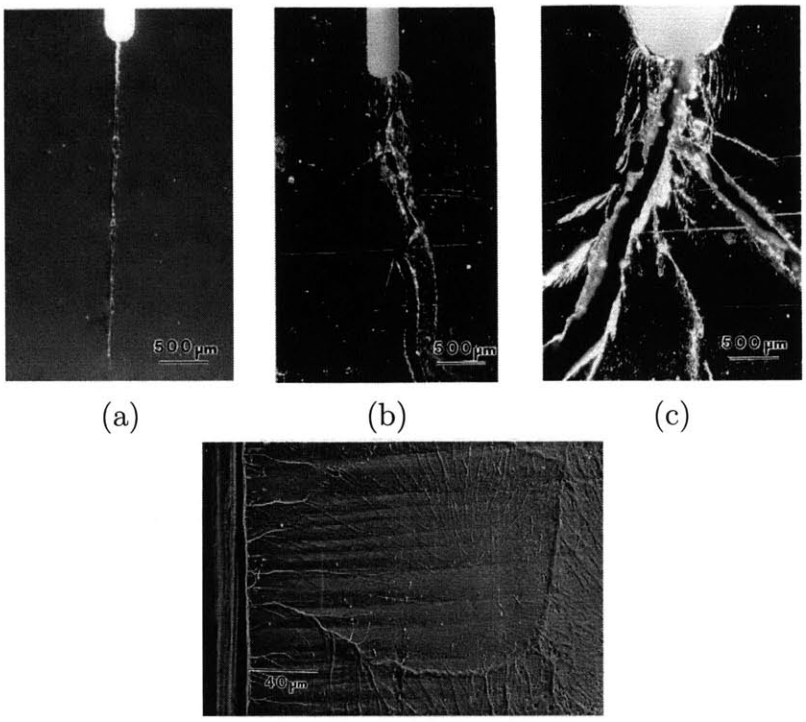

Figure 4-2: Typical macroscopic crack-path profiles of specimens tested with different notch-root radii: (a) fatigue pre-cracked; (b) root radius 65 μm; (c) root radius 250 μm. (d) Typical fracture surface of a notch specimen from a region near a notch root. Notch at left edge of figure; crack growth from left to right. From Lowhaphandu and Lewandowski [30].

edge-notched bend specimens. In specimens which were fatigue precracked to generate a sharp starter crack at a notch root, they reported a plane-strain Mode-I fracture toughness K_{Ic} of $\approx$ 18.5MPa$\sqrt{\mathrm{m}}$, while the specimens which were not fatigue pre-cracked, but had notch-root radii increasing from 65 μm to 250 μm had toughnesses K_{c} in the range of 101–131 MPa$\sqrt{\mathrm{m}}$, with the toughness K_{c} increasing linearly with $\sqrt{\rho}$, where ρ is the notch-root radius [31]. Here and henceforth, we denote the toughness of notched specimens which are *not fatigue precracked* by K_{c}. Figure 4-2, taken from Lowhaphandu and Lewandowski [30], shows that the crack path profile is also significantly affected by the notch-root radius. A fatigue pre-cracked specimen, Fig. 4-2(a), exhibits a relatively planar crack front, while notched specimens, Figs. 4-2(b) and (c), exhibit extensive shear-banding at the notch-root region, as well as significant crack-branching as the crack propagates. As discussed by these authors, the multiple shear-banding and crack-branching clearly absorb more energy than the planar fracture-mode exhibited by the fatigue pre-cracked specimens, which is consistent with the increased toughness in going from the fatigue pre-cracked specimens to those containing somewhat blunter notches. The notched specimens, cf. Fig. 4-2(d) for an example, exhibited "peculiar flat" features on the fracture surface, which were about 100 μm ahead of the notch

root. In describing such features, Lowhaphandu and Lewandowski [30] write "the fracture surface exhibited features suggestive of local melting and/or viscous flow, as revealed by the globular features and spattered appearance of the fracture surface." However, to us such flat features appear to be the initiation sites of cavitation-like fracture events ahead of the notch roots, similar to those observed by Flores and Dauskardt [32].

Thus, experiments [30–32] indicate that

1. *The notch toughness of metallic glasses decreases as the notch-root radius decreases, with K_c decreasing linearly with $\sqrt{\rho}$.*

2. *Fracture in notched specimens initiates ahead of the notch root where the mean normal stress reaches a maximum value.*

Further, from an extensive compilation of data for metallic glasses, Lewandowski et al. [33] have shown that there is a strong correlation between *intrinsic plasticity or brittleness* of these materials and their *elastic properties.* Specifically, they find that

3. *As the ratio μ/κ of the elastic shear modulus μ to the bulk modulus κ increases, the toughness K_c decreases, that is, the material becomes more brittle.*

This correlation is suggestive of the classical competition between plastic flow and brittle fracture, with the resistance to plastic deformation, which occurs by local shear transformations of clusters of atoms, being influenced by the elastic shear modulus μ, and the resistance to dilatation and bond breaking that occurs in the vicinity of a crack tip in Mode-I, influenced by the elastic bulk modulus κ.

Since the ratio μ/κ is related to the Poisson's ratio ν by $\mu/\kappa = (3/2)(1-2\nu)/(1+\nu)$, the decrease in K_c as μ/κ increases is often interpreted and reported as an effect that K_c increases as the Poisson's ratio ν increases. In order to understand the reasons for the observed high toughness in metallic glasses with high values of ν, in a recent paper Tandaiya et al. [67] have attempted to answer the question, "how does the Poisson's ratio modify the crack tip fields in BMGs?", by conducting a detailed finite element investigation of the effect of Poisson's ratio on the crack tip fields in metallic glasses under Mode-I, plane-strain, small-scale-yielding (SSY) conditions. In their study they compared the predictions of local crack-tip fields by employing the classical elastic-plastic Mises and Drucker-Prager theories, as well as the Anand-Su theory for metallic glasses [34, 35]. While their study sheds much light on the process of plastic deformation at sharp notches, and provides some plausible qualitative reasons for the effect of ν on K_c, it falls short of making any quantitative predictions since as these authors note, they did not consider any *fracture criterion* — a key ingredient which is required to make any quantitative predictions.

The purpose of this chapter is to

- Introduce an important modification of the finite elasticity relation in the large deformation elastic-plastic Anand-Su theory for metallic glasses (cf. Section 3.2.1) to account for the strongly nonlinear and eventually softening, dilatational volumetric

elastic response of the material. This automatically introduces a simple fracture criterion to model brittle fracture by an elastic cavitation phenomenon in the notch-tip region.

- Use the modified form of the Anand-Su theory to conduct detailed finite element simulations of notch-tip fracture initiation in a representative metallic glass under Mode-I, plane-strain, small-scale-yielding conditions, and show that this theory predicts the three enumerated items above; viz., fracture initiates ahead of the notch root where the mean normal stress reaches a maximum value, K_c increases linearly with $\sqrt{\rho}$, and K_c decreases as μ/κ increases.

We emphasize that even though we use the terminology of Linear Elastic Fracture Mechanics (LEFM), such as K-fields and the like, the fracture criterion we introduce is *local*. The fracture criterion is not based on the underlying ideas of LEFM where far-field applied stress and crack lengths are of primary concern, with the cracks considered to be mathematically sharp with singular stress fields; finite notch-root radii do not enter the LEFM theory. Also, from the outset we note that the model used in our numerical simulations of fracture of metallic glasses is a deterministic continuum-level model, and in its present form it is not capable of accounting for the variability in toughness values present in real materials due to variations in the processing conditions, composition fluctuations, and fluctuations in configurational atomic/molecular structure.

This chapter is organized as follows. In Section 4.2, we summarize a modified and specialized form of the constitutive theory of Anand and Su introduced in Chapter 3. In Section 4.3, we estimate material parameters for the theory for the deformation and fracture behavior of the widely studied Zr-based glass (Vitreloy-1) from data in the literature, and also by conducting detailed finite element simulations of notched-bar tension tests and attempting to match important aspects of the results from the simulations against corresponding experimental results reported by Flores and Dauskardt [32]. With the material parameters in the model calibrated, in Section 4.4, we numerically investigate various aspects of fracture initiation from sharp but finite-radii notch tips under Mode-I, plane-strain, small-scale-yielding conditions; viz., the effect of notch-root radius ρ, and the effect of the ratio of the elastic moduli μ/κ.

4.2 Constitutive theory

In this section, we introduce a modification to the finite elasticity relation in the Anand-Su theory, Section 3.2.1, to account for the nonlinear dilatational, and eventually softening, volumetric elastic response of the material. We also specialize the plasticity relations, Section 3.2.2, for temperatures ϑ well below the glass transition temperature ϑ_g of the material.

4.2.1 Modification of the elasticity relations

The elasticity relations of Section 3.2.1 used a simple generalization of the classical strain energy function and the equation for stress of isotropic linear elasticity, wherein they used Hencky's logarithmic measure of finite strain instead of the classical infinitesimal strain [27–29]:

$$\left.\begin{aligned} \psi(\mathbf{E}^{\mathrm{e}}) &= \mu|\mathbf{E}_0^{\mathrm{e}}|^2 + \tfrac{1}{2}\kappa(\mathrm{tr}\,\mathbf{E}^{\mathrm{e}})^2, \\ \mathbf{T}^{\mathrm{e}} &= \frac{\partial\psi(\mathbf{E}^{\mathrm{e}})}{\partial\mathbf{E}^{\mathrm{e}}} = 2\mu\mathbf{E}_0^{\mathrm{e}} + \kappa\,(\mathrm{tr}\,\mathbf{E}^{\mathrm{e}})\mathbf{1}, \end{aligned}\right\} \tag{4.1}$$

with $\mu > 0$ and $\kappa > 0$ the ground-state elastic shear and bulk moduli of the infinitesimal theory. These constitutive equations for the free energy and stress have been previously shown by Anand [25, 26] to be useful for modeling the response of nonlinear elastic materials for *moderately large elastic strains.*

In the vicinity of a sharp notch root in an elastic-plastic material, the magnitude of the deviatoric elastic strains are expected to be limited by the onset of plasticity; however, the elastic volumetric strains are not so limited and can get quite large. In Chapter 2, we explored situations involving large elastic volumetric strains but limited deviatoric elastic strains using molecular dynamics simulations and proposed a free energy function (2.40) that captures the nonlinear mean stress-volumetric strain response as well as volumetric-deviatoric coupling effects. However, we do not expect volumetric-deviatoric coupling effects to play a significant role in cavitation phenomena, and for the sake of simplicity, we neglect such effects. In such situations, the free energy function (2.40), reduces to the free energy function (2.14) proposed by Gearing and Anand [42], motivated by the "universal binding energy relation" (UBER) introduced by Rose et al. [41]. With

$$\epsilon^{\mathrm{e}} \stackrel{\mathrm{def}}{=} \mathrm{tr}\,\mathbf{E}^{\mathrm{e}} \tag{4.2}$$

denoting the volumetric part of the logarithmic elastic strain, the elasticity relations (4.1) are modified as follows:

$$\left.\begin{aligned} \psi(\mathbf{E}^{\mathrm{e}}) &= \mu\,|\mathbf{E}_0^{\mathrm{e}}|^2 + \kappa(\epsilon_{\mathrm{c}}^{\mathrm{e}})^2\left[1 - \left(1 + \frac{\epsilon^{\mathrm{e}}}{\epsilon_{\mathrm{c}}^{\mathrm{e}}}\right)\exp\left(-\frac{\epsilon^{\mathrm{e}}}{\epsilon_{\mathrm{c}}^{\mathrm{e}}}\right)\right], \\ \mathbf{T}^{\mathrm{e}} &= \frac{\partial\psi(\mathbf{E}^{\mathrm{e}})}{\partial\mathbf{E}^{\mathrm{e}}} = 2\mu\mathbf{E}_0^{\mathrm{e}} + \left[\kappa\exp\left(-\frac{\epsilon^{\mathrm{e}}}{\epsilon_{\mathrm{c}}^{\mathrm{e}}}\right)\right]\epsilon^{\mathrm{e}}\mathbf{1}, \end{aligned}\right\} \tag{4.3}$$

where $\epsilon_{\mathrm{c}}^{\mathrm{e}}$ is a critical value of the elastic volumetric strain (a material parameter), and as before μ and κ are the ground-state shear and bulk moduli of infinitesimal isotropic elasticity. These constitutive equations for the free energy and the stress have been used effectively by Gearing and Anand [42] to model the brittle cracking phenomenon observed experimentally

in states of high triaxial tension in front of sharp notches in amorphous polymers. *We adopt* (4.3) *to also model such phenomena in amorphous metallic glasses.*[1]

The mean normal stress

$$\sigma \stackrel{\text{def}}{=} \frac{1}{3}\text{tr}\mathbf{T}^{\text{e}}, \tag{4.4}$$

corresponding to $(4.3)_2$ is

$$\sigma = \left[\kappa \exp\left(-\frac{\epsilon^{\text{e}}}{\epsilon_{\text{c}}^{\text{e}}}\right)\right]\epsilon^{\text{e}}. \tag{4.5}$$

Hence, a *generalized (tangent) bulk modulus* for the constitutive model may be defined as

$$\bar{\kappa} \stackrel{\text{def}}{=} \frac{\text{d}\sigma}{\text{d}\epsilon^{\text{e}}} = \kappa\left(1 - \frac{\epsilon^{\text{e}}}{\epsilon_{\text{c}}^{\text{e}}}\right)\exp\left(\frac{\epsilon^{\text{e}}}{\epsilon_{\text{c}}^{\text{e}}}\right), \quad \text{with} \quad \bar{\kappa} \to \kappa \quad \text{as} \quad \epsilon^{\text{e}} \to 0. \tag{4.6}$$

Equation (4.5) for the mean normal stress may be rewritten as

$$\frac{\sigma}{\sigma_{\text{c}}} = \left(\frac{\epsilon^{\text{e}}}{\epsilon_{\text{c}}^{\text{e}}}\right)\exp\left(1 - \frac{\epsilon^{\text{e}}}{\epsilon_{\text{c}}^{\text{e}}}\right), \quad \text{where} \quad \sigma_{\text{c}} \stackrel{\text{def}}{=} \frac{\kappa\epsilon_{\text{c}}^{\text{e}}}{e}, \tag{4.7}$$

and e is the Naperian/Euler number. A plot of $(\sigma/\sigma_{\text{c}})$ versus $(\epsilon^{\text{e}}/\epsilon_{\text{c}}^{\text{e}})$ in Fig. 4-3 shows that the mean normal stress σ attains a maximum value of σ_{c} when $\epsilon^{\text{e}} = \epsilon_{\text{c}}^{\text{e}}$. Thus, the quantity σ_{c} represents the **cavitation strength** of the material. Further, the integral

$$\Phi_{\text{c}} = \int_0^\infty \sigma \text{d}\epsilon^{\text{e}} = e\sigma_{\text{c}}\epsilon_{\text{c}}^{\text{e}} = \kappa\left(\epsilon_{\text{c}}^{\text{e}}\right)^2 \tag{4.8}$$

represents a **cavitation fracture energy per unit volume** of the intermediate configuration. We emphasize that the cavitation fracture energy Φ_{c} is different in nature from the traditional *cohesive surface approach to fracture*, in which the fracture energy is per unit area, and not per unit volume.

Some Remarks: The constitutive equations (4.3) fall within a class of constitutive models called "softening hyperelasticity," considered in recent years for modeling fracture toughness of ideally brittle materials [e.g. 68–71]. In particular, Volokh [70] and Volokh and Trapper [71] have recently proposed several forms for the free energy of softening nonlinear hyperelastic models, *using the classical infinitesimal strain measure*, to model fracture of isotropic brittle solids. The models for the free energy that these authors propose, include *complicated coupling* of the elastic volumetric and shear response of the material (cf., e.g., Section 2 of

[1] In Chapter 2, we refrained from using the volumetric contribution to the free energy (2.29) to address cavitation phenomena on the grounds that heterogeneities in the microstructure are expected to initiate cavitation. However, we expect the form of the mean stress-volumetric strain response of a material containing heterogeneities in the microstructure to be similar to that observed in our molecular dynamics simulations of a nominally homogeneous material, i.e. softening with dilatation. Therefore, we adopt this same form (cf., the second term in $(4.3)_1$) with the aim of modeling cavitation in real metallic glasses, which contain heterogeneities. It is important to note the quantitative value of the material parameter $\epsilon_{\text{c}}^{\text{e}}$ determined in this chapter will be significantly different than that listed in (2.31).

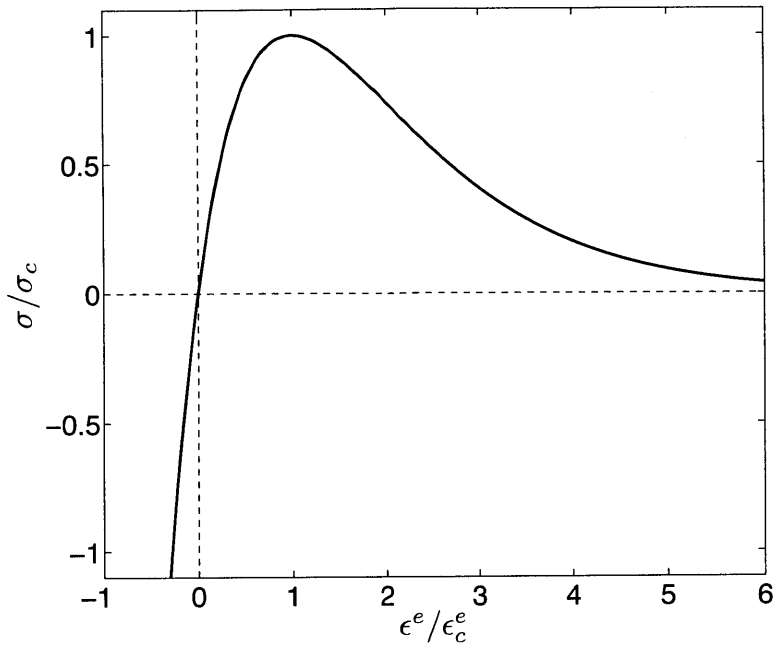

Figure 4-3: Relationship between normalized mean normal stress σ/σ_c, and normalized elastic volumetric strain ϵ^e/ϵ^e_c.

Volokh [70] and Section 2.5 of Volokh and Trapper [71]). Here, without entering into an extended discussion of the merits or demerits of the coupled free energy relations proposed by Volokh and co-workers, we limit our attention to *elastic-plastic* materials in which we expect that the norm of the strain deviator $|\mathbf{E}^e_0|$ is small relative to volumetric elastic strain ϵ^e, and limited by the onset of plasticity in the material. Accordingly, in writing (4.3) we have assumed that $|\mathbf{E}^e_0|$ does not affect the volumetric part of the free energy. Correspondingly, we have also assumed that the volumetric elastic strain ϵ^e does not affect the deviatoric part of the elastic free energy. In regard to this last approximative assumption, see Chapter 2 for a discussion of our extension of the constitutive equations (4.3) of Gearing and Anand [42] to account for such an effect. We believe that the constitutive equations (4.3), in which the deviatoric response is decoupled from the volumetric response, are sufficiently rich to capture the *essence of the physics* of brittle cavitation failure at sharp notches.

4.2.2 Specialization of the plasticity relations for low homologous temperatures

With the resolved shear stress $\tau^{(\alpha)}$ and compressive normal traction $\sigma^{(\alpha)}$ on each slip system defined by (3.10), the corresponding shearing rate (3.11) is take to be given by a simple

power-law flow function,

$$\nu^{(\alpha)} = \begin{cases} 0 & \text{if } (\tau^{(\alpha)} - \mu_{\text{fric}}\sigma^{(\alpha)}) \leq 0, \\ \nu_0 \left(\dfrac{\tau^{(\alpha)} - \mu_{\text{fric}}\sigma^{(\alpha)}}{S} \right)^{1/m} & \text{if } (\tau^{(\alpha)} - \mu_{\text{fric}}\sigma^{(\alpha)}) > 0, \end{cases} \tag{4.9}$$

where $S > 0$ is a stress-dimensioned internal variable representing the shear resistance to plastic flow, assumed for an isotropic material to be the same for all slip systems. Also, ν_0 is a reference plastic shear strain rate, and $m > 0$ is a strain-rate sensitivity parameter. For $\nu^{(\alpha)} > 0$, the flow function (4.9) may be inverted to read

$$\tau^{(\alpha)} - \mu_{\text{fric}}\sigma^{(\alpha)} = S \left(\frac{\nu^{(\alpha)}}{\nu_0} \right)^m . \tag{4.10}$$

Thus, the limit $m \to 0$ renders the theory rate-independent.

Recall that the internal variables of the theory are the isotropic resistance S and the order-parameter φ. In the Anand-Su theory the change in φ is taken to be due to the (small) shear-induced plastic volume change, cf. (3.17),

$$\varphi \stackrel{\text{def}}{=} \varphi_0 + \ln J^{\text{p}}, \tag{4.11}$$

with φ_0 a constant, so that the change in φ from its initial value φ_0 is due to the plastic volumetric strain ($\ln J^{\text{p}}$). Recalling (3.18), we have that

$$\dot{\varphi} = \beta \nu^{\text{p}}, \tag{4.12}$$

where

$$\nu^{\text{p}} \stackrel{\text{def}}{=} \sum_{\alpha=1}^{6} \nu^{(\alpha)} \tag{4.13}$$

is the sum of the shearing rates on all the slip systems. The shear-induced dilatancy function β is taken as

$$\beta = g_0 \left(1 - \frac{\varphi}{\varphi_{\text{cv}}} \right)^p , \tag{4.14}$$

where g_0, φ_{cv}, and p are positive-valued material parameters. Thus, $\beta = 0$ when $\varphi = \varphi_{\text{cv}}$, where φ_{cv} denotes the value of the value of the order-parameter in the fully-developed constant plastic volume state. With β given by (4.14), we have

$$\dot{\varphi} = g_0 \left(1 - \frac{\varphi}{\varphi_{\text{cv}}} \right)^p \nu^{\text{p}} \qquad \text{with initial value} \qquad \varphi(0) = \varphi_0. \tag{4.15}$$

Next, the isotropic shear resistance S is taken to depend on current value of the order-parameter φ according as

$$S = S_{\rm cv} + b\left(1 - \frac{\varphi}{\varphi_{\rm cv}}\right)^q \qquad \text{with initial value} \qquad S(0) = S_{\rm cv} + b \equiv S_0, \tag{4.16}$$

where $S_{\rm cv}$, b, and q are additional positive-valued material parameters. Thus, during plastic flow from a virgin state, the value of the order-parameter φ increases smoothly from zero to a steady state value $\varphi_{\rm cv}$, while the shear resistance S decreases smoothly from its initial value S_0 to a steady state value $S_{\rm cv}$.

4.2.3 Fracture criterion

At a fundamental level, brittle fracture by bond-breaking initiates at a critical value of tensile strain when the maximum in the cohesive stresses is reached. In our three-dimensional continuum theory, brittle fracture by cavitation initiates when the volumetric elastic strain $\epsilon^{\rm e}$ reaches the critical value $\epsilon^{\rm e}_{\rm c}$, at which point the mean normal stress σ also reaches its maximum value $\sigma_{\rm c}$, cf. Fig. 4-3. Thus a brittle fracture initiation criterion is built into our non-linear elasticity relation as a *constitutive instability*, and no separate fracture criterion is needed. However, in numerical calculations we need to introduce a simple criterion to delineate when final separation occurs and a material point loses all stress-carrying capability; to this end, we introduce the following simple criterion:

- Material separation and final failure is taken to occur when the local elastic volumetric strain $\epsilon^{\rm e}$ reaches a failure value $\epsilon^{\rm e}_{\rm f}$:

$$\epsilon^{\rm e} = \epsilon^{\rm e}_{\rm f} \qquad \text{with} \qquad \epsilon^{\rm e}_{\rm f} \gtrapprox 4 \times \epsilon^{\rm e}_{\rm c}. \tag{4.17}$$

When this local criterion is met in a given element of a finite element calculation, that element is deemed to have "failed" and is "removed" from the calculation.

We have implemented our constitutive model in the finite element computer program Abaqus/Explicit [36] by writing a user material subroutine (VUMAT). This finite element program permits the modeling of failure, when user-specified critical values of certain parameters are reached, by an element removal technique.

Using this finite element program, in the following sections we describe our simulations of the fracture response of notched-tension specimens, as well as various aspects of fracture initiation from sharp notch tips under Mode-I, plane-strain, small-scale-yielding conditions.

Remark: When the notches are not sufficiently sharp, or under Mode-II or Mode-III shear-dominated conditions, when the local hydrostatic tensions are not sufficiently elevated, fracture in metallic glasses is expected to initiate in well-developed shear bands instead of by the cavitation mechanism discussed above. The mathematical modeling of the transition

from deformation fields involving intense shear strains in narrow bands, to jump discontinuities in tangential displacements across surfaces, and eventual fracture, especially when the shear-banded plastic zone is constrained within a large elastic region, is non-trivial. We have not adequately pursued the modeling of such "ductile" failure phenomena, and are not in a position to report on such considerations in this thesis.

4.3 Material parameters used in numerical simulations

Although our considerations are generic and should be applicable to a wide variety of metallic glasses, for specificity the material parameters used in our numerical simulations are chosen to approximate those for Vitreloy-1. We follow Anand and Su [34] and choose the following values of the material parameters for use in our simulations:[2]

- *Elastic moduli* [12]: $E = 96\,\text{GPa}$, $\nu = 0.36 \Rightarrow \mu = 35.3\,\text{GPa}$, $\kappa = 114.3\,\text{GPa}$.
- *Internal friction coefficient* [53]: $\mu_{\text{fric}} = 0.04$.
- *Viscoplasticity parameters*: $\nu_0 = 0.001$, $m = 0.005$. The glass transition temperature of Vitreloy-1 is $\approx 623\,\text{K}$, and under room temperature conditions ($\approx 300\,\text{K}$) the mechanical response of these materials is observed to be *almost rate-insensitive*. The low value of the strain-rate sensitivity parameter $m = 0.005$ is chosen to model such a nearly rate-independent response.
- *Parameters in the evolution equation for the order-parameter* φ:

  For the evolution of φ, Eq. (4.15), we choose $g_0 = 0.04$ in compression ($\sigma_1 < 0$) and $g_0 = 0.4$ in tension ($\sigma_1 > 0$), also $\varphi_0 = 0$, $\varphi_{\text{cv}} = 0.005$, and $p = 1.2$.
- *Dependence of the shear resistance* S *on* φ:

  In (4.16) we choose

  $$S_{\text{cv}} = 890\,\text{MPa},\ b = 70\,\text{MPa},\ q = 2.0,$$

  such that when $\varphi = 0$,

  $$S_0 = 960\,\text{MPa}.$$

The stress-strain curves in tension, compression, and simple shear, obtained by using these material parameters in a finite-element calculation using a single element (Abaqus-C3D8R) are shown in Figs. 4-4(a) and (b), respectively.

Next, we turn to numerical simulations of the notched-tension experiments of Flores and Dauskardt [32] to estimate the cavitation failure parameters for Vitreloy-1 from the failure-strength versus notch-root radius data estimated from the results reported by these authors. We have numerically modeled notched round bars of the geometry used by Flores and Dauskardt [32] in their experiments: 44 mm length, 10 mm gauge section diameter, and

[2] Cf. Anand and Su [34] for a more complete discussion of this choice of material parameters for Vitreloy-1.

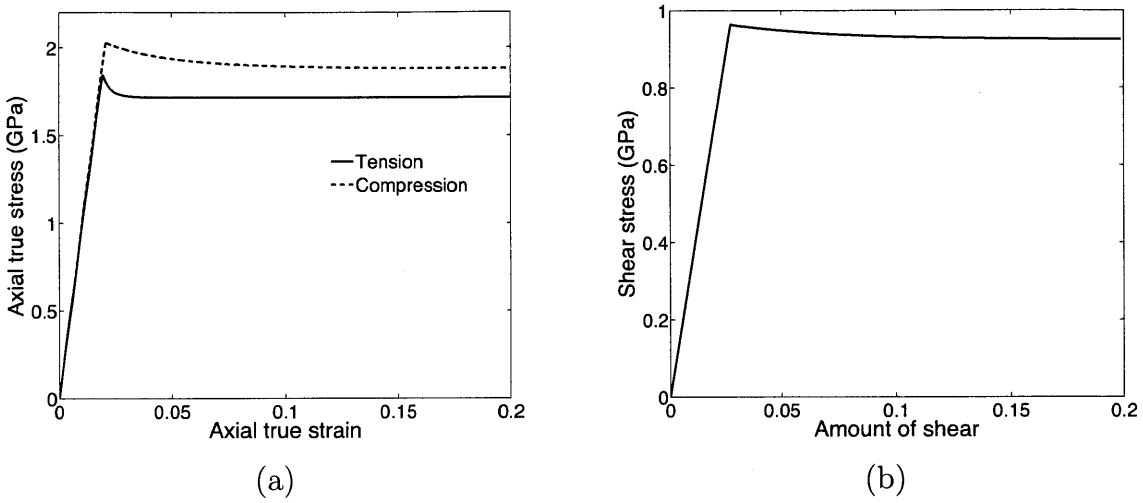

Figure 4-4: Stress-strain response of a single element in (a) simple tension and compression (absolute values); and (b) simple shear.

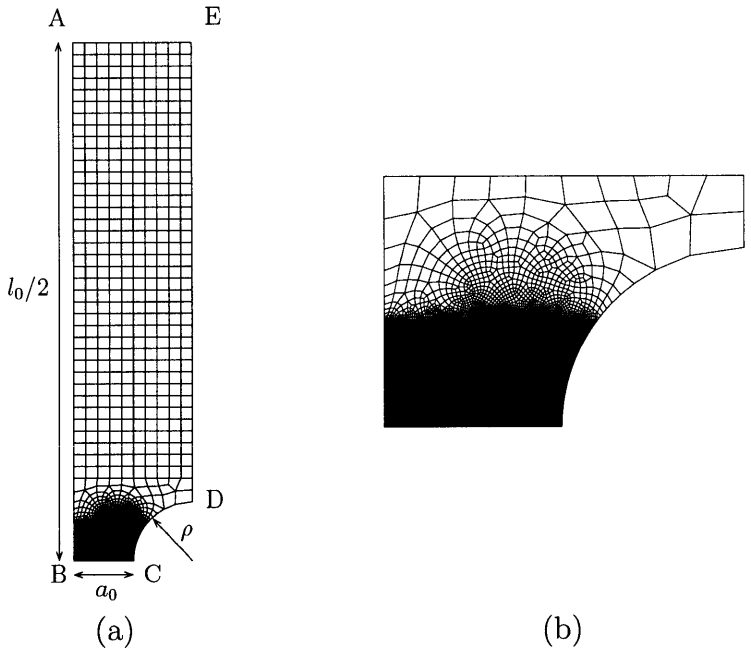

Figure 4-5: (a) Initial finite element mesh for a notched-tension specimen: $l_0 = 44\,\text{mm}$, $a_0 = 2.5\,\text{mm}$, $\rho = 2.5\,\text{mm}$. (b) Close-up of mesh at the notch root for the case of $\rho = 2.5\,\text{mm}$.

2.50 mm notch depth, with notch-root radii of 0.25, 0.5, 1.00, 1.50, 2.00, and 2.50 mm. The finite element analyses were performed assuming axisymmetric conditions, and applying symmetry boundary conditions across the plane of the notch. The finite element meshes consisted of a large number of Abaqus-CAX4R elements (exceeding 10,000 in number) for each notch-root radius. As an example, the mesh for the largest notch-root radius (2.5

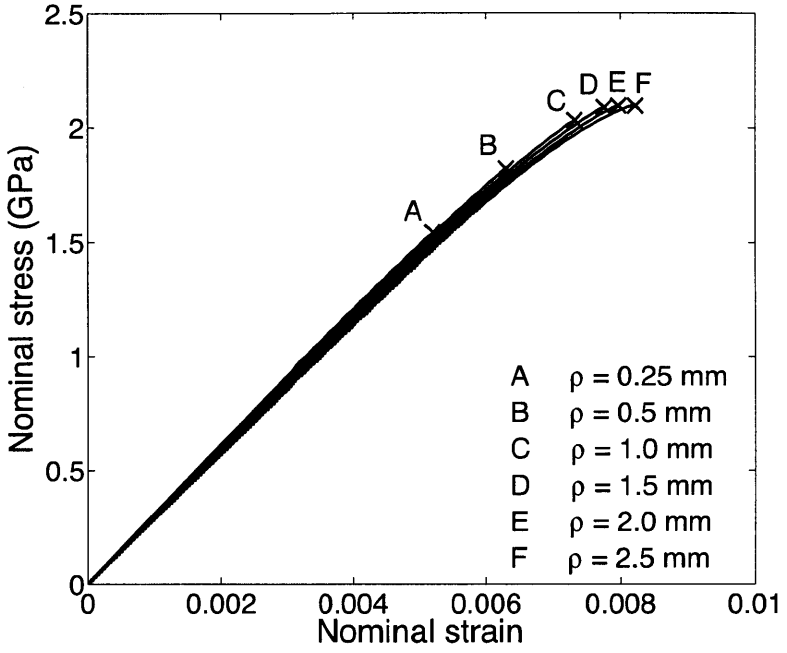

Figure 4-6: Nominal stress/strain curves for the notched-tension simulations.

mm) is shown, along with a close-up of the mesh in the region of the notch, in Fig. 4-5. Referring to this figure, the boundary AB is the axis of revolution, and symmetry boundary conditions were applied along the boundary BC. A vertical velocity of 10 μm/s was applied along the top boundary AE to effect the extension. With a_0 denoting the initial minimum radius of the notched bars, l_0 the initial length of the specimen (cf., Fig. 4-5), δ the applied displacement, and P the axial reaction force, we define a nominal stress by $P/(\pi a_0^2)$ and a nominal strain by δ/l_0. The nominal stress versus nominal strain for each notch-root radius is plotted in Fig. 4-6, and fracture is denoted by an "X". We conducted numerous numerical simulations and adjusted the values of $(\epsilon_c^e, \epsilon_f^e)$ in our softening-hyperelasticity relation and final separation criterion to approximately match the fracture-strength versus notch-root radius data of Flores and Dauskardt.[3] The following values of these parameters

$$\epsilon_c^e = 0.038, \qquad \epsilon_f^e = 4 \times \epsilon_c^e = 0.152,$$

[3]Our estimate of the failure strength versus notch-root data from Flores and Dauskardt [32] is approximate in that they never actually report values for all the different notch-root radii used in their experiments. In their paper the fracture-strength is reported indirectly as a function of a "stress-state parameter" which is a measure of the the stress triaxiality in the specimen, and includes the notch-root radius and the final deformed radius of the notched bar at its minimum cross-section. Since the change in the minimum radius of the notched bar is small, in order to extract the values of the actual root radii from their data we have approximated the final radius of the notched bar at its minimum cross-section as the initial value of this radius.

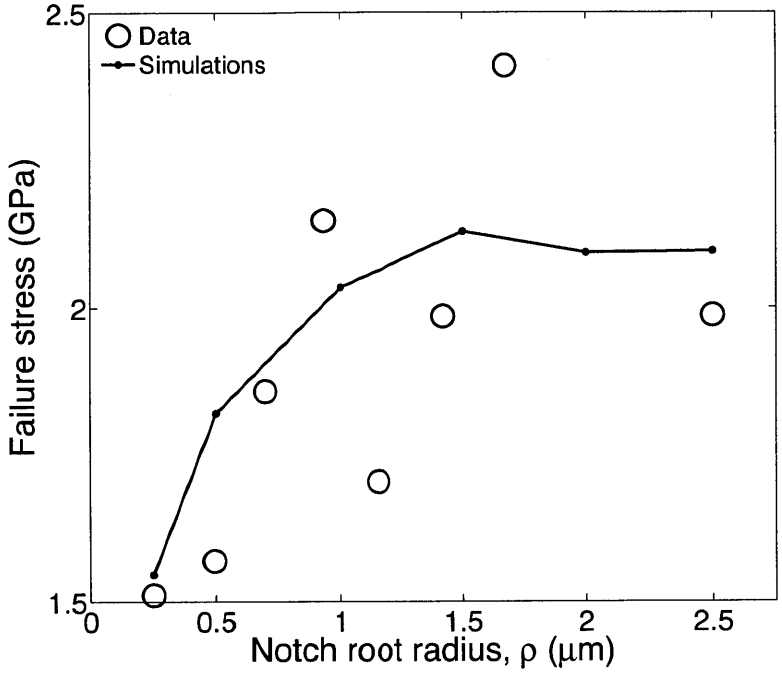

Figure 4-7: Failure stress versus notch-root radius in notched-tension specimens; the experimental data is estimated from Flores and Dauskardt [32].

provided the numerically-calculated results in the fracture strength versus notch-root radius shown in Fig. 4-7, which match the trend in the (scattered) experimental data showing failure strength levels increasing from $\approx$ 1.5 to 2.5 GPa as the notch-root radius increases from 0.25 mm to 2.5 mm. Note that a value of $\epsilon_c^e = 0.038$ and $\kappa = 114.3$ GPa, gives a value

$$\sigma_c \approx 1.6\,\text{GPa},$$

for the mean normal stress at cavitation for Vitreloy-1.

Recall that in their fractographic studies Flores and Dauskardt [32] noted that in their notched-tension experiments the site of failure initiation is ahead of the notch root inside the bulk of the material, rather than at the surface of the notch root. An important capability of our theory is the ability to capture this phenomenon. Figures 4-8(a,b,c) show contour plots of volumetric elastic strain ($\epsilon^e = \text{tr}\mathbf{E}^e$), mean normal stress ($\sigma = (1/3)\text{tr}\mathbf{T}^e$), and equivalent plastic strain ($\gamma^p = \int_0^t \nu^p(\zeta)\text{d}\zeta$) immediately prior to the initiation of cavitation in a notched-tension simulation for $\rho = 2.5$mm, while Fig. 4-8(d) shows initiation of cavitation in the region ahead of the plastic zone where the volumetric elastic strain and mean normal stress are the highest.

In the next section we utilize this simulation capability to model the evolution of various aspects of deformation and initiation of failure in a sharp notch tip under Mode-I loading.

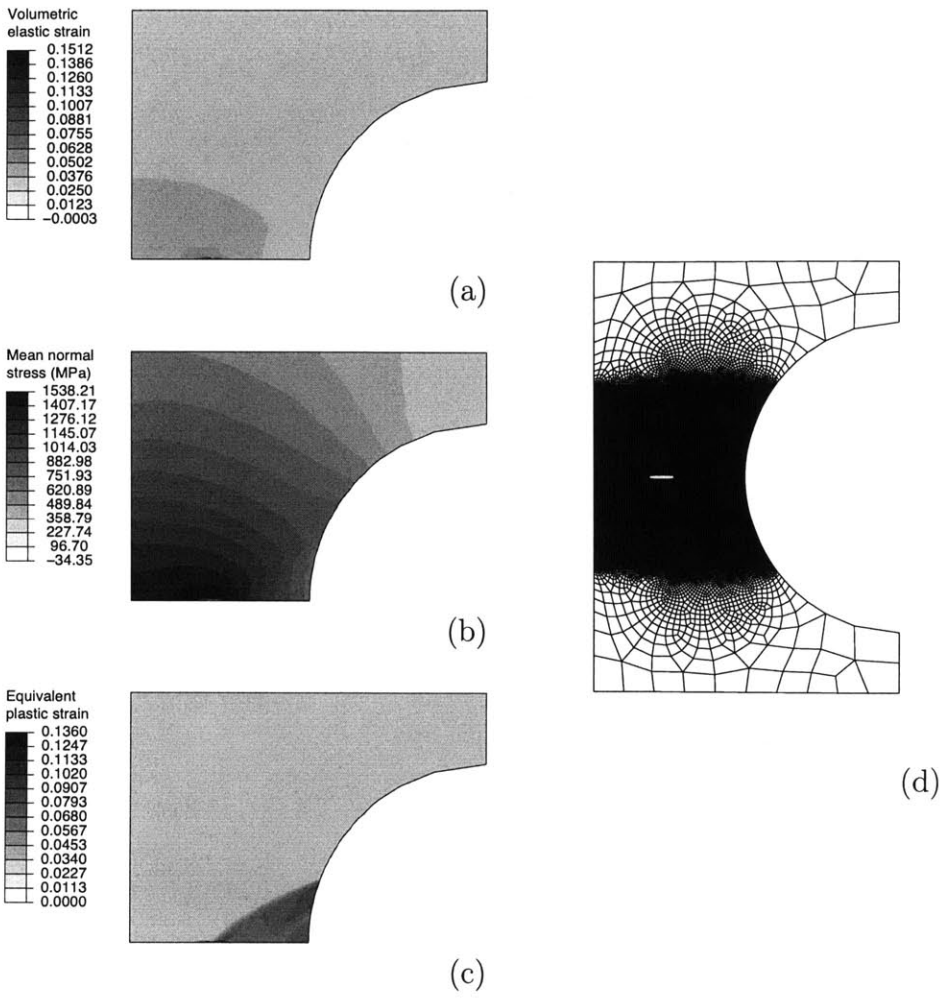

Figure 4-8: Contours of (a) volumetric elastic strain ϵ^{e}, (b) mean normal stress σ, and (c) equivalent plastic strain γ^{p} immediately prior to the initiation of cavitation in a notched-tension simulation for $\rho = 2.5$mm. (d) Initiation of cavitation in the region ahead of the plastic zone where the volumetric elastic strain and mean normal stress are the highest.

4.4 Simulations of fracture at notches under Mode-I, plane-strain, small-scale-yielding conditions

In this section we describe the numerical simulations which we have used to investigate various fracture related phenomenon which can be rationalized by the non-linear elasticity relation with cavitation failure introduced in Section 4.2.1. First, the deformation and failure at a prototypical notch tip under Mode-I, plane-strain, small-scale-yielding (SSY) conditions is described. Then, the effect of notch-root radius on the critical stress intensity parameter at fracture K_{c} is studied. Finally, the effect of the ratio μ/κ of the shear modulus to the bulk modulus on the plane-strain fracture toughness K_{c} is investigated

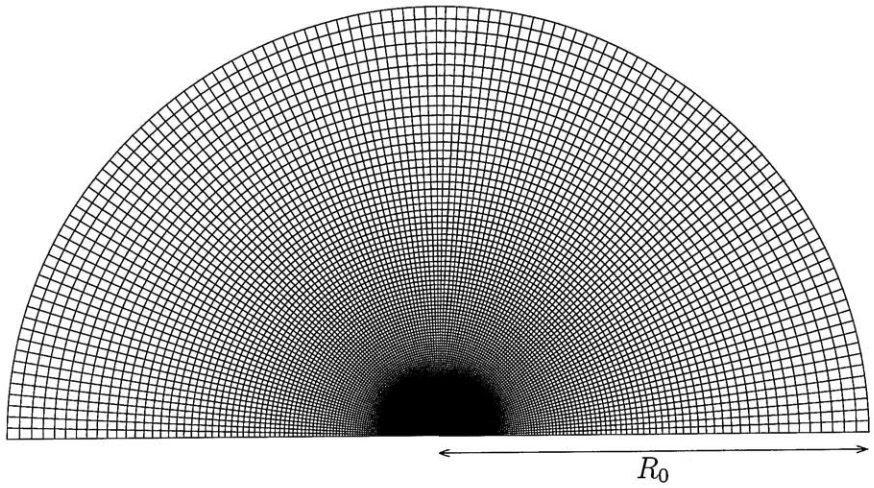

(a)

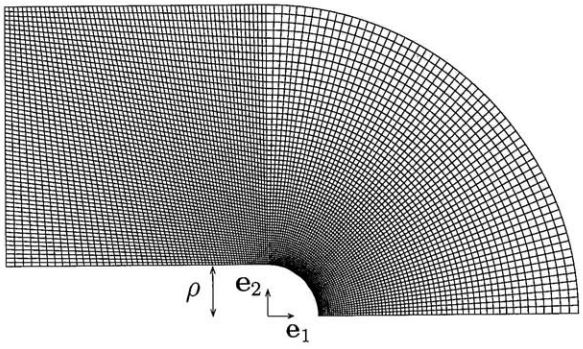

(b)

Figure 4-9: (a) Initial finite element configuration for Mode-I loading, and (b) close-up of the mesh at the notch root for the case of a notch-root radius of $\rho = 10\,\mu$m.

A two-dimensional, plane-strain, small-scale-yielding boundary layer formulation is employed in the numerical simulations. A large circular domain containing a notch along one of its radii is considered, and notch-root radii of $\rho = 10, 25, 50,$ and $100\,\mu$m were modeled. The finite element mesh corresponding to a notch-root radius of $\rho = 10\,\mu$m is shown in Fig. 4-9(a), and a close-up of the mesh surrounding the notch root is shown in Fig. 4-9(b). The origin of the global rectangular Cartesian coordinate system is at the center of curvature of the notch root. In order to ensure that the plastic zone is well-contained within the outer boundary of the computational mesh, the radius R_0 is boundary chosen as $R_0 = 7500\,\mu$m, which is 750 times the notch-root radius of the smallest notch $\rho = 10\,\mu$m, and 75 times the notch-root radius of the largest notch $\rho = 100\,\mu$m; for a further discussion of this issue see Appendix C. Due to the symmetry of Mode-I loading, only the upper-half plane is modeled

with finite elements as shown in Fig. 4-9. Meshes containing 27528, 23941, 20317, and 17935 Abaqus-CPE4R elements, respectively, were used for the different notch-root radii; the issue of mesh convergence is also further discussed in Appendix C. Symmetry boundary conditions were prescribed on the line leading up to the notch root, and the notch face was modeled as traction-free. Along the outer boundary of the circular domain of radius R_0, the following analytical asymptotic displacement field for Mode-I loading was prescribed:[4]

$$\left.\begin{aligned} u_1(r,\theta) &= \frac{K_{\mathrm{I}}}{2\mu}\sqrt{\frac{r}{2\pi}}\cos\left(\frac{\theta}{2}\right)\left[(3-4\nu)-1+2\sin^2\left(\frac{\theta}{2}\right)\right], \\ u_2(r,\theta) &= \frac{K_{\mathrm{I}}}{2\mu}\sqrt{\frac{r}{2\pi}}\sin\left(\frac{\theta}{2}\right)\left[(3-4\nu)+1-2\cos^2\left(\frac{\theta}{2}\right)\right]. \end{aligned}\right\} \tag{4.18}$$

In the simulations, the loading parameter K_{I} was ramped linearly from zero to failure at $5\,\mathrm{MPa}\sqrt{\mathrm{m}}/\mathrm{s}$. The value of K_{I} at which failure initiates is denoted as K_{c}.

As an example, consider the case of a notch-tip radius of $\rho = 10\,\mu\mathrm{m}$. As the Mode-I displacement field (4.18) is applied at $r = R_0$, the corresponding $\mathbf{e}_2$-component of the total reaction force is determined by integrating the corresponding nodal forces from the simulations over the outer radius. The total reaction force versus applied K_{I} is plotted in Fig. 4-10(a), and for the notch-root radius of $\rho = 10\,\mu\mathrm{m}$ fracture initiates at point A marked with an "X".[5] For $\rho = 10\,\mu\mathrm{m}$, the fracture toughness is $K_{\mathrm{c}} = 17.5\,\mathrm{MPa}\sqrt{\mathrm{m}}$.

Various aspects of the numerically-calculated evolution of the crack tip fields for $\rho = 10\,\mu\mathrm{m}$ are summarized in Figs. 4-11 and 4-12. The variation of the equivalent plastic strain γ^{p}, the volumetric elastic strain ϵ^{e}, and the mean normal stress σ along the line leading up to the notch tip ($\theta = 0$) are plotted in Fig. 4-11 for several values of applied $K_{\mathrm{I}}/K_{\mathrm{c}}$. As $K_{\mathrm{I}}/K_{\mathrm{c}}$ increases, the size of the plastic zone and the magnitude of γ^{p} ahead of the notch tip increases. As the plastic zone evolves, a region of high volumetric elastic strain and correspondingly high hydrostatic tension develops ahead of the plastic zone, *which intensifies as deformation progresses.* It is in this region that cavitation failure is triggered when σ approaches σ_{c}. Figures 4-12(a-c) show the state in the material ahead of the notch root immediately prior to the initiation of cavitation failure: the equivalent plastic shear strain is shown in Fig. 4-12(a), the volumetric elastic strain in Fig. 4-12(b), and the mean normal stress in Fig. 4-12(c). It is clear that the region in which the volumetric elastic strain and the mean normal stress are maximum occurs near the leading front of plastic deformation, and this is where cavitation failure is first initiated, as shown in Fig. 4-12(d); subsequent stages of crack growth are shown in Figs. 4-12(e) and (f).

[4]The displacement field is given in terms of polar coordinates (r,θ) with origin coinciding with that of the global rectangular coordinate system at the center of curvature of the notch root.

[5]Operationally, the point of failure initiation is determined as the point at which the reaction force goes through a maximum, or when the first element is deleted, which essentially occurs simultaneously.

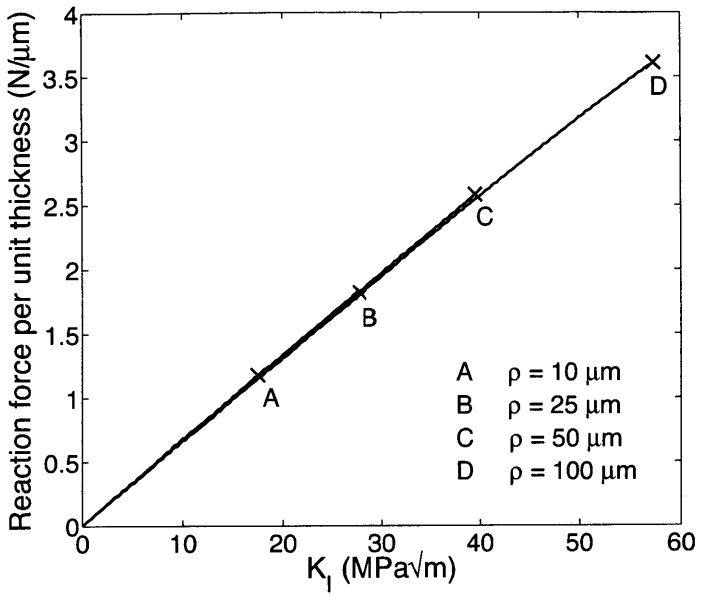

(a)

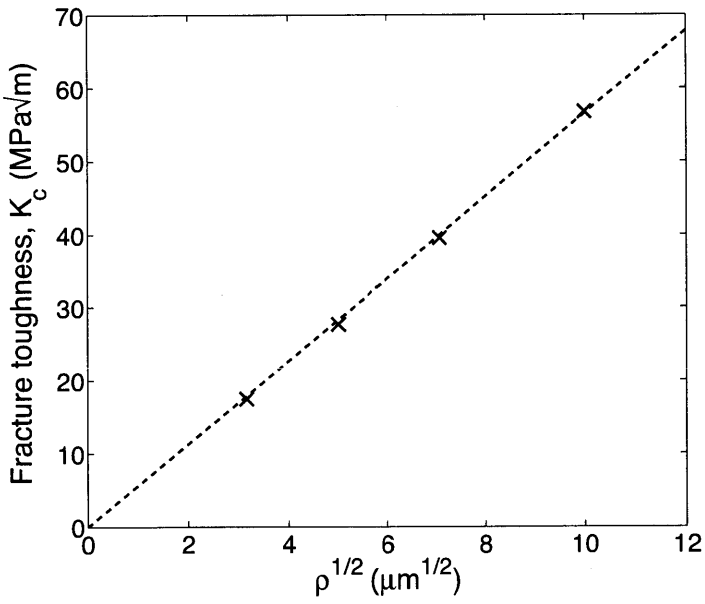

(b)

Figure 4-10: (a) Reaction force versus loading parameter for different notch-root radii. (b) Variation of fracture toughness with notch-root radius.

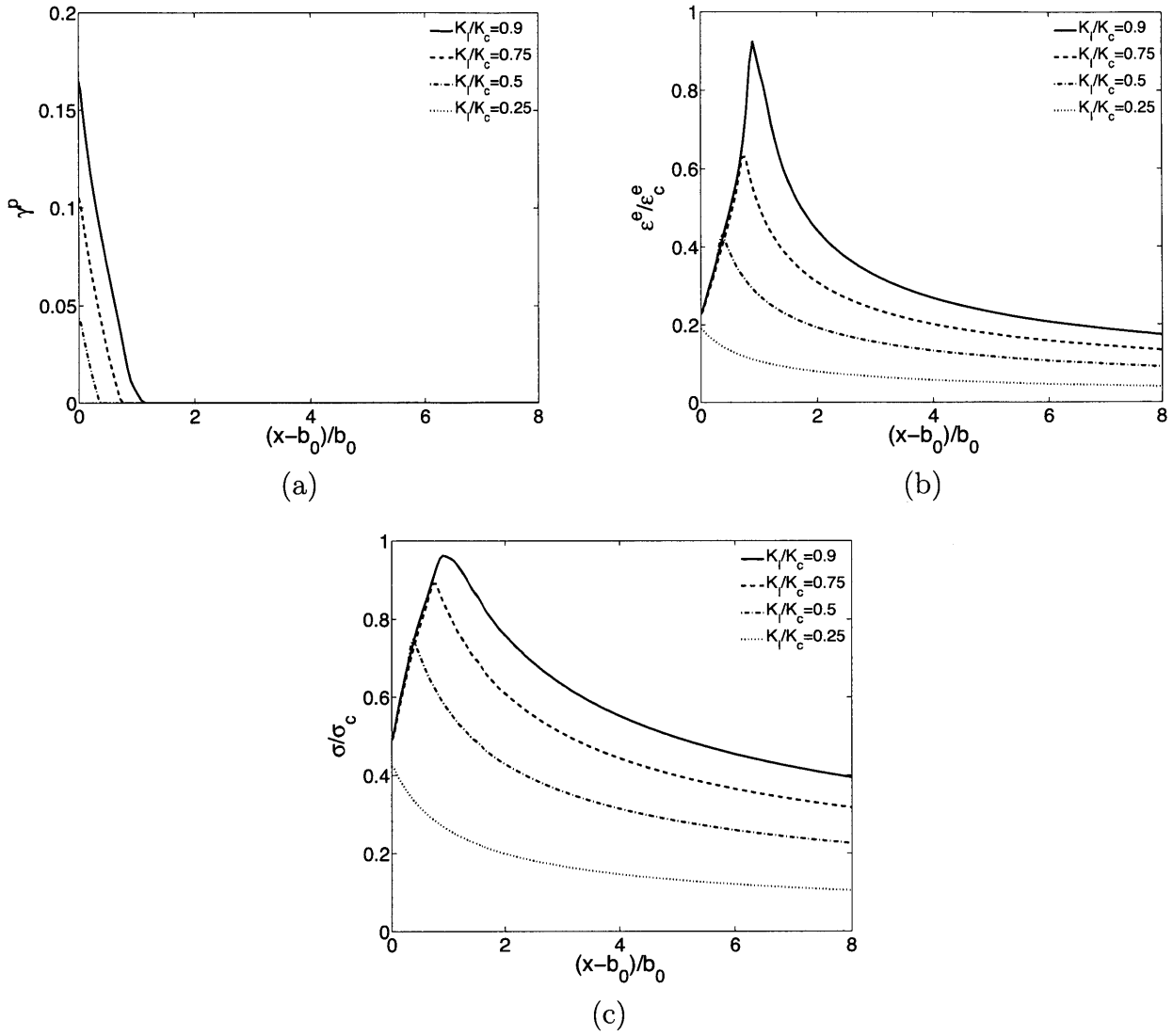

Figure 4-11: Variation of (a) equivalent plastic strain, (b) volumetric elastic strain, and (c) mean normal stress for a notch-root radius of $\rho = 10\,\mu$m at several values of applied K_I/K_c along the line ahead of the notch tip ($\theta = 0$).

4.4.1 Effect of notch-root radius

The calculations were repeated for the other notch-root radii of $\rho = 25$, 50, and $100\,\mu$m. The total reaction force versus applied K_I is plotted in Fig. 4-10(a), and for these notch-root radii, fracture initiates at points B, C, and D. The corresponding fracture toughness values K_c are plotted against the square root of the notch-root radius $\sqrt{\rho}$ in Fig. 4-10(b), and a linear relationship between K_c and $\sqrt{\rho}$ is evident. Such a scaling relationship has been

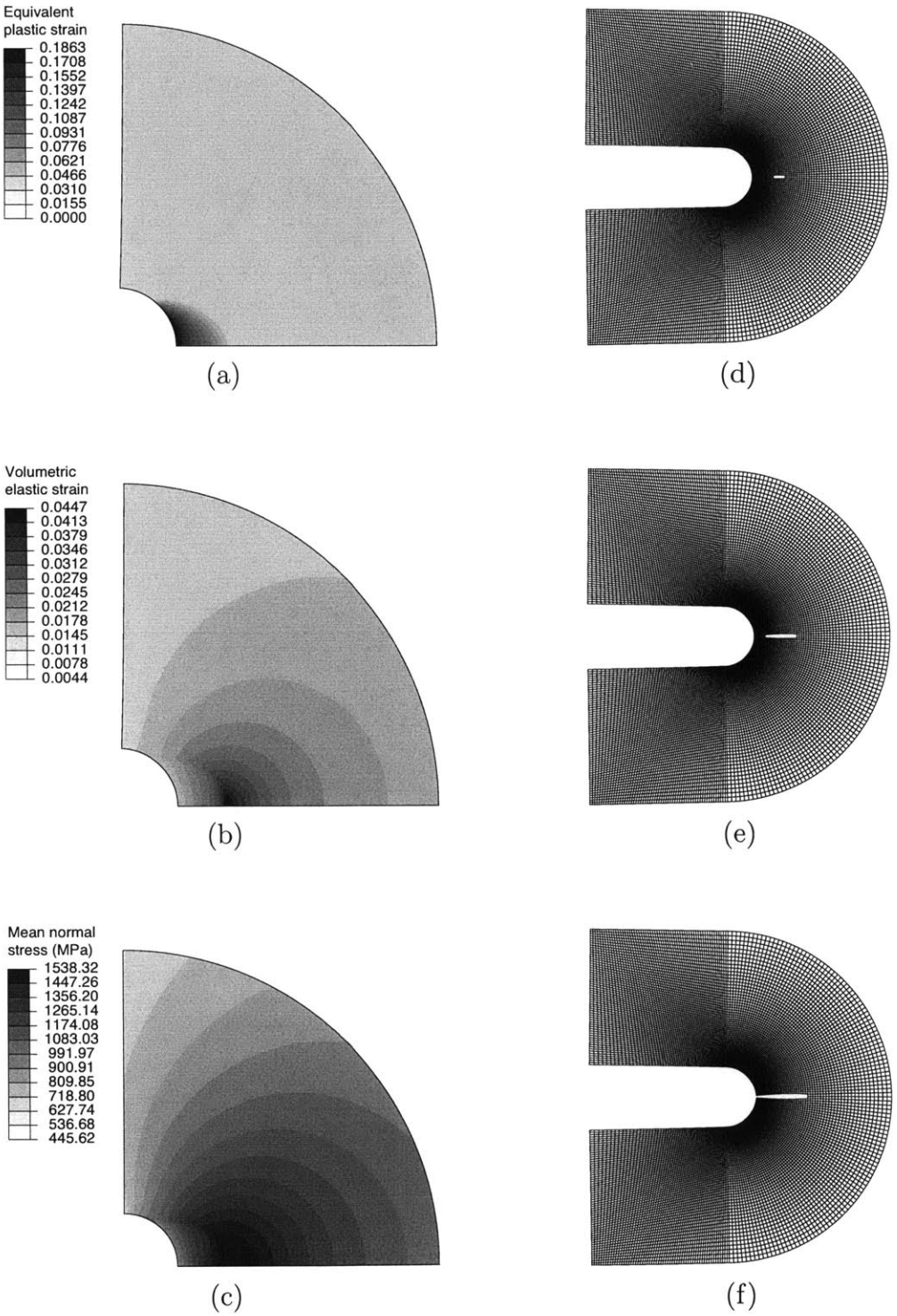

Figure 4-12: (a–c) State immediately prior to the initiation of cavitation. (d–f) Progressive stages of the cavitation failure.

reported by Lewandowski et al. [31] for Vitreloy-1, and is also seen in fracture experiments on brittle ceramics [cf., e.g. 69].

That K_c decreases as $\sqrt{\rho}$ decreases is in agreement with the well-known result of Inglis [72], who using classical linear elasticity, showed that the stress at the tip of an elliptic notch in a plate subject to far-field tension, strongly depends on the sharpness of the notch tip, and if the stress at the notch tip controls the fracture strength of the notched plate, then the notch sharpness must effect the onset of fracture. To make the Inglis-type fracture approach concrete, a separate local fracture criterion $\sigma_{\text{local}} = \sigma_{\text{fracture}}$ must be introduced. In contrast, in our "softening hyperelasticity" approach, the brittle failure of notched-component is modeled as a *constitutive instability* by the inclusion of *strain-softening in the non-linear volumetric elastic constitutive description of material* [cf., also, 68–71].

It is important to note that in our simulations the fracture toughness K_c extrapolates to zero as the notch-root radius ρ goes to zero. This is because our continuum constitutive theory possesses no intrinsic length-scale. In a real material, as the notch-root radius decreases and reaches some small microstructural length scale, then the $\sqrt{\rho}$ dependence of K_c will be broken, and the fracture toughness will become independent of the notch-root radius. In brittle ceramics this microstructural length scale is set by the grain size [cf., e.g. 69]. However, it remains unclear as to what microstructural length scale, if any, stabilizes the value of K_c in metallic glasses. In any event, it is clear the sharpness of the notch tip is crucially important in accurately determining the fracture toughness of a metallic glass.

4.4.2 Effect of elastic parameters

Next, we describe the effect of the ratio μ/κ of the elastic moduli on the toughness K_c. Table 4.1 lists five pairs of values for μ and κ, with the value of the shear modulus fixed at $\mu = 35.3\,\text{GPa}$, and the value of the bulk modulus κ increased from 76.5 GPa to 135.3 GPa. Simulations for a notch-root radius of $\rho = 10\,\mu\text{m}$, utilizing the five sets of elastic material parameters in Tab. 4.1, were carried out by following the methodology described above.

The integrated reaction force in the $\mathbf{e}_2$-direction at the outer boundary R_0 for each case is plotted against the loading parameter K_I in Fig. 4-13, and failure for each set of elastic constants, a through e in Tab. 4.1, is denoted by an "X" and marked by the associated letter. Note that the net reaction force versus applied K_I for the different cases essentially follows the same loading path prior to failure. The variation of K_c with the ratio μ/κ as well

Label	μ (GPa)	κ (GPa)	E (GPa)	ν	μ/κ
a	35.3	76.5	91.8	0.30	0.46
b	35.3	86.3	93.2	0.32	0.41
c	35.3	98.5	94.6	0.34	0.36
d	35.3	114.3	96.0	0.36	0.31
e	35.3	135.3	97.4	0.38	0.26

Table 4.1: Combinations of elastic moduli used in the Mode-I notch-tip simulations.

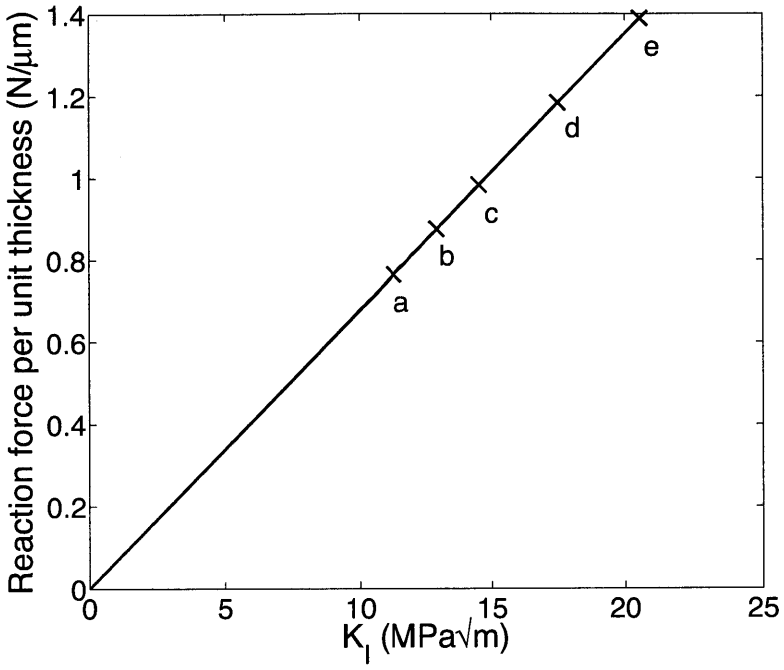

Figure 4-13: Reaction force versus loading parameter $K_{\rm I}$ for different combinations of elastic moduli. The labels a through e refer to the elastic moduli appearing in Tab. 4.1.

as Poisson's ratio ν is shown in Figs. 4-14(a) and (b), respectively. The trends evident in Fig. 4-14 qualitatively match the trends noted in Lewandowski et al. [33], viz., the fracture toughness of a metallic glass decreases as μ/κ increases. Recall from (4.7) that in our model the critical value of the mean normal stress is

$$\sigma_{\rm c} = \frac{\kappa \epsilon_{\rm c}^{\rm e}}{e}.$$

Hence, for fixed $\epsilon_{\rm c}^{\rm e}$, as κ decreases then so also does $\sigma_{\rm c}$, and for a fixed value of μ this results in the correlation that as μ/κ increases the fracture toughness $K_{\rm c}$ decreases. Thus while the results in Fig. 4-14 do not quantitatively match any specific experimental data, they do offer a plausible physical explanation for the effect of the ratio of the shear modulus to the bulk modulus on toughness $K_{\rm c}$.

4.5 Concluding remarks

Following Gearing and Anand [42], we have introduced an important modification to the finite elasticity relation in the Anand-Su theory for large elastic-plastic deformations of BMGs to account for the strongly nonlinear and eventually softening, dilatational volumetric elastic response of such materials. In this "softening-hyperelasticity" approach the brittle failure of a component with a notch is modeled as a *constitutive cavitation instability*, and no

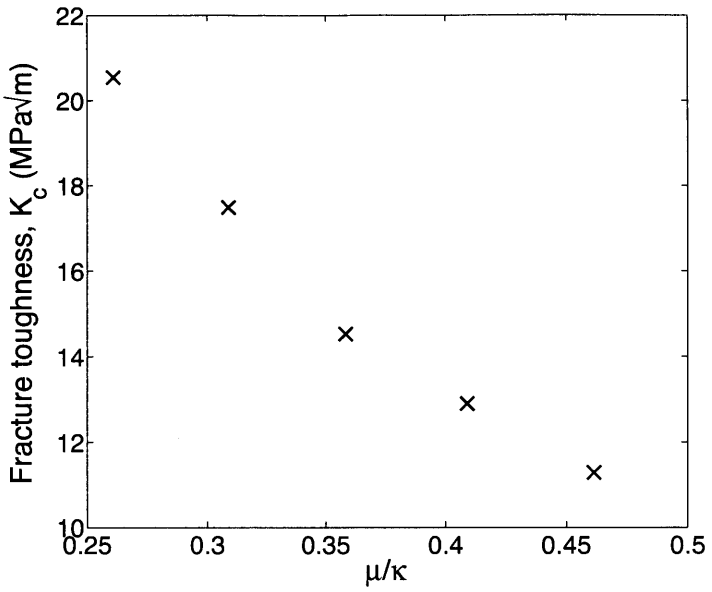

(a)

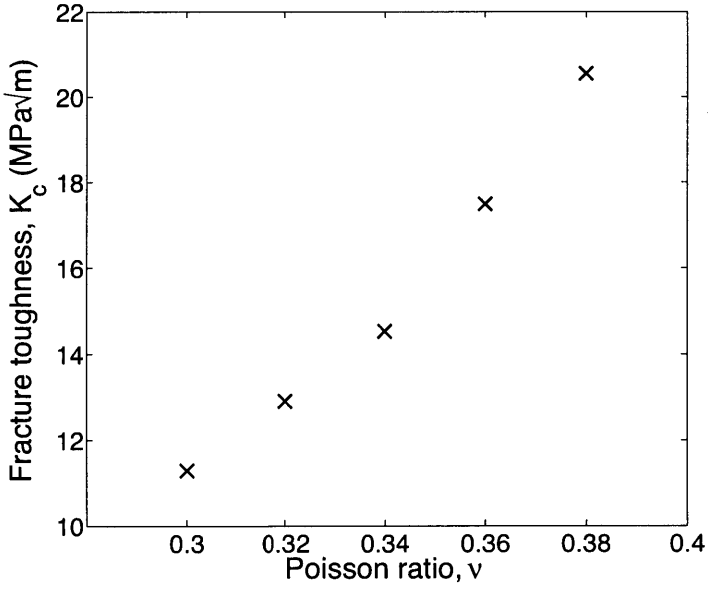

(b)

Figure 4-14: The variation of plane-strain fracture toughness K_c with (a) the ratio μ/κ, and (b) Poisson's ratio ν.

separate local fracture criterion is necessary. Using the modified form of the Anand-Su theory we have conducted detailed finite element simulations of notch-tip fracture initiation in a representative metallic glass under Mode-I, plane-strain, small-scale-yielding conditions, and

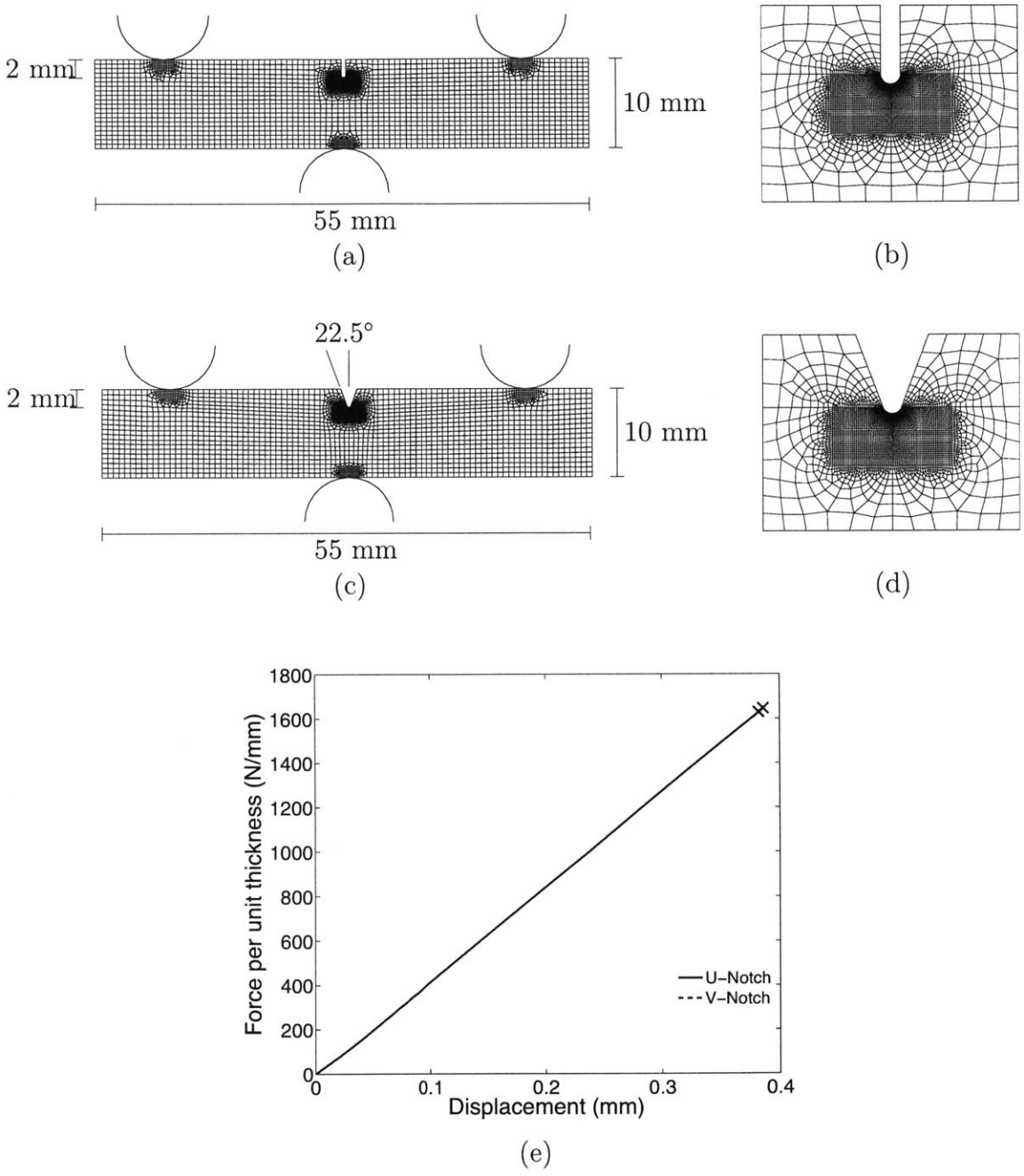

Figure 4-15: Initial finite element mesh configurations for three-point-bending of a (a) U-Notched beam including (b) a close-up of the notch root and (c) a V-Notched beam including (d) a close-up of the notch root. (e) Reaction force versus displacement for each case; failure occurs at points marked with an "X".

shown that our theory predicts three important experimentally-observed phenomena: (a) fracture initiates ahead of the notch root where the mean normal stress reaches a maximum

value; (b) fracture toughness K_c increases linearly with square-root of the notch-tip radius ρ; and (c) K_c decreases as the ratio of the elastic moduli μ/κ increases.

Finally, it is important to note that our "softening-hyperelasticity" approach to model the onset of brittle failure is a "local"-approach, dependent primarily on the local notch-root radius, and is essentially independent of the rest of the geometry of a notched component. To illustrate this point, consider plane-strain three-point-bending of two notched beams, one with a U-shaped notch and another with a V-shaped notch, but *each with the same notch-root radius.* Both beams have a length of 55 mm and a thickness of 10 mm with the notch extending 2 mm through the thickness, with a root radius of 0.25 mm. The initial finite element meshes for each case are shown in Figs. 4-15(a)-(d). The beams are loaded in three point bending over a span of 40 mm at a rate of 0.1 mm/s. The reaction force per unit thickness versus displacement is shown in Fig. 4-15(e). Note that there is virtually no difference in the bending force versus bending deflection curves for the two geometries, and the fracture loads for the two geometries are very close to each other: 1630 N/mm for the U-Notch which compares with 1646 N/mm for the V-Notch. This verifies our assertion above that brittle fracture as modeled by the "softening-hyperelasticity" approach, depends primarily on the local notch-root radius, and that the effect of the notch shape is secondary.

Chapter 5

A constitutive theory for the mechanical response of amorphous metals at high temperatures spanning the glass transition

5.1 Introduction

In recent years, an extremely promising method called thermoplastic forming has emerged [cf., e.g., 19–24]. In this process, the metallic glass is first obtained in the amorphous state by traditional die-casting. The metallic glass is then heated into the supercooled liquid region above the glass transition temperature of the material, where it may be isothermally formed to produce intricate microscale patterns and then slowly cooled. A specific thermoplastic forming process geared towards producing nano/microscale, high-aspect ratio, patterned features on surfaces is that of *micro-hot-embossing*. In this process, the metallic glass is formed in its supercooled liquid region by pressing it against a master-surface with the desired nano/microscale features (usually a patterned silicon wafer). The viability of this process has been demonstrated extensively in the literature [cf., e.g., 19–24]. However, as with any emerging technology, the scientific basis for this process is at present fragmented and limited. Experiments to determine the stress-strain response of metallic glasses in the appropriate temperature and strain-rate regime required to develop mechanistically-informed continuum-level constitutive equations useful for applications are just beginning to appear [cf., e.g., 12, 73]. Because of this, numerically-based process-simulation capabilities for thermoplastic forming of metallic glasses also do not exist, and most of the recent experimental micro-hot-embossing studies have been conducted by trial-and-error.

While no set of widely-accepted constitutive equations spanning the necessary range of processing temperatures and strain rates exists, some recent progress towards this end

has been made by Yang et al. [74] and Thamburaja and Ekambaram [75].[1] In addition, Anand and Su [77] have extended the constitutive framework of Chapter 3 to model the response of metallic glasses at high homologous temperatures in the range $0.7\vartheta_g \lesssim \vartheta \lesssim 0.9\vartheta_g$. The purpose of this chapter is to build on the constitutive framework of Anand and Su to represent the mechanical response of metallic glasses in the temperature range $0.9\vartheta_g \lesssim \vartheta \lesssim \vartheta_x$ where $\vartheta_x > \vartheta_g$ is the first crystallization temperature of the material; the higher-end of this temperature range is of utmost importance for thermoplastic forming.

This chapter is organized as follows. In Section 5.2 we specialize the Anand-Su theory presented in Chapter 3 to model the elastic-viscoplastic response of metallic glasses in the temperature range $0.9\vartheta_g \lesssim \vartheta \lesssim \vartheta_x$. In Section 5.3 we use the experimental data of Lu et al. [12] for the widely studied metallic glass $Zr_{41.2}Ti_{13.8}Cu_{12.5}Ni_{10}Be_{22.5}$ (Vitreloy-1) to estimate the material parameters appearing in our specialized equations, and using the specialized model, we compare the numerically-calculated stress-strain curves with the corresponding experimental results. Finally, in Section 5.4.1, we briefly describe a corresponding, simplified Mises-type version of the theory for use under conditions involving temperatures sufficiently higher than ϑ_g and strain rates that are sufficiently low.

5.2 Specialization of the constitutive equations

In this section, we specialize the constitutive theory outlined in Chapter 3 to model the elastic-viscoplastic response of metallic glasses in the temperature range $0.9\vartheta_g \lesssim \vartheta \lesssim \vartheta_x$.

Since there is not enough experimental information concerning the pressure-sensitivity of plastic flow of metallic glasses at high homologous temperatures, and since the pressure-sensitivity is expected to be small, from the outset we set the internal friction coefficient $\mu = 0$. In setting the internal friction to be zero, the Coulomb-type theory of Anand and Su reduces to a Tresca-type theory.

Next, we discuss the specialization of the important scalar flow rate equation (3.11). To do this, we first recall the classical one-dimensional model of Spaepen (1977) which is often used to represent the macroscopic inelastic response of metallic glasses.

5.2.1 The Spaepen model

A continuum-level one-dimensional model which has long been used to represent the inelastic response of metallic glasses is the *free volume model* proposed by Spaepen [6], and it is this model that was used by de Hey et al. [63] to analyze their experimental results. Briefly, let $|\dot{\epsilon}^p|$ denote the magnitude of the plastic strain rate in a *one-dimensional* setting. In such a setting, the flow equation proposed by Spaepen has the form

$$|\dot{\epsilon}^p| = 2\, c_f\, k_f \frac{\epsilon_0 v_0}{\Omega} \sinh\Big(\frac{|\sigma|\, \epsilon_0\, v_0}{2\, k_B\, \vartheta}\Big). \tag{5.1}$$

[1] Also see Lu et al. [12] and Kim et al. [76]; however, these two sets of authors use a "fictive-stress" model, whose physical basis we do not comprehend.

Here $|\sigma|$ is the absolute value of the stress, ϵ_0 is a local transformation strain, v_0 is an activation volume, Ω is an atomic volume, k_f is a temperature dependent rate factor, k_B is Boltzmann's constant, and

$$c_f = \exp\Big(-\frac{1}{\zeta}\Big) \equiv \exp\Big(-\frac{\gamma\, v^*}{v_f}\Big) \tag{5.2}$$

is the concentration of flow defects defined in terms of a normalized free volume parameter $\zeta = v_f/(\gamma\, v^*)$, where v_f is the average free volume per atom, v^* is a critical value of the free volume, and γ is a geometrical overlap factor with a value between 0.5 and 1. In de Hey et al. [63], the evolution of the defect concentration is taken as[2]

$$\dot{c}_f = \underbrace{\Big(a_\zeta\, c_f\, (\ln c_f)^2\Big)\, |\dot{\epsilon}^p|}_{\text{dynamic defect creation}} - \underbrace{k_r\, c_f\, (c_f - c_{f,eq})}_{\text{static thermal recovery}}\,, \tag{5.3}$$

with a_ζ a temperature dependent parameter, k_r a temperature dependent rate factor, and

$$c_{f,eq} = \exp(-\frac{1}{\zeta_{eq}}), \tag{5.4}$$

where

$$\zeta_{eq} = \frac{\vartheta - \vartheta_0}{B} \tag{5.5}$$

is the value of the free volume in thermal equilibrium at a temperature ϑ; here ϑ_0 and B are two material constants known as the Vogel-Fulcher-Tamann (VFT) [78–80] parameters.

A study of the paper by de Hey et al. [63] reveals that the flow equation (5.1) and the evolution equation (5.3), when suitably calibrated, are *not able to produce stress-strain curves that match their corresponding experimental stress-strain data* which show the phenomena of stress-overshoot and strain-softening in monotonic experiments at a given strain rate, and strain rate history effects in experiments involving strain rate increments and decrements.

In our opinion, even though the flow and evolution equations (5.1) and (5.3) are physically reasonably well-motivated, they leave out some important *coupling effects* and thereby are unable to quantitatively reproduce the stress-overshoot and strain-softening phenomenon which arise in a metallic glass due to deformation-induced microstructural disordering. In what follows, we propose suitable simple phenomenological modifications to the Spaepen model in order to provide additional flexibility to reproduce the experimentally-observed stress-strain response of metallic glasses in the temperature range $0.9\vartheta_g \lesssim \vartheta \lesssim \vartheta_x$.

[2]In Spaepen's original model [6], the evolution of the defect concentration is also controlled by diffusional mechanisms. However, the effects of diffusion of free volume at nominal strain rates $\gtrsim 10^{-5}\text{s}^{-1}$ and moderate strain levels is expected to be small, and is accordingly not considered here.

5.2.2 Modified Spaepen model

We begin by using the two internal variables, a resistance S and an "order-parameter" φ, to modify Spaepen's flow equation to better reproduce the stress-overshoot and strain-softening phenomena due to deformation-induced disordering. Guided by (5.1) and (5.2), the flow function for the scalar shearing rate on each slip system is taken as

$$\nu^{(\alpha)} = \nu_0 \exp\left(-\frac{1}{\zeta}\right) \exp\left(-\frac{\Delta F}{k_{\mathrm{B}}\vartheta}\right) \sinh\left(\frac{\tau_{\mathrm{eff}}^{(\alpha)} V}{2k_{\mathrm{B}}\vartheta}\right), \tag{5.6}$$

with ν_0 a pre-exponential factor of the order of the Debye frequency, ζ a free volume parameter as in Spaepen's theory, ΔF an activation energy, $V \equiv (\epsilon_0 v_0)$ an activation volume, and

$$\tau_{\mathrm{eff}}^{(\alpha)} \stackrel{\mathrm{def}}{=} \tau^{(\alpha)} - S \tag{5.7}$$

an *effective stress*, where S is the transient change in flow resistance accompanying the microstructural disordering of the material. The scalar flow rate $\nu^{(\alpha)}$ is positive whenever $\tau_{\mathrm{eff}}^{(\alpha)} > 0$, and is zero otherwise.

The evolution equation for the resistance S is *coupled* with the evolution equation for φ, and it is this coupling which is used to model the yield-peak observed in stress-strain response of metallic glasses.[3] Specifically we take the evolution of S to be governed by

$$\left.\begin{aligned} &\dot{S} = h\,\nu^{\mathrm{p}}, \qquad \text{with initial value} \qquad S(\mathbf{X},0) = S_0\,, \\ &h = h_0\,(S^* - S)\,, \qquad \text{and} \qquad S^* = \hat{S}^*(\nu^{\mathrm{p}}, \vartheta, \varphi). \end{aligned}\right\} \tag{5.8}$$

Next, recall from (3.18) that φ evolves as

$$\dot{\varphi} = \beta \nu^{\mathrm{p}} \qquad \text{with initial value} \qquad \varphi(\mathbf{X},0) = \varphi_0, \tag{5.9}$$

where β is the shear-induced plastic dilatancy function. We take this dilatancy function to be given by

$$\beta = g\,(\varphi^* - \varphi)\,, \qquad \text{with} \qquad \varphi^* = \hat{\varphi}^*(\nu^{\mathrm{p}}, \vartheta) \geq 0. \tag{5.10}$$

In these coupled evolution equations for S and φ, the parameters h_0, g, S_0 and φ_0 are constants. The function h represents the strain-hardening/softening function for the slip resistance during plastic flow: the material hardens ($h > 0$) if $S < S^*$, and softens ($h < 0$) if $S > S^*$. The critical value S^* of S controlling such hardening/softening transitions is assumed to depend on the current values of the plastic strain rate, temperature, and the order-parameter φ. In the dilatancy function, the parameter φ^* represents a strain rate and temperature dependent critical value for the order-parameter: the material dilates ($\beta > 0$) when $\varphi < \varphi^*$, and compacts ($\beta < 0$) when $\varphi > \varphi^*$. In a monotonic experiment at a given strain rate and temperature, the shear-induced dilatancy vanishes ($\beta = 0$) when $\varphi =$

[3] Coupled differential evolution equations of this type have previously been used to model yield peaks in granular materials, Anand and Gu [61], as well as amorphous polymeric materials, Anand and Gurtin [81].

φ^*. However, in an experiment in which the strain rate and temperature are varying (e.g. strain rate or temperature jump experiments), the material will in general dilate or compact, depending on the strain rate and temperature history, and because of the coupling between the evolution equations for S and φ, the resistance S will also vary.

Particular forms for the functions $\hat{\varphi}^*(\nu^{\mathrm{p}}, \vartheta)$ and $\hat{S}^*(\nu^{\mathrm{p}}, \vartheta, \varphi)$ need to be specified. The function φ^* controls the amount of disordering the material undergoes during deformation and is both strain rate and temperature dependent. The strain rate and temperature dependence of φ^* is quite nonlinear; φ^* is expected to decrease with increasing temperature at a fixed strain rate, and increase with strain rate at a fixed temperature. Guided by the experimental data for the stress overshoot, (cf. Figs. 5-1 and 5-2) we model this temperature and strain rate dependence of φ^* using the following functional form,

$$\varphi^* = \begin{cases} \varphi_{\mathrm{s}} \left[1 - \left(\dfrac{\vartheta - \vartheta_0}{\vartheta_{\mathrm{s}}} \right)^p \right]^q & \text{if } (\vartheta - \vartheta_0) \leq \vartheta_{\mathrm{s}}, \\ 0 & \text{if } (\vartheta - \vartheta_0) > \vartheta_{\mathrm{s}}, \end{cases} \tag{5.11}$$

with

$$\left.\begin{aligned} \varphi_{\mathrm{s}} &= k_1 + k_2 \ln \left(\frac{\nu^{\mathrm{p}}}{\nu_{\mathrm{ref}}} \right), \\ \vartheta_{\mathrm{s}} &= l_1 + l_2 \ln \left(\frac{\nu^{\mathrm{p}}}{\nu_{\mathrm{ref}}} \right), \end{aligned}\right\} \tag{5.12}$$

where $\{\vartheta_0, p, q, k_1, k_2, l_1, l_2, \nu_{\mathrm{ref}}\}$ are constants. At a fixed strain rate, φ_{s} and ϑ_{s} are constant, and (5.11) describes the temperature variation of φ^* in the range $[\vartheta_0, \vartheta_{\mathrm{s}}]$, with $\varphi^* = \varphi_{\mathrm{s}}$ when $(\vartheta - \vartheta_0) = 0$ and $\varphi^* = 0$ when $(\vartheta - \vartheta_0) = \vartheta_{\mathrm{s}}$; the parameters p and q control the nonlinear variation of φ^* between the limits $[\varphi_{\mathrm{s}}, 0]$. The assumed strain rate dependence of φ_{s} and ϑ_{s} is given in (5.12).[4]

Further, for the function S^*, which controls the magnitude of the stress-overshoot, we assume

$$S^* = b\,(\varphi^* - \varphi)\,, \tag{5.13}$$

so that the value of S^* depends linearly on the difference between the current value of φ and the parameter φ^*. Also, since experimental data (cf. Fig. 5-3) shows that the magnitude of the stress overshoot is different in strain rate decrement and increment tests, we assign different values for the constant b during dilation ($\varphi < \varphi^*$), and compaction ($\varphi > \varphi^*$):

$$b = \begin{cases} b_{\mathrm{dil}} & \text{if } \varphi < \varphi^*, \\ b_{\mathrm{com}} & \text{if } \varphi > \varphi^*. \end{cases} \tag{5.14}$$

[4]Cf. Fig. D-4, which schematically shows the temperature and strain rate variation of φ^* based on equations (5.11) and (5.12).

Next, we turn our attention to the term $\exp(-1/\zeta)$ in (5.6), which represents the concentration of flow defects. Having accounted for the deformation-induced disordering of the material via the internal variables S and φ, as discussed above, *we assume henceforth that the free volume ζ is only a function of temperature.*[5] Recall that in the Spaepen model the temperature dependence of the "equilibrium" value of ζ is taken in the linear Vogel-Fulcher-Tamann (VFT) form (5.5). Here, following Masuhr et al. [82] and Yang et al. [74], we adopt the Grest and Cohen [83] temperature dependent form for the free volume concentration,

$$\zeta(\vartheta) = \frac{1}{2d_1}\left[\vartheta - \vartheta_{\text{ref}} + \sqrt{(\vartheta - \vartheta_{\text{ref}})^2 + d_2\vartheta}\right], \tag{5.15}$$

where, d_1, d_2 and ϑ_{ref} are material constants. The non-linear Grest-Cohen relation (5.15) is well-defined at temperatures lower than ϑ_{ref}, and approaches a linear VFT-type relation at high temperatures.

In most previous models of viscoplastic flow of metallic glasses, attention has been restricted to temperature ranges either below ϑ_{g} or well-above ϑ_{g} (but below ϑ_{x}). In either of these two regimes, the activation energy ΔF and the activation volume V appearing in the thermally-activated model (5.6) may be assumed to have different but *constant* values in the two different temperature regimes. However, our interest here is in developing a simple model, which does not differ drastically from (5.6), but is able to capture the strain-rate and temperature dependent response of metallic glasses through the important, but difficult to model, temperature range of $0.9\vartheta_{\text{g}} \lesssim \vartheta \lesssim \vartheta_{\text{x}}$. We accomplish this by assuming that

- *the activation energy ΔF decreases, and the activation volume V increases, as the temperature increases from approximately $0.9\vartheta_{\text{g}}$ through ϑ_{g} to ϑ_{x}.*

Specifically, for the temperature dependence of the activation energy ΔF we adopt the following simple phenomenological form,

$$\Delta F(\vartheta) = \frac{1}{2}(\Delta F_{\text{gl}} + \Delta F_{\text{sc}}) - \frac{1}{2}(\Delta F_{\text{gl}} - \Delta F_{\text{sc}}) \tanh\left(\frac{1}{\Delta_{\text{F}}}(\vartheta - \vartheta_{\text{g}})\right), \tag{5.16}$$

where ΔF_{gl} and $\Delta F_{\text{sc}} (< \Delta F_{\text{gl}})$ are the values of the activation energies in the glassy and supercooled liquid regions; and $\Delta_{\text{F}} > 0$ is a parameter denoting the temperature range across which the assumed hyperbolic-tangent-type transition in the value of the activation energy from ΔF_{gl} to ΔF_{sc} occurs.

Similarly, for the temperature dependence of the activation volume V we adopt the form,

$$V(\vartheta) = \frac{1}{2}(V_{\text{gl}} + V_{\text{sc}}) - \frac{1}{2}(V_{\text{gl}} - V_{\text{sc}}) \tanh\left(\frac{1}{\Delta_{\text{V}}}(\vartheta - \vartheta_{\text{V}})\right), \tag{5.17}$$

[5] In our phenomenological macroscopic theory the order-parameter φ appears as an internal variable which is distinct from the free volume ζ in Spaepen's theory. However, physically, φ may be thought of as the *change* in the free volume due to deformation-induced disordering from the purely temperature dependent equilibrium value ζ .

where V_{gl} and $V_{sc}(> V_{gl})$ are values of the activation volumes in the glassy and supercooled liquid regions; ϑ_V is the temperature at which the activation volume begins to increase (not necessarily equal to ϑ_g); and $\Delta_V > 0$ is a parameter denoting the temperature range across which the transition occurs.

Finally, the elastic moduli also change as the temperature changes across the range of interest. Since measurements of temperature variations of elastic moduli are typically made for the Young's modulus E, we first consider the temperature variation of this constitutive modulus. Following the work of Dupaix and Boyce [84] on amorphous polymers, we assume that the temperature dependence of the Young's modulus may be adequately approximated by the function

$$E(\vartheta) = \frac{1}{2}(E_{gl} + E_{sc}) - \frac{1}{2}(E_{gl} - E_{sc})\tanh\left(\frac{1}{\Delta_E}(\vartheta - \vartheta_g)\right) - k_E(\vartheta - \vartheta_g), \tag{5.18}$$

where E_{gl} and $E_{sc}(< E_{gl})$ are representative moduli in the glassy and supercooled liquid regions; and Δ_E is a parameter denoting the temperature range across which this transition occurs, and k_E represents the slope of the temperature variation of E beyond the transition region, where

$$k_E = \begin{cases} k_{E_{gl}} & \vartheta \leq \vartheta_g, \\ k_{E_{sc}} & \vartheta > \vartheta_g. \end{cases} \tag{5.19}$$

Further, for the temperature dependence of Poisson's ratio we assume

$$\nu(\vartheta) = \frac{1}{2}(\nu_{gl} + \nu_{sc}) - \frac{1}{2}(\nu_{gl} - \nu_{sc})\tanh\left(\frac{1}{\Delta_E}(\vartheta - \vartheta_g)\right) \tag{5.20}$$

with ν_{gl} and ν_{sc} representative values of Poisson's ratio below and above the temperature ϑ_g respectively. Using (5.18) and (5.20), the temperature dependent values of the shear and bulk moduli may then be found by using the standard relations:

$$G(\vartheta) = \frac{E(\vartheta)}{2(1+\nu(\vartheta))}, \qquad K(\vartheta) = \frac{E(\vartheta)}{3(1-2\nu(\vartheta))}. \tag{5.21}$$

5.3 Stress-strain response of the metallic glass $Zr_{41.2}Ti_{13.8}Cu_{12.5}Ni_{10}Be_{22.5}$

We have estimated the materials parameters appearing in our constitutive model for $Zr_{41.2}Ti_{13.8}Cu_{12.5}Ni_{10}Be_{22.5}$ from the data published by Lu et al. [12], Masuhr et al. [82], and Tsau et al. [85] for this material. For ease of presentation, we relegate our procedure for material parameter estimation to Appendix D.

Figures 5-1 and 5-2 compares the one-dimensional stress-strain curves (dashed lines) calculated using our model, with the corresponding experimental results (solid lines) of Lu

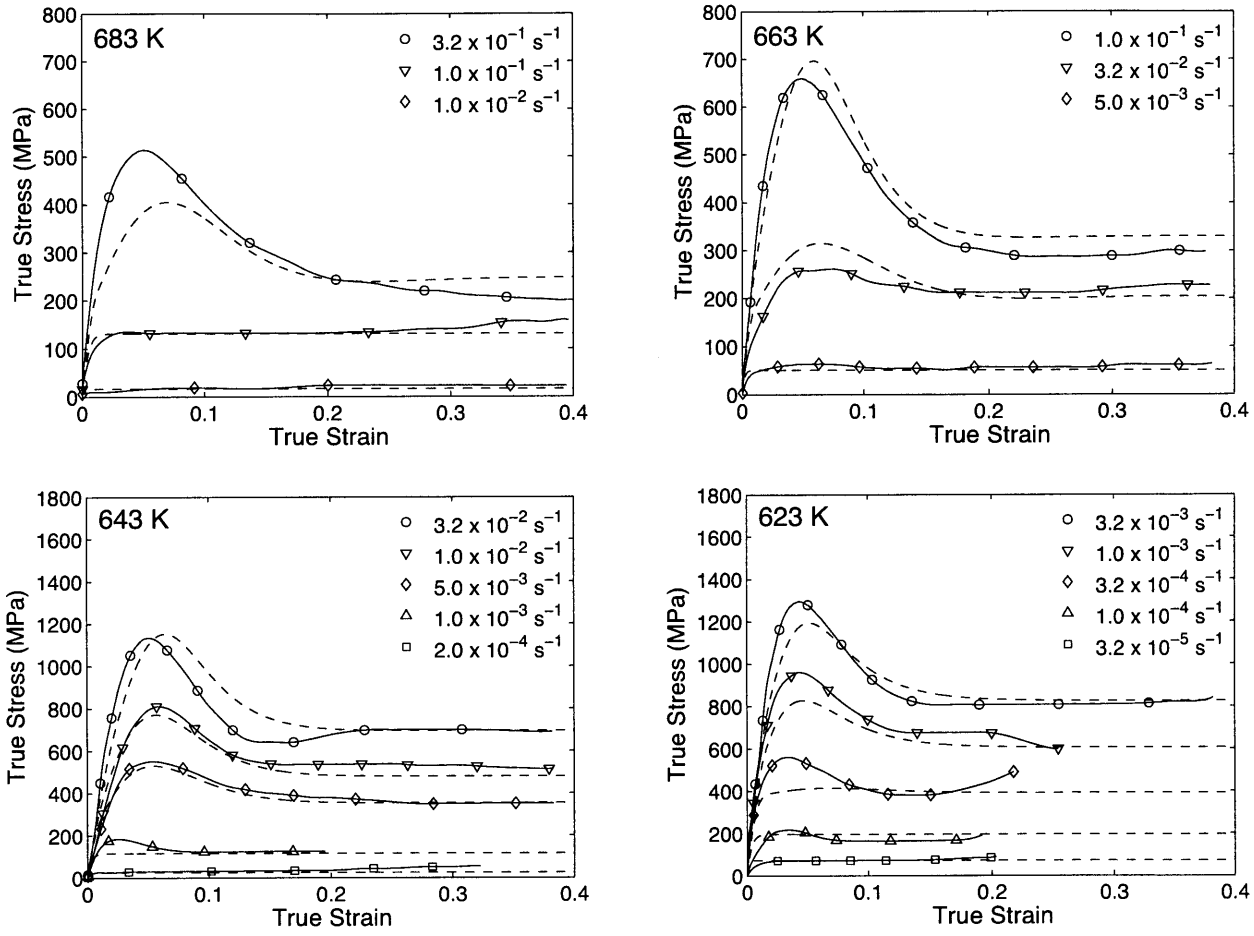

Figure 5-1: Stress-strain curves for Vitreloy-1 at various temperatures and strain rates from Lu et al. [12]. The solid lines are the experimental data, and the dashed lines are results from the model. Markers serve to distinguish data at different strain rates; they do not represent individual data points.

et al. [12], from which the material parameters were estimated. The quality of the fit over a wide range of temperatures and strain rates of interest is quite reasonable.

Predictions from the model were also compared against corresponding experimental data from the strain rate jump experiments of Lu et al. [12]. Figure 5-3 compares the experimental data and the model predictions for several of these strain rate increment and decrement experiments at temperatures both below and above ϑ_g. The quality of the predictions over a wide variety of strain rate histories is quite encouraging.

A feature of the stress-strain response of metallic glasses of particular interest is the "steady-state stress," that is, the stress level at a given temperature and strain rate beyond which the stress level reaches a plateau and is essentially constant; cf. Figs. 5-1 and 5-2. Our model, when specialized to a one-dimensional situation (cf. Appendix D), shows that in a

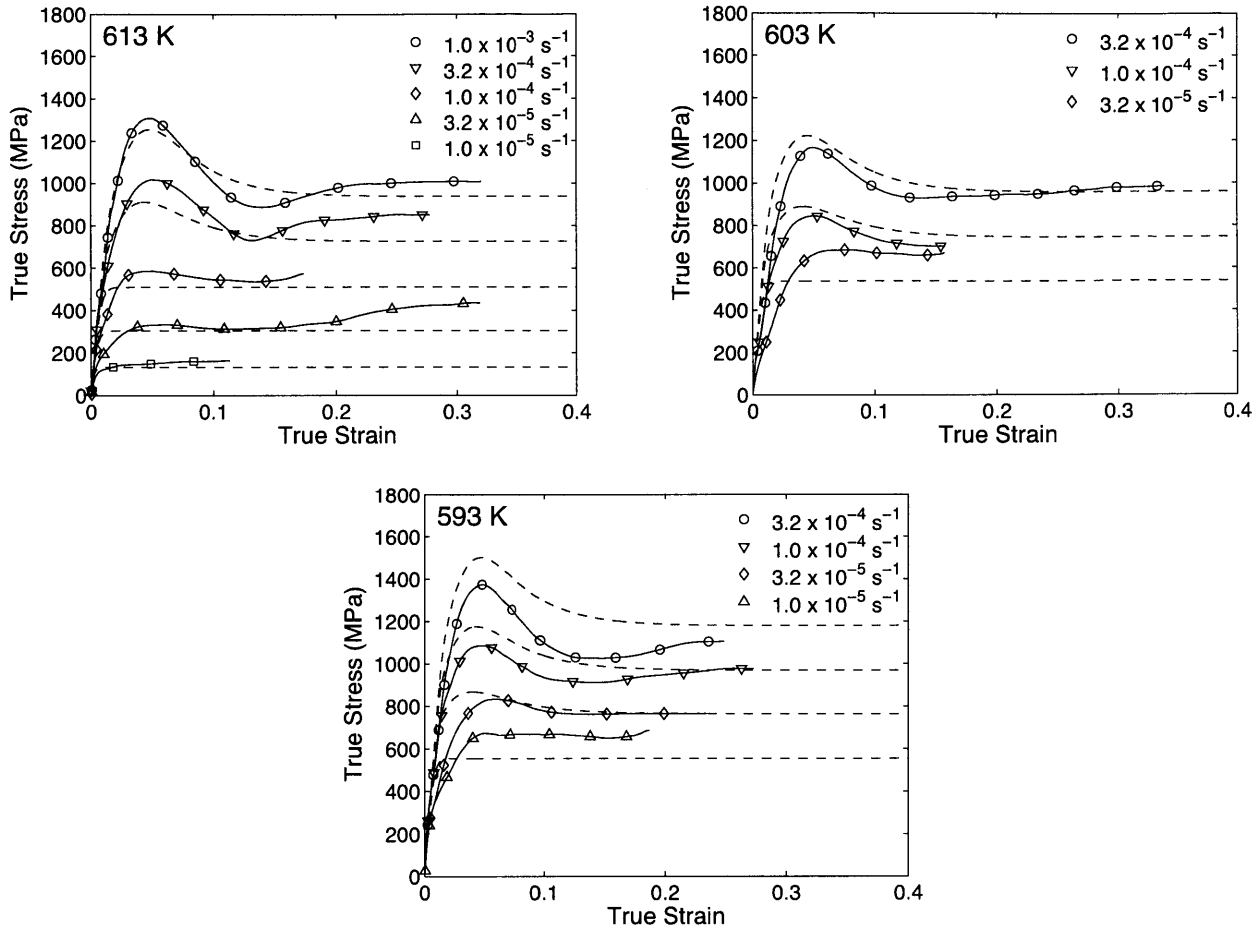

Figure 5-2: Stress-strain curves for Vitreloy-1 at various temperatures and strain rates from Lu et al. [12]. The solid lines are the experimental data, and the dashed lines are results from the model. Markers serve to distinguish data at different strain rates; they do not represent individual data points.

fully-developed state at a given temperature ϑ and an axial strain rate $\dot{\epsilon}$, the axial stress reaches the steady-state stress σ_{ss} given by

$$\sigma_{ss} = \frac{4k_B\vartheta}{V} \sinh^{-1}\left[\frac{\dot{\epsilon}}{2\nu_0} \exp\left(\frac{1}{\zeta}\right) \exp\left(\frac{\Delta F}{k_B\vartheta}\right)\right]. \tag{5.22}$$

Figure 5-4(a) shows the variation of the steady-state stress σ_{ss} versus the strain rate $\dot{\epsilon}$ at various temperatures, and compares it with the corresponding experimental data extracted from Lu et al. [12]. The quality of the fit of the model to the experimental data is quite reasonable.

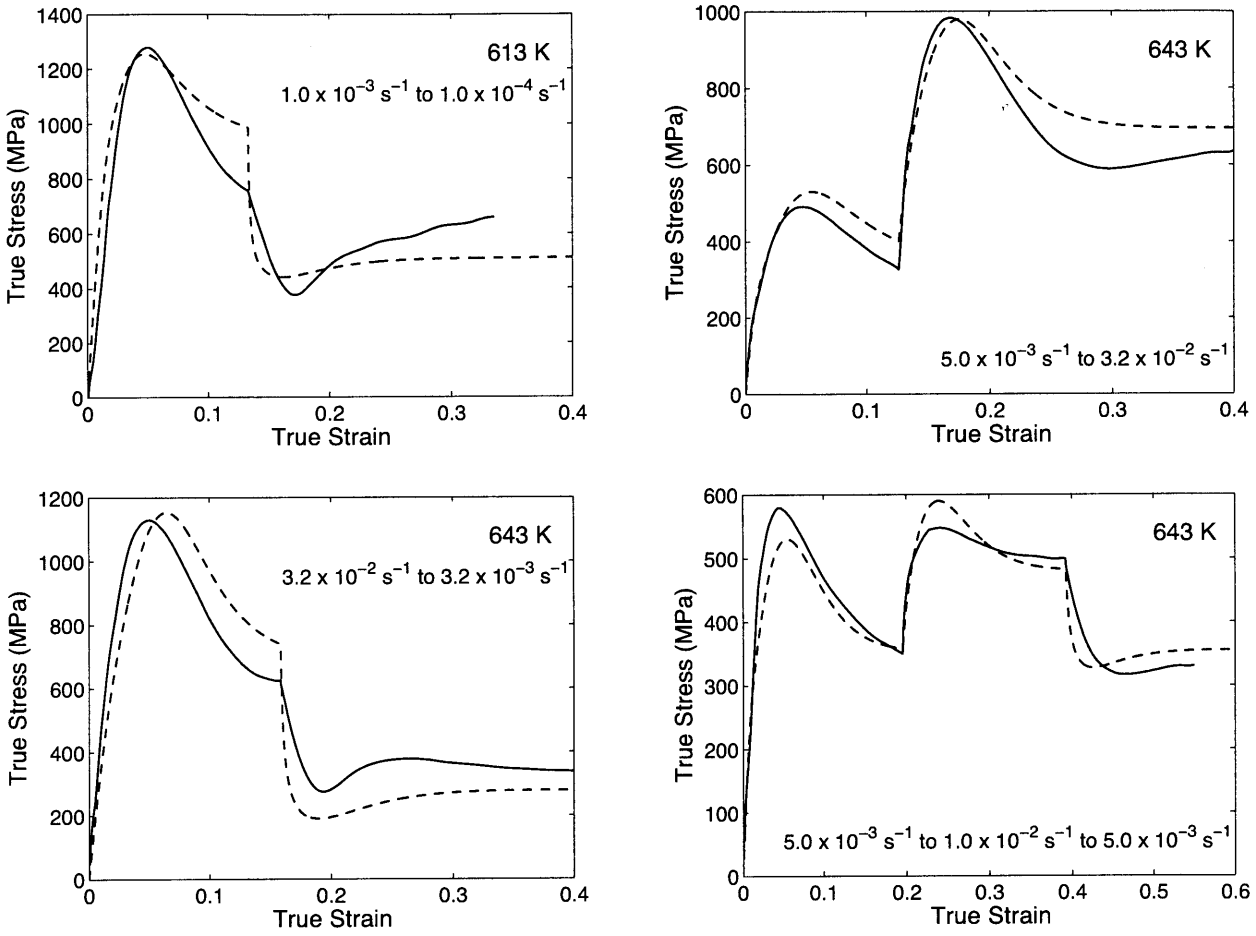

Figure 5-3: Stress-strain curves from strain rate decrement and increment experiments for Vitreloy-1 from Lu et al. [12]. The solid lines are the experimental data, and the dashed lines are results from the model.

Equation (5.22) may be used to define a strain rate and temperature dependent non-Newtonian shear viscosity

$$\eta\left(\dot{\epsilon},\vartheta\right) \stackrel{\text{def}}{=} \frac{\sigma_{ss}}{3\dot{\epsilon}} = \frac{4k_B\vartheta}{3V\dot{\epsilon}}\sinh^{-1}\left[\frac{\dot{\epsilon}}{2\nu_0}\exp\left(\frac{1}{\zeta}\right)\exp\left(\frac{\Delta F}{k_B\vartheta}\right)\right]. \tag{5.23}$$

Under high temperatures and low strain rates, the inverse hyperbolic sine term in (5.23) may be approximated by its argument to obtain an expression for a Newtonian viscosity which is only a function of temperature,

$$\eta_{\text{Newtonian}}\left(\vartheta\right) = \frac{2k_B\vartheta}{3V\nu_0}\exp\left(\frac{1}{\zeta}\right)\exp\left(\frac{\Delta F}{k_B\vartheta}\right). \tag{5.24}$$

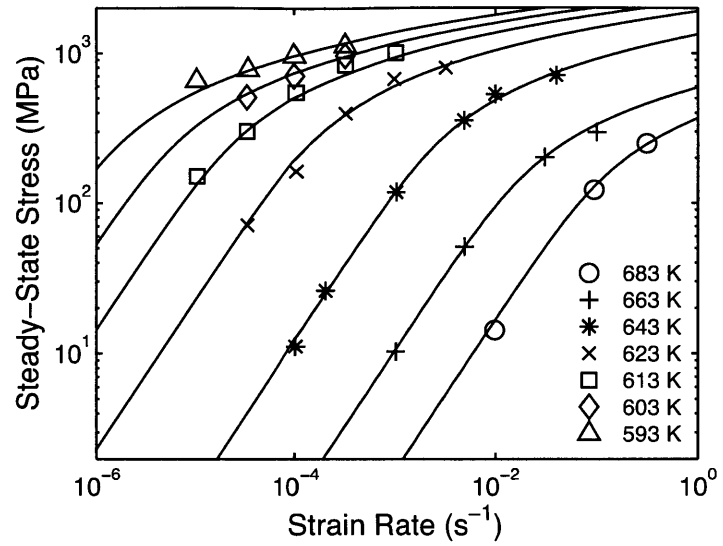

(a)

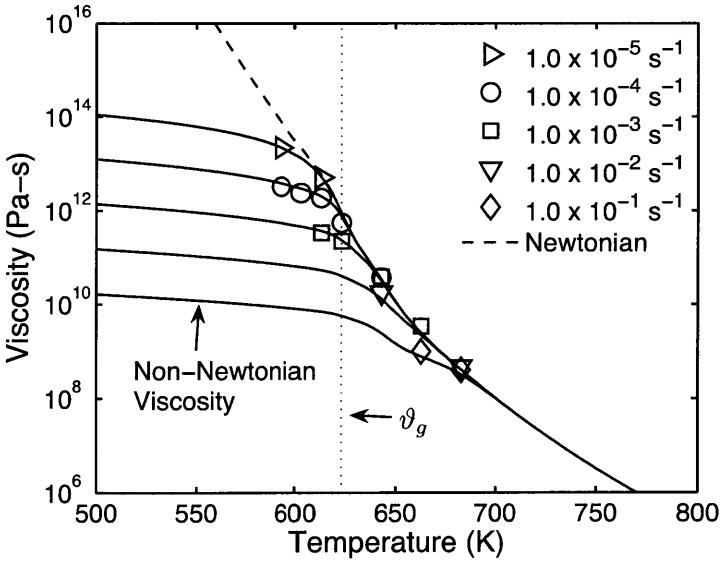

(b)

Figure 5-4: (a) Steady-state stress as a function of temperature and strain rate. (b) Viscosity as a function of temperature and strain rate. Points are data from Lu et al. [12]; each point represents a single monotonic compression experiment. Lines are the model prediction.

Figure 5-4(b) shows the experimental data of Fig. 5-4(a) re-plotted in terms of a non-Newtonian viscosity as a function of the temperature at various strain rates, and compared against the curves generated according to (5.23); the Newtonian approximation (5.24) is also shown in this figure as a dashed line. As is clear from this figure, the model nicely

reproduces the important transition of the viscosity from a non-Newtonian response to a Newtonian response as the material goes through the glass transition.

We have implemented the specialized constitutive model in the finite element program Abaqus/Explicit [36] by writing a user-material subroutine, and in Chapter 6, we use this simulation capability to determine appropriate processing conditions for a representative micron-scale hot-embossing process in a metallic glass.

5.4 Concluding remarks

We have specialized the finite-deformation constitutive theory of Anand and Su to represent the mechanical response of metallic glasses in the temperature range $0.9\vartheta_g \lesssim \vartheta \lesssim \vartheta_x$. The material parameters appearing in the theory have been estimated for Vitreloy-1 ($\vartheta_g = 623\,\mathrm{K}$) in a temperature range spanning 593 K to 683 K, and in a strain-rate range of $\approx 10^{-5}\ \mathrm{s}^{-1}$ to $10^{-1}\ \mathrm{s}^{-1}$. The calibrated constitutive model reproduces important aspects of the mechanical behavior, such as stress-overshoot and strain-softening as well as the the non-Newtonian viscous-type character of the steady-state response of Vitreloy-1 in this temperature and strain rate range. The constitutive model has been implemented in the finite element program Abaqus/ Explicit [36] by writing a user-material subroutine, and this simulation capability will be utilized in subsequent chapters.

5.4.1 A corresponding, simplified Mises-type theory

For future use, we note that if the processing conditions involve temperatures that are sufficiently higher than ϑ_g and strain rates that are sufficiently low then a considerably simpler constitutive theory may be employed. In the simplified theory one may use a Mises-type flow rule employing a scalar flow function and no internal variables instead of the more complex double-shearing flow rule employing internal variables. Specifically, in a simplified theory the evolution equation for $\mathbf{F}^p$ may be taken as

$$\dot{\mathbf{F}}^p = \mathbf{D}^p\mathbf{F}^p, \qquad \mathbf{F}^p(\mathbf{X},0) = \mathbf{1}, \tag{5.25}$$

with $\mathbf{D}^p$ given by

$$\begin{aligned} \mathbf{D}^p &= \sqrt{3/2}\,\dot{\epsilon}^p\,\mathbf{N}^p, \\ \mathbf{N}^p &= \sqrt{3/2}\left(\frac{\mathbf{T}^e_0}{\bar{\sigma}}\right), \\ \dot{\epsilon}^p &= \dot{\epsilon}_0 \exp\left(-\frac{1}{\zeta}\right)\exp\left(-\frac{\Delta F}{k_B\vartheta}\right)\sinh\left(\frac{\bar{\sigma}V}{k_B\vartheta}\right), \end{aligned} \tag{5.26}$$

where

$$\bar{\sigma} = \sqrt{3/2}\,|\mathbf{T}^e_0|, \qquad \dot{\epsilon}^p = \sqrt{2/3}\,|\mathbf{D}^p|, \tag{5.27}$$

are an *equivalent tensile stress* and an *equivalent tensile plastic strain rate*, respectively. The appropriate values for the elastic parameters (E, k, ν), activation energy ΔF, and the activation volume V, are those corresponding to the supercooled liquid region. Thus, for the simplified model the required material parameters/functions are[6]

$$\{E_{\rm sc}, k_{\rm E_{sc}}, \nu_{\rm sc}\} \qquad \text{and} \qquad \{\dot{\bar{\epsilon}}_0, \Delta F_{\rm sc}, V_{\rm sc}, \zeta(\vartheta)\},$$

which are substantially less numerous than those required for the more complete theory, which spans a much wider range of temperatures and strain rates.

[6]In converting from shear to equivalent tensile quantities, the reference strain rate ν_0 must be multiplied by two, $\dot{\bar{\epsilon}}_0 = 2\nu_0$, and the activation volume $V_{\rm sc}$ divided by two, $V_{\rm sc}^{\rm ten} = V_{\rm sc}^{\rm sh}/2$.

Chapter 6

Metallic glasses: viable tool materials for the production of surface microstructures in amorphous polymers by micro-hot-embossing

6.1 Introduction

There is a growing demand in the biomedical industry for microfluidic devices made from amorphous thermoplastic materials. Currently, depending on feature sizes and part quantities, such devices are made either by micro-hot-embossing or by injection-molding methods (cf., e.g., [86]). Both the micro-hot-embossing process and the injection-molding process require a tool containing the negative of the desired pattern to impart the pattern to a polymeric substrate. The tool must be robust and capable of producing many (thousands of) parts without any degradation of the pattern or failure of the tool. The property requirements for a material from which the tool is made include: (i) high stiffness; (ii) high strength; (iii) reasonably high fracture toughness; (iv) good surface finish; (v) good wear and corrosion resistances; and importantly (vi) a straightforward method for the production of the desired features in the tool material over a *wide range* of length-scales and aspect-ratios. Thus, as with any other thermo-mechanical forming process, the following questions are always of major concern: (a) from what material should the tools be made? and (b) how to produce the tools from the chosen material?

A number of different materials have been used for making tools for thermo-mechanical forming of amorphous polymers [86]. By far, the most widely-used tool material is

- **A single crystal silicon-wafer patterned by reactive-ion-etching**. The wide use of silicon as a tool material is primarily due to the existence of well-developed

processing methods, such as deep-reactive-ion-etching (DRIE), used in the production of integrated circuits and MEMS devices, which are easily adapted for making surface-patterns on silicon wafers for thermo-mechanical forming of microfluidic devices. However, silicon is fatally flawed as a tool material in that it is very brittle ($K_{Ic} \approx 1\,MPa\sqrt{m}$) and rarely survives more than a handful of production cycles for micro-hot-embossing of polymers before failing catastrophically.

Other tooling options include:

- **SU-8 on silicon.**[1] Tools made from SU-8 are primarily used for *casting* of polydimethylsiloxane (PDMS) for making microfluidic devices, and are ill-suited for micro-hot-embossing or injection-molding because (i) the SU-8 features tend to delaminate from the silicon substrate under repeated use, and (ii) the brittle silicon substrate tends to fracture.

- **Electroformed metallic tools.** Electroformed nickel-microstructures on a metallic substrate as embossing-tools for thermo-mechanical forming of polymers has gained substantial interest due to the dimensional precision and excellent surface finish with which the microscale features may be electroformed. The resulting tools possess most of the positive attributes of a desirable tool listed above. However, the electroforming process has several limitations: (i) it is slow and time-consuming; (ii) it is difficult to produce high-aspect ratio tools using this process; and (iii) electroformed features often fail by delamination from the substrate.

- **Micro-machined metallic tools.** Tools micro-machined from metals such as brass or stainless steel have good stiffness, strength, toughness, and wear resistance. However, the micro-machining process is capable of accurately producing features which are only $\approx 50\,\mu m$ and larger. Further, the micro-machining process usually leaves machining-marks and burrs, which can result in a poor surface finish.

It is the purpose of this chapter to introduce metallic glasses and the thermoplastic hot-embossing of these glasses as a **robust and attractive alternative** to the existing materials and methods for making tools for thermo-mechanical forming of amorphous polymers by micro-hot-embossing or injection-molding and to utilize the specialized constitutive theory of Chapter 5 and its numerical implementation to simulate the micro-hot-embossing of a metallic glass and select appropriate processing parameters.

$Zr_{44}Ti_{11}Be_{25}Cu_{10}Ni_{10}$, $Zr_{35}Ti_{30}Be_{27.5}Cu_{7.5}$, $Pd_{43}Ni_{10}Cu_{27}P_{20}$ and $Pt_{57.5}Ni_{5.3}Cu_{14.7}P_{22.5}$, with glass transition temperatures of $\vartheta_g \approx 623, 578, 575$, and $508\,K$, respectively, are currently among the most thermoplastically processable alloys known, reaching reasonably low values of viscosities ($\approx 10^4$ to 10^5 Pa-s) in the supercooled-liquid-region before the onset of

[1] SU-8 is an epoxy-based negative photoresist, commonly used in the microelectronics industry.

crystallization [87–89]. In this chapter we focus our attention on the Zr-based metallic glass $Zr_{44}Ti_{11}Be_{25}Cu_{10}Ni_{10}$ (Vitreloy-1b) for the following major reasons:[2]

(i) It is commercially-available.

(ii) As demonstrated by Schroers [88], compared to other readily-available alloys it has excellent thermoplastic formability.

(iii) The mechanical behavior of Vitreloy-1b is similar to that of Vitreloy-1 ($Zr_{41.2}Ti_{13.8}Be_{22.5}Cu_{12.5}Ni_{10}$), which has been recently thoroughly experimentally-characterized in Lu et al. [12] and mathematically-modeled in Chapter 5.

We emphasize that the central idea reported in this chapter is not limited to the use of Zr-based metallic glasses. Indeed any metallic glass with good thermoplastic formability may be used to manufacture dies for micro-hot-embossing of polymers, as long as the glass transition temperature of the specific metallic glass is well above that of the polymer being embossed.

The plan of this chapter is as follows. In Section 6.2, we describe the micro-hot-embossing process that we have used to produce a wide variety of micron-scale patterns in the metallic glass Vitreloy-1b. We also describe a polymer-embossing-tool that we have made from this metallic glass, which has the (negative) microchannel pattern for a simple microfluidic device. In Section 6.3, we describe the results of using the metallic glass tool to replicate the microchannel-channel pattern by micro-hot-embossing of the amorphous polymers poly(methyl methacrylate) ($\vartheta_g \approx 388\,\mathrm{K}$) and Zeonex-690R ($\vartheta_g \approx 409\,\mathrm{K}$) above their glass transition temperatures. The metallic glass tool was found to be very robust, and it was used to produce hundreds of high-fidelity micron-scale embossed patterns without degradation or failure. Lastly, in Section 6.4, we describe the production of a microstructural pattern in Vitreloy-1b with substantially smaller dimensions ($\approx 1\,\mu\mathrm{m}$), than those of the channels ($\approx 50\,\mu\mathrm{m}$) produced for the microfluidic-device embossing-tool, and show that the smaller-dimensioned pattern may also be successfully transfered to a polymeric substrate, thus demonstrating that our two-stage replication process is easily scaled in the 1 to $100\,\mu\mathrm{m}$ feature-size range.

6.2 Micro-hot-embossing of metallic glasses

A materials-processing method for fabricating microscale features and components made from metallic glasses is the *thermoplastic forming process*[3] conducted above the glass transition temperatures of these materials (e.g., [19–24, 91–96]).[4] In this process, a metallic

[2]There is some cause for concern in the use of Vitreloy-1b because of the high beryllium content of this alloy. If this proves to be a serious problem, then either the Pd or Pt-based metallic glass may be used instead, but these alloys are expensive, and not readily-available commercially.

[3]Thermoplastic forming of metallic glasses was first recognized by Patterson and Jones [90] in 1978.

[4]Since metallic glasses can be extended to very large elongations at high temperatures above the ϑ_g of the material, such forming processes are sometimes also called *superplastic forming processes.*

glass is first obtained by traditional casting methods at a sufficiently high cooling rate so as to obtain an amorphous state. The material is not cast into intricate shapes but into simple geometries such as plates or rods. The metallic glass is then heated into the *supercooled liquid* region above the glass transition temperature of the material, where it may be *isothermally formed* to produce intricate microscale patterns and then *slowly cooled.* A typical thermoplastic forming process for a metallic glass is shown schematically in Fig. 6-1 on a time-temperature-transformation (TTT) diagram. Since metallic glasses in their supercooled region are metastable, they eventually crystallize; however, the crystallization kinetics in glass-forming alloys are sluggish, and this results in a relatively large temperature-time processing window in which thermoplastic forming may be carried out without crystallization. Further, since the forming is done isothermally and the subsequent cooling is rather slow, and since there is no phase change on cooling, residual stresses and part distortion may be minimized.

A specific thermoplastic forming process suitable for producing microscale, high-aspect ratio, patterned features on metallic glass plates is *micro-hot-embossing.* This process has received considerable attention in the literature for producing metallic glass components for applications such as NEMS/MEMS [24, 91], optical gratings [92, 96], and micro-dies [20, 94]. In a typical process, a patterned silicon wafer is used as the master surface — a negative of the desired pattern is imparted to the silicon tool using deep-reactive-ion-etching (DRIE), which is capable of producing nano/micro-scale features with high dimensional accuracy. A flat sheet of metallic glass is then placed along with the patterned silicon tool between parallel heated compression platens. The assembly is then heated to an appropriate temperature above the glass transition temperature of the metallic glass, and a desired pressure is then applied over a set amount of time, after which the load is removed and the assembly is cooled. It is important to remember that after a certain amount of time at a given temperature above the glass transition temperature, a metallic glass will eventually crystallize, which is undesirable because it substantially degrades the properties of the formed product. Accordingly, it is important to consider this constraint when selecting appropriate temperature-time processing parameters for the micro-hot-embossing process.[5] During the embossing process, the metallic glass substrate and silicon wafer become mechanically locked together. Thus, following the embossing process, the metallic glass is separated from the silicon mold by etching away the silicon in a heated KOH bath, leaving the embossed metallic glass part. Hence, the silicon tool used in this process is *sacrificial.* Finally, any flash occurring as a result of the micro-hot-embossing process may be trimmed at this point, leaving the final part.

[5]Recall from Chapter 5 that the mechanical behavior of a metallic glass is highly temperature-dependent above its glass transition temperature, with the "viscosity" of the material decreasing dramatically as the temperature increases; and, as such, selecting as high a temperature as possible without risking crystallization is desirable.

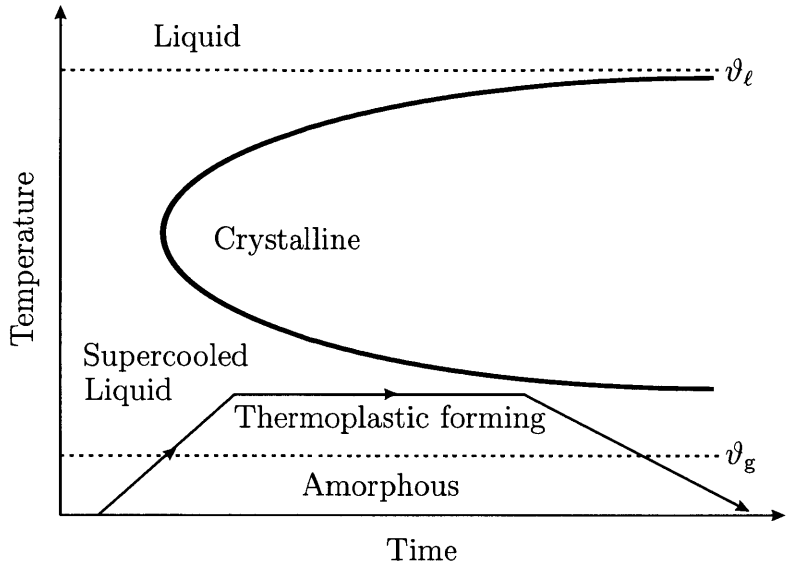

Figure 6-1: A schematic time-temperature-transformation (TTT) diagram for a typical glass-forming alloy, denoting the liquid, supercooled liquid, crystalline, and amorphous regions. The liquidus temperature is denoted by ϑ_ℓ and the glass transition temperature is denoted by ϑ_g. The processing route for thermoplastic forming is shown: the amorphous metal is heated into the supercooled liquid region, isothermally formed, and then slowly cooled.

6.2.1 Finite element simulation

We begin with a simple example of a micron-scale hot-embossing process: the embossing of a series of long raised ridges into a $Zr_{44}Ti_{11}Be_{25}Cu_{10}Ni_{10}$ (Vitreloy-1b) substrate. The pattern consists of channels which are 55 μm wide, 43.5 μm deep, and are spaced 92 μm apart. Figure 6-2(a) shows a schematic of the master pattern, and Fig. 6-2(b) shows a SEM micrograph of a portion of the silicon master produced through DRI-etching. In order to determine appropriate processing parameters for this geometry, namely (i) the embossing temperature, (ii) the applied pressure, and (iii) the hold time, a numerical simulation was carried out. Since the mechanical behavior of Vitreloy-1b is similar to that of Vitreloy-1, we use the simulation capability presented in Chapter 5, along with the material parameters determined for Vitreloy-1 therein, to simulate the current embossing of a Vitreloy-1b substrate.

Since the channels are long relative to their width, and there are a large number of them aligned in parallel, we employ a plane-strain idealization in our numerical simulation and consider only a single half-segment with suitable boundary conditions. Figure 6-2(c) shows the initial finite element mesh. The metallic glass substrate is modeled using 4098 Abaqus-CPE4R plane-strain elements, and the silicon master is modeled using an appropriately-shaped rigid surface. Contact between the substrate and tool was approximated as fric-

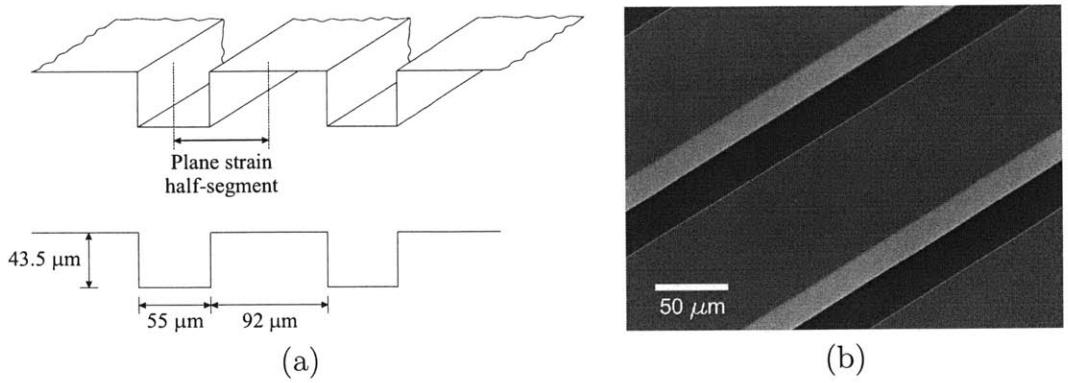

(a) (b)

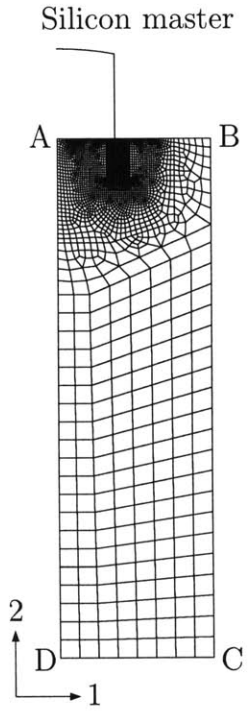

(c)

Figure 6-2: (a) Schematic of the plane-strain master. (b) SEM micrograph of a portion of the silicon master. (c) Finite element mesh for a plane-strain simulation showing the meshed substrate and the silicon master modeled as a rigid surface. The displacement boundary conditions on the portions AD and BC of the mesh boundary are $u_1 = 0$, while on the portion CD of the mesh, $u_1 = u_2 = 0$ are prescribed.

tionless. The displacement boundary conditions on the portions AD and BC of the mesh boundary are $u_1 = 0$, while on the portion CD of the mesh, $u_1 = u_2 = 0$ are prescribed.

The simulations were performed under typical conditions for micro-scale hot-embossing. We chose a temperature of 723 K and a process time of 2 minutes; for Vitreloy-1b, the risk of crystallization and the subsequent deterioration of mechanical properties under these process conditions is expected to be minimal (e.g. [97]). In our numerical simulations, we sought to determine a molding pressure that will result in good replication. After a few trial simulations, it was found that for the geometry under consideration, at 723 K, a pressure of 40 MPa would result in a filled mold after 2 minutes.

6.2.2 Experimental procedures and results

The corresponding hot-embossing experiment was carried out on a servohydraulic Instron testing machine equipped with heated compression platens. A 12 mm-square sheet specimen of Vitreloy-1b, and a 12 mm-square patterned-silicon master were aligned and placed between the heated compression platens. The embossing experiment was conducted under nominally isothermal conditions at a temperature of 723 K in air. The load was ramped up to produce a pressure of 40 MPa in 2 seconds, and thereafter held constant for another 2 minutes. Following the embossing process, the metallic glass substrate and silicon wafer, now locked together, are removed from the load frame, and the metallic glass is separated from the silicon mold by etching away the silicon in a heated KOH bath.

A SEM image of the embossed pattern is shown in Fig. 6-3(a), and a numerically-predicted pattern is shown in Fig. 6-3(b).[6] We further investigated the quality of the embossed features using an optical profilometer; Fig. 6-4 compares representative cross-sections of the embossed features in the metallic glass (circles), against the numerically-predicted channel profile (dashed line).[7] The final geometry of the embossed channels predicted by the numerical-simulation agrees well with the results from the micro-hot-embossing experiment.

Our results from two additional micro-hot-embossing experiments on the metallic glass Vitreloy-1b are shown in Fig. 6-5 — since both patterns involve similar depths and aspect ratios as in the plane-strain pattern above, the same processing parameters were utilized:

(i) Figure 6-5(a) shows SEM images of the silicon master and resulting metallic glass part and a corresponding optical profilometry trace of a set of concentric raised rings, each $\approx 50\,\mu$m wide and $\approx 45\,\mu$m high.

(ii) Figure 6-5(b) shows images of a simple gear-like pattern with a height of $\approx 51\,\mu$m.

Such embossed patterns in metallic glasses have also been previously reported in the literature (cf. e.g. [19]).

Next, we report on our results of thermoplastic forming of a metallic glass tool made from Vitreloy-1b, which has the (negative) microchannel pattern for a simple micromixer, a

[6]The numerical pattern has been mirrored and repeated during post-processing to ease comparison with the corresponding experimental result.

[7]The optical profilometry method that we used to measure the channel profile is not capable of providing data for the sharp vertical features.

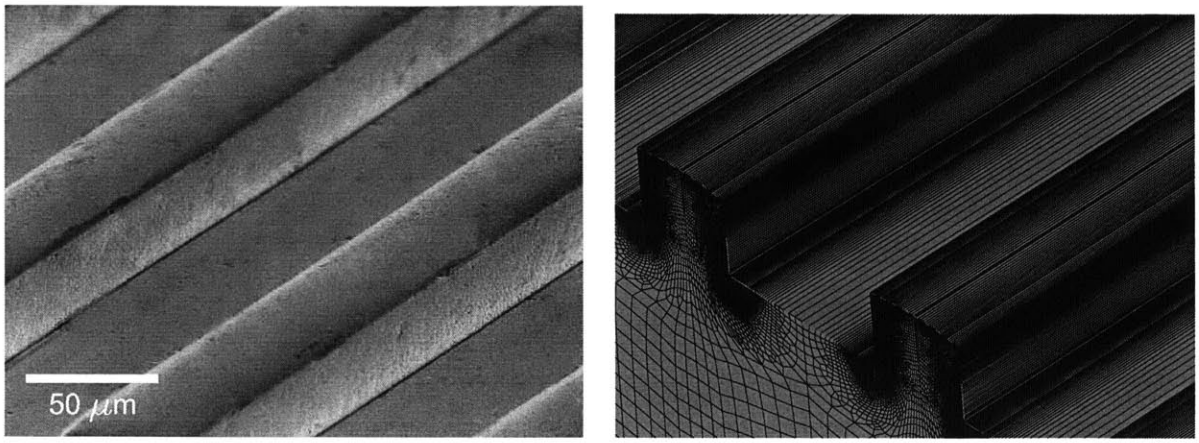

(a) (b)

Figure 6-3: (a) SEM micrograph of the embossed pattern in the metallic glass, and (b) the corresponding numerical prediction. The plane-strain simulation has been extruded and mirrored to make the comparison more clear.

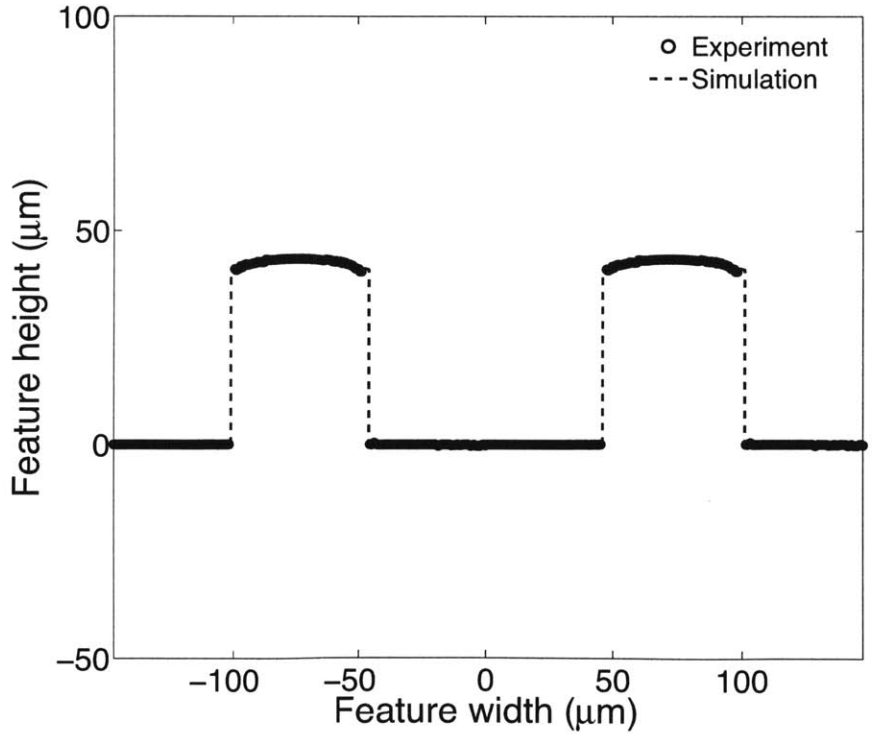

Figure 6-4: Comparison of the experimentally-measured (circles) and numerically-predicted channel profile (dashed line).

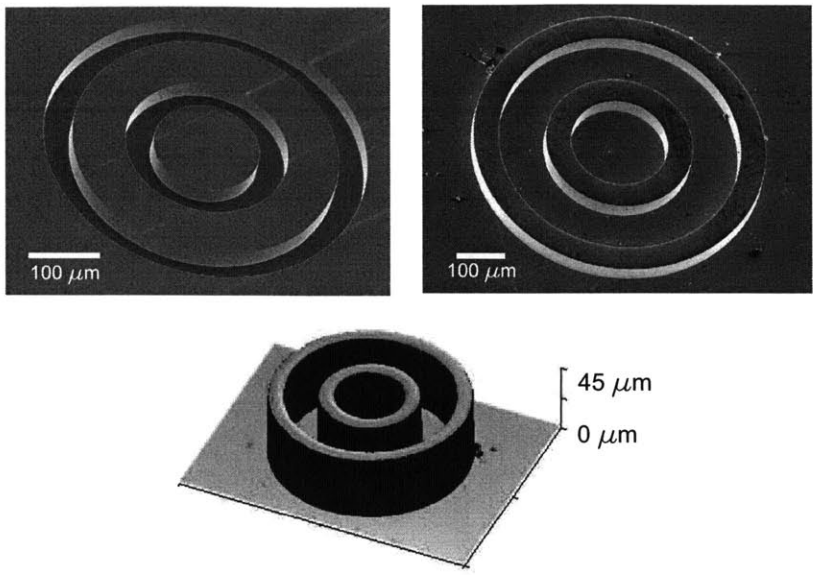

(a)

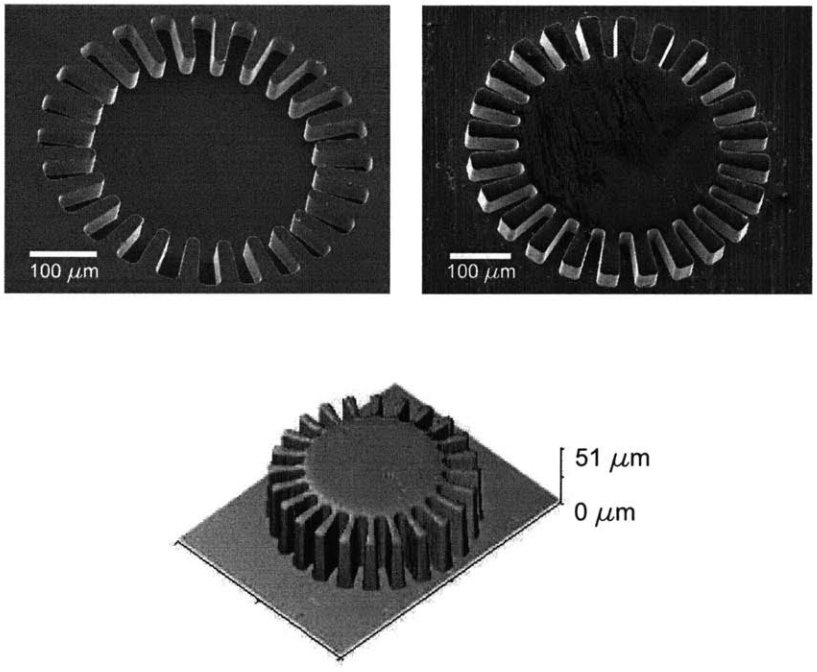

(b)

Figure 6-5: SEM images of the silicon master and resulting metallic glass part and corresponding optical profilometry measurements for a (a) concentric ring pattern and (b) a gear-like geometry.

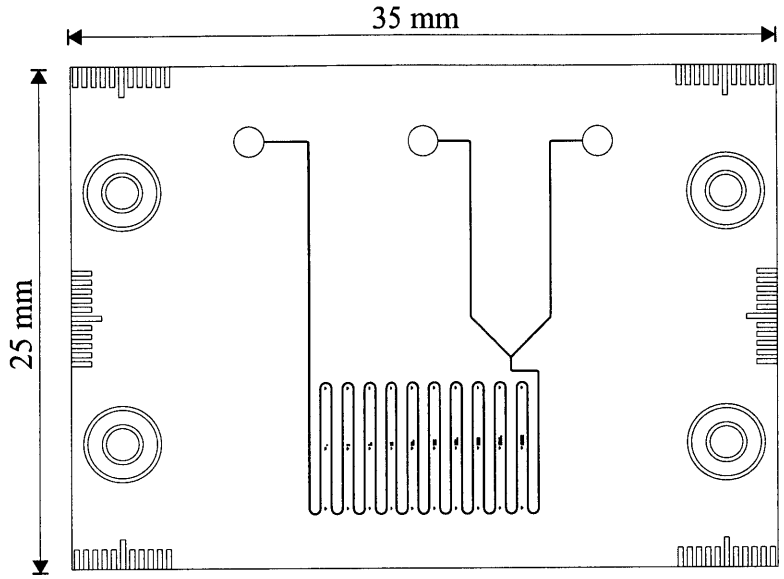

Figure 6-6: A schematic of the micromixer pattern.

schematic of which is shown in Fig. 6-6. The micro-mixer design has two inlets which converge into a single long serpentine mixing channel with a single outlet. The mixing channel is $\approx 50\,\mu$m wide, and was DRI-etched to a depth of $\approx 40\,\mu$m on a silicon tool. In addition to the serpentine micro-mixing channel, the pattern also has a number of micron-sizes markers and other features for alignment and diagnostics (e.g. rectangular and triangular features of the order of $100\,\mu$m). What is notable about this pattern is its overall size of 25 mm by 35 mm, which is large compared to other examples in the literature of hot-embossed metallic glass components, which are usually no more than a couple hundred microns in edge-length.

Using a DRI-etched silicon-master, the micromixer pattern was produced in a Vitreloy-1b substrate by embossing at a temperature of 723 K under a pressure of 40 MPa for 2 minutes. These processing parameters were chosen due to the similarity of the depths and aspect ratios of this pattern compared to the plane-strain pattern simulated previously. The relatively large area of the micro-mixer design under consideration requires good temperature control and smooth, parallel compression platens in the embossing set-up for the metallic glass tool to be successfully produced. Figure 6-7 shows SEM images from various parts of the silicon master and the resulting embossed metallic glass tool. The figure shows a close-up of one of the straight portions, one of the bends, several straight portions, and the Y-section where the two inlets meet. It is clear that the pattern from the silicon master has been faithfully replicated in the metallic glass over the entirety of the pattern. Several such metallic glass tools were produced, and in the next section we summarize their application to produce large quantities of embossed polymeric microfluidic chips.

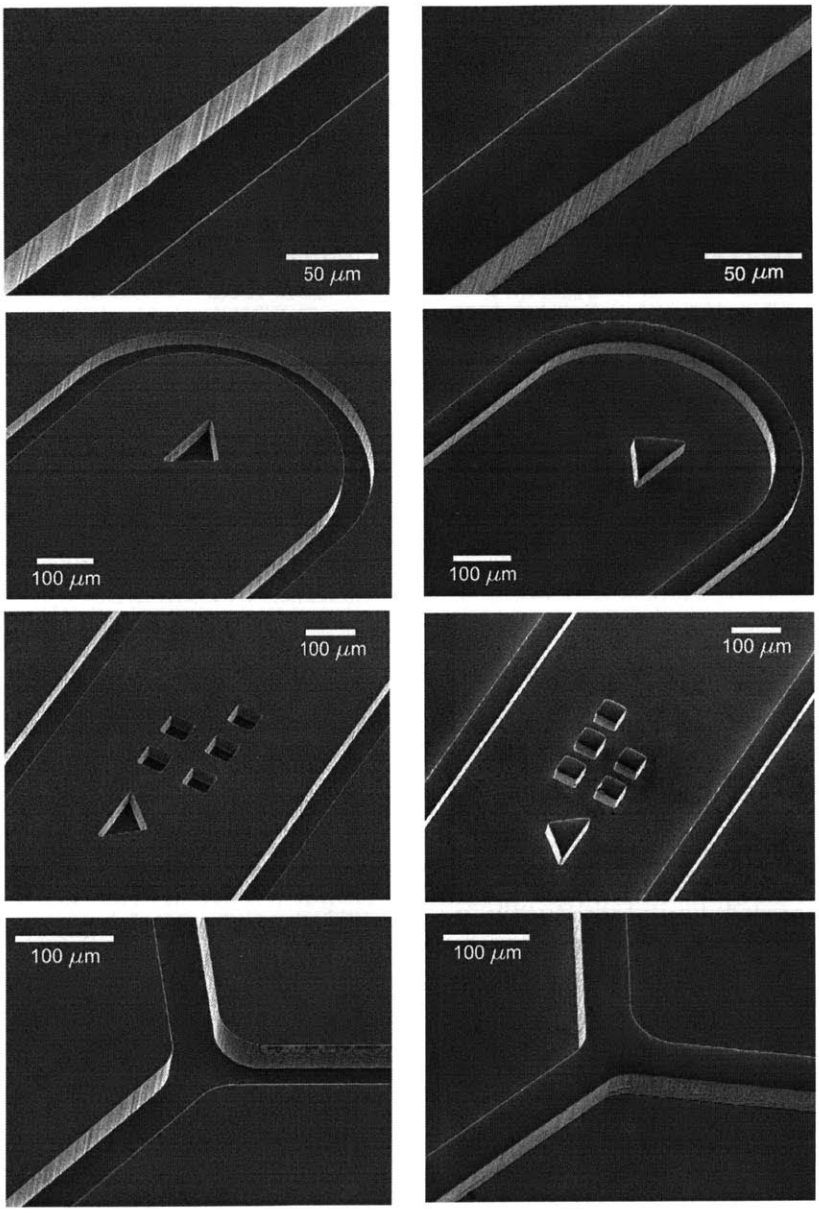

Figure 6-7: SEM micrographs of (a) features in the silicon master and (b) corresponding features in the metallic glass tool.

6.3 Micro-hot-embossing of amorphous polymers using metallic glass tooling

A number of different amorphous polymers have been used for making microfluidic chips. Some common choices are poly(methyl methacrylate) (PMMA), cyclo-olefin-polymers (such as Zeonex), cyclo-olefin-copolymers (such as Topas), polystyrene (PS), and polycarbonate (PC). Here, we focus attention on PMMA and the cyclo-olefin-polymer Zeonex-690R.[8] The nominal glass transition temperatures of these two materials are

$$\text{PMMA: } \vartheta_g \approx 388\,\text{K} \qquad \text{and} \qquad \text{Zeonex-690R: } \vartheta_g \approx 409\,\text{K}.$$

Details of the processes used to manufacture and test functional microfluidic-devices made from PMMA are presented in Hardt et al. [99] and Hale and Hardt [100]. Briefly, the micro-hot-embossing process consists of applying a nominal pressure of 1.5 MPa while heating the PMMA substrate to a temperature of 423 K over the course of 50 seconds and subsequently cooling to a temperature of 353 K over the course of 80 seconds, at which point the pressure is removed, and the metallic glass tool and embossed polymeric substrate are separated. This process of demolding below the glass transition of the polymer is done so that the embossed geometries are locked-in and features are not damaged upon demolding [86]. The process has been designed such that the total cycle time is under 3 minutes, allowing for a high volume of parts (hundreds) to be produced in a relatively short amount of time [100].

SEM images of one of the resulting PMMA parts, before the part is capped, are shown in Fig. 6-8(a). As in Fig. 6-7, Fig. 6-8 shows close-ups of one of the straight portions, one of the bends, several straight portions, and the Y-section where the two inlets meet.

Hundreds of PMMA microfluidic chips with this pattern were produced without any noticeable degradation in quality, indicating that the metallic glass tool withstood numerous thermal-mechanical loading cycles with negligible wear, and without failure [99]. As evidence of this claim, Fig. 6-9(a) shows an SEM image of one of the straight portions on a metallic glass tool that has not been used, while Fig. 6-9(b) shows the same section of a tool after it was subjected to ≈ 350 embossing cycles. A comparison of these two figures (as well as images from several other sections of the used and unused tools, not reported here) shows that no observable degradation of the metallic glass tool has occurred after ≈ 350 embossing cycles.

The micromixer pattern was also embossed in the cyclo-olefin-polymer Zeonex-690R using a process-cycle similar to that described above, but with a peak temperature of 433 K, a nominal pressure of 2 MPa, and a demolding temperature of 358 K. Figure 6-8(b) shows SEM images of various portions of the resulting Zeonex part. Figure 6-10 shows a comparison of the straight portions of ridge/channel cross-sections between the metallic glass tool and the embossed Zeonex; the measurements were made with using a Zygo optical profilometer. This figure clearly shows, in quantitative terms, that the desired pattern was faithfully reproduced in the Zeonex substrate.

[8] For detailed thermo-mechanical constitutive modeling of PMMA, Zeonex, and PC, as well as process modeling of the micro-hot-embossing of these materials, see Srivastava et al. [98].

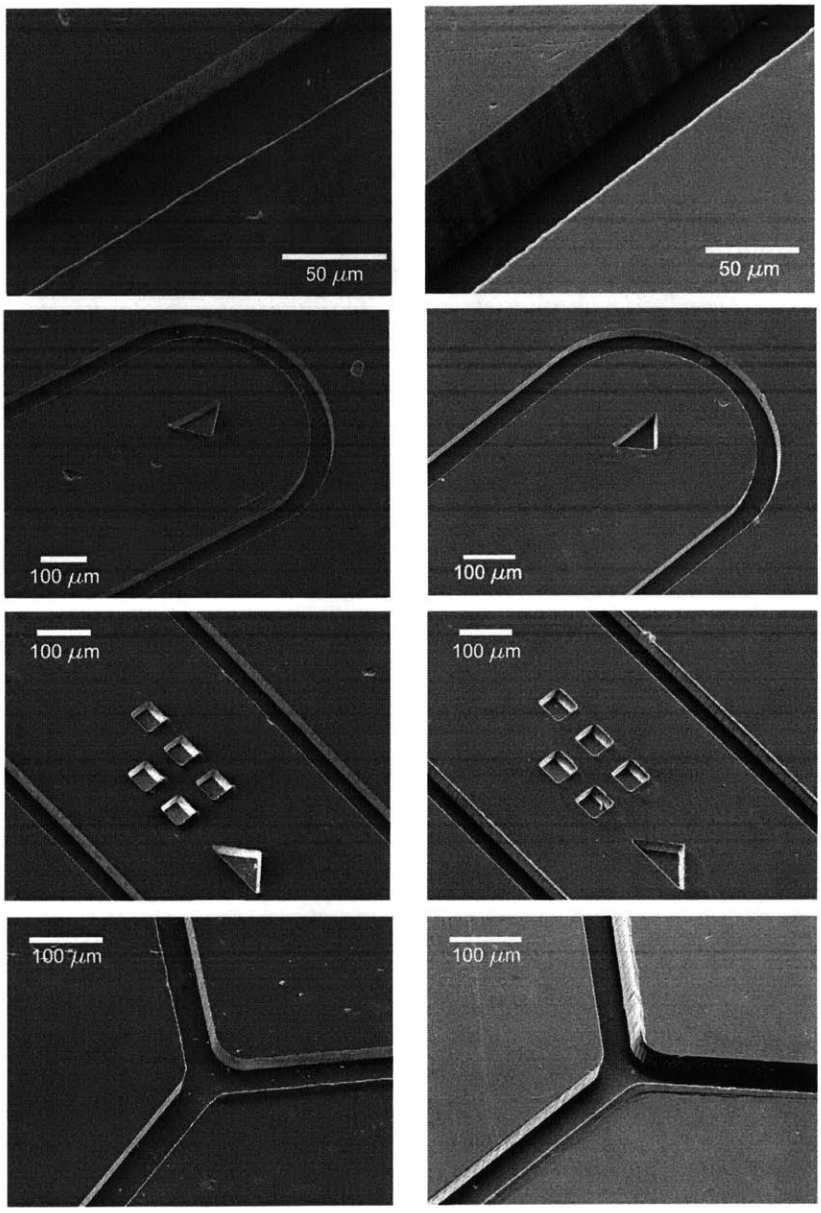

Figure 6-8: SEM micrographs of (a) features in a PMMA part and (b) features in a Zeonex part.

Finally, we note that metallic-glass tooling may also be used in other manufacturing methods used to produce polymeric microfluidic devices. Indeed, metallic-glass tooling has been effectively used by Mazzeo [101] for high-volume production of PDMS microfluidic devices using centrifugal casting methods, and is currently being used by Tor and Fu [102] in high-volume production using injection-molding of amorphous polymers.

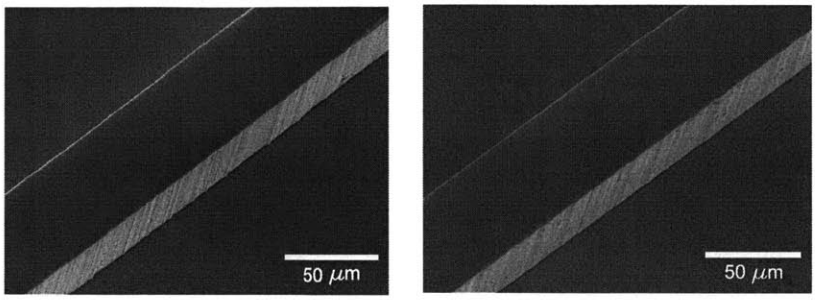

(a) (b)

Figure 6-9: SEM micrographs of one of the straight portions on a metallic glass tool that has been (a) unused and (b) subjected to ≈ 350 embossing cycles.

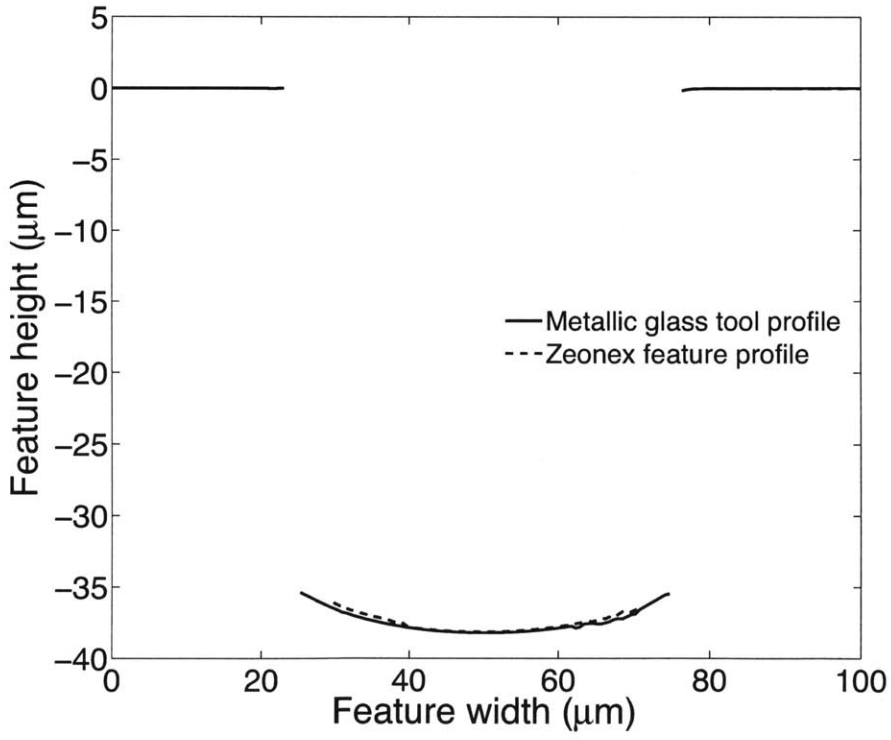

Figure 6-10: Comparison of the cross-sectional profiles from corresponding straight sections on the metallic glass tool and the resulting Zeonex part obtained through optical profilometry measurements.

6.4 Production of small-scale, high-aspect-ratio, high-density micropatterned surfaces

One of the major advantages of using a metallic glass tool is that the polymer hot-embossing procedure described above may be scaled to produce micropatterns which are much smaller in length-scale, are of higher aspect-ratio, and are of higher density than those in the micro-mixer pattern, by simply adjusting the temperature, pressure, and time used in the micro-hot-embossing process.

We produced a silicon-master with the pattern shown in Fig. 6-11(a). Note that the pattern is more complex than a simple array of square posts — a wavy geometry occurs at the bottom of the trenches on the silicon tool. The surface edge-length of each nominally-square feature on the silicon-master is $\approx 1\,\mu$m, and the depth of the "post" is $\approx 10\,\mu$m, yielding an aspect ratio of 1:10. This pattern was hot-embossed in a Vitreloy-1b substrate using a process-cycle similar to that described in the previous section; but because of the density of the microstructure, the embossing pressure was increased to 50 MPa, and the hold time was increased to 4 minutes. Figure 6-11(b) shows a view of the embossed metallic glass substrate, and Fig. 6-11(c) shows the embossed metallic glass from a different angle, looking down into the resulting trenches. From this angle, it is clear that the posts from the top-part of the silicon tool have resulted in an array of square wells at the bottom of the metallic glass part.

The high-density metallic glass tool was then used to emboss a PMMA substrate at a temperature of 403 K, under a pressure of 50 MPa for 10 minutes, and demolded at a temperature of 358 K. The resulting PMMA part is shown in Fig. 6-11(d). As is clear from this figure, the pattern in the original silicon tool shown in Fig. 6-11(a) is faithfully replicated in the PMMA substrate.

This exercise demonstrates that the process of micro-hot-embossing a metallic glass substrate with a silicon tool, and then using the resulting metallic glass part as a tool to hot-emboss patterns on polymeric substrates is *scalable* in producing surface microstructural feature sizes ranging from 1 to 100 μm without any change in methodology, but by only changing the pressure and the hold-times during the two successive embossing process. Indeed, even smaller ($< 1\,\mu$m) microstructural surface features may be produced in metallic glasses through micro-hot-embossing. Kumar et al. [103] have produced posts with diameters of ~ 100 nm in a Pt-based metallic glass by micro-hot-embossing with porous alumina.

6.5 Concluding remarks

This numerical simulation capability of Chapter 5 has then been used to determine appropriate processing parameters in order to carry out a representative micronscale hot-embossing operation. By carrying out corresponding hot-embossing experiments, we have demonstrated that micron-scale features in Vitreloy-1b may be accurately replicated under the processing conditions determined by use of the numerical simulation and design capability.

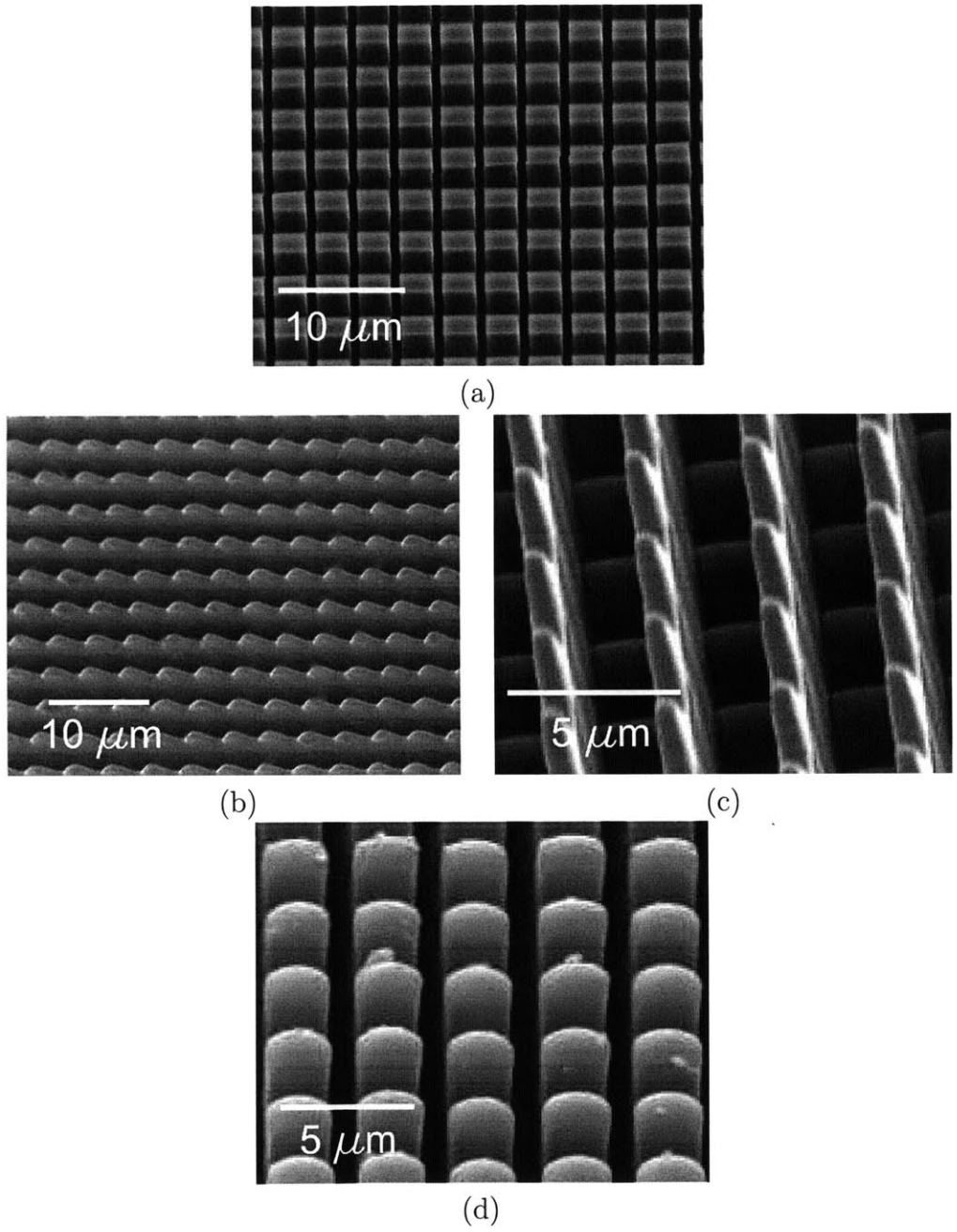

Figure 6-11: SEM images summarizing the micro-hot-embossing of small-scale, high-aspect-ratio, high-density surfaces, including (a) the silicon tool, (b),(c) the resulting metallic glass part, and (d) the resulting PMMA part.

A tool with a micro-mixer pattern was produced by micro-hot-embossing a Vitreloy-1b metallic glass substrate with a sacrificial DRI-etched silicon master tool, and the result-

ing metallic glass part was used *several hundred times* as a robust tool to hot-emboss the micro-mixer pattern on PMMA and Zeonex-690R polymeric substrates. Further, we have demonstrated that the silicon-to-metallic glass tool-spawning processes is *scalable* in producing surface microstructural feature sizes ranging from 1 to 100 μm without any change in methodology, but by only changing the pressure and the hold-times during the two successive embossing processes. Thus, metallic glasses are robust, attractive, and viable tool materials for micro-hot-embossing of polymeric substrates for use in manufacture of microfluidic devices. Due to the superior combination of mechanical properties, good wear resistance, and homogeneity to the atomic-scale, tools made of Vitreloy-1b address the persistent problems of short tool life in polymer micro-hot-embossing processes.

Chapter 7

Surface tension-driven shape-recovery of micro/nanometer-scale surface features in a $Pt_{57.5}Ni_{5.3}Cu_{14.7}P_{22.5}$ metallic glass in the supercooled liquid region

7.1 Introduction

In a recent paper Kumar and Schroers [37] have shown that in the metallic glass $Pt_{57.5}Ni_{5.3}Cu_{14.7}P_{22.5}$, which has a glass transition temperature ϑ_g of 503 K, micron-scale features imprinted on the glass using thermoplastic forming at 523 K could be erased by subsequent annealing in the supercooled liquid region at a temperature of 543 K. Figure 7-1 from their paper shows SEM images of two different micron-scale features, one with an as-printed height of $\approx 5\,\mu$m, and another with an as-printed height of $\approx 2\,\mu$m. This figure also shows images of the microfeatures after annealing at 543 K for 60, 300, and 1200 s. A significant change in shape and height of the features is observed after only 60 s. Upon further annealing the features continue to decrease and merge into the base metallic glass, and after 1200 s each feature is effectively *erased*, with the initially smaller feature erasing more completely than the larger feature. Kumar and Schroers [37] propose that the kinetics of the decay in height of the pyramidal protrusions is determined by the initial height/curvature of the protrusions, the surface tension, and the viscosity of the metallic glass. They argue that *the mechanism of shape-recovery is surface tension-driven viscous flow, with the surface tension*

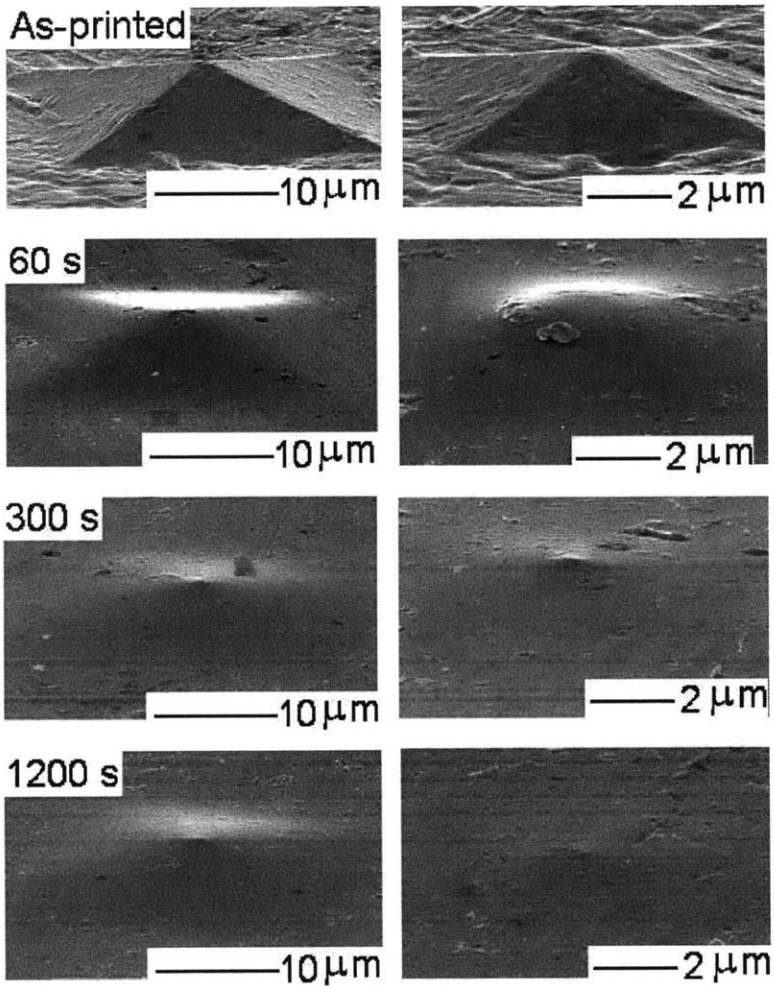

Figure 7-1: SEM micrographs of pyramidal microfeatures of two different initial heights ($\approx 5\,\mu$m and $\approx 2\,\mu$m) after annealing at 543 K for 60, 300, and 1200 s. From Kumar and Schroers [37].

driving the shape-recovery, which is opposed only by the low viscosity of the metallic glass in its supercooled liquid state.[1]

Kumar and Schroers [37] suggest that the phenomenon of surface tension-driven shape-recovery has at least two possible applications: (i) in tandem with micro-hot-embossing, as a method of ultrahigh density re-writable data storage; and (ii) as a method of surface-smoothing of micron-scale metallic glass components. Each of these two prospective applications is discussed further below.

[1] One possible alternative explanation for the shape-recovery of microfeatures during annealing is atomic surface diffusion. However, this mechanism would be equally active in the crystalline and amorphous states, and as noted by Kumar and Schroers [37], once the metallic glass crystallizes the process of shape-recovery halts. This leads them to state with confidence that the process is surface tension-driven.

(i) Currently, a method of ultrahigh-density data-storage is IBM's "millipede" system [104–106]. In this data-storage technology, bits of information are written by indenting a thin *polymeric substrate* (typically PMMA) using an array of heated AFM cantilever tips. The AFM cantilever tips are heated to well above the glass transition of the polymer, and used to indent the polymeric substrate: a residual indent represents a "1", while an unindented region represents a "0". Instead of polymeric materials, metallic glasses may be used as an alternative substrate material, since these materials possess a much higher thermal conductivity than polymers, and they also possess the additional capability of surface tension-driven shape-recovery which may be used as a novel erasing mechanism — thus allowing for the possibility of ultrahigh-density *re-writable* data-storage.

(ii) Micro-patterned silicon tools, which are produced by deep-reactive-ion-etching (DRIE), are beginning to be used to thermoplastically form metallic glasses using a micro-hot-embossing process [94]. The corrugations left on the silicon master due to the DRIE process result in corrugated surfaces on the vertical side walls of metallic glass components produced by micro-hot-embossing. Surface tension-driven shape-recovery may be used to erase these unwanted features; cf. Fig. 4 of Kumar and Schroers [37]. The surface tension-driven shape-recovery process may also be used to precisely control the dimensions of *intentionally produced* corrugated surfaces for use as optical gratings or microdies.

In order for these potential applications to be realized, a deeper scientific understanding of the phenomenon and a numerical simulation capability for surface tension-driven shape-recovery are necessary. The latter requires a constitutive theory for the bulk response of the material, as well as a method for calculating surface curvatures for arbitrary three-dimensional geometries, and a method for incorporating surface tension effects into the boundary conditions of the numerical solution methodology. Accordingly, the purpose of this chapter is to (i) develop an elastic-viscoplastic constitutive theory for the metallic glass $Pt_{57.5}Ni_{5.3}Cu_{14.7}P_{22.5}$ in the super-cooled liquid temperature range relevant to the surface tension-driven shape-recovery process; (ii) develop a numerical method to calculate the curvature of *arbitrary surface geometries* and to account for the effects of surface tension as a suitable boundary condition; (iii) estimate the surface tension of $Pt_{57.5}Ni_{5.3}Cu_{14.7}P_{22.5}$ in the temperature range of interest; and (iv) demonstrate that our numerical simulation capability employing the constitutive model in conjunction with our method for incorporating surface tension effects is capable of reproducing the experimental results of shape-recovery of micro/nano-scale features recently reported in the literature.

This chapter is organized as follows. In Section 7.2, we review a simple elastic-viscoplastic constitutive theory for metallic glasses in the super-cooled liquid temperature range at low strain rates, introduced in Section 5.4.1. In Section 7.3, we use the experimental data of Harmon et al. [38] for $Pt_{57.5}Ni_{5.3}Cu_{14.7}P_{22.5}$ to estimate the material parameters appearing in the constitutive equations for the bulk response of the metallic glass. We have implemented our constitutive model in the finite element program Abaqus/Standard [36]. In

Section 7.4, we first describe our numerical methodology for calculating surface mean curvatures and incorporating surface tension effects in finite element simulations. By carrying out three-dimensional finite-element simulations of the shape-recovery experiments of Kumar and Schroers [37], and using the independently-determined material parameters for the bulk glass, we estimate the surface tension of $Pt_{57.5}Ni_{5.3}Cu_{14.7}P_{22.5}$ at the temperature at which the shape-recovery experiments were conducted. Finally, with the material parameters for the underlying elastic-viscoplastic bulk response as well as a value for the surface tension of the Pt-based metallic glass fixed, we validate our simulation capability by comparing predictions from our numerical simulations of shape-recovery experiments of Berkovich nanoindents, against corresponding recent experimental results of Packard et al. [39] who reported shape-recovery data of nanoindents on the same Pt-based metallic glass.

7.2 Constitutive theory

In Chapter 5, we presented a three-dimensional, elastic-viscoplastic, finite-deformation constitutive theory for metallic glasses in a high temperature range spanning the glass transition and for a large range of strain rates $[10^{-5}, 10^{-1}]\,\mathrm{s}^{-1}$. In surface tension-driven shape-recovery processes, only temperatures above the glass transition, as well as relatively low strain rates ($\sim 10^{-5}$–$10^{-3}\,\mathrm{s}^{-1}$), are encountered. Accordingly, in this chapter, we will utilize the simplified version of the theory from Section 5.4.1 for use in simulations of surface tension-driven shape-recovery.

Briefly summarizing the plasticity relations, the evolution equation for $\mathbf{F}^{\mathrm{p}}$ is

$$\dot{\mathbf{F}}^{\mathrm{p}} = \mathbf{D}^{\mathrm{p}}\mathbf{F}^{\mathrm{p}}, \qquad \mathbf{F}^{\mathrm{p}}(\mathbf{X}, 0) = \mathbf{1}, \tag{7.1}$$

with $\mathbf{D}^{\mathrm{p}}$ given by

$$\mathbf{D}^{\mathrm{p}} = \sqrt{3/2}\,\dot{\bar{\epsilon}}^{\mathrm{p}}\,\mathbf{N}^{\mathrm{p}}, \qquad \mathbf{N}^{\mathrm{p}} = \sqrt{3/2}\left(\frac{\mathbf{M}_0^{\mathrm{e}}}{\bar{\sigma}}\right), \tag{7.2}$$

where

$$\bar{\sigma} = \sqrt{3/2}\,|\mathbf{T}_0^{\mathrm{e}}|\,, \tag{7.3}$$

is an *equivalent tensile stress* and

$$\dot{\bar{\epsilon}}^{\mathrm{p}} = \sqrt{2/3}\,|\mathbf{D}^{\mathrm{p}}| \tag{7.4}$$

is an *equivalent tensile plastic strain rate*, given by a flow function

$$\dot{\bar{\epsilon}}^{\mathrm{p}} = f(\bar{\sigma}, \vartheta) \geq 0. \tag{7.5}$$

The flow function for the equivalent tensile plastic strain rate is taken as

$$\dot{\bar{\epsilon}}^{\mathrm{p}} = \dot{\bar{\epsilon}}_0 \exp\left(-\frac{1}{\zeta}\right) \exp\left(-\frac{\Delta F}{k_{\mathrm{B}}\vartheta}\right) \sinh\left(\frac{\bar{\sigma}V}{2k_{\mathrm{B}}\vartheta}\right). \tag{7.6}$$

Here, $\dot{\bar{\epsilon}}_0$ is a pre-exponential factor of the order of the Debye frequency; ζ is an "order-parameter" commonly called the "free volume"; ΔF is an activation energy; k_B is Boltzmann's constant; and V is an activation volume. The term $\exp(-1/\zeta)$ in equation (7.6) represents a concentration of flow defects. At the low strain rates relevant to the surface tension-driven shape-recovery process, deformation-induced disordering is expected to be negligible. Accordingly, we assume here that the free volume ζ is only a function of temperature, and take it to be given by the classical Vogel-Fulcher-Tammann (VFT) [78–80] form

$$\zeta(\vartheta) = \frac{\vartheta - \vartheta_0}{B}, \tag{7.7}$$

where B and ϑ_0 are constants. Thus the material parameters needed to describe viscoplastic flow of the glass are

$$\{\dot{\bar{\epsilon}}_0, \Delta F, V, B, \vartheta_0\}.$$

For a fully-developed flow at a given temperature ϑ and axial strain-rate $\dot{\epsilon}(= |\dot{\epsilon}|)$, when the stress reaches a steady-state "plateau" value $\sigma_{ss}(= |\sigma|)$ and $\dot{\epsilon} \approx \dot{\epsilon}^p$, equation (7.6) for a one-dimensional situation may be inverted to read

$$\sigma_{ss} = \frac{2k_B\vartheta}{V} \sinh^{-1}\left[\frac{\dot{\epsilon}}{\dot{\bar{\epsilon}}_0} \exp\left(\frac{B}{\vartheta - \vartheta_0}\right) \exp\left(\frac{\Delta F}{k_B\vartheta}\right)\right]. \tag{7.8}$$

Equation (7.8) may then be used to define a strain rate and temperature-dependent *non-Newtonian shear viscosity*

$$\eta(\dot{\epsilon}, \vartheta) \stackrel{\text{def}}{=} \frac{\sigma_{ss}}{3\dot{\epsilon}} = \frac{2k_B\vartheta}{3V\dot{\epsilon}} \sinh^{-1}\left[\frac{\dot{\epsilon}}{\dot{\bar{\epsilon}}_0} \exp\left(\frac{B}{\vartheta - \vartheta_0}\right) \exp\left(\frac{\Delta F}{k_B\vartheta}\right)\right]. \tag{7.9}$$

Note that under high temperatures and low strain rates, the inverse hyperbolic sine term in equation (7.9) may be approximated by its argument to obtain an expression for a Newtonian viscosity which is only a function of temperature,

$$\eta_{\text{Newtonian}}(\vartheta) = \frac{2k_B\vartheta}{3V\dot{\bar{\epsilon}}_0} \exp\left(\frac{B}{\vartheta - \vartheta_0}\right) \exp\left(\frac{\Delta F}{k_B\vartheta}\right). \tag{7.10}$$

7.3 Material parameters for the metallic glass $Pt_{57.5}Ni_{5.3}Cu_{14.7}P_{22.5}$

We have estimated the material parameters appearing in our constitutive theory for $Pt_{57.5}Ni_{5.3}Cu_{14.7}P_{22.5}$ from the data published by Harmon et al. [38] for this material. Although Harmon et al. [38] provide data for the elastic shear modulus at various temperatures, they do so for temperatures in the range 470 to 503 K ($\equiv \vartheta_g$) but not for temperatures above the glass transition temperature of this material. For our numerical simulations which are carried out at temperatures in the supercooled liquid region above ϑ_g — based on previous

experience with modeling metallic glasses, cf. Tab. D.3 — we assume constant nominal values of

$$G \approx 10\,\text{GPa}, \quad \nu \approx 0.45, \tag{7.11}$$

for the elastic shear modulus and the Poisson's ratio, respectively. We emphasize that precise values of the elasticity parameters are *not crucial* for simulation of the shape-recovery process.[2]

In their Fig. 1, Harmon et al. [38] provide data for the strain-rate and temperature-dependent non-Newtonian viscosity $\eta(\dot{\epsilon}, \vartheta)$, which they estimated from their compression experiments on $Pt_{57.5}Ni_{5.3}Cu_{14.7}P_{22.5}$. We have used their data to obtain the material parameters appearing in our constitutive equation (7.9); our curve-fitting procedure yields

$$\begin{aligned} &\dot{\epsilon}_0 = 9.0 \times 10^{11}\,\text{s}^{-1}, \quad \Delta F = 5.47 \times 10^{-20}\,\text{J}, \quad V = 1.28 \times 10^{-28}\,\text{m}^3, \\ &B = 2700\,\text{K}, \qquad\qquad \vartheta_0 = 400\,\text{K}. \end{aligned} \tag{7.12}$$

The quality of the fit of equation (7.9) using the list of parameters (7.12) to the data of Harmon et al. [38] is shown in Fig. 7-2(a,b); the fit is quite reasonable. Figure 7-2(a) shows the viscosity as a function of strain rate for each of the temperatures for which data is reported in Harmon et al. [38], and Fig. 7-2(b) shows the viscosity as a function of temperature for several selected strain rates, where the number of strain rates for which data is plotted has been reduced for clarity. The Newtonian approximation (7.10) is also shown in Fig. 7-2(b) as a dashed line. As is clear from this figure, the model nicely reproduces the important transition of the viscosity from a non-Newtonian response to a Newtonian response at the lowest strain rates as the material goes through the glass transition.

The constitutive theory described in Section 7.2 was implemented in Abaqus/Standard [36] by writing a user-material subroutine (UMAT). This numerical implementation, together with the material parameters for the bulk response of $Pt_{57.5}Cu_{14.7}Ni_{5.3}P_{22.5}$ estimated here, is used in the next section to simulate the surface tension-driven shape-recovery experiments of Kumar and Schroers [37]. These simulations are used to *estimate* a value for the surface tension of this material in the supercooled liquid region.

7.4 Numerical simulations of surface tension-driven shape-recovery

In this section, we present our numerical simulations of surface tension-driven shape-recovery. First, we describe how surface tension boundary conditions are incorporated into our simulations. We then report on our estimate for the surface tension of $Pt_{57.5}Cu_{14.7}Ni_{5.3}P_{22.5}$ in the supercooled liquid region from the shape-recovery data of Kumar and Schroers [37]. Finally, with the material parameters for the underlying elastic-viscoplastic bulk response as well as

[2]Indeed numerical calculations show that the results from our shape-recovery simulations, which use a value for the shear modulus of 10 GPa, are indistinguishable from those which are obtained by using a value of either 3 GPa or 30 GPa.

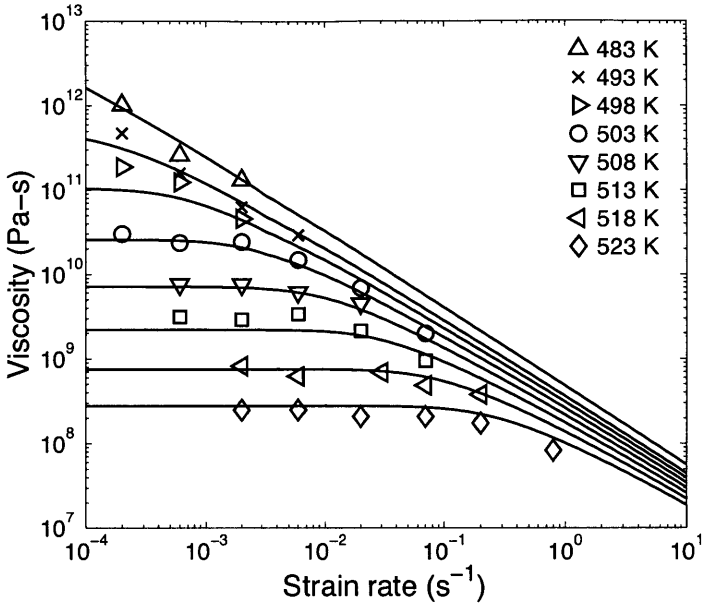

(a)

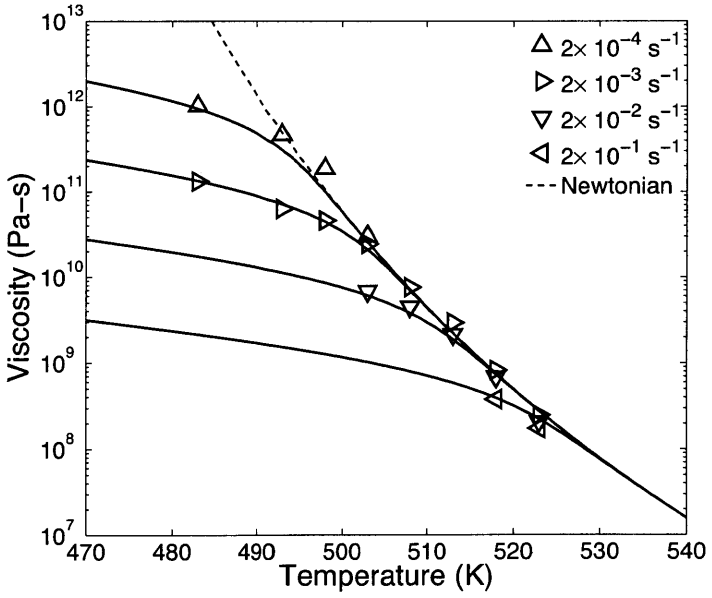

(b)

Figure 7-2: Viscosity (a) as a function of strain rate at various temperatures, and (b) as a function of temperature for several selected strain rates. Points are data from Harmon et al. [38]; lines are the model prediction.

a value for the surface tension of the Pt-based metallic glass fixed, we validate our simulation capability by comparing predictions from our numerical simulations of shape-recovery experiments of Berkovich nanoindents, against corresponding recent experimental results of

Packard et al. [39] who reported shape-recovery data of nanoindents on the same Pt-based metallic glass.

7.4.1 Traction boundary condition for surface tension

Recall that with $\mathbf{T}$ the Cauchy stress and $\mathbf{n}$ the outward unit normal to the boundary of the body, the standard traction boundary condition is of the form

$$\mathbf{T}\mathbf{n} = \hat{\mathbf{t}} \qquad \text{upon} \qquad \mathcal{S}_t, \tag{7.13}$$

with $\hat{\mathbf{t}}$ a given function of $\mathbf{x}$ and t, and where $\mathcal{S}_t$ is the portion of the boundary $\partial\mathcal{B}_t$ of the deformed body where the traction is prescribed. For example, if p is a prescribed scalar field, and if

$$\mathbf{T}\mathbf{n} = -p\,\mathbf{n} \qquad \text{upon} \qquad \mathcal{S}_t, \tag{7.14}$$

then the body is subjected to the *pressure* p upon $\mathcal{S}_t$. An important special kind of pressure is that exerted by *surface tension*. The pressure due to surface tension reflects the nature of the body as well as its shape and nature of its surroundings, and is given by

$$\left.\begin{aligned} &p = 2\gamma\kappa, \\ &\kappa = \text{ mean curvature of } \mathcal{S}_t \text{ at } \mathbf{x}, \\ &\gamma = \text{coefficient of } \textit{surface tension}. \end{aligned}\right\} \tag{7.15}$$

Thus, equation (7.13) may be written as

$$\mathbf{T}\mathbf{n} = -2\gamma\kappa\,\mathbf{n} \qquad \text{upon} \qquad \mathcal{S}_t. \tag{7.16}$$

In our simulations we apply this normal traction to the load integration points on the free surface of the finite element model. This is done by programming an Abaqus/Standard subroutine called a DLOAD that allows for user-defined distributed loads, i.e. normal tractions. The primary tasks then reduce to (i) a calculation of the mean curvature κ, the details of which we relegate to Appendix E; and (ii) an estimation of the surface tension γ. We turn to this latter task in the next section.

7.4.2 Estimate of the surface tension of $Pt_{57.5}Cu_{14.7}Ni_{5.3}P_{22.5}$

Using the independently-determined material parameters for the bulk glass, we have estimated the surface tension of $Pt_{57.5}Ni_{5.3}Cu_{14.7}P_{22.5}$ by carrying out full three-dimensional finite-element simulations of the shape-recovery experiments of Kumar and Schroers [37], and adjusting the value of γ until the simulations are able to reproduce the shape-recovery experimental results reported by these authors.

In their experiments, Kumar and Schroers [37] first indented a Zr-based metallic glass ($Zr_{44}Ti_{11}Cu_{10}Ni_{10}Be_{25}$) substrate with a Vickers pyramidal indenter to three different depths,

and then used the Zr-based glass with the indents as an embossing tool to generate pyramidal-shaped protrusions on the surface of a polished $Pt_{57.5}Cu_{14.7}Ni_{5.3}P_{22.5}$ substrate by hot-embossing at 523 K at an applied pressure of 100 MPa.[3] To create the initial mesh for our shape-recovery simulations we follow a similar path; that is, we first simulate the embossing of the pyramid-shaped microfeatures into the $Pt_{57.5}Cu_{14.7}Ni_{5.3}P_{22.5}$ substrate, which is modeled using 32000 Abaqus-C3D8H elements.[4] Figure 7-3(a,b) shows the final shape after embossing.[5] Specifically, Fig. 7-3(a) shows a three-dimensional perspective view of a pyramidal microfeature and the surrounding material, and Fig. 7-3(b) shows a two dimensional projection of the side view of the domain. The initial height of the microfeature is denoted as h_0, and the surrounding material consists of a square $b \times b$ domain of depth of t. Following the experiments of Kumar and Schroers [37], we consider three different values of the initial height h_0 of the pyramidal microfeatures:

$$4.67\,\mu\text{m}, \qquad 2.86\,\mu\text{m}, \qquad \text{and} \qquad 1.55\,\mu\text{m}.$$

For the 4.67 μm-high microfeature, we employ a base width of $b = 60\,\mu$m and a base depth of $t = 30\,\mu$m. The values of b and t are scaled appropriately for the smaller features.

For the shape-recovery simulations, symmetry boundary conditions were specified on the sides and bottom of the finite element mesh. Specifically, with respect to Fig. 7-3, we set $u_x = 0$ on sides ABCD and EFGH, $u_y = 0$ on the sides BFGC and AEHD, and $u_z = 0$ on the bottom CGHD. On the top surface, we applied the surface tension boundary condition described in the previous subsection. The pyramidal microfeatures of the three initial heights were "numerically annealed" at a temperature of 543 K for 1200 s, and the decay in the height of the pyramids versus annealing time was calculated. Several iterations of these simulations were run to match the corresponding data reported by Kumar and Schroers [37] (their Fig. 3), in order to determine a suitable value for the surface tension. The value that best fit their experimental data was

$$\gamma = 0.19\,\text{N/m}.$$

Figure 7-4 shows the feature height h of each of the three microfeatures as a function of time. The symbols are experimental data from Kumar and Schroers [37], and the dashed lines are the results from our numerical simulations using the independently-determined material parameters for the bulk glass, and the value of the surface tension γ listed above. The quantitative agreement between the simulations and the experimental data is quite good.

Figure 7-5(a) from Kumar and Schroers [37], shows SEM images of the largest pyramidal microfeature ($h_0 = 4.67\,\mu$m) at various times; viz., the initial shape, and after annealing for 60, 300, and 1200 s. Figure 7-5(b) shows corresponding images of the microfeature from our

[3] At this embossing temperature the Zr-based glass is well below its glass transition temperature of 623 K.

[4] This was done primarily to generate a highly-structured initial mesh for our shape-recovery simulations. This affords a more accurate calculation of local curvature than if the surface mesh is unstructured.

[5] A slight rounding of the edges of the pyramidal microfeature was introduced in order to ease the calculation of curvature in the vicinity of these edges.

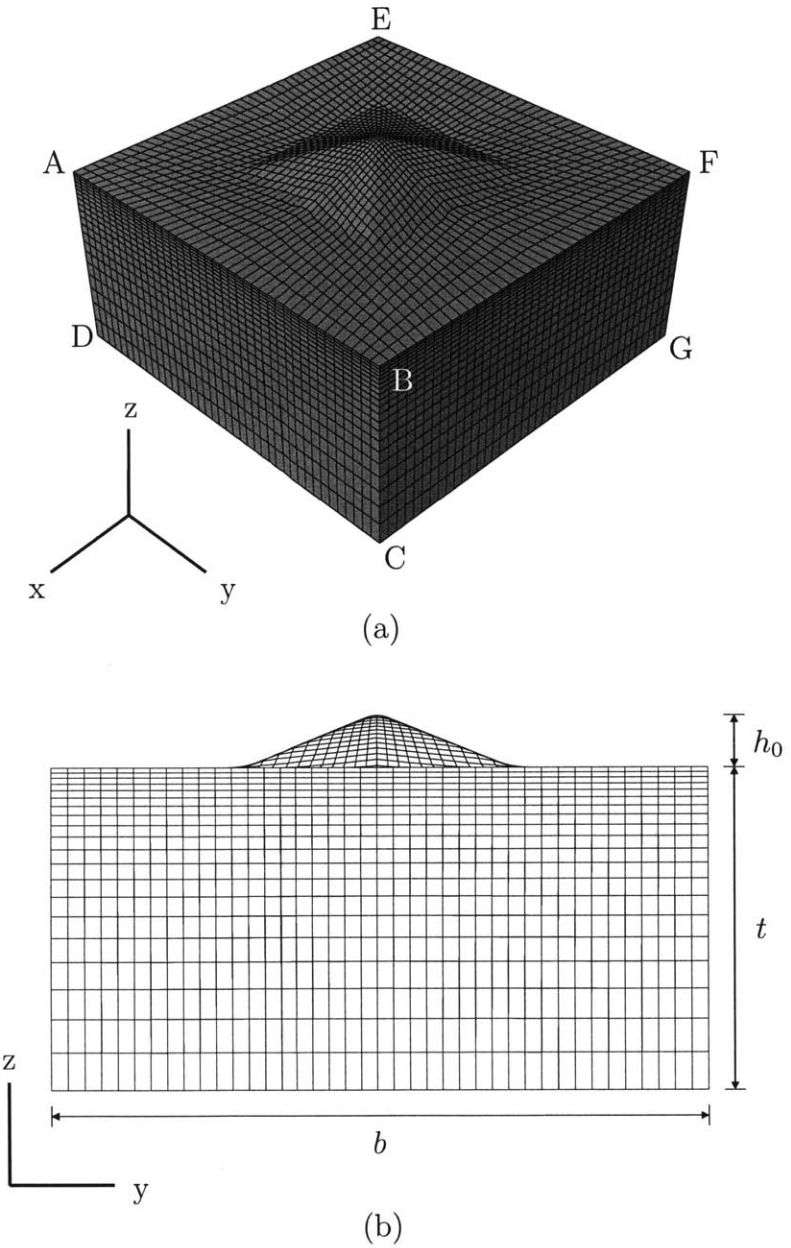

Figure 7-3: Initial finite element mesh configuration for the simulations of the shape-recovery of raised pyramidal microfeatures: (a) a three-dimensional perspective view, and (b) a two-dimensional projection of the side view of the domain.

numerical simulations at the same times. The numerically-calculated evolution of the shape of the microfeature compares favorably with that which is experimentally observed.

Thus, using a calibrated constitutive model for the elastic-viscoplastic response of the bulk material, and our numerical modeling capability for applying surface-tension related traction boundary conditions on free surfaces, one can use three-dimensional finite-element

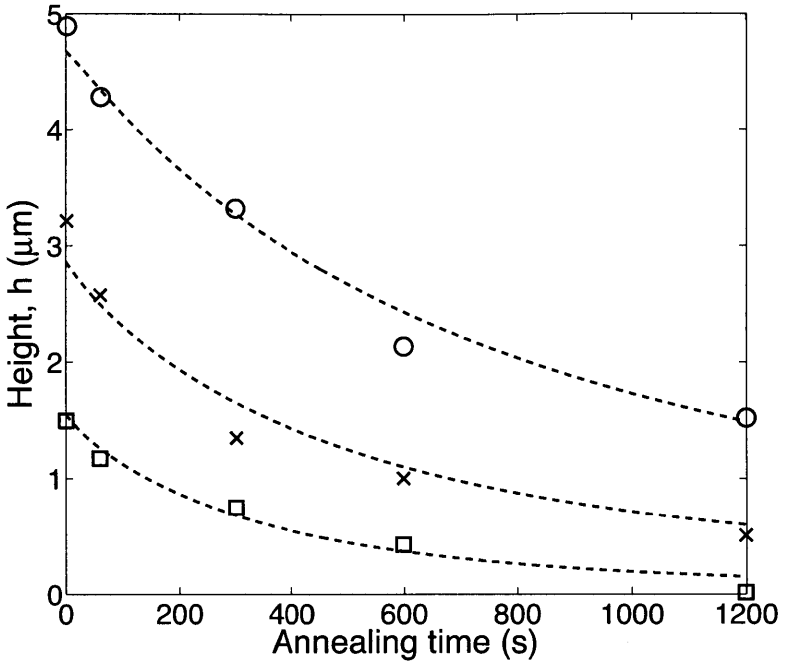

Figure 7-4: Feature height h as a function of annealing time at 543 K for the pyramidal microfeatures of three different initial heights. The symbols are experimental data from Kumar and Schroers [37], and the dashed lines are the results from our numerical simulations.

simulations of shape-recovery to *determine* the surface tension of $Pt_{57.5}Cu_{14.7}Ni_{5.3}P_{22.5}$. The value of surface tension γ so obtained, is expected to be as accurate as the independent experimental measurements of the non-Newtonian viscosity and the shape-recovery response.

7.4.3 Validation of the simulation capability

Here we report on our study to validate our simulation capability. Specifically, we compare predictions from our numerical simulations of shape-recovery experiments of Berkovich nanoindents, against corresponding recent experimental results of Packard et al. [39] who reported shape-recovery data of nanoindents on the same Pt-based metallic glass.

As in the previous section, the initial mesh was obtained by first simulating the indentation of a $Pt_{57.5}Cu_{14.7}Ni_{5.3}P_{22.5}$ substrate with a Berkovich tip. As before, the metallic glass substrate was modeled using 32000 Abaqus-C3D8H elements. Figure 7-6(a,b) shows the final shape after indentation which is used as the initial mesh for our shape-recovery simulations. Figure 7-6(a) shows a three-dimensional perspective view of the residual Berkovich indent and the surrounding material, and Fig. 7-6(b) shows a two-dimensional projection of the side view of the domain. The initial depth of the residual indent is denoted as h_0, and the surrounding material consists of a square $b \times b$ domain with a depth of t. Following the experiments of Packard et al. [39], we consider different values of the initial depth h_0 of the

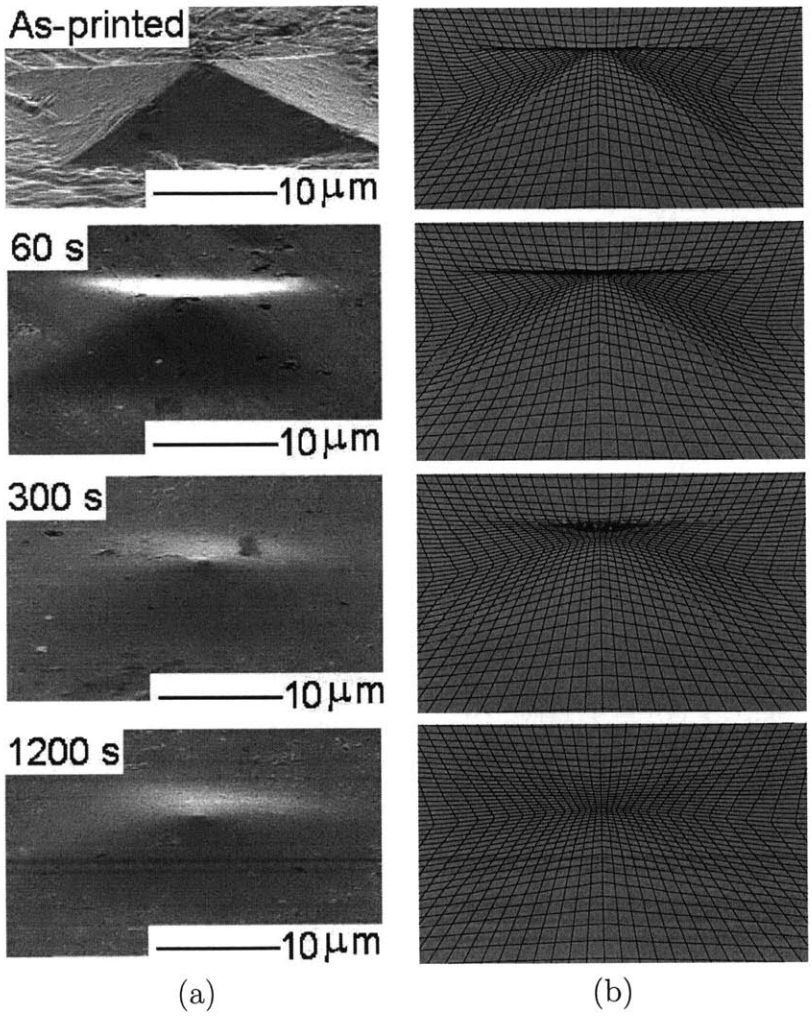

Figure 7-5: (a) SEM micrographs (from Kumar and Schroers [37]) and (b) corresponding numerical predictions of the largest pyramidal feature ($h_0 = 4.67\,\mu$m) after annealing at 543 K for 60, 300, and 1200 s.

indent:

$$264\,\text{nm}, \quad 180\,\text{nm}, \quad \text{and} \quad 146\,\text{nm}.$$

For the 264 nm-high microfeature, we employ a base width of $b = 5\,\mu$m and a base depth of $t = 2.5\,\mu$m. The values of b and t are scaled appropriately for the smaller features.

For the recovery simulations, symmetry boundary conditions were specified on the sides and bottom of the finite element mesh. Specifically, with respect to Fig. 7-6, we prescribed $u_x = 0$ on sides ABCD and EFGH, $u_y = 0$ on the sides BFGC and AEHD, and $u_z = 0$ on the bottom CGHD. On the top free surface, we applied the surface tension boundary condition described previously. The indented specimens of initial heights $h_0 = 264$ nm and $h_0 = 180$ nm were "numerically annealed" at a temperature of 523 K for 3600 s, and the indented specimen

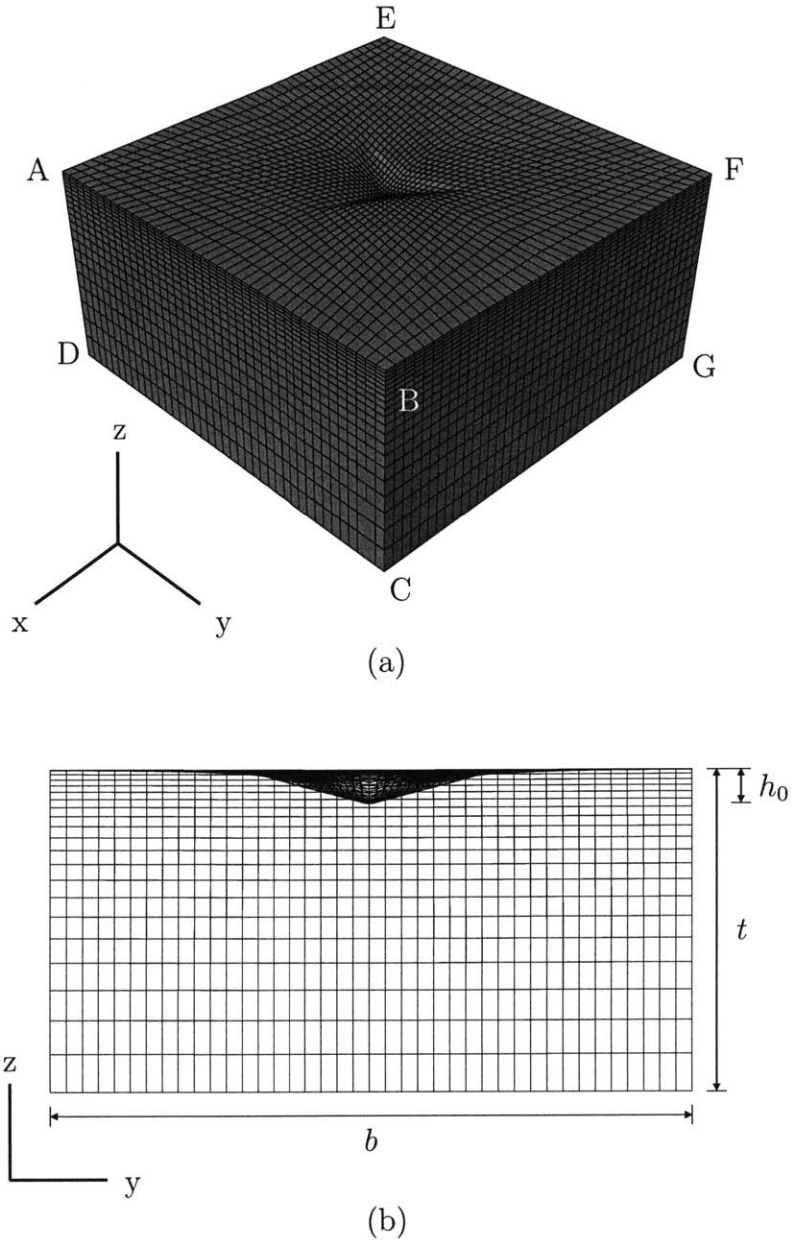

Figure 7-6: Initial finite element mesh configuration for the simulations of the shape-recovery of residual Berkovich indents, including (a) a three-dimensional perspective view and (b) a two-dimensional projection of the side view of the domain.

of initial height $h_0 = 146\,\text{nm}$ was "annealed" at 513 K for 3600 s. Figure 7-7(a,b) shows the indent depth h as a function of annealing time for the indents annealed at 523 K and 513 K,

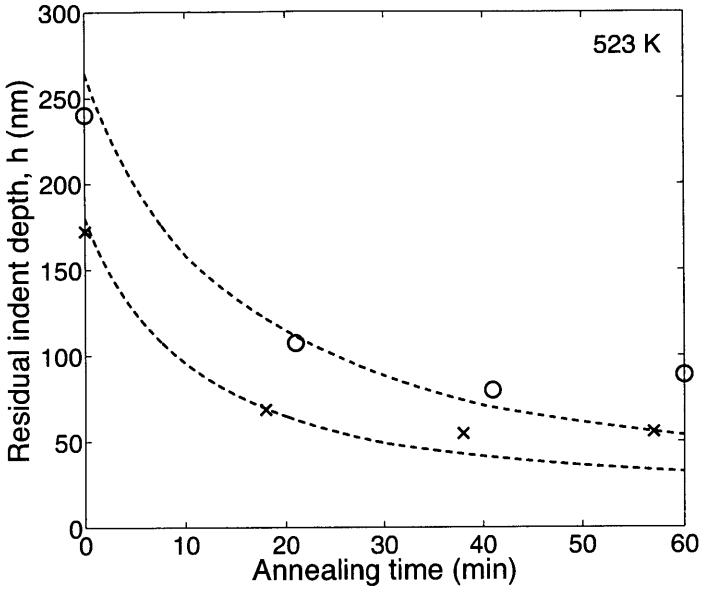

(a)

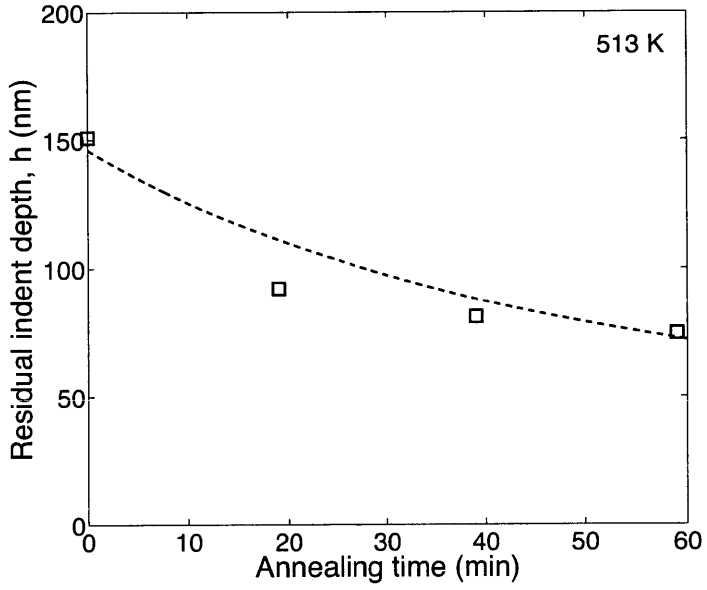

(b)

Figure 7-7: Residual indent depth h as a function of annealing time for residual Berkovich indents annealed (a) 523 K and (b) 513 K. The symbols are experimental data from Packard et al. [39], and the dashed lines are the results from our simulations.

respectively, along with the corresponding experimental measurement by Packard et al. [39]. The agreement between the simulations and the experimental data is quite reasonable.[6]

[6]The simulations and the experimental data differ at the longest annealing times at 523 K; this is likely due to the experimental difficulties in measuring feature depths below 100 nm at elevated temperatures.

Figure 7-8(a) from Packard et al. [39] shows topographic contour plots of the largest residual Berkovich indent (h_0=264 nm) annealed at 523 K at various times, viz., the initial shape, and after annealing for 20 minutes, 30 minutes, and 60 minutes. Figure 7-8(b) shows corresponding topographic contour plots of the residual indent from our simulation.[7] The numerically-calculated shape-recovery of the indent compares favorably with that which is experimentally observed.

Thus, using the value of surface tension determined in the previous section for the annealing of *micron-sized* four-sided pyramidal protrusions at 543 K, one can reasonably accurately predict the shape-recovery behavior of *nanometer-sized* three-sided Berkovich indents in $Pt_{57.5}Cu_{14.7}Ni_{5.3}P_{22.5}$ at annealing temperatures of 523K and 513K. This indicates that the value of the surface tension $\gamma = 0.19$ N/m over this 30 degree temperature range may be considered to be essentially constant.

7.4.4 Scaling considerations for the shape-recovery process

The relevant physical quantities related to the shape-recovery response at a *fixed* temperature include characteristic initial and final geometrical "length" scales associated with the microstructural features, the material properties, and the annealing time t. The relevant material properties are the Newtonian viscosity η and the surface tension γ at the given temperature. For microstructural features such as pyramidal protrusions or Berkovich indents, in which the initial and recovering protrusions (indents) are geometrically self-similar, the characteristic dimensions are the initial and evolving heights (depths) h_0 and h, respectively.[8] For such problems the relevant physical parameters are

$$(h_0, h, \eta, \gamma, t).$$

From these five quantities it is possible to form two dimensionless groups,

$$\frac{h}{h_0} \quad \text{and} \quad \frac{\gamma t}{\eta h_0}, \tag{7.17}$$

and presume that the recovery response scales as

$$\frac{h}{h_0} = F\left(\frac{\gamma t}{\eta h_0}\right), \tag{7.18}$$

where the function F is the shape-recovery response function for *a given pyramidal geometry.*

In order to evaluate whether this scaling argument holds, we plot in Fig. 7-9(a) the shape-recovery data of Kumar and Schroers [37] for the four-sided pyramidal protrusions of three initial heights annealed at 543 K, along with our corresponding simulations (shown

[7]The color scale bars in Figs. 7-8(a) and (b) are not exactly the same, but are close enough to allow for a qualitative comparison between the simulations and the experiments.

[8]To fully specify the geometry, additional dimensionless quantities are needed, such as the included angle for a conical or pyramidal geometry.

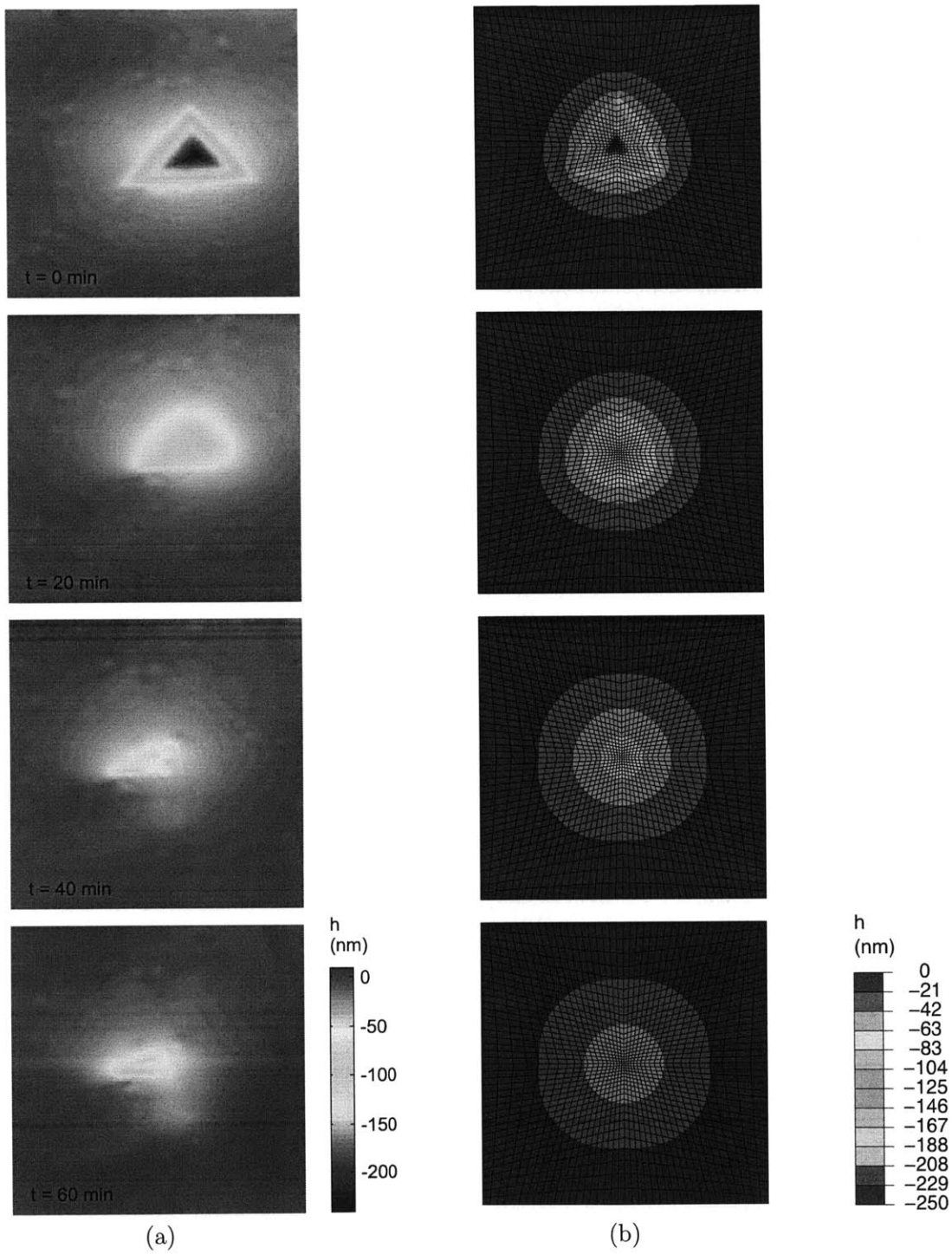

Figure 7-8: (a) Experimentally-measured topographic contour plots (from Packard et al. [39]) and (b) corresponding simulated contour plots of the largest residual Berkovich indent ($h_0 = 264\,\text{nm}$) after annealing at 523 K for 20, 40 and 60 minutes.

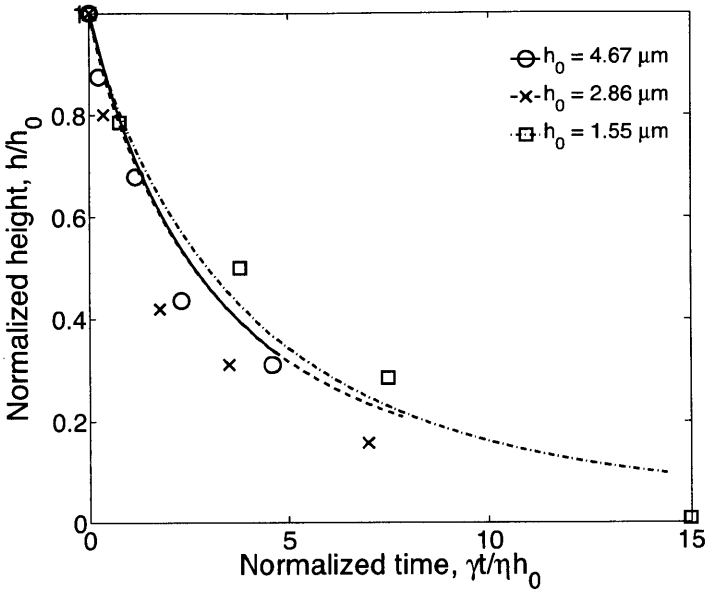

(a)

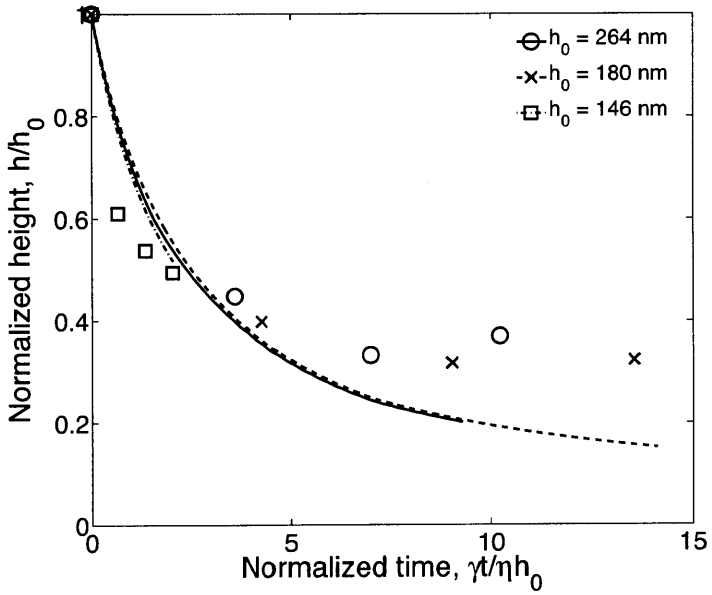

(b)

Figure 7-9: Normalized feature height h/h_0 as a function of normalized annealing time $\gamma t/\eta h_0$ for (a) pyramidal microfeatures annealed at 543 K and (b) residual Berkovich indents annealed 523 K and 513 K. The results from the numerical simulations are shown as dashed lines.

as dashed lines), in the normalized coordinates (7.17). In plotting these results we used $\eta(\vartheta = 543\,\mathrm{K}) = 1.02 \times 10^7\,\mathrm{Pa\text{-}s}$, $\gamma = 0.19\,\mathrm{N/m}$, and the appropriate values for h_0. The

experimental data and numerical simulation results essentially collapse to a single trend-line, confirming our scaling argument.[9]

Figure 7-9(b) shows the the recovery data of Packard et al. [39] for the three-sided Berkovich indents of three initial heights annealed at 523 K or 513 K, along with the corresponding simulations. In plotting these results we used $\eta(\vartheta = 523\,\mathrm{K}) = 2.78 \times 10^8$ Pa-s, $\eta(\vartheta = 513\,\mathrm{K}) = 2.21 \times 10^9$ Pa-s, $\gamma = 0.19\,\mathrm{N/m}$, and the appropriate values for h_0. As in Fig. 7-9(a) for the pyramidal protrusions, a similar reduction to a single trend-line is observed here for the recovery of the Berkovich indents.

Thus, if the shape-recovery response F for a given self-similar geometric feature is calculated or measured, the recovery for another initial geometry or recovery at another temperature my be estimated, as long as the surface tension and the Newtonian viscosity as a function of temperature is known.[10]

7.5 Concluding remarks

By integrating (i) a reasonably simple elastic-viscoplasticity theory for metallic glasses in the supercooled liquid state above the glass transition temperature, and (ii) a new methodology to numerically account for surface-tension effects, we have developed a computational capability which when coupled with (a) a knowledge of the elastic-viscoplastic response of the bulk glass from compression experiments, and (b) shape-recovery experiments of micro/nanoscale surface features on the metallic glass in its supercooled liquid region, may be used to *determine* the surface tension of the glass at the temperature at which the recovery experiment is conducted. We have demonstrated the use of this procedure to determine that the surface tension of $Pt_{57.5}Cu_{14.7}Ni_{5.3}P_{22.5}$ at 543 K is $\gamma = 0.19\,\mathrm{N/m}$, and we have shown that this value of γ may be considered to be essentially constant over a temperature range of 30 degrees from 543 K to 513 K. The numerical simulation capability presented in this paper provides a basis for further simulation-based studies of surface tension-driven shape-recovery of arbitrarily shaped micro/nano-dimensioned surface features (not just pyramidal protrusions or intrusions!) on metallic glasses in the supercooled liquid region. Also, in conjunction with hot-nanoindentation, the phenomenon of surface tension-driven shape-recovery may prove to be an attractive basis for ultrahigh density re-writable data storage.

[9]The small differences in the numerically calculated curves may be attributed to different values of the normalized time step $\gamma\Delta t/\eta h_0$ used in the different simulations.

[10]Particular scaling functions F for Vickers pyramids and Berkovich indents may be sought by non-linear curve-fitting of the data in Fig. 7-9(a,b); however, we refrain from doing so here.

Chapter 8

Conclusion

8.1 Summary

Scientifically, metallic glasses are a very interesting class of relatively-new structural materials. They offer the remarkable combination of the ability to precisely form complex geometries through thermoplastic forming and superior structural properties. Consequently, they have potential for numerous applications, especially at the micro/nano-scale. Understanding the mechanics of this class of materials is crucial as their usage grows. This work has addressed several outstanding questions related to the elasticity, inelasticity, and fracture of metallic glasses. To conclude, we briefly summarize the main contributions of this thesis.

- Based on molecular dynamics simulations of a metallic glass, we have developed a continuum-level, finite-deformation isotropic elastic free energy that accounts for volumetric-deviatoric coupling under circumstances involving large volumetric strains.

- We have introduced a cavitation mechanism to our large-deformation, elastic-plastic constitutive theory for metallic glasses at low homologous temperatures that accounts for important experimentally-observed features of brittle fracture of metallic glasses at notches.

- We have formulated a constitutive theory for metallic glasses in a temperature range spanning the glass transition. The theory has been implemented in a finite element program, and the numerical simulation capability has been used to determine appropriate processing parameters for a representative micro-hot-embossing procedure.

- We have produced a metallic glass polymer-embossing tool via thermoplastic forming, which has a microchannel pattern for a simple microfluidic device. The metallic glass tool was found to be very robust, and it was used to produce hundreds of high-fidelity micron-scale embossed patterns without degradation or failure.

- We have developed a numerical simulation capability for surface tension-driven shape-recovery of metallic glasses and used this capability to quantitatively determine the surface tension of a Pt-based metallic glass in the supercooled liquid region.

8.2 Outlook

While much has been accomplished, more remains to be done. Some outstanding issues are discussed below.

- Further scale-bridging work is needed to connect continuum-level theories for metallic glasses with knowledge of the physical processes of deformation. Specifically, further work is needed in (i) justifying the direction of plastic flow in the Mohr-Coulomb-based theory of Chapter 3 and (ii) connecting observations of structure from molecular dynamics simulations with structural internal variables in continuum-level theories.

  (i) The specification of the direction of plastic flow is a crucial aspect of a constitutive theory for inelasticity, and since metallic glasses are frictional, plastically-dilatant materials, this aspect requires special attention. The theory of Chapter 3 employs a Mohr-Coulomb-based flow rule to determine the direction of plastic flow, as opposed to a simpler Drucker-Prager flow rule. This flow rule is capable of accurately describing shear band patterns in inhomogeneous loading conditions, but further atomistic study is needed to justify this type of flow rule under various stress states.

  (ii) The recent review by Cheng and Ma [16] details aspects of structure in a variety of metallic glass alloys through molecular dynamics simulations, addressing atomic packing and short-range-order and their effect on mechanical properties. To connect this knowledge with continuum-level theories, quantitative aspects of ordering in metallic glasses must be linked to structural internal variables, such as φ in the current work. Atomistic simulations may also be able to inform specific evolution equations for structural internal variables and how they depend stress-state.

- The failure and fracture of metallic glasses is a fertile area for research. The cavitation model proposed in Chapter 4 is a simple method for modeling brittle fracture phenomena in metallic glasses; however, much work needs to be done to more completely understand and describe fracture mechanisms in these materials. Specifically, more effort is needed pertaining to (i) ductile fracture in these materials and (ii) the role of defects in both brittle and ductile fracture phenomena.

  (i) Under shear-dominated conditions, when the local hydrostatic tensions are not sufficiently elevated, fracture in metallic glasses initiates in well-developed shear bands instead of by the cavitation mechanism discussed in Chapter 4. The mathematical modeling of the transition from deformation fields involving intense shear

strains in narrow bands, to jump discontinuities in tangential displacements across surfaces, and eventual fracture, especially when the shear-banded plastic zone is constrained within a large elastic region, is non-trivial. It is not clear what is the most effective continuum-level technique, i.e. damage models, cohesive zone models, etc., for modeling fracture in shear bands that form in arbitrarily-loaded bodies, and more attention is needed to this subject.

(ii) Initiation of cavitation in brittle fracture and the initiation of a shear bands in ductile fracture are expected to significantly influenced by the presence of defects. Defects that initiate failure in metallic glasses do not just include inclusions or voids but more often are related to structural fluctuations and heterogeneity. This atomic-level variation in structure lead to fluctuations in mechanical properties, such as stiffness and strength. The more rigid regions form a backbone that supports the weaker, less stable zones, which may be thought of as a type of inclusion. As shear deformation is applied, these less stable regions deform inelastically first, and eventually, they coalesce to form a coherent shear band. One would also expect these unstable regions to serve as initiation sites for cavitation, which leads to brittle failure, but this is undocumented at present. Further research is needed to understand these processes and incorporate them into a continuum-level theory to model both ductile and brittle failure of metallic glasses

- Our constitutive theories do not contain any intrinsic material length-scale. Thus, they are unable to model the widths of localized shear bands or damage zones. In order to describe shear banding and failure in metallic glasses, it is necessary to extend our theory to account for material length-scale phenomena to control the widths of shear bands and damage zones. However, it is important to note that the physical origins of "gradient effects" in metallic glasses are not clear and need further study.

- Finally, the specialized constitutive equations presented in this work are intended either for low homologous temperatures or a temperature range spanning the glass transition. In order to apply the theory to situations involving both of these temperature ranges, the specialized equations need to be modified to smoothly transition from one temperature range to the other. A specialized theory of this type is needed to model the full thermoplastic forming process cycle including heating up and cooling down as well as for situations in which heat dissipation due to plastic flow is important, such as in shear bands.

Bibliography

[1] W. Klement, R. H. Willens, and P. Duwez. Non-crystalline structure in solidified gold-silicon alloys. *Nature*, 187:869–870, 1960.

[2] A. Inoue. Stabilization of metallic supercooled liquid and bulk amorphous alloys. *Acta Materialia*, 48:279–306, 2000.

[3] W. L. Johnson. Bulk amorphous metal – an emerging engineering material. *JOM*, 54: 40–43, 2002.

[4] W. L. Johnson. Bulk glass-forming metallic alloys: Science and technology. *MRS Bulletin*, 24:42–56, 1999.

[5] C. A. Schuh, T. C. Hufnagel, and U. Ramamurty. Mechanical behavior of amorphous alloys. *Acta Materialia*, 55:4067–4109, 2007.

[6] F. Spaepen. A microscopic mechanism for steady state inhomogeneous flow in metallic glasses. *Acta Metallurgica*, 25:407–415, 1977.

[7] A. S. Argon. Plastic deformation in metallic glasses. *Acta Metallurgica*, 27:47–58, 1979.

[8] P. E. Donovan. Compressive deformation of amorphous $Pd_{40}Ni_{40}P_{20}$. *Materials Science and Engineering*, 98:487–490, 1988.

[9] P. E. Donovan. A yield criterion for $Pd_{40}Ni_{40}P_{20}$ metallic glass. *Acta Metallurgica*, 37: 445–456, 1989.

[10] D. Deng, A. S. Argon, and S. Yip. Simulation of plastic deformation in a two-dimensional atomic glass by molecular dynamics IV. *Philosophical Transactions of the Royal Society of London. Series A, Mathematical and Physical Sciences*, 329:613–640, 1989.

[11] M. L. Falk and J. S. Langer. Dynamics of viscoplastic deformation in amorphous solids. *Physical Review E*, 57:7192–7205, 1998.

[12] J. Lu, G. Ravichandran, and W. L. Johnson. Deformation behavior of the $Zr_{41.2}Ti_{13.8}Cu_{12.5}Ni_{10.0}Be_{22.5}$ bulk metallic glass over a wide range of strain-rates and temperatures. *Acta Materialia*, 51:3429–3443, 2003.

[13] A. S. Argon and M. J. Demkowicz. Atomistic simulation and analysis of plasticity in amorphous silicon. *Philosophical Magazine*, 86:4153–4172, 2006.

[14] N. P. Bailey, J. Schiotz, and K. W. Jacobsen. Atomistic simulation study of the shear-band deformation mechanism in Mg-Cu metallic glasses. *Physical Review B*, 73:064108, 2006.

[15] Y. F. Shi and M. L. Falk. Atomic-scale simulations of strain localization in three-dimensional model amorphous solids. *Physical Review B*, 73:214201, 2006.

[16] Y. Q. Cheng and E. Ma. Atomic-level structure and structure-property relationship in metallic glasses. *Progress in Materials Science*, 56:379–473, 2011.

[17] O. Reynolds. On the dilatancy of media composed of rigid particles in contact. *Philosophical Magazine*, 20:469–481, 1885.

[18] J. Li, F. Spaepen, and T. C. Hufnagel. Nanometre-scale defects in shear bands in a metallic glass. *Philosophical Magazine A*, 82:2623–2630, 2002.

[19] J. Schroers. The superplastic forming of bulk metallic glasses. *JOM*, 57:35–39, 2005.

[20] Y. Saotome, S. Miwa, T. Zhang, and A. Inoue. The micro-formability of Zr-based amorphous alloys in the supercooled liquid state and their application to micro-dies. *Journal of Materials Processing Technology*, 113:64–69, 2001.

[21] Y. Saotome, K. Itoh, T. Zhang, and A. Inoue. Superplastic nanoforming of Pd-based amorphous alloys. *Scripta Materialia*, 44:1541–1545, 2001.

[22] Y. Saotome, K. Imai, S. Shioda, S. Shimizu, and A. Inoue. The micro-nanoformability of Pt-based metallic glass and the nanoforming of three-dimensional structures. *Intermetallics*, 10:1241–1247, 2002.

[23] Y. Saotome, Y. Noguchi, T. Zhang, and A. Inoue. Characteristic behavior of Pt-based metallic glass under rapid heating and its application to microforming. *Materials Science and Engineering A*, 375–377:389–393, 2004.

[24] J. Schroers, Q. Pham, and A. Desai. Thermoplastic forming of bulk metallic glass – a technology for mems and microstructure fabrication. *Journal of Microelectromechanical Systems*, 16:240–247, 2007.

[25] L. Anand. On H. Hencky's approximate strain-energy function for moderate deformations. *Journal of Applied Mechanics*, 46:78–82, 1979.

[26] L. Anand. Moderate deformations in extension-torsion of incompressible isotropic elastic materials. *Journal of the Mechanics and Physics of Solids*, 34:293–304, 1986.

[27] H. Hencky. Über die form des elastizitätsgesetzes bei ideal elastischen stoffen. *Zeitschrift für technische Physik*, 9:215–223, 1928.

[28] H. Hencky. The law of elasticity for isotropic and quasi-isotropic substances by finite deformations. *Journal of Rheology*, 2:169–176, 1931.

[29] H. Hencky. The elastic behavior of vulcanised rubber. *Rubber Chemistry and Technology*, 6:217–224, 1933.

[30] P. Lowhaphandu and J. J. Lewandowski. Fracture toughness and notched toughness of bulk amorphous alloy: Zr-Ti-Ni-Cu-Be. *Scripta Materialia*, 38:1811–1817, 1998.

[31] J. J. Lewandowski, M. Shazly, and A. S. Nouri. Intrinsic and extrinsic toughening of metallic glasses. *Scripta Materialia*, 54:337–341, 2006.

[32] K. M. Flores and R. H. Dauskardt. Mean stress effects on flow localization and failure in a bulk metallic glass. *Acta Materialia*, 49:2527–2537, 2001.

[33] J. J. Lewandowski, W. H. Wang, and A. L. Greer. Intrinsic plasticity or brittleness of metallic glasses. *Philosophical Magazine Letters*, 85:77–87, 2005.

[34] L. Anand and C. Su. A theory for amorphous viscoplastic materials undergoing finite deformations, with application to metallic glasses. *Journal of the Mechanics and Physics of Solids*, 53:1362–1396, 2005.

[35] C. Su and L. Anand. Plane strain indentation of a Zr-based metallic glass: Experiments and numerical simulation. *Acta Materialia*, 54:179–189, 2006.

[36] Abaqus, 2008. Reference manuals.

[37] G. Kumar and J. Schroers. Write and erase mechanisms for bulk metallic glass. *Applied Physics Letters*, 92:031901, 2008.

[38] J. S. Harmon, M. D. Demetriou, and W. L. Johnson. Rheology and ultrasonic properties of $Pt_{57.5}Ni_{5.3}Cu_{14.7}P_{22.5}$ liquid. *Applied Physics Letters*, 90:171923, 2007.

[39] C. E. Packard, J. Schroers, and C. A. Schuh. In situ measurements of surface tension-driven shape-recovery in a metallic glass. *Scripta Materialia*, 60:1145–1148, 2009.

[40] M. E. Gurtin, E. Fried, and L. Anand. *The Mechanics and Thermodynamics of Continua*. Cambridge University Press, New York, 2010.

[41] J. H. Rose, J. R. Smith, and J. Ferrante. Universal features of bonding in metals. *Physical Review B*, 28:1835–1845, 1983.

[42] B. P. Gearing and L. Anand. Notch-sensitive fracture of polycarbonate. *International Journal of Solids and Structures*, 41:827–845, 2004.

[43] R. G. Veprek, D. M. Parks, A. S. Argon, and S. Veprek. Erratum to "non-linear finite element constitutive modeling of mechanical properties of hard and superhard materials studied by indentation". *Materials Science and Engineering A*, 448:366–378, 2007.

[44] F. D. Stacey and P. M. Davis. High pressure equations of state with applications to the lower mantle and core. *Physics of the Earth and Planetary Interiors*, 142:137–184, 2004.

[45] D. Frenkel and B. Smit. *Understanding Molecular Simulation, Second Edition: From Algorithms to Applications.* Academic Press, Boston, 2002.

[46] A. J. Cao, Y. Q. Cheng, and E. Ma. Structural processes that initiate shear localization in metallic glass. *Acta Materialia*, 57:5146–5155, 2009.

[47] Y. Q. Cheng, H. W. Sheng, and E. Ma. Atomic level structure in multicomponent bulk metallic glass. *Physical Review Letters*, 102:245501, 2009.

[48] B. A. Remington, P. Allen, E. M. Bringa, J. Hawreliak, D. Ho, K. T. Lorenz, H. Lorenzana, J. M. McNaney, M. A. Meyers, S. W. Pollaine, K. Rosolankova, B. Sadik, M. S. Schneider, D. Swift, J. Wark, and B. Yaakobi. Material dynamics under extreme conditions of pressure and strain rate. *Materials Science and Technology*, 22:474–488, 2006.

[49] J.-P. Poirier and A. Tarantola. A logarithmic equation of state. *Physics of the Earth and Planetary Interiors*, 109:1–8, 1998.

[50] F. Birch. Elasticity and constitution of the earth interior. *Journal of Geophysical Research*, 57:227–286, 1952.

[51] P. E. Donovan. Plastic-flow and fracture of $Pd_{40}Ni_{40}P_{20}$ metallic glass under an indentor. *Journal of Materials Science*, 24:523–535, 1989.

[52] H. A. Bruck, T. Christman, A. J. Rosakis, and W. L. Johnson. Quasi-static constitutive behavior of $Zr_{41.2}Ti_{13.8}Cu_{12.5}Ni_{10.0}Be_{22.5}$ bulk amorphous alloys. *Scripta Materialia*, 30: 429–434, 1993.

[53] J. J. Lewandowski and P. Lowhaphandu. Effects of hydrostatic pressure on the flow and fracture of a bulk amorphous metal. *Philosophical Magazine A*, 82:3427–3441, 2002.

[54] C. A. Coulomb. Sur une application des regles de maximis et minimis à quelques problèmes de statistique relatifs a l'architecture. *Académie Royale des Sciences Mémoires de Mathématique et de Physique par Divers Savants*, 7:343–382, 1773.

[55] O. Mohr. Welche umstände bedingen die elastizitätsgrenze und den brusch eines materials. *Zeitschrift des Vereines Deutscher Ingenieure*, 44:1524–1530, 1900.

[56] A. J. M. Spencer. A theory of the knematics of ideal soils under plane strain conditions. *Journal of the Mechanics and Physics of Solids*, 12:337–351, 1964.

[57] A. J. M. Spencer. Deformation of ideal granular materials. In H. G. Hopkins and M. G. Sewell, editors, *Mechanics of Solids*, pages 607–652, Oxford and New York, 1982. Pergamon Press.

[58] M. M. Mehrabadi and S. C. Cowin. Initial planar deformation of dilatant granular materials. *Journal of the Mechanics and Physics of Solids*, 26:269–284, 1978.

[59] S. Nemat-Nasser, M. M. Mehrabadi, and T. Iwakuma. On certain macroscopic and microscopic aspects of plastic flow of ductile materials. In S. Nemat-Nasser, editor, *Three-dimensional Constitutive Relations and Ductile Fracture*, pages 157–172, Amsterdam, 1981. North-Holland Publishing Co.

[60] L. Anand. Plane deformations of ideal granular materials. *Journal of the Mechanics and Physics of Solids*, 31:105–122, 1983.

[61] L. Anand and C. Gu. Granular materials: constitutive equations and strain localization. *Journal of the Mechanics and Physics of Solids*, 48:1701–1733, 2000.

[62] M. H. Cohen and G. S. Grest. Liquid-glass transition, a free-volume approach. *Physical Review B*, 20:1077–1098, 1979.

[63] P. de Hey, J. Sietsma, and A. van den Beukel. Structural disordering in amorphous $Pd_{40}Ni_{40}P_{20}$ induced by high temperature deformation. *Acta Materialia*, 46:5873–5882, 1998.

[64] C. J. Gilbert, R. O. Ritchie, and W. L. Johnson. Fracture toughness and fatigue-crack propagation in a Zr-Ti-Ni-Cu-Be bulk metallic glass. *Applied Physics Letters*, 71:476–478, 1997.

[65] R. D. Conner, A. J. Rosakis, W. L. Johnson, and D. M. Owen. Fracture toughness determination for a beryllium-bearing bulk metallic glass. *Scripta Materialia*, 37:1373–1378, 1997.

[66] M. E. Launey, R. Busch, and J. J. Kruzic. Influence of structural relaxation on the fatigue behavior of a $Zr_{41.25}Ti_{13.75}Ni_{10}Cu_{12.5}Be_{22.5}$ bulk amorphous alloy. *Scripta Materialia*, 54:483–487, 2006.

[67] P. Tandaiya, U. Ramamurty, G. Ravichandran, and R. Narasimhan. Effect of Poisson's ratio on crack tip fields and fracture behavior of metallic glasses. *Acta Materialia*, 56: 6077–6086, 2008.

[68] H. Gao and P. Klein. Numerical simulation of crack growth in an isotropic solid with randomized internal cohesive bonds. *Journal of the Mechanics and Physics of Solids*, 46:187–218, 1998.

[69] F. G. Emmerich. Tensile strength and fracture toughness of brittle materials. *Journal of Applied Physics*, 102:073504, 2007.

[70] K. Y. Volokh. Nonlinear elasticity for modeling fracture of isotropic brittle solids. *Journal of Applied Mechanics*, 71:141–143, 2004.

[71] K. Y. Volokh and P. Trapper. Fracture toughness from the standpoint of softening hyperelasticity. *Journal of the Mechanics and Physics of Solids*, 56:2459–2472, 2008.

[72] C. E. Inglis. Stresses in a plate due to the presence of cracks and sharp corners. *Transactions of the Institute of Naval Architects*, 55:219–230, 1913.

[73] B. Gun, K. J. Laws, and M. Ferry. Superplastic flow of a Mg-based bulk metallic glass in the supercooled liquid region. *Journal of Non-crystalline Solids*, 352:3896–3902, 2006.

[74] Q. Yang, A. Mota, and M. Ortiz. A finite-deformation constitutive model of bulk metallic glass plasticity. *Computational Mechanics*, 37:194–204, 2006.

[75] P. Thamburaja and R. Ekambaram. Coupled thermo-mechanical modelling of bulk-metallic glasses: Theory, finite-element simulations and experimental verification. *Journal of the Mechanics and Physics of Solids*, 55:1236–1273, 2007.

[76] H. S. Kim, H. Kato, A. Inoue, and H. S. Chen. Finite element analysis of compressive deformation of bulk metallic glasses. *Acta Materialia*, 52:3813–3823, 2004.

[77] L. Anand and C. Su. A constitutive theory for metallic glasses at high homologous temperatures. *Acta Materialia*, 55:3735–3747, 2007.

[78] H. Vogel. Das temperaturabhängigkeitsgesetz der viskosität von flüssigkeiten. *Physikalische Zeitschrift*, 22:645–646, 1921.

[79] G. S. Fulcher. Analysis of recent measurements of the viscosity of glasses. *Journal of the American Ceramic Society*, 8:339–355, 1925.

[80] V. G. Tammann and W. Hesse. Die abhängigkeit der viscosität von der temperatur bei unterkühlten flüssigkeiten. *Zeitschrift für anorganische und allgemeine Chemie*, 156: 245–257, 1926.

[81] L. Anand and M. E. Gurtin. A theory of amorphous solids undergoing large deformations, with application to polymeric glasses. *International Journal of Solids and Structures*, 40:1465–1487, 2003.

[82] A. Masuhr, T. A. Waniuk, R. Busch, and W. L. Johnson. Time scales for viscous flow, atomic transport, and crystallization in the liquid and supercooled liquid states of $Zr_{41.2}Ti_{13.8}Cu_{12.5}Ni_{10}Be_{22.5}$. *Physical Review Letters*, 82:2290–2293, 1999.

[83] G. S. Grest and M. H. Cohen. Liquids, glasses and the glass transition: a free-volume approach. In I. Prigogine and S. A. Rice, editors, *Advances in Chemical Physics, Volume 48*, pages 455–525, Hoboken, NJ, 1981. John Wiley & Sons, Inc.

[84] R. B. Dupaix and M. C. Boyce. Constitutive modeling of the finite strain behavior of amorphous polymers in and above the glass transition. *Mechanics and Materials*, 39: 39–52, 2007.

[85] C. H. Tsau, C. C. Wu, and S. S. Wu. The thermal stability and mechanical behaviors of Zr-Cu-Ni-Ti-Be bulk metallic glasses. *Journal of Materials Processing Technology*, 182:257–261, 2007.

[86] H. Becker and C. Gärtner. Polymer microfabrication technologies for microfluidic systems. *Analytical and Bioanalytical Chemistry*, 390:89–111, 2008.

[87] G. Duan, A. Wiest, M. L. Lind, J. Li, W. K. Rhim, and W. L. Johnson. Bulk metallic glass with benchmark thermoplastic processability. *Advanced Materials*, 19:4272–4275, 2007.

[88] J. Schroers. On the formability of bulk metallic glass in its supercooled liquid state. *Acta Materialia*, 56:471–478, 2008.

[89] A. Wiest, J. S. Harmon, M. D. Demetriou, R. D. Conner, and W. L. Johnson. Injection molding metallic glass. *Scripta Materialia*, 60:160–163, 2009.

[90] J. P. Patterson and D. R. H. Jones. Molding of a metallic glass. *Materials Research Bulletin*, 13:583–585, 1978.

[91] P. Sharma, N. Kaushik, H. Kimura, Y. Saotome, and A. Inoue. Nano-fabrication with metallic glass – an exotic material for nano-electromechanical systems. *Nanotechnology*, 18:035302, 2007.

[92] Y. Saotome, Y. Fukuda, I. Yamaguchi, and A. Inoue. Superplastic nanoforming of optical components of Pt-based metallic glass. *Journal of Alloys and Compounds*, 434: 97–101, 2007.

[93] J. Schroers, T. Nguyen, S. O'Keefe, and A. Desai. Thermoplastic forming of bulk metallic glass – applications for mems and microstructure fabrication. *Materials Science and Engineering A*, 449:898–902, 2007.

[94] G. Kumar, H. X. Tang, and J. Schroers. Nanomoulding with amorphous metals. *Nature*, 457:868–872, 2009.

[95] J. A. Bardt, G. R. Bourne, T. L. Schmitz, J. C. Ziegert, and W. G. Sawyer. Micromolding three-dimensional amorphous metal structures. *Journal of Materials Research*, 22: 339–343, 2007.

[96] J. P. Chu, H. Wijaya, C. W. Wu, T. R. Tsai, C. S. Wei, T. G. Nieh, and J. Wadsworth. Nanoimprint of grating on a bulk metallic glass. *Applied Physics Letters*, 90:034101, 2007.

[97] T. Waniuk, J. Schroers, and W. L. Johnson. Timescales of crystallization and viscous flow of the bulk glass-forming Zr-Ti-Ni-Cu-Be alloys. *Physical Review B*, 67:184203, 2003.

[98] V. Srivastava, S. A. Chester, N. M. Ames, and L. Anand. A thermo-mechanically-coupled large-deformation theory for amorphous polymers in a temperature range which spans their glass transition. *International Journal of Plasticity*, 26:1138–1182, 2010.

[99] D. E. Hardt, B. W. Anthony, and S. B. Tor. A teaching factory for polymer microfabrication – μFac. *International Journal of Nanomanufacturing*, 6:137–151, 2010.

[100] M. Hale and D. E. Hardt. Development of a low-cost rapid-cycle hot embossing system for microscale parts. In *Proceedings of the ASME International Mechanical Engineering Congress and Exposition*, volume 13, pages 19–23, 2009.

[101] A. D. Mazzeo. *Centrifugal casting and fast curing of polydimethylsiloxane (PDMS) for the manufacture of micro and nano featured components.* PhD thesis, Massachusetts Institute of Technology, 2009.

[102] S. B. Tor and G. Fu, 2009. Personal communication.

[103] G. Kumar, A. Desai, and J. Schroers. Bulk metallic glass: The smaller the better. *Advanced Materials*, 23:461–476, 2011.

[104] P. Vettiger, G. Cross, M. Despont, U. Drechsler, U. Dürig, B. Gotsmann, W. Häberle, M. A. Lantz, H. E. Rothuizen, R. Stutz, and G. K. Binnig. The "millipede" – nanotechnology entering data storage. *IEEE Transactions on Nanotechnology*, 1:39–55, 2002.

[105] E. Eleftheriou, T. Antonakopoulos, G. K. Binnig, G. Cherubini, M. Despont, A. Dholakia, U. Dürig, M. A. Lantz, H. Pozidis, H. E. Rothuizen, and P. Vettiger. Millipede – a mems-based scanning-probe data-storage system. *IEEE Transactions on Magnetics*, 39:938–945, 2003.

[106] H. Pozidis, W. Häberle, D. Wiesmann, U. Drechsler, M. Despont, T. R. Albrecht, and E. Eleftheriou. Demonstration of thermomechanical recording at 641 Gbit/in^2. *IEEE Transaction on Magnetics*, 40:2531–2536, 2004.

[107] P. M. Gullett, M. F. Horstemeyer, M. I. Baskes, and H. Fang. A deformation gradient tensor and strain tensors for atomistic simulations. *Modelling and Simulation in Materials Science and Engineering*, 16:015001, 2008.

[108] P. H. Saksono and D. Perić. On finite element modelling of surface tension – Variational formulation and applications – Part I: Quasistatic problems. *Computational Mechanics*, 38:265–281, 2006.

Appendix A

Molecular dynamics simulations of isochoric tension and isochoric compression

At the beginning of Section 2.2, we argued that for small deviatoric strains we expect the contribution to the free energy from $I_3 = \mathrm{tr}\,\mathbf{E}_0^3$ (which is third-order in $\mathbf{E}_0$) to be significantly smaller than the effect of $I_2 = \mathrm{tr}\,\mathbf{E}_0^2$ (which is second-order in $\mathbf{E}_0$), and accordingly we neglected any dependence of the free energy on I_3. In this appendix, we conduct numerical experiments in which I_3 is non-zero, and explore the effects of I_3 on the stress-strain response for circumstances under which $|\mathbf{E}_0|$ is small and limited to values for which $\gamma = \sqrt{2}|\mathbf{E}_0| \leq 0.04$, so that the sample remains in the elastic range. Specifically, to explore the effects of I_3 we consider,

- **Isochoric extension and isochoric compression**: In these two deformations, the sample is subjected to volume-conserving deformation in which the principal stretches are given by

$$\lambda_1 = 1/\sqrt{\lambda}, \quad \lambda_2 = \lambda, \quad \text{and} \quad \lambda_3 = 1/\sqrt{\lambda}, \tag{A.1}$$

with $\lambda > 1$ corresponding to isochoric extension, and $\lambda < 1$ corresponding to isochoric compression. A schematic of the deformed body $\mathcal{B}_t$ for isochoric extension is shown in Fig. A-1(a), while that for isochoric compression is shown in Fig. A-1(b).

In this case,

$$I_3 = \mathrm{tr}\,\mathbf{E}_0^3 = \pm\frac{3}{4}|\ln\lambda|^3, \tag{A.2}$$

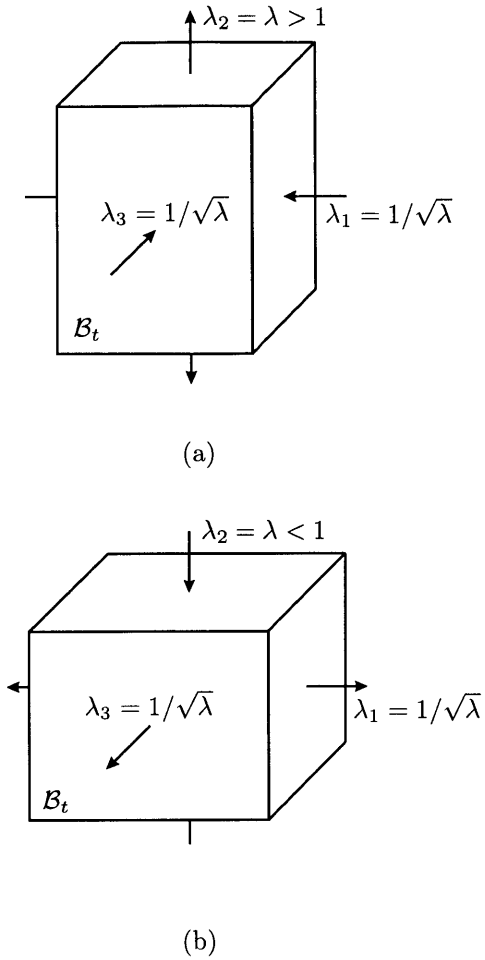

Figure A-1: Schematics of the deformed configuration of the body in (a) isochoric extension, $\lambda > 1$, and (b) isochoric compression, $\lambda < 1$.

with I_3 positive in tension and negative in compression.[1] Since we are restricting our attention to circumstances in which

$$\gamma = \sqrt{2}|\mathbf{E}_0| = \sqrt{3}|\ln\lambda| \leq 0.04,$$

we have $|\ln\lambda| \leq 0.04/\sqrt{3}$, which when substituted in (A.2) gives that I_3 lies in the range $[-9.24 \times 10^{-6}, 9.24 \times 10^{6}]$ for the isochoric extension and compression experiments under consideration here.

The molecular dynamics reference body, Fig. 2-3, was subjected to isochoric extension and compression at an axial strain rate of $\pm 1 \times 10^8\,\mathrm{s}^{-1}$ to a final shear strain of $\gamma = 0.04$. The resulting equivalent shear stress τ versus equivalent shear strain γ curves are plotted in Fig. A-2(a). The dependence of τ on γ in this range of shear strains for both isochoric

[1] Recall that in the case of pure shear considered earlier, $I_3 = 0$.

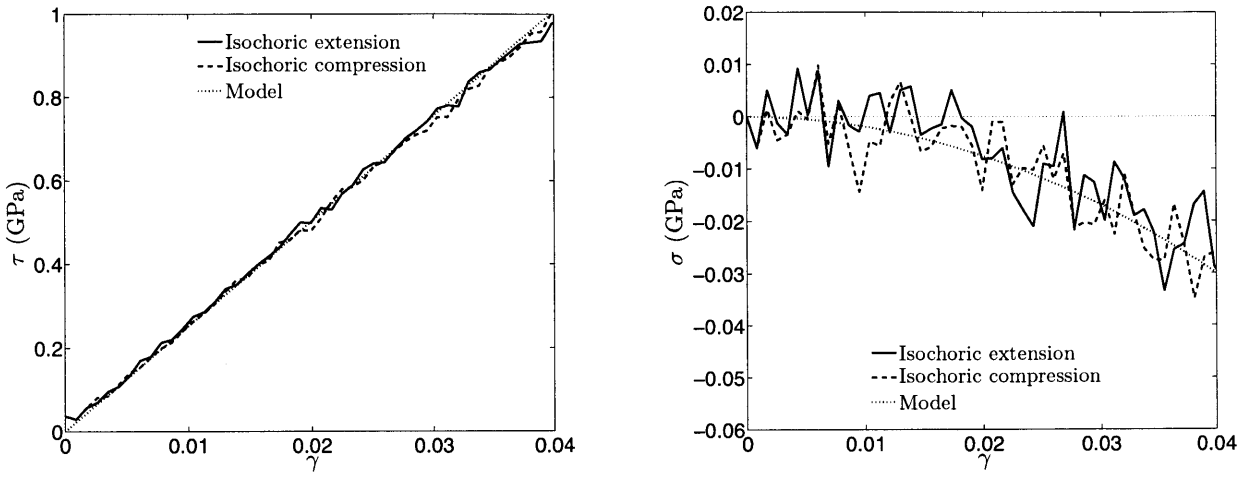

(a) (b)

Figure A-2: Variation of (a) the shear stress and (b) the mean normal stress with elastic shear strain in iscohoric extension and isochoric compression. The solid and dashed lines are the result of the MD simulations, and the dotted lines are the result of the calibrated hyperelasticity model.

extension and compression is *essentially linear and identical to each other*, as well as identical to the response in pure shear, cf. Fig. 2-7(a), in which $I_3 = 0$. Also shown Fig. A-2(a) as a dotted line is the prediction of our calibrated hyperelasticity model, which ignores any dependence of I_3. Additionally, Fig. A-2(b) shows the (small) non-zero mean normal stress that develops during isochoric extension and compression — again the results from the two MD simulations overlap each other, and correspond well to that predicted by (2.34) for the calibrated hyperelasticity model which ignores any dependence of I_3. Thus, we have demonstrated that

- for the small deviatoric strains $\gamma \leq 0.04$, the third invariant I_3 has no discernible effect on the stress-strain response, and our assumption that the free energy function (2.16) does not depend upon I_3 is well-justified.

Appendix B

Molecular dynamics simulations of deformation of metallic glasses at low homologous temperatures

The purpose of this appendix is to highlight some important features of the micro-mechanisms of deformation in metallic glasses at low homologous temperatures using two-dimensional molecular dynamics simulations of simple tension and indentation.

Following Cao et al. [46] and Cheng et al. [47] as in Chapter 2, we consider a metallic glass with a composition of $Cu_{64}Zr_{36}$ and use the embedded atom potential developed and validated (using density functional theory calculations) for this system by these authors. To prepare a metallic glass specimen, we use a two-dimensional box of 10,000 atoms under periodic boundary conditions in both dimensions. The sample was first equilibrated for 2 ns at 2000 K and zero external pressure to ensure melting and then quenched at a rate of 10 K/ns to a temperature of 50 K at zero external pressure using a Nose-Hoover thermostat and the NPT ensemble. Figure B-1 shows the specific enthalpy as a function of temperature during quenching. The markers represent the average of the specific enthalpy over temperature spans of 50 K.[1] Figure B-2 shows the radial distribution functions for Cu-Cu, Cu-Zr, and Zr-Zr pairs, confirming that the as-quenched sample is *amorphous*. From the data in Fig. B-1, the glass transition temperature ϑ_g and the specific heat at constant pressure c_p below ϑ_g for the simulated amorphous alloy were determined to be

$$\vartheta_g = 664\,\mathrm{K} \quad \text{and} \quad c_p = 0.21\,\frac{\mathrm{J}}{\mathrm{g\ K}}, \tag{B.1}$$

respectively. A snapshot of the molecular configuration of the as-quenched sample is shown

[1]The error bars in these figures denote the maximum and minimum values of the quantity measured over temperature spans of 50 K during the quenching simulations.

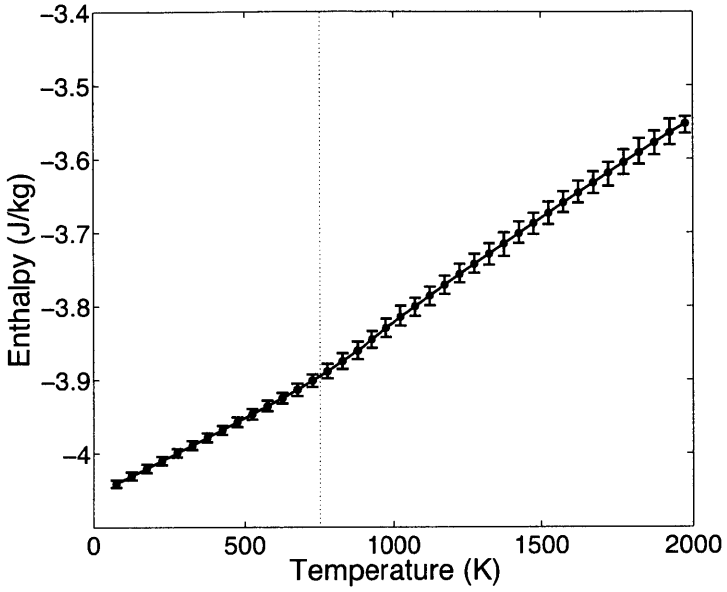

Figure B-1: Specific enthalpy versus temperature.

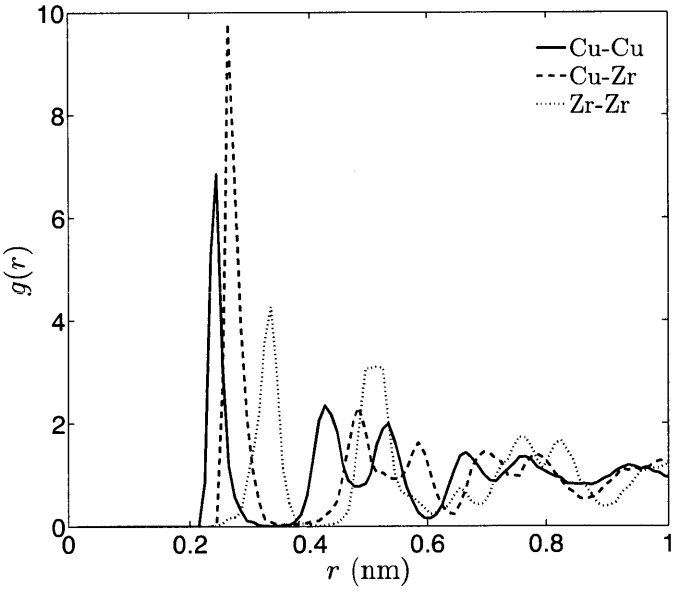

Figure B-2: The radial distribution functions in the quenched state for Cu-Cu, Cu-Zr, and Zr-Zr pairs, confirming the amorphous structure of the as-quenched sample.

in Fig. B-3; the copper atoms are copper-colored and the zirconium atoms are white. The sample after quenching has dimensions of 25.2 nm×25.2 nm.

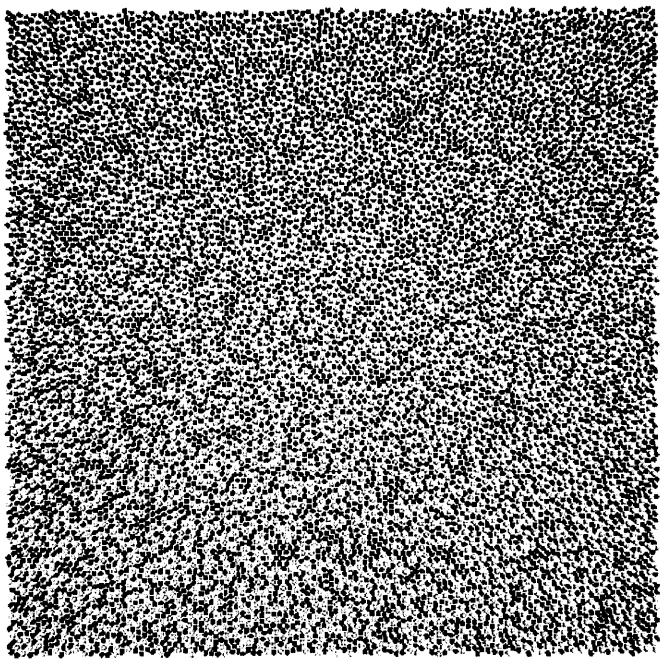

Figure B-3: Snapshot of the quenched configuration.

The 10,000 atom cells were tiled to form a 320,000 atom supercell, which was used to perform a two-dimensional simple tension simulation. A schematic of the supercell, which we will refer to as the reference configuration of the body B, is shown in Fig. B-4(a). The sample has dimensions of 100.8 nm and 201.6 nm in the 1 and 2-directions, respectively.

Periodic boundary conditions are applied in the 2-direction, while the boundaries are free in the 1-direction. The sample is subjected to uniaxial straining in the 2-direction at a true strain rate of $1 \times 10^8\,\mathrm{s}^{-1}$ to a final true strain of approximately 0.1 at a constant temperature of 50 K. A schematic of the deformed body $\mathcal{B}_t$ for such a deformation is shown in Fig. B-4(b). The components of the Cauchy (true) stress may be determined from the virial stress. Figure B-5(a) shows the true stress in the 2-direction as a function of the true strain in the 2-direction.[2] The stress-strain behavior is characterized by a stress peak, followed by strong strain softening.

Several points (A–D) are marked on the stress-strain curve in Fig. B-5(a) and corresponding snapshots of the molecular dynamics configuration are shown in Fig. B-5(b). Contours of equivalent shear strain ($|\mathbf{E}_0|$) are shown on these snapshots, calculated using the methods of Gullett et al. [107]. Point A designates the peak of the stress-strain curve and the onset of softening; at this point, virtually no localization is discernible in Fig. B-5(b). At point B,

[2]The component of stress in the 1-direction remains zero due to the free boundary condition in that direction.

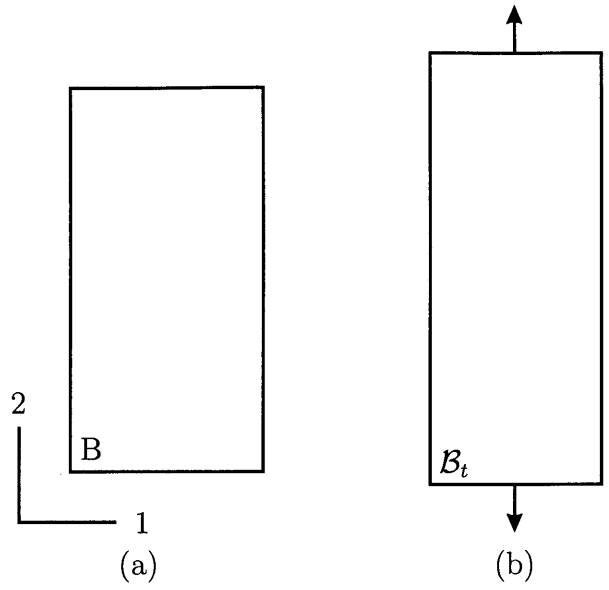

Figure B-4: Schematics of the (a) undeformed and (b) strained configurations for simple tension.

softening has progressed, and the nucleation of *several* shear bands is observable. By point C, one shear band has grown dominant, and by point D, all further deformation is accommodated by that shear band. It is important to note that during the process of softening, many shear bands activate before a single shear band dominates.

For our molecular dynamics simulation of indentation, the 10,000 atom cells were again tiled to form a 320,000 atom supercell. A schematic of the reference configuration for indentation is shown in Fig. B-6. With reference to this figure, the sample has dimensions of 201.6 nm and 100.8 nm in the 1 and 2-directions, respectively. Periodic boundary conditions are applied on sides AD and BC. The upper boundary AB is free, and a thin layer of atoms are frozen along the bottom boundary CD in order to create a fixed boundary condition. The upper boundary AB is then indented by a circular indenter with a radius of 75 nm at a rate of 10 m/s to a final depth of 10 nm.

Snapshots of the MD configuration at indentation depths of 2.5 nm, 5 nm, 7.5 nm, and 10 nm are shown in Figs. B-7(a-d). The contours are of equivalent shear strain as before. Deformation under the indenter is accommodated by a network of shear bands, with a (nearly) symmetrical spiral shape pointing towards the interior of the sample. The extent of the network of shear bands and the intensity of the shear bands grows as deformation progresses. In Fig. B-7(d), at an indentation depth of 10 nm, slip steps on the free surface are observable on either side of the indent. The morphology of the shear band patterns is quite similar to that observed experimentally and computationally in plane-strain indentation by Su and Anand [35].

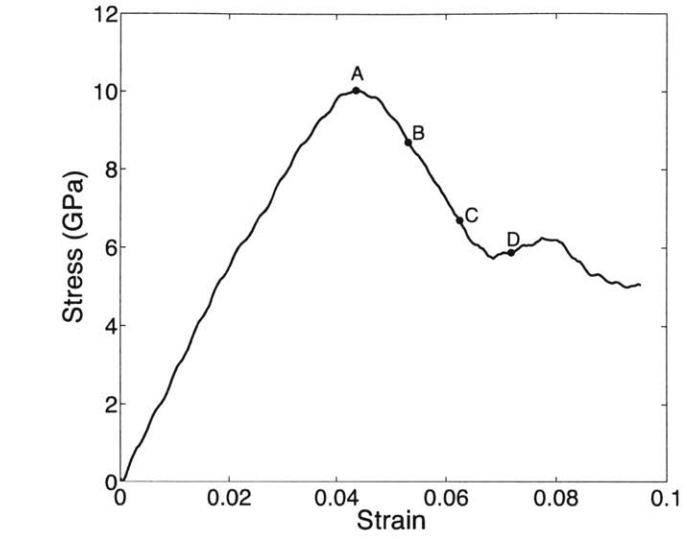

(a)

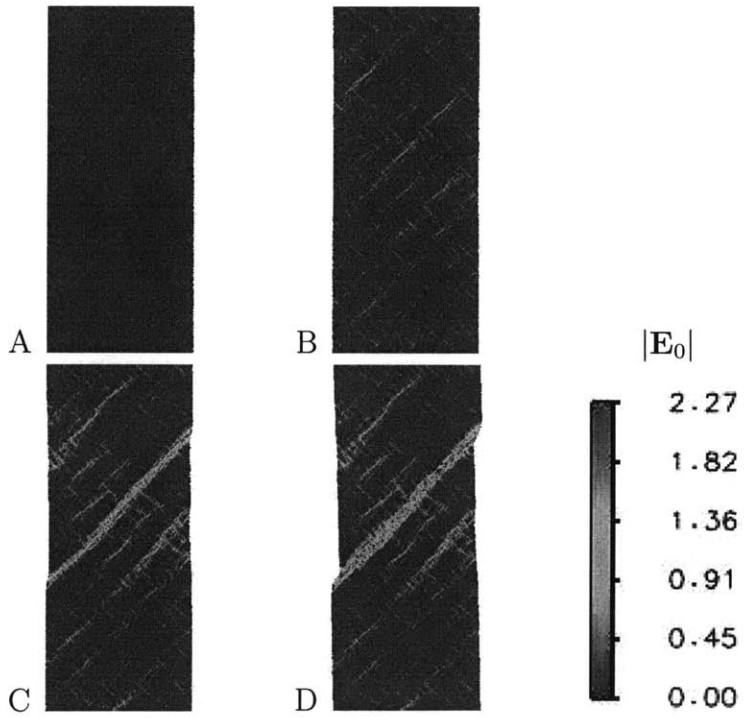

(b)

Figure B-5: (a) Stress-strain curve for simple tension in two dimensions, and (b) snapshots of the MD configuration at four stages of deformation. Contours are of equivalent shear strain.

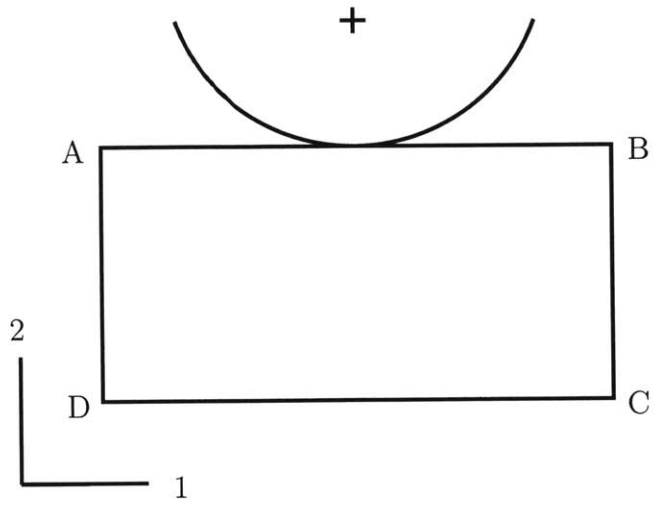

Figure B-6: Schematic of the reference configuration for indentation.

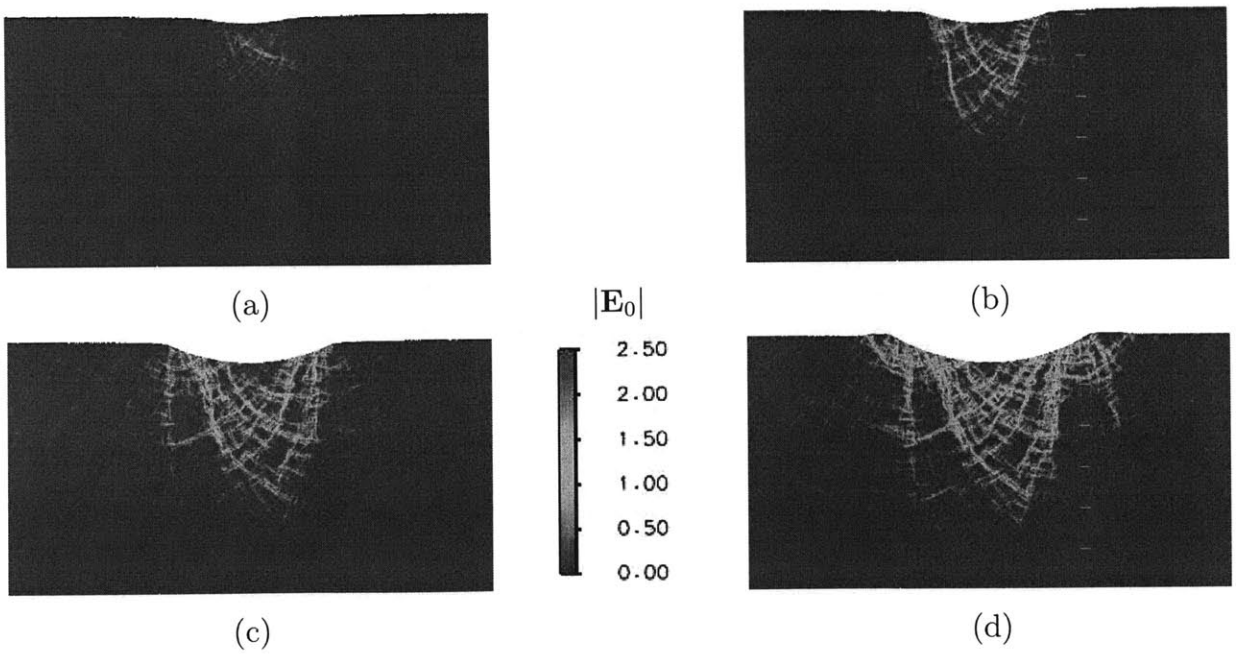

Figure B-7: Snapshots of the MD configuration at indentation depths of (a) 2.5 nm, (b) 5 nm, (c) 7.5 nm, and (d) 10 nm. Contours are of equivalent shear strain.

Appendix C

Convergence tests for Mode I, plane-strain, small-scale-yielding simulations

In this appendix, we perform two convergence tests to verify the validity of our numerical results in Section 4.4: first with respect to the outer K_{I}-dominance radius R_0, and second with respect to the variation of the results as the mesh-size is varied.

First, we verify that our choice of outer radius R_0 in Section 4.4 is sufficiently large to provide a valid Mode-I, plane-strain, small-scale-yielding, notch-tip simulation. Specifically, we need the outer radius R_0 to be large enough so that the plastic zone associated with the finite notch root is well-contained within the domain. However, there are practical limits on the choice of R_0. First, there is the additional computational cost associated with modeling a larger domain. Further, in a dynamic, explicit analysis, as in the present work, an overly large domain, containing a large variation in element size, will lead to a solution with excessive numerical fluctuations and therefore an unreliable result. Thus, we wish to choose an outer radius R_0 that is large enough to achieve small scale yielding but small enough to obtain a "good" numerical solution. To this end, a convergence test was carried out to verify that the R_0 chosen in Section 4.4 is indeed large enough by repeating the Mode-I notch-tip calculation with a notch-root radius of $\rho = 100\,\mu\mathrm{m}$ with an increased outer radius of $R_0 = 15000\,\mu\mathrm{m}$. This notch-root radius was chosen because it is the largest notch, having the largest plastic zone, and thus requiring the largest domain. The reaction force versus K_{I} is shown in Fig. C-1. The resulting fracture toughness is essentially the same as that obtained with an outer radius of $R_0 = 7500\,\mu\mathrm{m}$ ($56.1\,\mathrm{MPa}\sqrt{\mathrm{m}}$ compared to $57.4\,\mathrm{MPa}\sqrt{\mathrm{m}}$). Thus, we may conclude that the choice of $R_0 = 7500\,\mu\mathrm{m}$ used in Section 4.4 is sufficiently large to provide a valid Mode-I, plane-strain, small-scale-yielding, notch-tip simulation.

Finally we note that the mesh-size does play a role in predicting the onset of fracture. However, if the mesh is fine enough, then the mesh-dependacy is *not significant*, and this is

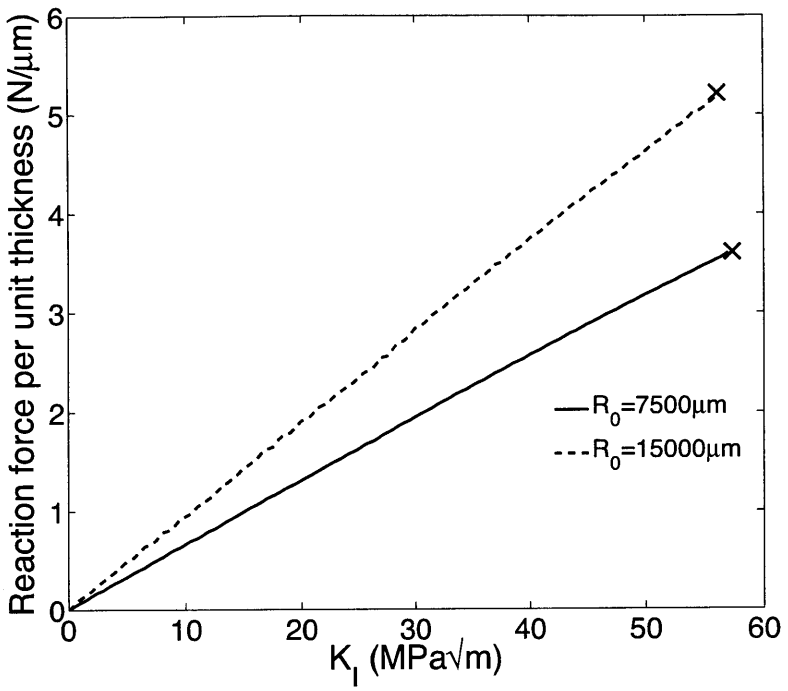

Figure C-1: Demonstration of convergence with respect to the outer radius with a fixed notch-root radius of $\rho = 100\,\mu$m.

supported by our mesh-convergence study described next. Consider the case of a notch-root radius of $\rho = 100\,\mu$m with an outer $K_{\rm I}$-dominance radius of $R_0 = 7500\,\mu$m. The base-line mesh used in the main body of the paper consists of 17935 elements with 60 elements along the notch root. For the mesh-convergence study we considered (i) a finer mesh consisting of 40470 elements with 90 elements along the notch root, and (ii) a coarser mesh consisting of 4483 elements with 30 elements along the notch root. Close-ups of all three meshes at the notch root are shown in Fig. C-2(a-c). The reaction force versus applied $K_{\rm I}$ for each case, denoted by the number of elements $N(= 30, 60, 90)$ along the notch root, is shown in Fig. C-2(d); the failure point for each case is marked with and "X". As is clear from Fig. C-2(d), there is only a slight variation in the resulting fracture toughness: the toughness decreases from $58.8\,\text{MPa}\sqrt{\text{m}}$, to $57.4\,\text{MPa}\sqrt{\text{m}}$, and finally to $56.4\,\text{MPa}\sqrt{\text{m}}$ as the mesh is refined. We conclude therefore that for sufficiently refined meshes, as those considered here, the predicted toughness is almost independent of the mesh size.

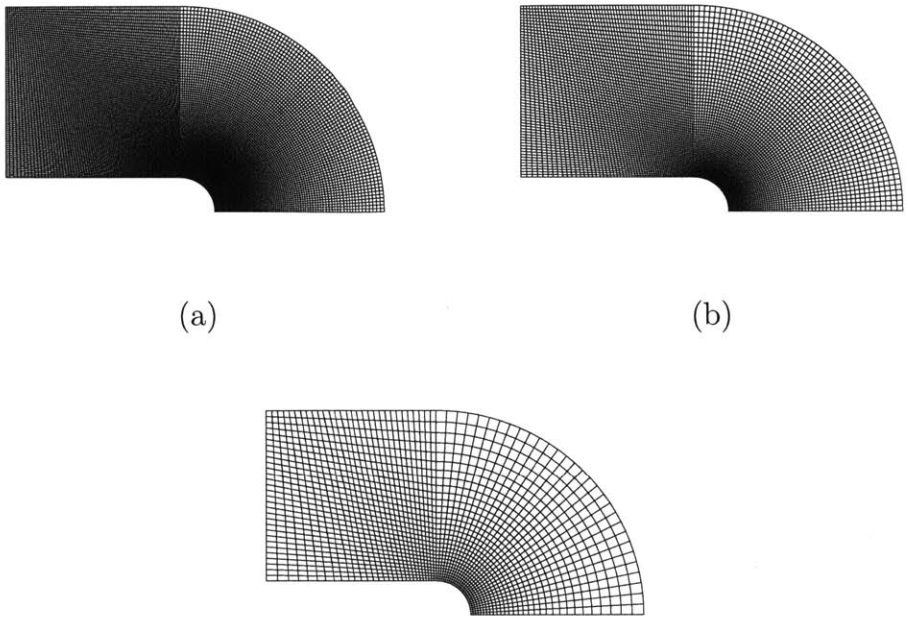

(a)

(b)

(c)

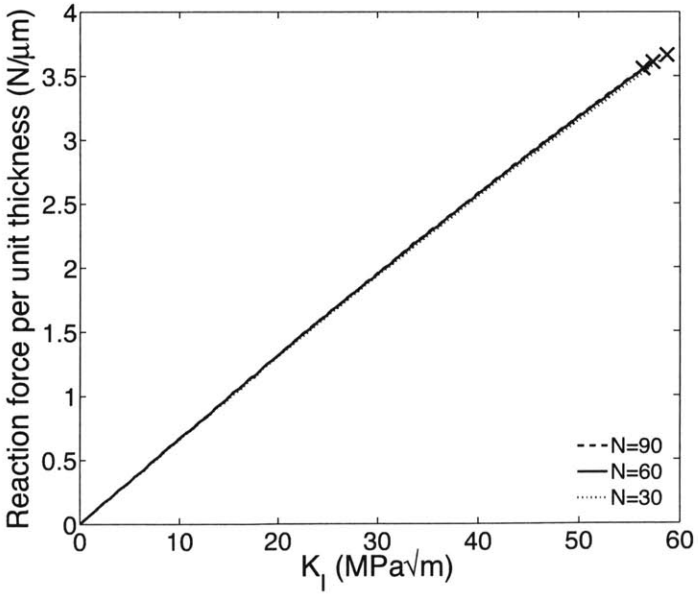

(d)

Figure C-2: Close-up of the mesh at the notch root for the cases of (a) $N = 90$, (b) $N = 60$, and (c) $N = 30$ elements along he notch root and a notch-root radius of $\rho = 100\,\mu$m. (d) Reaction force versus loading parameter K_{I} for each of these cases; failure occurs at points marked with an "X".

Appendix D

A heuristic procedure for material parameter estimation

The constitutive model summarized in Chapter 5 contains 33 material parameters which are used to represent the elastic-viscoplastic behavior of a metallic glass through its glass transition temperature.[1] The material parameters may be grouped according to the following three lists:

(MP1) $\{\nu_0, d_1, d_2, \vartheta_{\text{ref}}, \Delta F_{\text{gl}}, \Delta F_{\text{sc}}, \Delta_{\text{F}}, V_{\text{gl}}, V_{\text{sc}}, \Delta_{\text{V}}, \vartheta_{\text{V}}\}$ used to represent the "steady-state" viscoplastic flow;

(MP2) $\{S_0, h_0, b_{\text{dil}}, b_{\text{com}}, \varphi_0, g, \vartheta_0, p, q, k_1, k_2, l_1, l_2, \nu_{\text{ref}}\}$ used to represent the transient stress-overshoot and strain-softening response of the material due to microstructural disordering; and

(MP3) $\{E_{\text{gl}}, E_{\text{sc}}, \Delta_{\text{E}}, \vartheta_{\text{g}}, k_{\text{E}_{\text{gl}}}, k_{\text{E}_{\text{sc}}}, \nu_{\text{gl}}, \nu_{\text{sc}}\}$ used to represent the temperature dependence of the elastic moduli of the material.

In this appendix, we outline a heuristic procedure for estimating the values of these parameters for a metallic glass. Using available experimental data in the literature [12, 82, 85], we illustrate this procedure by estimating the material parameters for Vitreloy-1 in the temperature range $[593, 683]\,\text{K}$ and strain rate range $[10^{-5}, 10^{-1}]\,\text{s}^{-1}$. The literature value of the glass transition temperature of this material is

$$\vartheta_{\text{g}} = 623\,\text{K}. \tag{D.1}$$

[1] We acknowledge that this is a rather long list, but most of these parameters enter the phenomenological functions employed to represent the strong temperature dependence of the underlying physical quantities.

D.1 Estimation of the parameter list MP1

In simple compression, the principal stresses are

$$\sigma_1 = \sigma_2 = 0, \qquad \sigma_3 < 0. \tag{D.2}$$

Straight-forward calculations using (3.6), (3.9) and (3.10) show that in this case the resolved shear stresses on the slip systems are given by

$$\tau \stackrel{\text{def}}{=} \tau^{(1)} = \tau^{(2)} = \tau^{(5)} = \tau^{(6)} = -\frac{1}{2}\sigma_3, \quad \tau^{(3)} = \tau^{(4)} = 0. \tag{D.3}$$

Thus, (5.6) dictates that the shearing rate on the slip systems must obey,

$$\nu^{(1)} = \nu^{(2)} = \nu^{(5)} = \nu^{(6)} > 0, \quad \text{and} \quad \nu^{(3)} = \nu^{(4)} = 0. \tag{D.4}$$

Further, it is easy to verify that the non-zero resolved shear stresses and shearing rates on the slip systems are given by

$$\tau = \tau^{(1)} = \tau^{(2)} = \tau^{(5)} = \tau^{(6)} = \frac{1}{2}\sigma, \quad \text{and} \quad \nu^{(1)} = \nu^{(2)} = \nu^{(5)} = \nu^{(6)} = \frac{1}{2}\dot{\epsilon}^{\text{p}}, \tag{D.5}$$

where $\sigma > 0$ and $\dot{\epsilon}^p > 0$ are the axial stress and axial plastic strain rate in a compression test. Thus, in one dimension (5.6) gives

$$\dot{\epsilon}^{\text{p}} = 2\nu_0 \exp\left(-\frac{1}{\zeta}\right) \exp\left(-\frac{\Delta F}{k_{\text{B}}\vartheta}\right) \sinh\left(\frac{(\frac{1}{2}\sigma - S)V}{2k_{\text{B}}\vartheta}\right) \geq 0. \tag{D.6}$$

In a fully-developed flow state at given temperature ϑ and strain rate $\dot{\epsilon}$, when the stress reaches a steady-state "plateau" value σ_{ss}, $\dot{\epsilon} \approx \dot{\epsilon}^{\text{p}}$ and

$$\tau_{\text{ss}} \stackrel{\text{def}}{=} \frac{1}{2}\sigma_{\text{ss}}, \quad \text{and} \quad \nu^{\text{p}} \stackrel{\text{def}}{=} \sum_{\alpha=1}^{6} \nu^{(\alpha)} = 2\dot{\epsilon}\,. \tag{D.7}$$

Further, at steady-state at given temperature and strain rate, the order-parameter reaches its steady-state value φ^*, the disordering resistance S goes to zero (cf. (5.13)), and (D.6) reduces to

$$\dot{\epsilon} = 2\nu_0 \exp\left(-\frac{1}{\zeta}\right) \exp\left(-\frac{\Delta F}{k_{\text{B}}\vartheta}\right) \sinh\left(\frac{\sigma_{\text{ss}} V}{4k_{\text{B}}\vartheta}\right) \geq 0. \tag{D.8}$$

Equation (D.8) is easily inverted to obtain an expression for steady-state stress as a function of applied strain rate and temperature

$$\sigma_{\text{ss}} = \frac{4k_{\text{B}}\vartheta}{V} \sinh^{-1}\left(\frac{\dot{\epsilon}}{2\nu_0} \exp\left(\frac{1}{\zeta}\right) \exp\left(\frac{\Delta F}{k_{\text{B}}\vartheta}\right)\right). \tag{D.9}$$

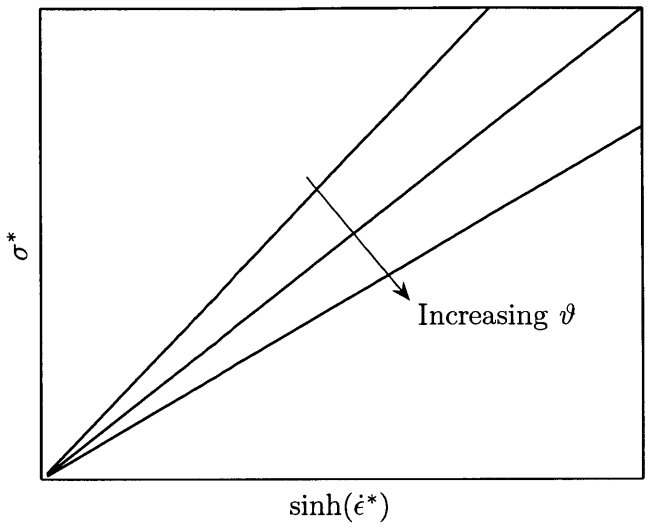

Figure D-1: Schematic of the fit of temperature-compensated strain rate to temperature-compensated stress.

Equation (D.9), along with experimental data for the steady-state stress as a function of strain rate and temperature [12], as well as the variation of the viscosity of the material with temperature at high temperatures [82], allow one to estimate numerical values for the parameter list MP1.

The procedure that we have used for estimating the values of these parameters is as follows. First, let

$$\sigma^* \stackrel{\text{def}}{=} \frac{\sigma_{\text{ss}}}{\vartheta}, \qquad \text{and} \qquad \dot{\epsilon}^* \stackrel{\text{def}}{=} \frac{\dot{\epsilon}}{2\nu_0} \exp\left(\frac{1}{\zeta}\right) \exp\left(\frac{\Delta F}{k_{\text{B}}\vartheta}\right), \tag{D.10}$$

define "temperature-compensated" values of σ_{ss} and $\dot{\epsilon}$, respectively, so that (D.9) may be written as

$$\sigma^* = \frac{4k_{\text{B}}}{V} \sinh^{-1}(\dot{\epsilon}^*). \tag{D.11}$$

Thus, at each temperature, σ^* depends linearly on $\sinh^{-1}(\dot{\epsilon}^*)$ as shown schematically in Fig. D-1; however, note that the slope of this line depends on temperature because the activation volume is temperature dependent. Note that values of σ^* are known directly from the experimental data of Lu et al. [12]. However, to determine values for $\dot{\epsilon}^*$ one needs a value for the reference strain rate ν_0 and the parameters $\{d_1, d_2, \vartheta_{\text{ref}}, \Delta F_{\text{gl}}, \Delta F_{\text{sc}}, \Delta_{\text{F}}\}$.

We choose a reference strain rate ν_0 of 5×10^{12} s^{-1} which is on the order of the Debye frequency. For the parameters, d_1, d_2, and ϑ_{ref} in the Grest-Cohen equation (5.15), we employ the viscosity data reported in [82] for Vitreloy-1. These authors fit the temperature

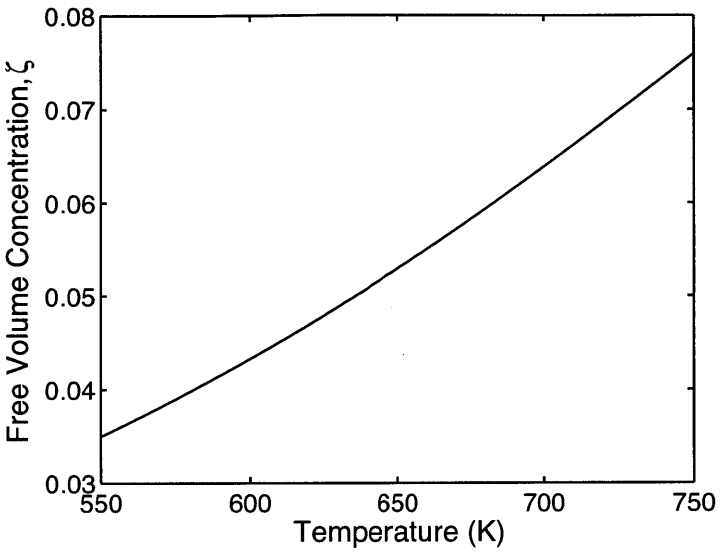

Figure D-2: Free volume concentration as a function of temperature.

dependence of the high-temperature viscosity data using the following functional form

$$\eta(\vartheta) = \eta_0 \exp\left(\frac{1}{\zeta}\right), \quad \text{with} \quad \zeta(\vartheta) = \frac{1}{2d_1}\left[\vartheta - \vartheta_{\text{ref}} + \sqrt{(\vartheta - \vartheta_{\text{ref}})^2 + d_2\vartheta}\right], \tag{D.12}$$

which differs from (5.24) of the present theory, in that it does not contain an activation energy term $\exp(\Delta F/k_{\text{B}}\vartheta)$. We use the values $d_2 = 162\text{K}$ and $\vartheta_{\text{ref}} = 672\text{K}$ from [82]; however, we adjust their value of d_1 in order to fit the non-Newtonian viscosity (5.23) estimated by using the data of [12]. Values of d_1 and ΔF were determined by using an iterative procedure. The starting value of d_1 was taken as $d_1 = 4933\text{K}$ [82], and an activation energy ΔF was estimated for each temperature that would result in the linear relationship (D.11) at that temperature. This process was repeated until the values of d_1 and ΔF for each temperature provided acceptable fits to (D.11). Once the temperature dependence of ΔF was determined, the values of the subsidiary values $\{\Delta F_{\text{gl}}, \Delta F_{\text{sc}}, \Delta_{\text{F}}\}$ were determined by fitting this data to (5.16). The temperature dependent free volume concentration of (5.15) is plotted in Fig. D-2, and the resulting temperature dependent values of the activation energy along with the fit to (5.16) are shown in Fig. D-3(a).[2] Finally, with the values of $\dot{\epsilon}^*$ determined at each temperature, the activation volume V for each temperature was determined from the slopes of the σ^* versus $\sinh^{-1}(\dot{\epsilon}^*)$ plots at each temperature. The values of activation volume determined in this manner are plotted in Fig. D-3(b), and the subsidiary values $\{V_{\text{gl}}, V_{\text{sc}}, \Delta_{\text{V}}, \vartheta_{\text{V}}\}$ were determined by fitting (5.17) to this data. The values of the parameters in the list MP1, determined using this procedure, are given in Tab. D.1.

[2]It is important to note that while the variation of ΔF with temperature appears to be quite small — from $\Delta F_{\text{gl}} = 1.64 \times 10^{-19}$ J to $\Delta F_{\text{sc}} = 1.51 \times 10^{-19}$ J — it is necessary to account for this variation to obtain a good fit to the values of the steady-state stress over a wide range of temperatures.

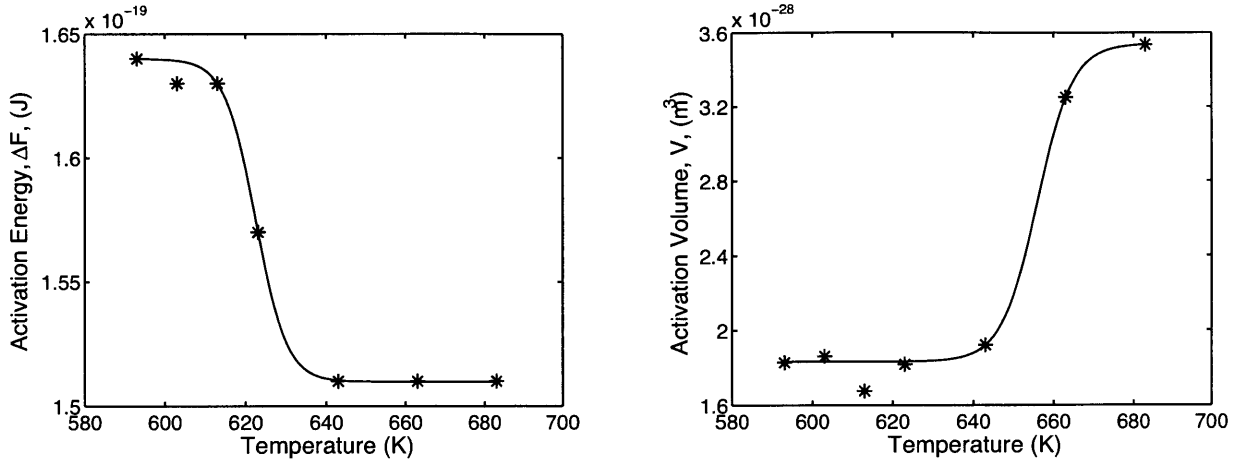

Figure D-3: (a) Activation energy as a function of temperature. (b) Activation volume as a function of temperature.

D.2 Estimation of the parameter list MP2

Once the steady-state levels of the flow stress at each temperature and strain rate have been fit adequately by the constitutive model, it remains to determine the parameters $\{S_0, h_0, b_{\text{dil}}, b_{\text{com}}, \varphi_0, g, \vartheta_0, p, q, k_1, k_2, l_1, l_2, \nu_{\text{ref}}\}$ which determine the evolution of S and φ, and control the levels of stress-overshoot and strain-softening in the stress-strain curves. The parameters S_0 and φ_0 describe the initial values of the internal variables. We assume that the material begins in a well-annealed, "ground" state as far as the internal variables S and φ are concerned. Thus, we take S_0 and φ_0 to be zero. The parameter h_0 controls the strain-hardening slope of the curves, b_{dil} affects the peak value, and g controls how quickly the strain-softening occurs, while $\{\vartheta_0, p, q, k_1, k_2, l_1, l_2, \nu_{\text{ref}}\}$ affect the strain rate and tem-

Parameter	Value
ν_0 (s^{-1})	5×10^{12}
d_1 (K)	2865.8
d_2 (K)	162
ϑ_{ref} (K)	672
ΔF_{gl} (J)	1.64×10^{-19}
ΔF_{sc} (J)	1.51×10^{-19}
Δ_{F} (K)	7.57
V_{gl} (m^3)	1.82×10^{-28}
V_{sc} (m^3)	3.54×10^{-28}
ϑ_{V} (K)	655.63
Δ_{V} (K)	9.18

Table D.1: List MP1.

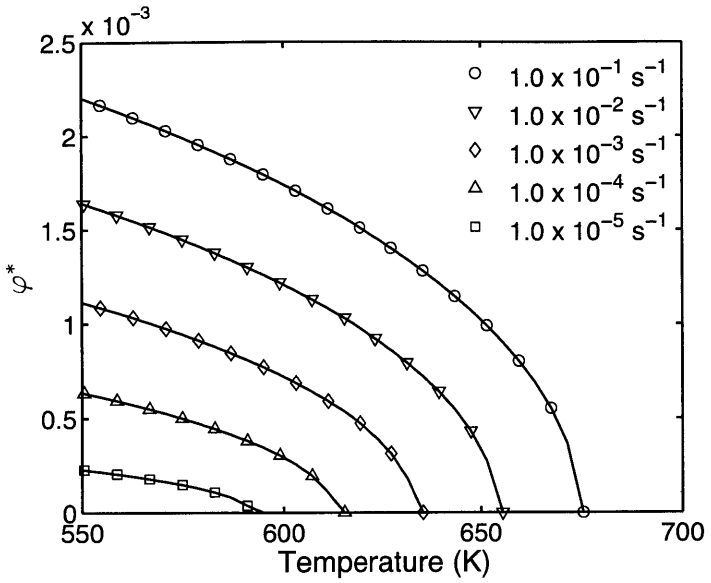

Figure D-4: Dependence of φ^* on strain rate and temperature.

perature sensitivity of the peak value of the stress. First, the values of h_0, g, and b_{dil} were selected following a few trials using different values of these parameters. Next, the necessary value of φ^* to attain the appropriate stress peak value was determined for each stress-strain curve. Then, the values of $\{\vartheta_0, p, q, k_1, k_2, l_1, l_2, \nu_{\text{ref}}\}$ were adjusted to fit the dependence of φ^* on strain rate and temperature. This dependence is shown in Fig. D-4. Lastly, an appropriate value for b_{com} was selected based on magnitude of the stress trough in strain rate decrement tests. The values of the parameters in the list MP2 are given in Tab. D.2.

Parameter	Value
S_0 (MPa)	0
h_0	40
b_{dil} (GPa)	500
b_{com} (GPa)	125
φ_0	0
g	12.5
ϑ_0 (K)	300
p	1.5
q	0.5
k_1	5.0×10^{-4}
k_2	3.00×10^{-4}
ν_{ref} (s^{-1})	2.00×10^{-5}
l_1 (K)	292
l_2 (K)	9

Table D.2: List MP2.

Parameter	Value
E_{gl} (GPa)	80.7
E_{sc} (GPa)	30.0
Δ_{E} (K)	24.0
$k_{\mathrm{E_{gl}}}$ (MPa)	39.0
$k_{\mathrm{E_{sc}}}$ (MPa)	39.0
ν_{gl}	0.360
ν_{sc}	0.447

Table D.3: List MP3.

D.3 Estimation of the parameter list MP3

The temperature dependence of Young's modulus was estimated from the DMA data of [85] for Vitreloy-1. This data provides guidance in choosing values for E_{gl}, Δ_{E}, and $k_{\mathrm{E_{gl}}}$. However, due to the onset of crystallization during a DMA test, reliable data for E is inaccessible for higher temperatures, leaving definite values for E_{sc} and $k_{\mathrm{E_{sc}}}$ unclear; for these parameters we simply assume plausible extrapolated values. Likewise, we choose a value for ν_{gl} based on the room temperature value of the Poisson's ratio, and we base our choice for ν_{sc} on the assumption that material is almost incompressible above the glass transition temperature. The values of the parameters in the list MP3, determined using this iterative procedure, are given in Tab. D.3.

Using the temperature dependent functions (5.18) and (5.20) for the Young's modulus and the Poisson's ratio, we may calculate the temperature dependence of the shear and bulk moduli using (5.21). The temperature dependence of the estimated elastic moduli for Vitreloy-1 is shown in Fig. D-5.

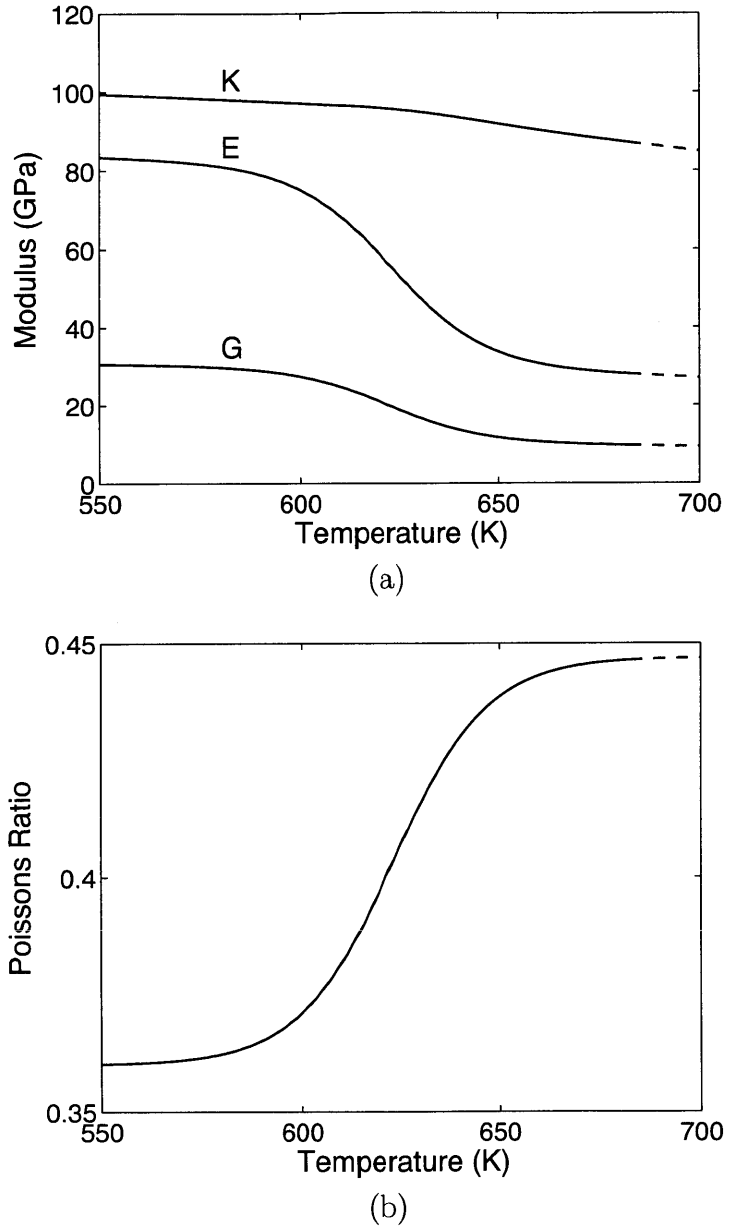

Figure D-5: (a) Temperature dependence of elastic moduli. (b) Temperature dependence of Poisson's ratio.

Appendix E

A method for calculating surface curvature

Recall from Section 7.4.1 that the surface tension boundary condition is equivalent to an externally-applied traction of the form

$$\mathbf{T}\mathbf{n} = -2\,\gamma\,\kappa\,\mathbf{n} \qquad \text{upon} \qquad \mathcal{S}_t, \tag{E.1}$$

where γ is the surface tension, κ is the mean curvature, and $\mathbf{n}$ is the outward unit normal to $\mathcal{S}_t$. This traction boundary condition is applied through a user-subroutine DLOAD in Abaqus/Standard that allows for user-defined distributed loads, i.e. normal tractions. In this appendix, we focus attention on the calculation of the mean curvature κ.[1]

The DLOAD subroutine is called at each *load integration point* located on the free surface, for each iteration in a given time increment. Load integration points are distinct from material integration points. Material integration points are used to calculate the stiffness matrix for a given element in a finite element calculation, and it is at these points that quantities such as the stress and strain are calculated. Analogously, load integration points are used calculate the external force array for a given finite element located on the free surface, and likewise, it is at these points that the applied surface tractions are calculated. In our discussion when we use the term "integration point," we refer to load integration points, and not material integration points.

In the DLOAD subroutine, only the coordinates of the integration point are available, and data for the neighboring integration points are unavailable. However, in order to calculate the mean curvature at an integration point, the coordinates of the integration points surrounding that point are needed. We obtain this data by using the following strategy: we utilize

[1]Saksono and Perić [108] have recently developed and implemented a finite element program in which they incorporate surface tension effects based on a weak form of (E.1). Here, for ease of implementation in a commercial finite element program, we apply (E.1) directly as a boundary condition.

a FORTRAN module which is available globally during the analysis. During each time increment, the current coordinates of all integration points are stored in the global module. Also the integration points nearest to each integration point are determined and stored in an array in the global module, and a global variable is used as a counter to determine the total number of load integration points processed in each time increment. At the beginning of a new time increment, the coordinates of each integration point and its nearest neighbors (stored from the previous step) are used to calculate the mean curvature at that point, and these values are stored in the global module and used to determine the surface tension-related traction boundary condition at that integration point. For subsequent iterations in a given time increment, the mean curvatures calculated from the previous time increment are utilized. Thus, while the overall calculation is implicit, the application of the surface tension boundary conditions is explicit, with the load in a given time increment calculated using the mean curvature from the previous time increment. One must keep this in mind when choosing a time step for simulations, and as such, it was verified that the time step was small enough in the simulations presented in Section 7.4.

To demonstrate how the mean curvature is calculated at a given load integration point, we first consider the two-dimensional case, and then extend our methodology to three-dimensions. Consider the case of a free surface in a two-dimensional, plane-strain simulation, which uses four-node reduced integration elements. In this case each element possesses a single load integration point; cf. Fig. E-1(a). Nodes are denoted by a filled, black circle, and the load integration points are denoted by an X; the coordinates of the integration points are given in terms of the global coordinate system Oxy. To calculate the mean curvature at the center integration point A, we fit a parabola through the point A and its two nearest neighbors, B and C, and use the resulting fit to calculate the mean curvature at A. However, when fitting a parabola through three discrete points, the resulting parabola, and hence the calculated mean curvature, is highly dependent on the orientation of the coordinate system used. Thus, we choose to calculate the mean curvature at A in the coordinate frame with origin located at A and y-axis aligned with the local surface normal $\mathbf{n}$, shown as $Ax'y'$ in Fig. E-1(a). The local surface normal is calculated as the normal vector to the line passing through the two nearest neighbor points B and C, denoted by the dotted line in Fig. E-1(a).[2] In general, the form for a parabolic fitting function is $y' = ax'^2 + bx' + c$; however, in using a local coordinate system with origin at the point A and y-axis aligned with the local surface normal, the first derivative of the fitting function, as well as the value of function itself, should be zero at the point ($y' = \dfrac{dy'}{dx'} = 0$ at $x' = 0$). Thus, we force $b = c = 0$ and take the fitting function to be in the form $y' = ax'^2$. The resulting mean curvature is $\kappa = -\dfrac{1}{2}\dfrac{\partial^2 y'}{\partial x'^2} = -a$.

[2]Note that the normal vector is determined up to its sign. Thus, some knowledge of orientation of the free surface is necessary to ensure that the normal vector $\mathbf{n}$ is the outward-facing surface normal and not incorrectly inward-facing.

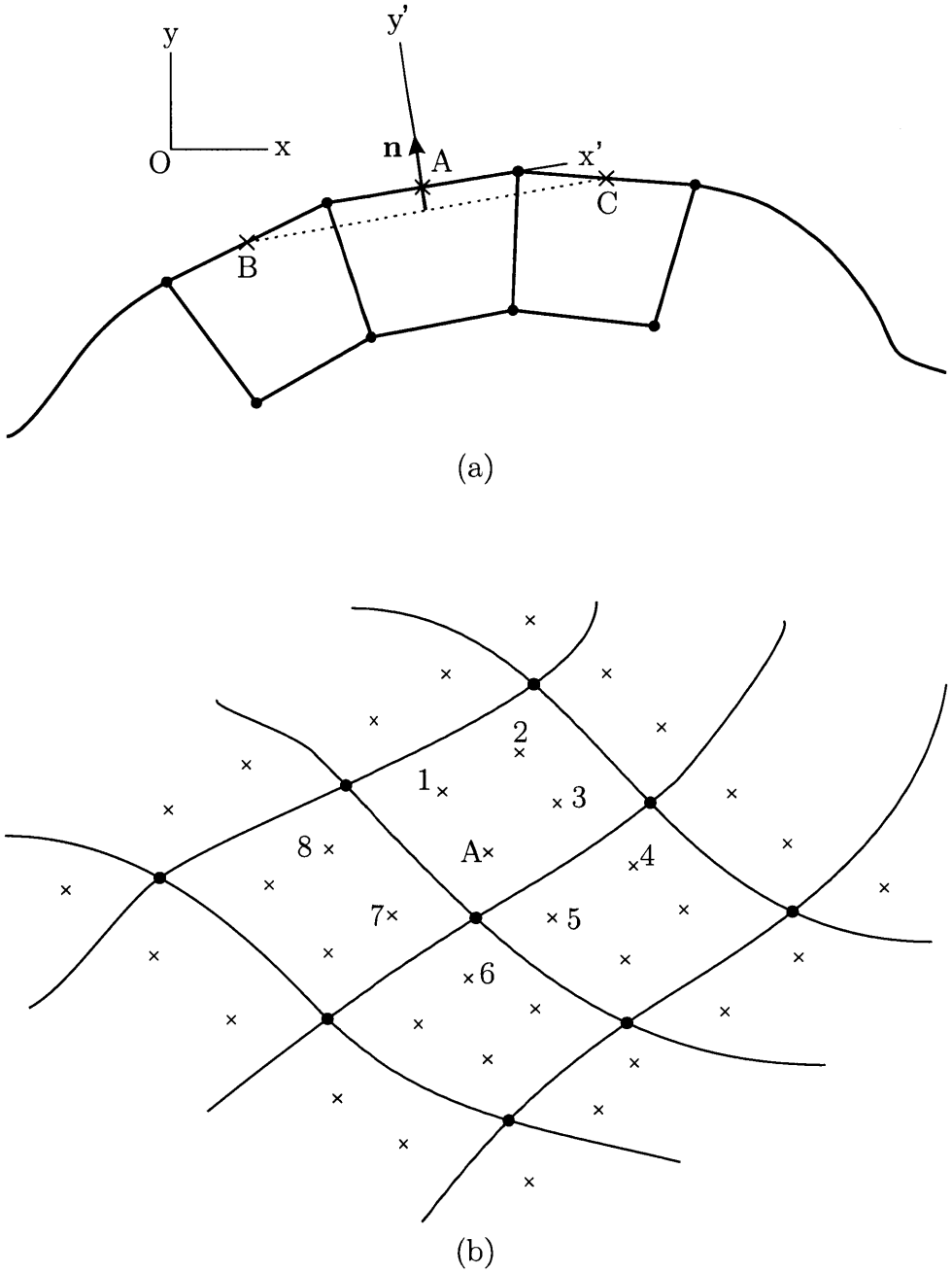

Figure E-1: (a) Schematic of a free surface in a two-dimensional, plane-strain setting, using four-node reduced-integration elements. (b) Schematic of a free surface in a three-dimensional setting, using eight-node fully-integrated elements. Nodes are denoted by a filled, black circle, and load integration points are denoted by an X.

In summary, in a two-dimensional, plane-strain setting, given the global coordinates of the integration point A, (x_0, y_0), and the coordinates of the two nearest neighbors B and C, (x_1, y_1) and (x_2, y_2), the mean curvature at A is calculated as follows:

1. Calculate the components of the local outward surface normal $\mathbf{n} = n_x\mathbf{e}_x + n_y\mathbf{e}_y$ in the global coordinate system from the coordinates of the two nearest neighbor points:

$$n_x = \frac{-(y_2 - y_1)}{\sqrt{(y_2 - y_1)^2 + (x_2 - x_1)^2}}, \qquad n_y = \frac{(x_2 - x_1)}{\sqrt{(y_2 - y_1)^2 + (x_2 - x_1)^2}}. \tag{E.2}$$

2. Calculate the rotation matrix relating the primed (local) and unprimed (global) coordinate systems:

$$[\mathbf{Q}] = \begin{bmatrix} n_y & -n_x \\ n_x & n_y \end{bmatrix}. \tag{E.3}$$

3. Calculate the coordinates of the nearest neighbors in the primed (local) coordinate system:

$$\begin{aligned} \begin{bmatrix} x_1' \\ y_1' \end{bmatrix} &= [\mathbf{Q}] \begin{bmatrix} x_1 - x_0 \\ y_1 - y_0 \end{bmatrix}, \\ \begin{bmatrix} x_2' \\ y_2' \end{bmatrix} &= [\mathbf{Q}] \begin{bmatrix} x_2 - x_0 \\ y_2 - y_0 \end{bmatrix}. \end{aligned} \tag{E.4}$$

4. Fit a parabola of the form

$$y' = ax'^2 \tag{E.5}$$

to the points by performing a linear least squares fit to the system of equations

$$\begin{bmatrix} y_1' \\ y_2' \end{bmatrix} = a \begin{bmatrix} x_1'^2 \\ x_2'^2 \end{bmatrix}, \tag{E.6}$$

which yields

$$a = \frac{x_1'^2 y_1' + x_2'^2 y_2'}{x_1'^4 + x_2'^4}. \tag{E.7}$$

5. The mean curvature is then given by[3]

$$\kappa = -\frac{1}{2}\frac{\partial^2 y'}{\partial x'^2} = -a. \tag{E.9}$$

[3]In an axisymmetric setting, the mean curvature is given as

$$\kappa = \frac{1}{2}\left[-\frac{\partial^2 y'}{\partial x'^2} + \frac{-\left(\frac{n_x}{n_y}\right)}{r\left(1 + \left(-\frac{n_x}{n_y}\right)^2\right)^{1/2}} \mathrm{sign}(n_y) \right], \tag{E.8}$$

where r is the distance from the point to the axis of revolution. The first term is due to the in-plane curvature and the second term is due to the out-of-plane curvature.

The procedure to calculate the mean curvature in three-dimensions is analogous but slightly more complex. In a three-dimensional simulation which uses eight-node, fully-integrated elements (as used in Section 7.4), there are four load integration points per surface element. A schematic of a free surface in a three-dimensional setting is shown in Fig. E-1(b); nodes are denoted by a filled, black circle, and integration points are denoted by an X. To calculate the mean curvature at the point A in this case, we fit a paraboloid through A (with global coordinates (x_0, y_0)) and its *eight* nearest neighbors (enumerated 1-8 in Fig. E-1(b) and with global coordinates (x_i, y_i) for $i = 1, 8$) and use the resulting fit to calculate the mean curvature at A. The details of the procedure are described below:

1. Calculate the components of the local outward surface normal $\mathbf{n} = n_x\mathbf{e}_x + n_y\mathbf{e}_y + n_z\mathbf{e}_z$ in the global coordinate system. This is done by first fitting a plane of the form $z = a_0x + b_0y + c_0$ to the *eight* nearest neighbors. The local surface normal is then calculated as the normal vector to this plane. Its components are given by[4]

$$n_x = \frac{-a_0}{\sqrt{a_0^2 + b_0^2 + 1}}, \qquad n_y = \frac{-b_0}{\sqrt{a_0^2 + b_0^2 + 1}}, \qquad n_z = \frac{1}{\sqrt{a_0^2 + b_0^2 + 1}}. \tag{E.10}$$

2. Calculate the rotation matrix relating the primed (local) and unprimed (global) coordinate systems:[5]

$$[\mathbf{Q}] = \begin{bmatrix} \dfrac{(n_x^2 n_z + n_y^2)}{n_x^2 + n_y^2} & \dfrac{-n_x n_y (1 - n_z)}{n_x^2 + n_y^2} & -n_x \\ \dfrac{-n_x n_y (1 - n_z)}{n_x^2 + n_y^2} & \dfrac{(n_x^2 + n_y^2 n_z)}{n_x^2 + n_y^2} & -n_y \\ n_x & n_y & n_z \end{bmatrix}. \tag{E.11}$$

3. Calculate the coordinates of the nearest neighbors in the primed coordinate system:

$$\begin{bmatrix} x_i' \\ y_i' \\ z_i' \end{bmatrix} = [\mathbf{Q}] \begin{bmatrix} x_i - x_0 \\ y_i - y_0 \\ z_i - z_0 \end{bmatrix} \quad \text{for } i = 1, 8 \text{ (eight nearest points).} \tag{E.12}$$

4. Fit a paraboloid of the form[6]

$$z' = ax'^2 + by'^2 + cx'y' \tag{E.13}$$

[4] As in the two-dimensional case, the normal vector is determined up to its sign, and care must be taken to ensure $\mathbf{n}$ is outward-facing.

[5] This rather complicated rotation matrix represents a rotation of the coordinate axes about the unit vector $\dfrac{(\mathbf{e}_z \times \mathbf{n})}{|\mathbf{e}_z \times \mathbf{n}|}$ aligning $\mathbf{e}_z'$ with $\mathbf{n}$.

[6] As before, in using a local coordinate system with origin located at the point A and z-axis aligned with the local surface normal, the first derivatives of the fitting function, as well as the value of function itself, should be zero at the point. Therefore, these terms are left out of the fitting function.

to the points by performing a linear least squares to the system of equations

$$z'_i = ax'^2_i + by'^2_i + cx'_i y'_i \quad \text{for } i = 1,8 \text{ (eight nearest points).} \tag{E.14}$$

Hence, from the eight neighboring points, we get eight equations for the three unknowns (a, b, c). With $[d]$ denoting a 3×1 matrix for the three unknowns (a, b, c) as its components, $[z]$ denoting a 8×1 matrix with the eight z'_i values as its components, and $[A]$ a 8×3 matrix with corresponding $(x'^2_i, y'^2_i, x'_i y'_i)$ values in each row, the system of equations for determining $[d]$ may be written in matrix form as

$$[A][d] = [z]. \tag{E.15}$$

An optimal solution for this over-determined system is obtained through a linear least-squares fit by using a standard result from linear algebra:

$$[d] = ([A]^\top [A])^{-1} [A]^\top [z]. \tag{E.16}$$

5. The mean curvature is then given by

$$\kappa = -\frac{1}{2}\left(\frac{\partial^2 z'}{\partial x'^2} + \frac{\partial^2 z'}{\partial y'^2}\right) = -(a+b). \tag{E.17}$$

The above procedure was implemented in a DLOAD user-subroutine in Abaqus/Standard [36]. It was verified in finite element simulations using the DLOAD that the correct internal pressure was obtained for simple geometries such as a sphere and a long cylinder. The DLOAD was then used in the simulations reported in Section 7.4.